The Dissertation Committee for Kyle Christopher Klavetter Certifies that this is the approved version of the following dissertation:

Alloy-type and Conversion-type Anode Materials for Enhanced Performance as Lithium Ion Battery Anode Materials

Committee:

_____
Charles Buddie Mullins, Supervisor

_____
Adam Heller

_____
Christopher Ellison

_____
Gyeong Hwang

_____
Simon Humphrey

Alloy-type and Conversion-type Anode Materials for Enhanced Performance as Lithium Ion Battery Anode Materials

by

Kyle Christopher Klavetter, B.S. C. E.

Dissertation

Presented to the Faculty of the Graduate School of

The University of Texas at Austin

in Partial Fulfillment

of the Requirements

for the Degree of

Doctor of Philosophy

The University of Texas at Austin

December 2015

Dedication

To my parents, Elmer and Karen, who taught me to think and create.

To my wife, Kyra, who is my constant companion and support in this work I do.

Acknowledgements

The work presented in this dissertation is the result of individual initiative supported by a team of exceptional mentors, colleagues, friends and family. First, I would like to express my deep gratitude to my advisor, Prof. C. Buddie Mullins, for his enduring commitment to this work. He is a teacher, guide and friend. His presence during these years has been like that of a father, advising in both personal and professional matters. I would also like to thank Prof. Adam Heller for his insight, wisdom and engineering perspective. His approach to this work is a model I shall strive to imitate and has helped shape my worldview as both a researcher and person.

I am also grateful to my collaborators, foremost amongst these being my colleague and friend, Pedro de Souza. It has been an honor to have worked these past four years with someone with such a combination of creativity, dedication, intelligence and character.

To my other undergraduate assistants, I am grateful for your dedication, skill and friendship in the pursuit of our many projects: Sindhu, Julie, Meredith, Han, Mark, Trevor, Katy, Nick and Jon.

The work of an experimentalist requires the manipulation of atoms: things must be purchased, made and maintained. For his tireless and enthusiastic work in design and machining that has proven critical to my research, I thank Shallaco McDonald. I also would like to thank Eddie Ibarra for his help purchasing the many items, large and small; Butch Cunningham for instruction, design and fabrication in the machine shop; Jim Smitherman for his help keeping the labs in good working order; Kate Baird for her administrative assistance; Mike Ronalter and Adam Kennedy for their services in the glass shop; Kevin Haynes for keeping us stocked with the

necessary compressed gases; and Randy Rife and Jason Barborka for keeping our computers running smoothly.

The characterization of my materials has been conducted with the innovation and expertise of several scientists, most especially Andrei Dolocan (ToF-SIMS), Karalee Jarvis (HRTEM), Hugo Celio (XPS), Dwight Romanovicz (SEM/TEM) and Vince Lynch (XRD). Also, to Prof. Ravi-Chandar, who generously provided the Keyence digital microscope for my experiments, I am most deeply grateful.

I would like to acknowledge the many friends and colleagues with whom I have worked: Prof. Ellison whose ideas and collaboration has inspired two projects; Prof. Simon Humphrey for his insight and collaboration along with Dr. Stephany Garcia on one project; Dr. Yong-Mao Lin, my mentor; Dr. Paul Abel, my colleague and teacher; Dr. Alex Rettie, Dr. Joon Hee Cho, Heonjoo Ha and the many other members, past and present, of the Mullins group.

To my parents, brother and wife, I am indebted. They have been the foundation for who I am and what I do. They have supported me, challenged me and inspired me in this work which constitutes the great part of my life.

For financial support, I would like to thank the taxpayer who provided funding for both my graduate fellowship (NSF-GRFP) and the many chemicals, materials and instruments. I would also like to thank the University of Texas at Austin Cockrell School of Engineering for the Thrust 2000 Fellowship.

Finally, I wish to express my gratitude to the Creator of all I study and put to writing my conviction that the mystery and beauty of that which I study could only proceed from the design

and providence of, as Newton once wrote, “an intelligent and powerful Being.” It is my joy to discover what He has made and to imitate Him in the act of creation.

Alloy-type and Conversion-type Anode Materials for Enhanced Performance as Lithium Ion Battery Anode Materials

Kyle Christopher Klavetter, Ph.D.

The University of Texas at Austin, 2015

Supervisor: Charles Buddie Mullins

Charge storage in the contemporary lithium-ion battery is at an energy density too low to support the function of long-range electric vehicles and other electronically powered technologies. To obtain up to two times or greater higher energy density than what is available by intercalation of lithium ions into graphite, the prevalent anode material in commercial batteries, materials with a higher storage density of lithium may be used, including materials that alloy with lithium or undergo a reversible conversion reaction to form lithium oxide.

In this work, several such materials are considered – Ge, SnO_2, Co_3O_4, and $Ge_{0.1}Se_{0.9}$ – and focus is directed to first demonstrating significantly enhanced cycling stability and capacity retention at variable charge/discharge rates and, second, to explaining the electrochemical performance in terms of key physical and chemical properties. Particular attention is given to assessing the formation of the solid electrolyte interphase (SEI) formed upon the anode material during charge/discharge cycling by means of microscopy and chemical characterization.

Table of Contents

List of Tables

List of Figures

Chapter 1: Introduction

MOTIVATION FOR ENERGY STORAGE R&D

The preeminent rechargeable electrical energy storage technology is the lithium-ion battery. Employing the lightest solid, room temperature element with a low red/ox potential (-3.06 V vs SHE) as the ionic charge carrier, the lithium-ion battery employing a graphite based anode and metal oxide cathode can achieve bare cell energy densities in excess of 200 Wh/L and near 600 Wh/L at up to a charge rate of one full charge per *c.*100 minutes and discharge rate of up to one full discharge in 30 minutes (Panasonic NCR18650).[1] Note that in practice, the useable volumetric and gravimetric specific energy densities decrease owing to the need for additional components and to the nature of the quality of deliverable voltage in a battery system (Fig. 1.1).[2]

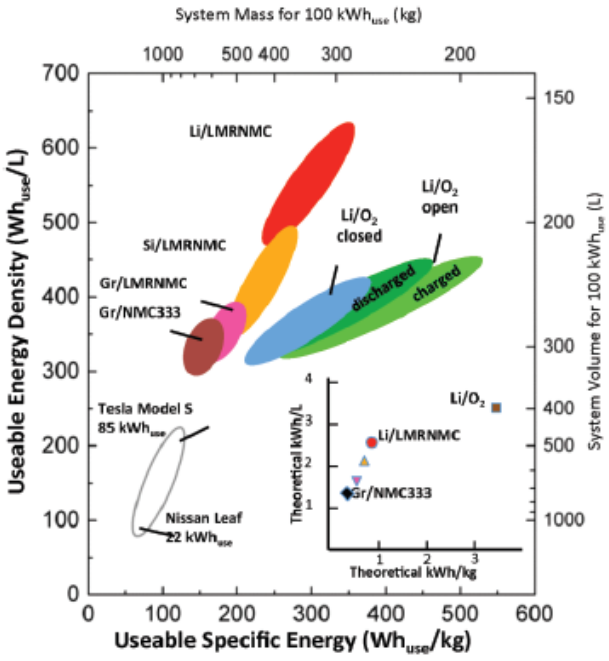

Fig. 1.1 [from Ref. 2] The usable volumetric energy density and gravimetric specific energy for various batteries, assuming science challenges are overcome, such as reversing the lithium-oxygen discharge reaction and protecting pure metal anodes under repeated stripping/plating.

However, dramatic advances in energy density are required to support the range of electronically powered items servicing modern living, including one of the major contemporary technological challenges, the full or partial electrification of vehicles. To accomplish this endeavor, the United States' Joint Center for Energy Storage Research (JCESR) proposes that batteries with 800 Wh/L and 800 Wh/kg at 0.2*C* rate are required.[3] Other metrics including reducing materials and assembly costs, ensuring battery safety, long lifetime and enhancing power density performance are simultaneously critical. To achieve a battery that satisfies these diverse and generally incompatible requirements, something of a technological miracle is necessary. To achieve this, new or significantly enhanced materials are required for nearly all components of the battery, but especially for the anode and cathode charge storage materials.

INTRODUCTION TO LITHIUM-ION BATTERIES

The lithium ion battery is a system that can be considered as a repeating two electrode unit, each capable of storing lithium (as an ion or as an alloyed atom) and electrons. What defines the cathode is that its charge storage material has a high half cell potential (the electrochemist's equivalent measure of Gibbs free energy change) defined relative to the red/ox potential of Li/Li^+. Significantly, this high potential must persist throughout the majority of all phases of charge/discharge, i.e., when the cathode material is Li-poor to when the cathode material is Li-rich. Similarly, the anode is defined by its charge storage material possessing a half cell potential vs Li/Li^+ throughout the majority of all phases of charge/discharge, i.e., when the anode material is Li-rich to when the anode material is Li-poor.

Ion transport between the electrodes is through a dielectric medium (so as to prevent short circuiting) that is ionically conductive through a wide range of temperatures and thermally stable

(so as to diminish to near-zero the possibility of thermal events during battery operation). Additionally, for the popular category of liquid electrolytes, it is also required that the dielectric (salt + solvent) be compatible with a solid membrane that ensures physical separation of the electrodes and, importantly, reduces to form a stable solid electrolyte interphase on the anode during the initial charging of the battery. There currently exist no liquid electrolyte formulations that are thermodynamically stable throughout the entire range of voltages bounded by the operation of typical anode and cathode materials and so their instability must be controlled through self-limiting kinetics.[4] This kinetics, i.e. the electrolyte-electrode reaction rates, can be limited at the anode by a thin, mechanically and chemically stable layer of an ionically conductive but electronically insulating layer, allowing the anode to operate outside of the window of its thermodynamic stability. This layer is referred to as the solid-electrolyte interphase or SEI. A SEM image of some SEI formed upon a micron-sized germanium particle is shown in Fig. 1.2.

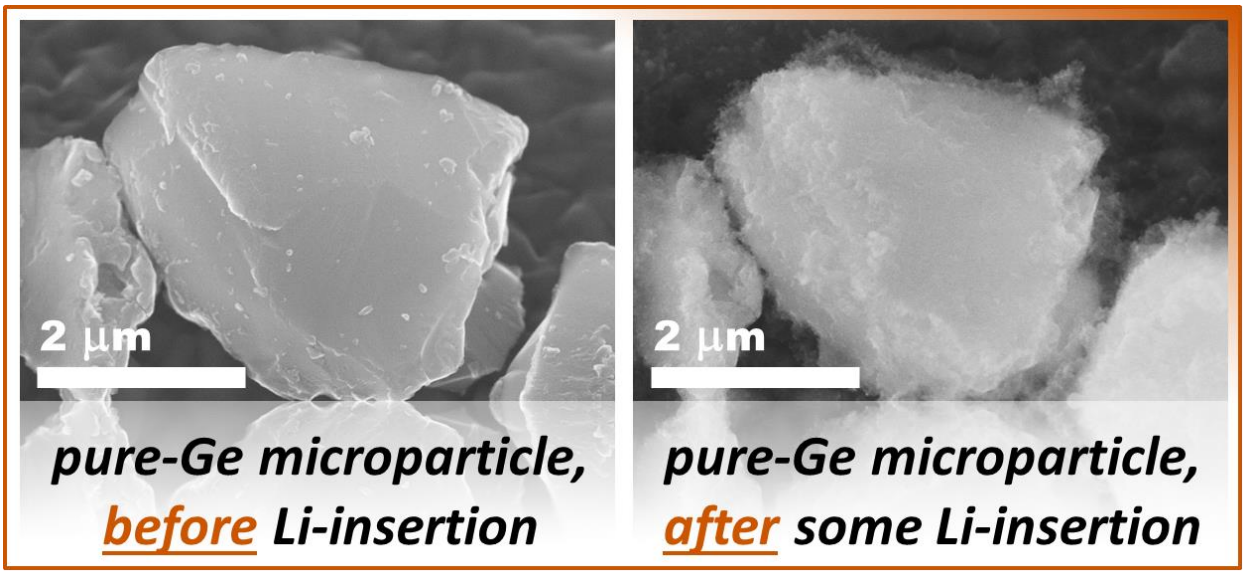

Fig. 1.2 SEM (unpublished work of the author) of Ge microparticle on TEM grid before and after some Li-insertion. The porous material coating the microparticle after Li-insertion is SEI.

Electron transport from the charge storage materials in the electrodes is generally assisted by the incorporation of a network of graphitic nanoparticles (~50 nm diameter) within the electrode infrastructure. Once the electrons reach the substrate supporting the electrode film – this substrate is conventionally a metal foil selected for current conduction, absence of reaction with Li, mechanical properties of durability and flexibility, and resistance to corrosion – they can be easily transported out of the battery terminals and may do work during battery discharge.

To supply a greater density of charge per unit volume or mass of a battery system, R&D efforts can be directed toward the charge storage materials – improving existing materials such as by enhancing electrical conductivity or modifying their particle shape so as to allow for more efficient packing within a defined volume in the electrode film – the polymers holding the charge storage materials, the conductive additive that transports electrical charge within the film, creating alternative electrode architectures by means of redesigned current collectors, improving the ionic conductivity or SEI formed from the electrolyte, etc.[5]

The focus of this dissertation is upon improving the charge storage material for the anode: increasing the density of Li that can be stored per unit mass or volume of charge storage material, improving the useful lifetime of the charge storage material (sometimes by pairing the material with an advanced electrolyte formulation) and increasing the rate at which charge can be stored or removed from the material. For context, as shown in Fig. 1.3, it is important to recognize that given existing cathode materials which only provide up to *c.* 150-200 mA h g^{-1}, there is limited return on increasing the capacity of an anode material beyond *c.* 1000 mA h g^{-1}.[6] However, this value is about three times the existing capacity of the commercially popular graphite charge storage material and so represents what would be a significant improvement in the state of Li-ion battery technology, should it be realized.

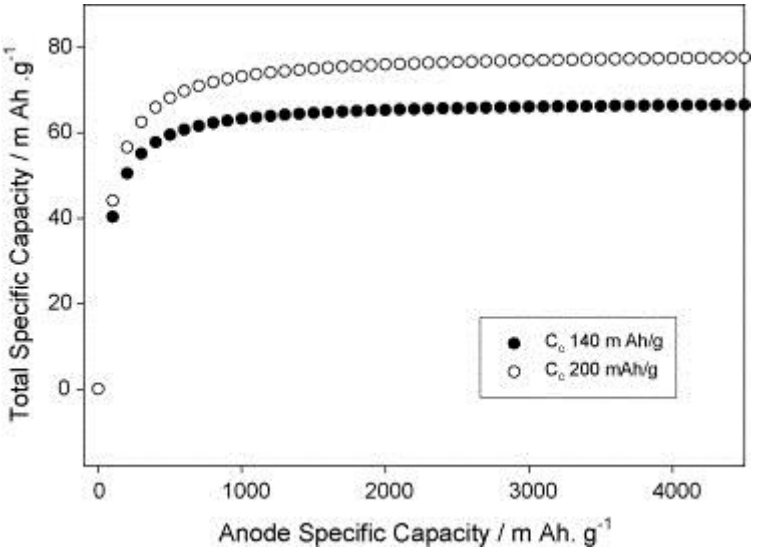

Fig. 1.3 [from Ref. 6] Total capacity of 18650 Li-ion cell as a function of anode capacity (C_A), including masses of other required internal components and case. The capacities of cathodes considered were 140 and 200 mAh g^{-1}.

DISSERTATION OVERVIEW

This dissertation contains six chapters. Chapter 1 provides an introduction to the subject matter, summarizing the chemistry and physics governing the operation of the lithium-ion battery. Design rules for advancing the state of technology from the standpoint of the anode are outlined to provide perspective on the subsequent chapters that detail specific studies of novel anode materials. Chapters 2 – 5 contain studies of a diverse array of alternative anode materials: Ge, Sn, Co_3O_4 and $Ge_{0.9}Se_{0.1}$. The advantages of each anode material are presented, generally in the context of a concurrent evaluation of more than one electrolyte formulation.

In Chapter 2, the performance of a commercial germanium particle anode material is evaluated with conventional carbonate electrolyte $LiPF_6$ in an ethylene carbonate (EC) solvent or in a fluoroethylene carbonate (FEC) solvent substitute. The selection of FEC resulted in dramatically improved cycling performance that was attributed to the formation of a more stable solid electrolyte interphase (SEI). Supporting the electrochemical measurements are transmission electron microscope (TEM) images obtained on ultramicrotomed sections of cross-sections of electrodes.

Chapter 3 considers a commercial, high tap density SnO_2 particle that is contained within a free-standing, flexible film formed spontaneously by the delamination of a drying slurry formed of carboxymethyl cellulose polymer and Super P Li conductive additive in water.

In Chapter 4, a mesoporous cobalt oxide, Co_3O_4, is studied with interest given to whether its array of long, interior 1D channels are retained after extensive charge/discharge testing. With *ex-situ* TEM characterization complementing cycling testing, these channels were found to be preserved from damage after extensive cycling testing in Li-ion and Na-ion cells.

In Chapter 5, a high tap density $Ge_{0.9}Se_{0.1}$ material discovered in this lab by Paul Abel was studied in comparison to pure Ge formed by an analogous synthesis procedure. With high angle annular dark field (HAADF) scanning transmission electron microscopy (STEM) characterization, the inclusion of ~10 atomic percent Se in the Ge was found to prevent particle fracture during cycling tests as the Ge distributed into nanocrystalline domains regularly separated within a Se-Li-Ge containing matrix. This particle has been recently sent to Argonne National Labs for testing in a prototype battery.

A summary of this work and conclusions drawn from it are presented in Chapter 6. Additionally, recommendations on future research directions are given.

REFERENCES

1. P. E. Company, Lithium Ion NCR18650, http://industrial.panasonic.com/lecs/www-data/pdf2/ACA4000/ACA4000CE240.pdf.

2. G. Crabtree, AIP Conference Proceedings, 2015, 112.

3. G. Crabtree.

4. K. Xu, Chemical Reviews, 2014, 114, 11503-11618.

5. J. B. Goodenough and K.-S. Park, Journal of the American Chemical Society, 2013, 135, 1167-1176.

6. U. Kasavajjula, C. Wang and A. J. Appleby, Journal of Power Sources, 2007, 163, 1003-1039.

Chapter 2: A high-rate germanium-particle slurry cast Li-ion anode with high Coulombic efficiency and long cycle life[1]

INTRODUCTION

High-power and energy-dense lithium-ion batteries are desired for portable electronics and wide-spread adoption to power electric vehicles.[1] Transitioning from the commercially-used graphite carbon anode (372 mAh g^{-1}) to metallic silicon, germanium, or various metal oxides could theoretically increase the anode capacity by up to an order of magnitude. However, these electrode materials commonly show capacity fade and inadequate Coulombic efficiencies, particularly at high current densities.

Ge has attracted attention as an alternative anode material because of its large theoretical capacity (1384 mAh g^{-1} or 7366 mAh cm^{-3} corresponding to $Li_{15}Ge_4$),[2-3] high electrical conductivity (10^4 times higher than in silicon)[4-5] and exceptional Li^+ ion diffusivity (400 times greater than in silicon at room temperature).[5-6] Although Ge is about as abundant as tin, there are no concentrated germanium ores and there is very little demand for germanium; for these reasons its price is presently excessive for use in vehicular applications, but applications might be found for mobile electronics requiring long-lasting, energy-dense and high-power batteries.

As in the case of silicon, the repeated volume change in germanium (230%)[5] transitioning to its fully lithiated phase results in large strain gradients that may lead to the cracking and pulverization of particles and the exfoliation of the anode film from the current collector.[7-8]

[1] The content in this chapter has been copied (with minor edits) from its original publication in the *Journal of Power Sources* in 2012.

Freshly-exposed fractured surfaces are coated by reduced electrolyte solvents that decompose to form an electrically insulating solid electrolyte interphase (SEI) through irreversible reactions with Li, resulting in both diminished Coulombic efficiency and capacity fade due to slowed Li-ion transport through the surface film and the electrical isolation of fractured material. [9-11] At high current densities, the effects of mechanical strain are more pronounced, leading to poor cycle life as a consequence of particle fracture [5] and a dynamic, continually degrading and reforming SEI resulting from the instability of the Ge-organic electrolyte interface induced by the particle volume changes.[12-13]

Nanostructured germanium morphologies for thin films,[14-15] nanoparticles, [16-17] nanowires, [18-19] nanotubes,[17] nanocomposites[20-21] and nanocomposite-carbon matrices[22-23] have been investigated in part because small grained materials are known to superplastically deform to accommodate greater than 200% elongation.[24-26] An *in situ* TEM study by Liu *et al.* showed the mechanical robustness of germanium nanowires (40-125 nm diameter) reversibly cycled between bulk germanium and $Li_{15}Ge_4$ in under one minute.[3] The nanoscale morphologies better accommodate high strain[27-28] provide shorter Li diffusion distances[29-30] and, as has been demonstrated recently for some Si-based anode designs,[31-36] may lead to a more stable SEI/active-material interface.

Advances in the design of germanium anode materials through attention to decreasing Li-ion diffusion distances and improving the structural stability of the particle and SEI have led to exceptional high-rate performance in thin film electrodes[14-15,27,37,38] and more recently to potentially manufacturable slurry cast films. [7,17-19,39] For example, Cho and co-workers reported high rate capacity, slurry cast germanium anodes with stable performance at high rates for up to many hundreds of cycles by using novel nanotube,[7] honeycomb[17] and nanostructured clustered

germanium/carbon morphologies.[39] In these electrodes, the Ge particles used were specifically designed for fast Li diffusion and, moreover, partially or fully shielded from contact with the electrolyte or designed to allow for volumetric expansion away from the SEI into empty space. For the nanostructured clustered germanium/carbon morphologies, after capacity fade from an initial capacity close to 1200 mAh g^{-1}, a stable specific capacity of 360 mAh g^{-1} was reached after 100 cycles at 40*C* (64 A g^{-1})[39] and minimal capacity fade was observed for 400 cycles at 0.3/0.6*C* (0.5/1.0 A g^{-1}) lithiation/delithiation rates.[7]

Recently, Chockla *et al.* reported an alternative means to improving the SEI/particle interface stability by using fluorinated ethylene carbonate (FEC) based electrolytes for the slurry cast germanium nanowire-based to achieve stable cycling performance.[40] Here we expand upon this work and similar research into the use of FEC for Si-based electrodes,[41-44] studying the evolution of the Ge/EC-based and Ge/FEC-based electrode systems through many cycles with electrochemical testing and detailed study of the electrode architecture by SEM and TEM to demonstrate the effectiveness of the FEC-based electrolyte.

Without the mechanical advantages and short Li-diffusion distances of nanowires as an active material like those used by Chockla et al., and without the improved SEI stability that might otherwise be obtained by using Ge nanostructures intentionally designed to address the repetitive volumetric expansions and contractions that continuously degrade the Ge nanoparticle/SEI interface,[35] we report much improved electrode performance, with higher capacity, Coulombic efficiency and specific power output over longer cycle lifetimes for a slurry cast Ge-based electrode. Made with poly-disperse, untailored, commercially-scalable Ge nanopowder and using a FEC-based rather than EC-based electrolyte, the electrode described herein achieves stable performance throughout a 2,500 cycle variable, high *C*-rate test (through nine, successive 200-

cycle iterations at 1*C*, 5*C* and 10*C* followed by 700 cycles at 1*C*, *C*=1.624 Ah g^{-1}) and a capacity near 700 mAh g^{-1} at 10*C* rate with an average Coulombic efficiency near 100% through 500 cycles. Capacities over 1000 mAh g^{-1} were observed when discharging the electrode at up to 20*C* while charging at 1*C* and a capacity of 425 mAh g^{-1} was achieved for a discharge rate of 50*C*. These results complement the recent progress in slurry cast Ge-based electrode research which has focused on improving cycling performance through structural and chemical modifications to the active material. The notable cycling stability of the electrode in FEC-electrolyte, sustained through both extended cycling and high *C*-rate testing, indicates that the improved performance may be found in the role of FEC forming a SEI that better protects the Ge nanoparticle active material from contact with the electrolyte, a consequence of the different surface films likely rich in lithium fluoride, alkoxy and polycarbonate species which have been found to be the result of FEC reduction[43,45]. This results in higher CE as a consequence of a more stable SEI/particle interface, and, from considering the evolution of the electrode differential capacity profiles, an enhanced stability toward oxidation that significantly delays capacity fade and corresponding oxidation of the Ge nanoparticle active material, a finding analogous to the result recently reported by Etacheri et al. in their study on FEC and Si NW[45]. Herein we report how the FEC-based electrolyte with a Ge-based electrode is an effective means to improving the SEI so as to minimize irreversible losses and better protect the Ge nanoparticle from oxidation, thereby improving the battery performance parameters of interest: long cycle life, specific capacity, capacity retention, Coulombic efficiency and high *C*-rate capability.

EXPERIMENTAL METHODS

Ge nanoparticle electrode preparation and battery assembly. Ge nanoparticles (99.9%, American Elements) were used as the active material in the electrode. The reported average

particle size was 70-120 nm. However, the actual particle size distribution ranged up to several microns (a typical TEM of Ge particles after dispersing via sonication is shown in Supplementary Information Figure SI.2.1). Slurries of 40:20:40 w/w/w Ge nanoparticles:poly-acrylic acid binder (PAA-450 kDA, Sigma):Super-P Li conductive additive (Timcal) with ethanol as solvent were cast on a copper foil current collector to prepare the electrode for battery testing. This film, composed of a high weight fraction of conductive additive, was selected to diminish the effect on cycling performance of losing a sustained electrical percolating network as a consequence of particle shifting due to the volumetric expansion and contraction of the Ge nanoparticles during cycling after preliminary screening for slurry compositions with a film composed of 80:10:10 w/w/w (Ge nanoparticles:PAA-450 kDA:Super-P Li conductive additive) showed capacity fade after only 100 cycles at a rate of 1*C*: 0.49 mAh g^{-1} (or 0.05%) capacity fade per cycle with an areal capacity of 0.26 mAh cm^{-2} (Supplementary Information Figure SI.2.2). The contribution of this high content of conductive additive to the specific capacity of the 40:20:40 w/w/w electrode was estimated to be near ten percent (Supplementary Information Figure SI.2.3). For the electrode binder, PAA, demonstrated to have enabled better cycling stability for Si-based electrodes,[46] was selected rather than the typically polyvinylidene fluoride (PVDF) after a preliminary binder screening cycling test (Supplementary Information Figure SI.2.4). In a typical procedure, the slurry is mixed and probe-sonicated (1/4" tip, QSonica) prior to being doctor-bladed onto Cu foil. The film is dried overnight at 120°C and then 11 mm diameter circular electrodes are hole-punched. The typical electrode mass loading used here of 300-500 μg cm^{-2} delivers an areal capacity of 0.15-0.06 mAh cm^{-2} (for 1*C* – 10*C* rates), an order of magnitude lower than current commercial anodes such as the 18650 cell (4 mAh cm^{-2}).[47] From TEM cross-sectional imaging (Supplementary Information Figure SI.2.5) the electrode density is estimated to be near 0.9 mg/cm^3 (0.35 mg of

Ge nanoparticle/cm^3). The electrodes are assembled in an Ar-filled glovebox (<0.1 ppm O_2) with a Li foil (Alfa) counter/reference electrode and Celgard 2400 membrane separator (25 μm in thickness) in 2032 stainless steel coin cells. The effect of the Li-plating/dissolution kinetics in the electrolytes studied herein, particularly at high current densities, was evaluated (Supplementary Information Figure SI.2.6) by testing coin cells made of two electrodes of Li foil assembled in a similar manner as for the Ge nanoparticle based electrodes. The electrolyte was composed of either 1M $LiPF_6$ (≥ 99.99%, Aldrich) in ethylene carbonate/di-methyl carbonate (EC/DMC, 1:1) (LP30, EMD Chemicals), selected as representative of the conventionally used EC-based electrolytes for the typical Ge-based electrode, or 1M $LiPF_6$ in FEC (> 99%, Solvay Fluor)/diethyl-carbonate (DEC, ≥ 99%, Aldrich) (1:1, v/v), the electrolyte shown by Chockla, et al. to have enabled the best cycling performance.[40] The Solvay product was used because FEC procured from MTI and TCI America was observed to decompose into a black-colored liquid. To assess the performance of electrodes made using more active material and with higher mass loadings (greater than 1300 μg/cm^2), additional cycling tests (Supplementary Information Figure SI.2.7) were done with a slurry of 60:20:20 w/w/w Ge nanoparticle:PAA: Super-P Li conductive additive.

Electrode characterization. Scanning electron microscopy (SEM) images were acquired using a Hitachi S5500 SEM with an accelerating voltage of 10 kV and current of 20 μA. The electrodes were prepared for SEM after soaking in DMC overnight and were exposed to air for less than 60 seconds during transfer from a vacuum transfer box into the SEM high vacuum chamber. Transmission electron microscopy (TEM) images were acquired using either a FEI Tecnai Spirit BioTwin TEM operated at 80kV or a field emission JEOL 2010F TEM operated at 200 kV. TEM samples were prepared by ultramicrotome sectioning of epoxy-embedded electrodes

to 50-70 nm thicknesses using a diamond knife (35° Ultra, DiATOME). A detailed description of the sectioning procedure is provided in the Supporting Information.

An electrochemical analyzer (CHI 604D, CHInstruments) was used for electrochemical impedance spectroscopy (EIS), measured over a wide frequency range from 100 kHz to 0.001 Hz with an AC perturbation voltage of 5 mV. Cells were poised at the selected potential for longer than 5 minutes before taking the spectra.

The electrode performance was measured using a multichannel battery test system (BT 2043, Arbin) to run cycling tests with constant current between 0.01 and 1 V vs Li/Li^+. For all tests done, a conditioning cycle at *C*/20 was run in order to form a consistent SEI prior to commencing the testing schedules at high *C*-rates. Capacity values are reported as the Li-extraction capacity and are based upon active material only. Although $Li_{15}Ge_4$ is the ultimate phase thermodynamically achievable for electrochemistry done at room temperature, for the convenience of the reader who might compare these results with those in previous literature, the cycling rates are reported based on the $Li_{22}Ge_5$ theoretical capacity, i.e., 1*C*=1624 mAh g^{-1}. The specific capacity values reported in the text are gravimetric, specific to the mass loading of the Ge nanoparticles in the electrode. For the cycling data presented in graphical form, the specific gravimetric capacity, specific to the mass loading of the Ge nanoparticles and also, as denoted in bracketed values on the primary ordinate axis, specific to the mass loading of the electrode film (made of Ge nanoparticles, binder and conductive additive), is provided. The CE values are reported with an uncertainty of up to 0.2%, reflecting the level of accuracy in current measurement on the Arbin battery testers. Four separate Arbin battery tester units were used to test cells in an effort to increase confidence in the repeatability of the reported data and also in order to minimize the extent to which instrument error impacted the reported data; the CE values reported for the

selected tests are representative of several results from each Arbin tester used. The terms charge and discharge are used as they would be for a full Li-ion cell, with discharge referring to Li-extraction from the Ge electrode.

RESULTS AND DISCUSSION

Ge Nanoparticle Li-Ion Cell Performance

Li-ion cells with Ge nanoparticle anodes were tested using poly-acrylic acid (PAA) binder, conductive carbon (2:1:2 w/w/w Ge:PAA:C) and 1.0M $LiPF_6$ electrolyte in two mixtures of carbonates. Figure 2.1 shows the reversible capacity of electrodes cycled 600 times between 0.01 and 1 V vs Li/Li^+ at a rate of 1*C* (200 cycles), 5*C* (200 cycles) and 10*C* (200 cycles). As reported, [19,42,48] the use of fluorinated carbonates as co-solvents or as additives was found to improve electrode performance, resulting in stable performance, higher Coulombic efficiencies and higher capacities.

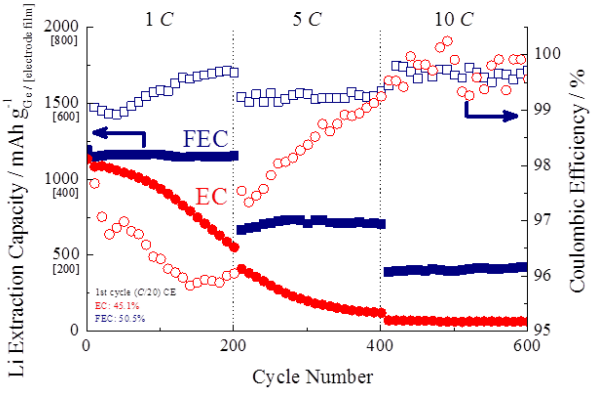

Figure 2.1: Cycling performance of Ge nanoparticle electrodes tested at 1C, 5C and 10C in EC/DMC and FEC/DEC electrolytes

During the first cycle, the electrode tested in FEC:DEC showed marginally improved CE compared to when tested in EC:DMC, 50.5% vs. 45.1%, likely reflecting a thinner SEI as has been reported by others for Si-based systems tested with FEC. [44-45] After 200 cycles at 1*C*, the anode cycled in FEC/DEC yielded a capacity of 1152 mAh g^{-1}, corresponding to a negligible gain of 0.18% relative to the 10th cycle. (The 10th cycle was selected as the basis for comparison because the cycling behavior for the electrode showed capacity increase during the first several cycles before reaching a relatively stable value: selecting an earlier cycle than the 10th would artificially inflate the capacity retention values reported.) During this period, the Coulombic efficiency increased from 99.1% to 99.7%. From the 10th to 200th cycle, the anode tested in EC/DMC showed significant capacity fade, decreasing from 1083 to 552 mAh g^{-1}, and its Coulombic efficiency fell from 97.7% to 96.0%. Through the first 200 cycles of testing, the electrode cycled in EC/DMC is calculated to have accumulated greater than 2 μg of Li per μg of Ge nanoparticle as a result of irreversible losses. By comparison, through the same number of cycles, the electrode cycled in FEC/DEC accumulated only 0.74 μg of Li per μg of Ge nanoparticle, with 41% of this irreversible consumption of Li occurring during the first cycle (as compared with only 17.5% for the electrode cycled in EC/DMC). Even after 2,500 cycles of testing at variable *C*-rates, the electrode cycled in FEC/DEC only accumulated marginally higher irreversible losses than the electrode cycled in EC/DMC for 200 cycles: 2.4 vs 2.0 μg of Li per μg of Ge nanoparticle.

At higher rates, the differences in performance were more pronounced. From the 210th to 400th cycles run at 5*C*, the anode cycled in FEC/DEC retained over 60% of the 1*C* capacity and cycled stably, showing a slight increase in capacity from 667 to 706 mAh g^{-1}. During this period, the anode cycled in EC/DMC showed continued capacity fade from 410 to 121 mAh g^{-1}. From the 410th to 600th cycles run at 10*C*, the anode cycled in FEC/DEC retained about 35% of the 1*C*

capacity and cycled stably, showing a slight increase in capacity from 389 to 423 mAh g^{-1}. When at 10*C*, the anode cycled in EC/DMC showed very low capacities, ranging from 72 to 62 mAh g^{-1}.

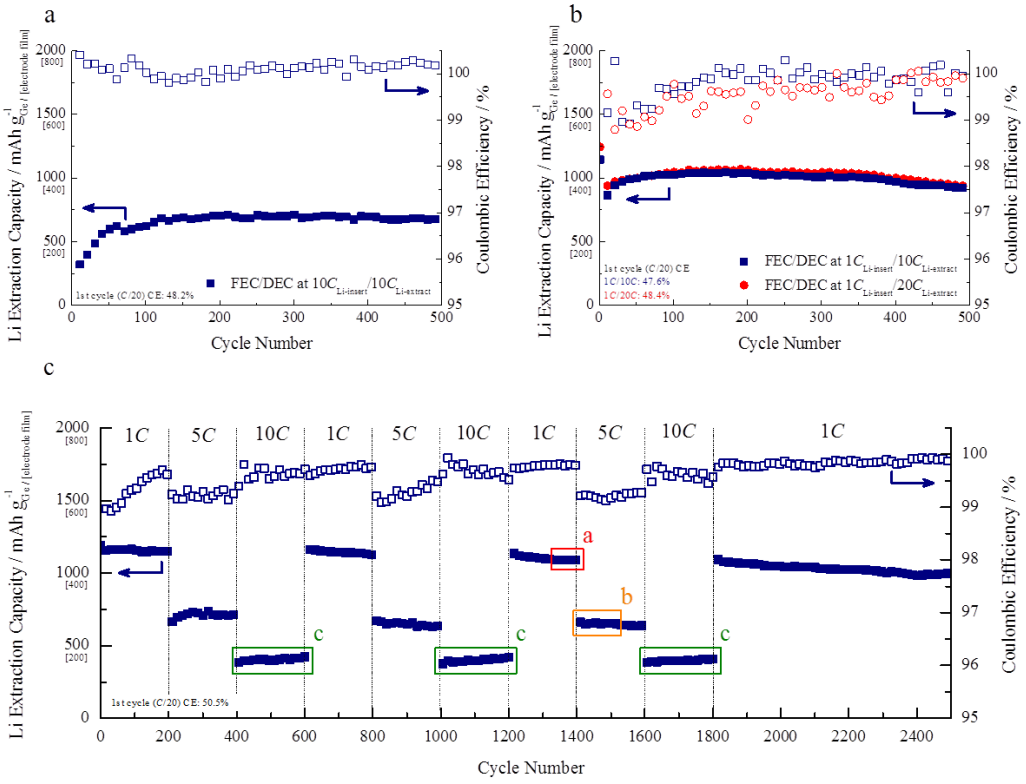

Figure 2.2: Cycling performance of Ge nanoparticle electrode cycled in the FEC/DEC electrolyte (a) at 10C, (b) at 10C or 20C discharge rate with 1C charge rate and (c) at intervals of 1C, 5C and 10C through 2,500 cycles.

Long-cycle life was also observed for the electrode cycled 500 times in the FEC/DEC electrolyte at 10*C*. Interestingly, a separate cycling test (Figure 2.2.a) showed that the anode cycled in FEC/DEC demonstrates capacities of near 700 mAh g^{-1} and high Coulombic efficiencies

between 99.8-100.2% when tested for 500 cycles at 10*C* without prior extended testing. These results were also found for a variable rate test at 1*C*, 5*C* and 10*C* when the anode cycled only 100 times at each rate (Supporting Information Figure SI.2.8). From the 10th to the 100th cycle tested at 1*C*, there was an increase in capacity from 1144 to 1186 mAh g^{-1} with a corresponding increase in Coulombic efficiency from 99.2% to 99.3%. During the 110th to 200th cycles run at 5 *C*, the anode retained 75% of the 1*C* capacity and cycled stably, showing an increase in capacity from 870 to 929 mAh g^{-1} and Coulombic efficiencies between 99.7-99.9%. When tested at 10*C* in FEC/DEC, the electrode retained over 53% of the 1*C* capacity and cycled stably, showing an increase in capacity from 631 to 657 mAh g^{-1} and lower Coulombic efficiencies between 99.0-99.4%. Electrodes tested at these and other high rates in the EC/DMC electrolyte were observed to perform poorly, showing either negligible capacities or severe capacity fade.

These cycling results done with commercial Ge nanoparticles in an electrode matched with an FEC-based electrolyte build upon the recent body of work done in improving the state of Ge-based slurry-cast anodes, notably by Park et al., who reported only minimal capacity fade for a Ge nanotube based anode from an initial value near 1000 mAh g^{-1} through 400 cycles at 500 mA g^{-1} / 1000 mA g^{-1} (~0.3/0.6*C*) charge/discharge high rate, although capacity fade from near 750 mAh g^{-1} was observed over the 5 cycles shown at 1000 mA g^{-1} (~0.6*C*).[7] Chockla et al. recently reported[19] capacities of >1000 mAh g^{-1} after 300 cycles for a Ge nanowire based anode using a current density of 138 mA g^{-1} (~*C*/12). When tested at 1.38 A g^{-1} (~0.85*C*) the capacity dropped but was stable near 700 mAh g^{-1} for over 1000 cycles. Seng et al. reported impressive high rate capabilities up to 40*C* but still capacity fade was evident at all rates, with the capacity retention at 1*C* testing being 74% after 120 cycles.[39] Xue et al. reported observing 50 cycles at high capacities

but with capacity fade and low Coulombic efficiencies (91%) for a nanocomposite anode cycled at 1600 mAh g^{-1} (1*C*).[21]

High C-rate performance

For certain applications requiring high current densities such as in the acceleration of an electric vehicle, the capability to rapidly discharge the anode is desired. The Ge nanoparticle based electrodes in FEC/DEC were subjected to long-term cycling tests with two discharge rates in which the charge rate was held constant at 1*C*. This test was done because the Li transport through the SEI and Li-insertion process is known to be the limiting step in the cycling of the cell, where Li plates on the surface of the particles when charged above a critical current density, as is similarly the case for the graphite-based anode.[49] When the highly charged Ge nanoparticles were discharged, unlike for the graphite anode which undergoes small volumetric contraction during de-intercalation of its stored Li, the Ge nanoparticles volumetric contraction during these high *C*-rate tests is estimated to be near the theoretical value given the high capacities observed (near 1000 mAh g^{-1}). Despite the strain endured during the short time allowed for the morphological transition during these tests, the Ge nanoparticles perform with high capacity and high CE through many cycles, suggesting that the FEC-derived SEI enables a stable SEI/particle interface. As was shown by Chockla et al.[40] for Ge nanowire-based slurry cast films, we observed good capacity retention for a discharge rate of 10*C* or 20*C* (Figure 2.2.b) through 500 cycles, and also with very high capacity retention for the electrodes discharged at different rates. The maximum capacity attained for the 10*C* discharge rate anode was 1049 mAh g^{-1} (cycle 170) and the 20*C* discharge rate anode was 1069 mAh g^{-1} (cycle 191) after which gradual capacity fade was observed. The capacity retention at the 500th cycle for the 10*C* discharge rate anode was 86.8% of the maximum value and the 20*C* discharge rate anode was 87.7%. For both cells, the fast rate of Li-extraction led to high

Coulombic efficiencies, averaging 99.8% (10*C*) and 99.6% (20*C*) from the 5th to 500th cycles. When the cell was discharged at 50*C* rate (discharge completed in 19 seconds), we observed a capacity near 425 mAh g^{-1} for close to ten cycles (Supplementary Information Figure SI.2.9). After this initially stable cycling performance, this rapid discharge testing (at 50*C*) resulted in unusual behavior in which the Li-extraction capacity gradually increased and exceeded the Li-insertion capacity for each cycle through the 250th cycle. It is conceivable that overheating damaged the separator membrane[50] or that the high overpotential required for Li plating during discharge was the cause of this result. Further testing done using Li foil treated with tetraethyl orthosilicate[51], a process intended to minimize the growth of dendrites and to diminish impedance of Li^+ ion transport at the Li foil, showed improved cycling stability at this high discharge rate (Supplementary Information Figure SI.2.10).

Long-term cycling performance and stability

Long term stability was examined for the Ge-nanoparticle-based electrode cycled in FEC/DEC using an 2,500 cycle test with sequential 200 cycle intervals at rates of 1*C*, 5*C* and 10*C* (Figure 2.2.c). A table detailing the performance and capacity retention of this electrode may be found in the Supplementary Information Table SI.2.1. Because the useful lifetime of a battery is measured by the cycles for which its capacity retention is greater than 80%,[52] the capacity retention after the second, third and fourth sets of 1*C* testing is considered here and found to be 97.8%, 94.8% and 87.0% (through 800, 1400 and 2,500 cycles, respectively) as compared to the capacity achieved during the initial 1*C* testing after the electrode attained a relatively steady capacity by cycle 10. For this extended cycling, the Coulombic efficiency was marginally improved from nearly 99.7% to fractionally above 99.8% for cycles 800, 1,400 and 2,500. We observed that during the third set of 1*C* cycling (from cycles 1200-1400), the electrode performance improved after

showing a typical rate of capacity fade (about 0.4 mAh g^{-1} per cycle), stabilizing between cycles 1330 and 1400. Through these cycles there was less than 2 mAh g^{-1} total capacity fade (corresponding to a 0.1% change, shown in red-lined box, *a*, in Figure 2.2.c and in Supplementary Information Figure SI.2.11a). This stable cycling performance continued through over the next 100 cycles tested at 5*C* (shown in the orange-lined box, *b*, and in Supporting Information Figure SI.2.11b) before gradual capacity fade at a rate of about 0.25 mAh g^{-1} per cycle resumed. When testing at 10*C* (shown in the green-lined boxes, *c*), we observed that the cycling performance showed marked capacity increase throughout each 200 cycle series. It may be that this better-than-stable-cycling behavior is due to minimal fracturing of the SEI/Ge nanoparticle interface which undergoes limited volumetric expansion when the Ge nanoparticles are being only partially lithiated at this high *C*-rate. During the last 50 cycles tested at 1*C*, the response to the dramatic change in rate from 10*C* to 1*C* was observed to stabilize after about 30 cycles (shown in the purple-lined box, *d*, and in Supplementary Information Figure SI.2.11c) in a manner similar to what was observed for the performance between cycles 1200-1400.

Voltage Profiles, Differential Capacity Plots

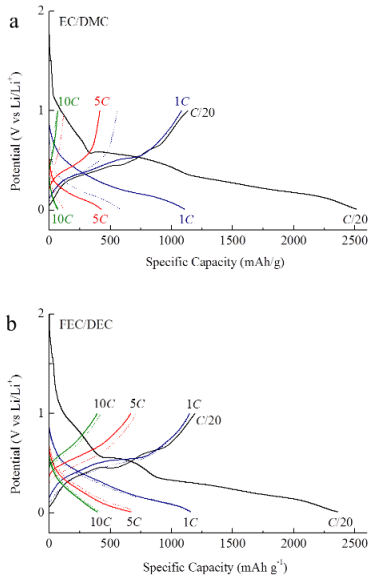

Figure 2.3: Voltage profile for Ge nanoparticle electrode cycled in EC/DMC for 601 cycles: 1 conditioning cycle at C/20 followed by 200 cycles at 1C, 200 cycles at 5C and 200 cycles at 10C with (a) EC/DMC as the electrolyte and (b) FEC/DEC as the electrolyte. Solid/dotted lines represent data from the 10th/200th cycle in each series.

Figure 2.3 shows the voltage profiles at variable high *C*-rates for Ge-nanoparticle electrodes cycled in the EC/DMC and FEC/DEC electrolytes. Information about the evolution of bulk Li_xGe phase transitions and the irreversible reactions, particularly the formation of the SEI, is obtained from the cycling voltage profiles shown in differential form (Figure 2.4).

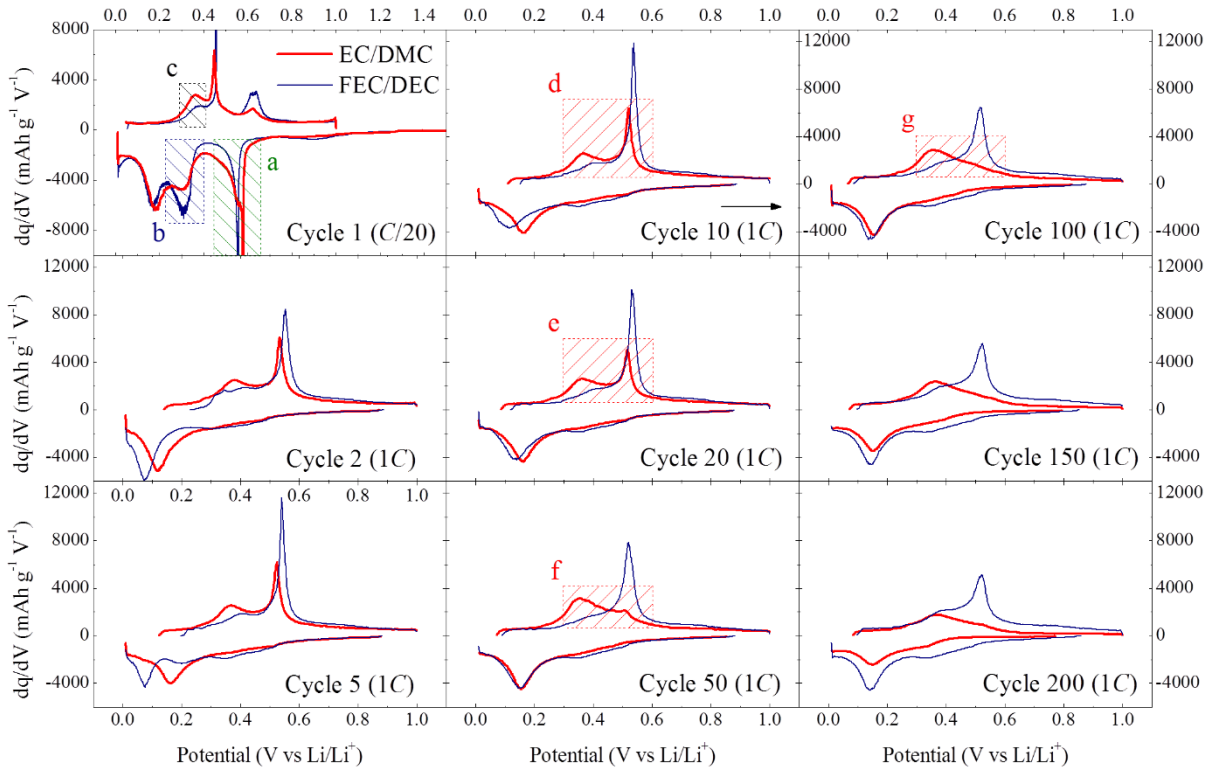

Figure 2.4: Differential capacity profiles for Ge nanoparticle electrodes cycled in EC/DMC (red line) and FEC/DEC (blue line) with the initial cycle at *C*/20 and the remaining 199 cycles at 1*C*.

The contribution of the Li foil to the overpotential required to charge/discharge the electrode is estimated to be near half of the operating voltage measured for the stripping/plating of Li in coin cells made using the EC and FEC based electrolytes with Li foil as both the positive and negative electrodes (Supplementary Figure SI.2.6). When at high current densities (approximating the 10*C* rate tests done on the electrodes of relatively small mass loadings reported here), the overpotential required for plating/stripping of Li begins to become significant and is estimated to be near 75 mV. Notably, cycling the Li vs Li cells tested in FEC:DEC consistently required higher overpotentials than those tested in EC:DMC.

The first cycle differential capacity profile (Figure 2.4) shows that both electrodes possess the same sequence of Li-insertion and Li-extraction features. The initial reduction of the electrolyte to form SEI is shown in Supplementary Information Figure SI.2.12a. As has been reported previously for a Si-based anode,[44] the reduction of FEC begins at a lower overpotential than that for EC. After this initial SEI formation feature occurs, another larger irreversible feature near 550 mV (highlighted in the green-lined box, marked *a*) which for the electrode cycled in EC/DMC is broader and larger than that for the electrode cycled in FEC/DEC. This corresponds to the lower first cycle Coulombic efficiency reported for the EC/DMC electrode, 45.1% vs 50.5% (at *C*/20) for the electrode cycled in FEC/DEC.

For the first cycle, the Li insertion behavior is changed depending upon the electrolyte used, as depicted in Figure 2.4. The first Li insertion feature at 310 mV (highlighted in the blue-lined box, *b*) for the electrode cycled in EC/DMC is smaller in magnitude, both in comparison to the feature of the electrode cycled in FEC/DEC and when compared to the second Li insertion feature at 175 mV. These two Li-insertion peaks likely correspond to the two-step mechanism through which Li first inserts as a nearest neighbor to Ge in the Ge crystal lattice prior to a second wave of Li insertion to sites where Li is primarily surrounded by other Li.[53] As reported by Baggetto, et al.[9] in their in-situ XRD study of deposited Ge thin films, no known Li_xGe crystalline phase forms (although several amorphous transitions were believed to have been observed) during the Li-insertion process before the ultimate thermodynamically-accessible phase, $Li_{15}Ge_4$ is attained between 130 and 30 mV, a finding with which the small Li-insertion feature observed in this study near 50 mV is consistent. Additionally, Baggetto etl al reported evidence for short range ordering of the LiGe and then Li_7Ge_2 phases[2] through making measurements of Ge-Ge and Ge-Li interatomic distances using in-situ X-ray adsorption spectroscopy during Li-insertion which may

correspond to the two defined Li-insertion peaks observed in this study near 120 and 75 mV. The two prominent Li-extraction features may be explained by the reversal of these phase transitions, proceeding back to de-lithiated Ge nanoparticles via the local coordination reflecting the $Li_{15}Ge_4$ / Li_7Ge_2 phase transition (near 360 mV) and Li_7Ge_2 / LiGe phase transition (near 530 mV).

In the first cycle, the Li extraction behavior for the electrodes tested in the two different electrolytes is likewise similar in kind, but not in magnitude, with a larger fraction of the Li extraction occurring for the electrode cycled in EC/DMC at the feature near 350 mV (highlighted in the black-lined box, *c*). This extraction feature corresponds to the larger insertion feature seen in the EC/DMC electrode at 175 mV. At 450 mV, a sharp peak appears superimposed on the broader Li extraction feature with its peak at 350 mV. This sharp feature, also observed by Chockla et al.,[19] has little magnitude and is observed for both electrode systems, possibly corresponding to a two-phase transition in which Li extracts from the small amount of crystalline $Li_{15}Ge_4$. Although the major Li-insertion features are observed with 135 mV spacing, the last significant oxidation feature is observed near 630 mV, close to 280 mV after the first extraction feature, and in subsequent cycles this feature does not appear. For the electrode cycled in FEC/DEC, a small shoulder feature is observed 750 mV, and, for the electrode cycled in EC/DMC another feature is observed to grow as the upper voltage limit (1.0 V vs Li/Li^+) is approached (Supplementary Information Figure SI.2.12b). The location of these two minor features appearing at high potentials and exclusive to the first cycle suggests that they may represent partial the oxidation of the large amount of SEI formed in this cycle.

The second cycle differential capacity profiles reflect the lithiation of a more amorphous material, showing broad Li-insertion features with peaks at 120 mV and 75 mV for the electrodes cycled in EC/DMC and FEC/DEC respectively. For both electrodes, although more noticeably for

the electrode cycled in FEC/DEC, a shallow, broad feature was observed between 500 and 250 mV. The Li-extraction for the electrode cycled in EC/DMC began at 140 mV, far lower than the 227 mV for the electrode cycled in FEC/DEC. This difference in the initial discharge potential was seen throughout the 200 cycles examined and reflects significant differences in the polarization of the two electrode/electrolyte systems after Li-insertion. The higher potential at which the differential capacity profile begins for the electrode tested in FEC/DEC may reflect a more rapid Li-diffusion rate of Li deposited or alloyed near the surface of the active material particles into the bulk of the material. By the 200^{th} cycle this disparity in the polarity between the two electrodes following Li insertion was lessened to about 15 mV as a result of the initial discharge potential for the electrode tested in FEC/DEC decreasing throughout testing. After the electrode cycled in EC/DMC began to exhibit significant capacity fade after about its 50^{th} cycle, a similar divergence between the electrodes in their initial charging potential was observed. From the 50^{th} to 200^{th} cycles, the initial charging potential for the electrode tested in EC/DMC following Li extraction decreased from 857 mV to 770 mV while that of the electrode cycled in FEC/DEC only marginally decreased from 883 to 859 mV, indicating more facile Li extraction for this electrode system. The plot of the relaxation currents for the cycles discussed here is in Supplementary Information Figure SI.2.13.

Throughout the first 20 cycles, during which there was a marginal increase in capacity for both electrodes, the Li-insertion features for the electrode cycled in FEC/DEC continuously evolved as its primary Li-insertion peak shifts to lower overpotentials, from 75 mV (cycle 2) to 140 mV (cycle 20). The shift of this peak in the electrode cycled in EC/DMC was less pronounced, from 120 mV (cycle 2) to 160 mV (cycle 20). Although there were as many as three identifiable Li-insertion features observed for the FEC/DEC electrode (cycle 5), by cycle 20, these merged

into one broad, flat feature that remained constant throughout the remainder of the 200 cycle testing. This observation suggests that after the first several cycles, the successive phase transitions from the initially crystalline Ge proceeded through amorphous Li_xGe phases, not through alloys with long-range lattice order that would transition through distinct voltage windows. During these first 20 cycles, the Li-extraction features for both electrodes were relatively constant. At cycle 20, a smaller, broader feature was seen at 360 mV for the EC/DMC electrode before a sharper peak at 515 mV. For the electrode cycled in FEC/DEC, a broad shoulder rather than distinguishable peak was observed, beginning at 285 mV before merging with the sharp peak (530 mV) similar to that seen in the profile for the EC/DMC electrode.

After the 20th cycle, as capacity fade in the electrode cycled in EC/DMC became apparent, the Li-extraction behavior for this system changed. Highlighted by the red-lined boxes (labeled d-g) in Figure 2.4, the ratio of the magnitude of the broad feature (360 mV) to the sharp peak (515 mV) increased, with most of the Li extraction occurring at lower potentials. By cycle 100, there was no noticeable peak near 515 mV, although the Li insertion behavior for the electrode remained unaltered. After cycle 100, there was only a change in magnitude, not a change in kind, of the differential capacity profile for the electrode cycled in EC/DMC. The features present in the 100th cycle profile diminished in magnitude in proportion to one another. In contrast to the change in the Li-extraction behavior for the EC/DMC electrode, the differential capacity profiles reflect the enhanced cycling stability of the FEC/DEC electrode. By the 200th cycle, the sharp peak observed in cycle 20 had broadened but otherwise the features remained nearly identical in both magnitude and shape. The significance of this difference in the differential capacity profiles between the two electrode systems is further discussed in section 4.2.

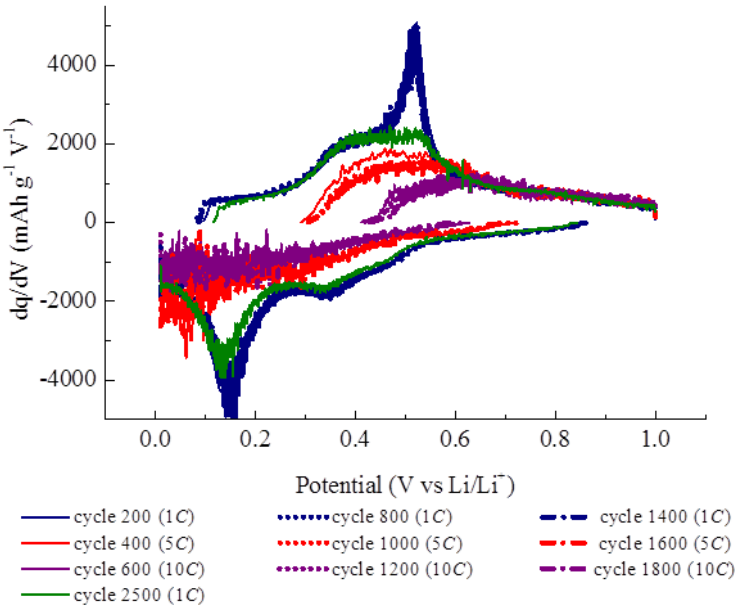

Figure 2.5: Differential capacity profiles for Ge nanoparticle electrodes cycled in FEC/DEC after 1C (blue lines), 5C (red lines), 10C (purple lines) after the first (solid line), second (dotted line) and third (dashed lined) cycle sets. The green line indicates the differential capacity profile for the 2,500th cycle, after 700 cycles at 1C following the third set of high rate testing.

In Figure 2.5, differential capacity profiles are shown for the last cycle in each of the 200 cycle series that made up the long-term cycling test for the FEC/DEC electrode. The three nearly identical 1*C* profiles (separated by intervals of 600 cycles of cycling at 5*C*, 10*C* and then 1*C*) shown for the electrode demonstrate the thermodynamic reversibility of this electrode system. There was a slight attenuation in the amplitude of the profile of the 800th cycle compared with that observed for the 200th cycle, reflecting the lower capacity (97.8% capacity retention comparing cycles 800 to 200). Likewise, the profile of the 1400th cycle overlaid that of the 200th cycle, with a capacity retention compared to cycle 200 close to 94.8%. A similar result was observed in comparing the 400th, 1000th and 1600th cycles (tested at 5*C*) and the 600th, 1200th and 1800th cycles

(tested at 10*C*), where the profiles of the differential capacity plots remained were observed to change only in magnitude, with a small decrease in the amplitude of their features.

During the last seven-hundred cycles ending at cycle 2,500, sustained capacity fade on the order of 0.1 mAh g^{-1} per cycle is observed, and the differential capacity profile shows that the sharp Li-extraction feature near 500 mV has largely disappeared in a manner similar to the behavior of this same feature for the electrode cycled in EC/DMC electrolyte through 200 cycles. For both electrodes, the preservation of this feature correlates with stable cycling performance, and we suggest that the decay of this feature and corresponding capacity fade in the performance of the electrode may be related to the rate of oxidation of the germanium active material. As has been shown by Etacheri et al.[41] in their excellent study on the effect of FEC on Si-nanowire anodes, reported by Choi et al.[44] when considering FEC as an electrolyte additive and observed by Nakai, et al.[43] in their detailed XPS depth profiling of evaporated thin Si-films, the fluorinated electrolyte solvent may stabilize cycling performance by minimizing the extent to which the active material oxidizes during cycling, a reaction likely resulting from the presence of trace concentrations of water in the coin cell and electrolyte. A comparison of the electrode cycled in FEC:DEC after 2,500 cycles and of the electrode cycled in EC:DMC after 200 cycles to a similarly prepared GeO_2-based slurry cast electrode (Supplementary Information Figure SI.2.14b) indicates that after cycling has progressed to the onset of significant capacity fade, the Ge nanoparticle may have become partially oxidized – albeit at a far slower rate for the electrode cycled in FEC:DEC than in EC:DMC – and to the extent that the partially oxidized Ge nanoparticle-based electrode's thermodynamic Li-insertion and Li-extraction pathways closely resemble those of the GeO_2 nanoparticle-based electrode, the Li-insertion and Li-extraction features matching in both location (potential) and amplitude (Supplementary Information Figure 15).

Electrochemical Impedance Spectroscopy

The information provided by differential capacity profiles can be supplemented by the results of electrochemical impedance spectroscopy (EIS) taken at intervals throughout galvanostatic testing in order to provide a more comprehensive picture of the evolution of nominally identical Ge nanoparticle-based anodes cycled using the different electrolytes. Differential capacity profiles provide a means to locate and determine the extent of the chemistry of surface film growth and the lithiation of the Ge nanoparticle. The surface film formed by the reduction of electrolyte can be a significant variable in explaining the observed differences in cycling performance between the nominally identical anodes tested in the two different electrolytes. EIS can be used to analyze properties related to the chemistry, morphology and thickness of this surface film, which are factors which limit the extent of lithiation of the Ge nanoparticle due to added impedance regarding Li^+ ion transport and charge transfer.

The impedance of the transport of Li-ions through multilayered surface films is modeled as a series of parallel resistor/capacitor (R||C) circuits represented in the spectra as semicircles in the high and medium frequency regions and a Warburg resistance represented as a sloped line in the low frequency region. The very high frequency region that captures the impedance through the electrolyte and separator membrane is observed as a combined resistor, measured as the resistance up to the beginning of the first semi-circular feature. The diameter of the high frequency semicircle corresponds to impedance regarding Li^+ ion migration through the SEI, and the diameter of the medium frequency semicircle corresponds to charge transfer resistance at the interface of the SEI and active material surface.

Due to the complexity of the slurry-cast anode, these impedances must be represented by constant phase elements in the equivalent circuit, reflecting the non-ideality of the system arising from (a) the surface roughness and 3D morphology of the electrode, (b) the distribution of reaction rates on the Ge nanoparticle surface (probably as a consequence of uneven SEI growth, asymmetric particle geometry and the random orientation of the active and inactive materials in the film), (c) the varying thickness of the film and non-uniform composition due to imperfect stirring of the slurry and (d) non-uniform current distribution (both in the subject electrode and on the Li/Li^+ foil counter/reference electrode surface due to dendritic growths). The initial linear profile of the spectra in the low frequency region is attributed to impedance resulting from solid state Li diffusion limitations. The steeper sloped linear profile in the very low frequency region is due to insertion capacitance. The low frequency region of the spectra is generally not considered when comparing electrolyte effects because it is assumed that the bulk properties of the cycled Ge particles are independent of the electrolyte used.[45]

The model commonly used[54] to represent this system should describe each of the anodes tested, but a quantitative analysis of the EIS spectra is not meaningful due to the complex morphology of slurry cast electrode system studied here. However, useful information may be obtained from a relative comparison between the types and magnitudes of features from anodes tested using different electrolytes or between spectra taken at various stages in the cycling of a single anode.

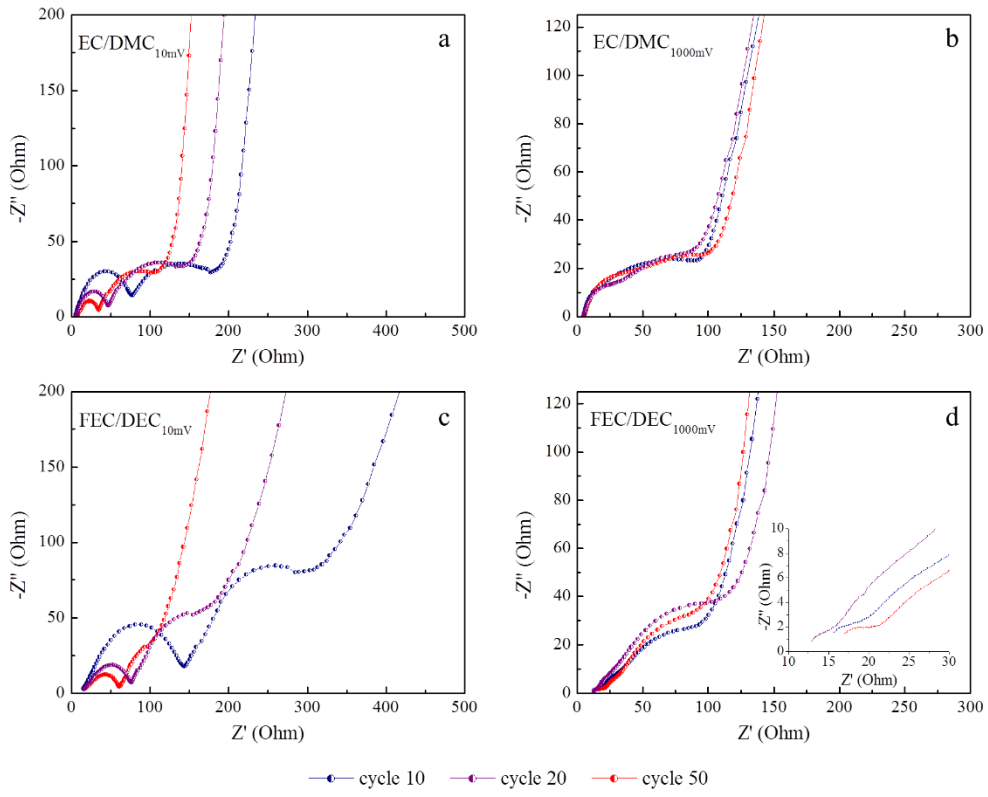

Figure 2.6: Evolution of the electrochemical impedance spectra for Ge nanoparticle electrode cycled 10, 20 and 50 times at 1*C* in EC/DMC electrolyte in the (a) fully lithiated state (10mV) and (b) fully delithiated state (1000 mV) and in the FEC/DEC electrolyte at (c) fully lithiated state (10mV) and (d) fully delithiated state (1000 mV).

The EIS for the electrodes cycled in EC/DMC and FEC/DEC in the fully lithiated (10mV) and delithiated states (1000mV) are shown in Figure 2.6.a-d. Through 50 cycles, total impedance is lower in the electrode cycled in EC/DMC, most noticeably when comparing the different electrode systems in their fully lithiated state, this result correlating with the lower overpotential required to drive the stripping/plating of Li in the EC/DMC electrolyte vs. the FEC/DEC electrolyte during the testing of coin cells composed of two electrodes of Li foil (Supplementary Information Figure 2.6). The solution resistance for the electrode cycled in EC/DMC is nearly

three times less than for the electrode cycled in FEC/DEC (6 vs 16 Ohm). The impedance through the SEI is significantly greater for the electrode cycled in FEC/DEC when in the fully-lithiated state in which the SEI is more fully formed. The impedance through the SEI depends upon the potential of the electrode because the ratio of the impedance through the SEI to the impedance due to charge transfer increases as the voltage increases. In the fully-lithiated state, the impedance through the SEI and due to charge transfer is greater in the electrode cycled in FEC/DEC. In the fully-delithiated state, the electrode cycled in EC/DMC has the larger impedance through the SEI, although in both electrodes, impedance from charge transfer is greater. For the electrode cycled in FEC/DEC, an additional source of impedance was observed besides that attributed to transport through the SEI and charge transfer at the active material interface. As shown in the inset for Figure 2.6.d, the electrode cycled in FEC/DEC possesses an additional feature in its spectra observed at 1000 mV, a small semicircle of diameter about 5 Ohm recorded during perturbations at high frequencies. To the best of our knowledge, this has not been reported for a Ge-based or other negative electrode system.

SEM, TEM Characterization

Electrodes were examined by SEM and TEM in their fully-delithiated state. The electrodes were removed from the coin cell in the glovebox, washed with dimethyl carbonate (DMC) and then examined by SEM. Between transfer from a vacuum tight container filled with Ar from the glovebox to the high vacuum SEM chamber, the samples were exposed to air for less than 60 seconds.

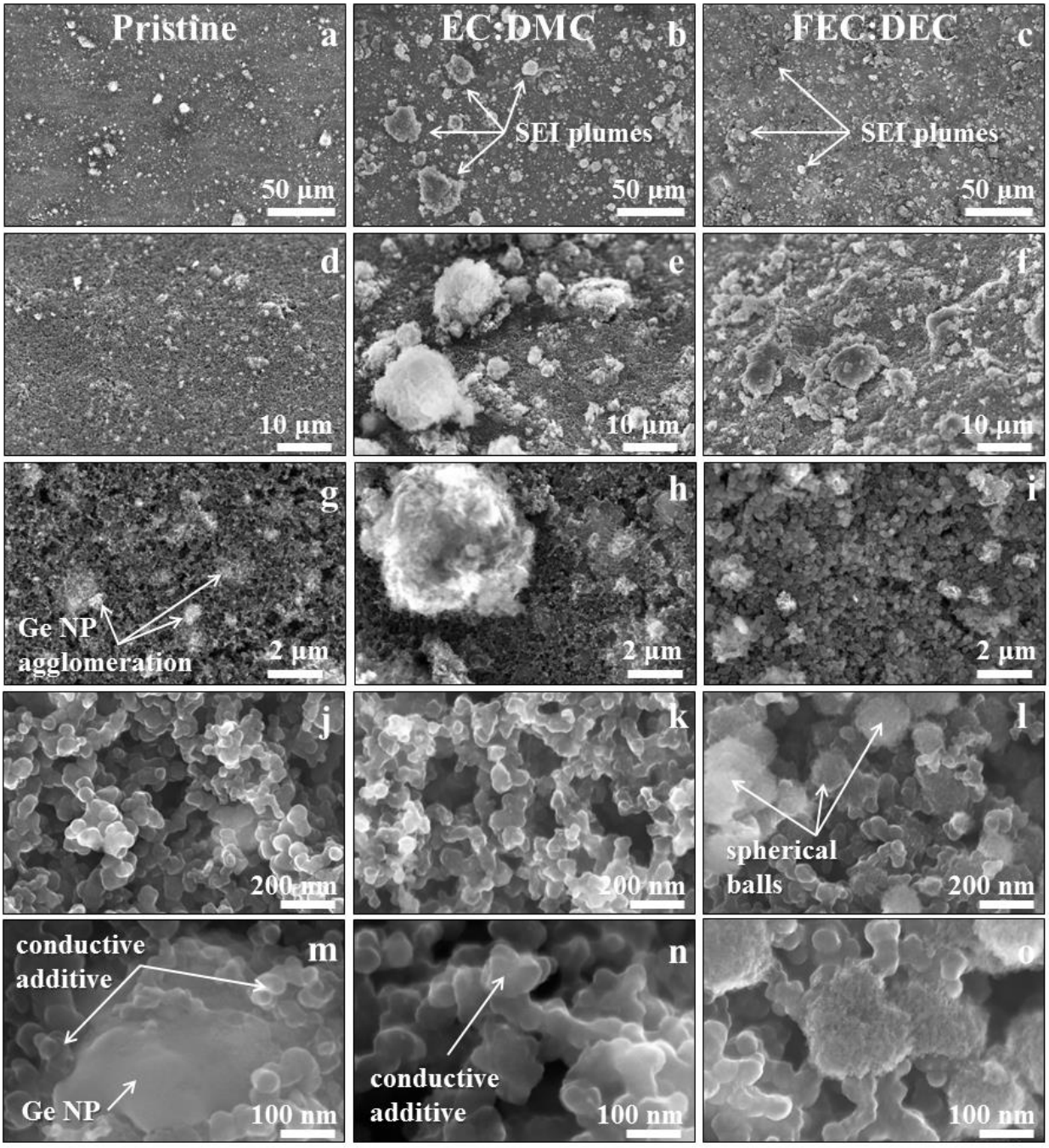

Figure 2.7: SEM of Ge-based anodes films not cycled (a, d, g, j, m) and cycled 100 times at 1C in the EC:DMC (b, e, h, k, n), and FEC:DEC (c, f, i, l, o) electrolytes. Magnifications of 500 (a, b, c), 2k (e, f, g at 37 degree tilt), 10k (i, j, k), 100k (j, k, l) and 200k (m, n, o) are shown.

The SEM wide-field view of the electrodes cycled 100 times at 1*C* in EC/DMC (Figure 2.7.b) and FEC/DEC (Figure 2.7.c) shows the formation of micron-scale growths, protruding like plumes from the film surface. Using EDX mapping, the locations of these growths was correlated to the positions of large Ge particles or agglomerations within the electrode film (Supplementary Information Figure SI.2.16). These growths on the surface of the electrode cycled in EC/DMC appear to be up to an order of magnitude larger in size than many of the growths appearing on the surface of the electrode cycled in FEC/DEC and have a more noticeably reticulated surface. The growths on the electrode cycled in FEC/DEC more frequently appeared mesa-like, with smooth surfaces or, for smaller growths, the SEI surrounding the Ge nanoparticles in the electrode cycled in FEC/DEC appeared to be a collection of folded sheets forming a terraced structure (Supplementary Information Figure SI.2.17). Using cross-sectional TEM, the growths on the electrode cycled in FEC/DEC were shown to have a similar structure, despite their generally more smooth exterior appearance. A high energy electron beam was used to penetrate the outer surface, revealing the porous growth on an electrode cycled in EC/DMC (Figure 2.7.h, Supplementary Information Figure SI.2.18.c).

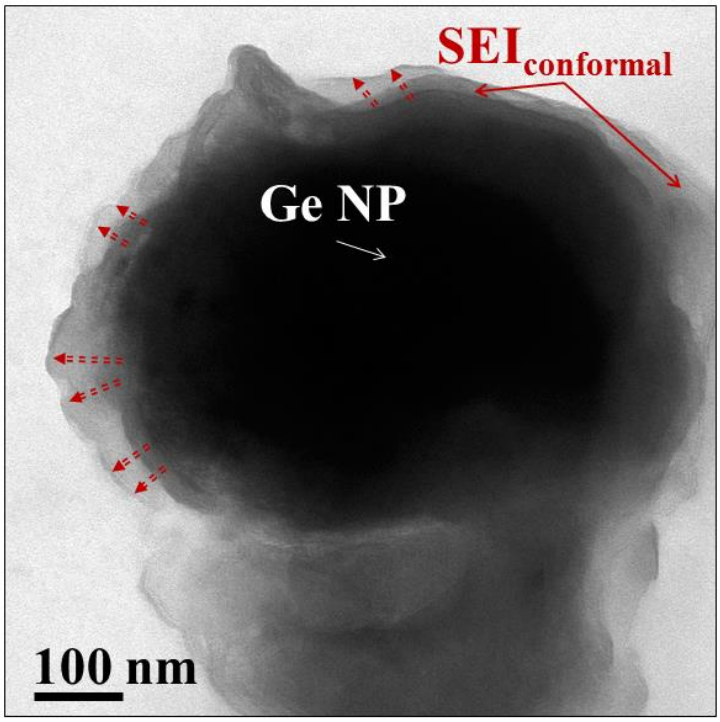

Figure 2.8: TEM cross-section of Ge nanoparticle electrode cycled 700 times (200 cycles at 1*C*, 5*C* and 10*C* followed by 50 cycles at 5*C* and then 1*C*) in the FEC/DEC electrolyte. The single Ge nanoparticle is surrounded by a roughly conformal coating of SEI. The red arrows indicate the direction in which successive layers of SEI move to accommodate the volumetric expansion of the particle.

In Figure 2.8, a cross section view of an organic growth on the electrode cycled in FEC/DEC is shown using TEM. Beneath the surface of the growth is a branch-like network of loosely entwined organic/inorganic components. Appearing to be fiber or sheet-like with a thickness of about 20-50 nm, this SEI growth typically begins at the surface of several Ge nanoparticles and apparently also on the surface of conductive additive Super-P Li particles. As cycling progresses, the density of the entwined components and the size of the growth increases (Supplementary Information Figure SI.2.18.e-g). As described in section 4.4, the expansion may

occur as a consequence of evolved gas from reduction reactions near the active material surface.[55-56]

From cross-sectional TEM imaging, we find that these growths are not confined to the surface of the electrode but occur throughout the interior of the electrode film and at the Cu foil / film interface (Figure 2.9). With these, we show what we believe are the first such images that depict the SEI and its arrangement within the morphology of a slurry-cast cycled negative electrode. The roughly conformal film of SEI immediately surrounding the Ge nanoparticles (Figure 2.8) was observed to be 10-50 nm. Moving further away from the particle surface, there is a noticeable transition from this smooth, more dense, semi-conformal SEI into the porous growths described above (Supplementary Information Figure, SI.2.19). These porous growths of SEI occur throughout both electrodes considered herein, developing off of the surfaces of the electrically conductive active materials (Figure 2.9.a-b) and from the Cu current collector (Figure 2.9.c).

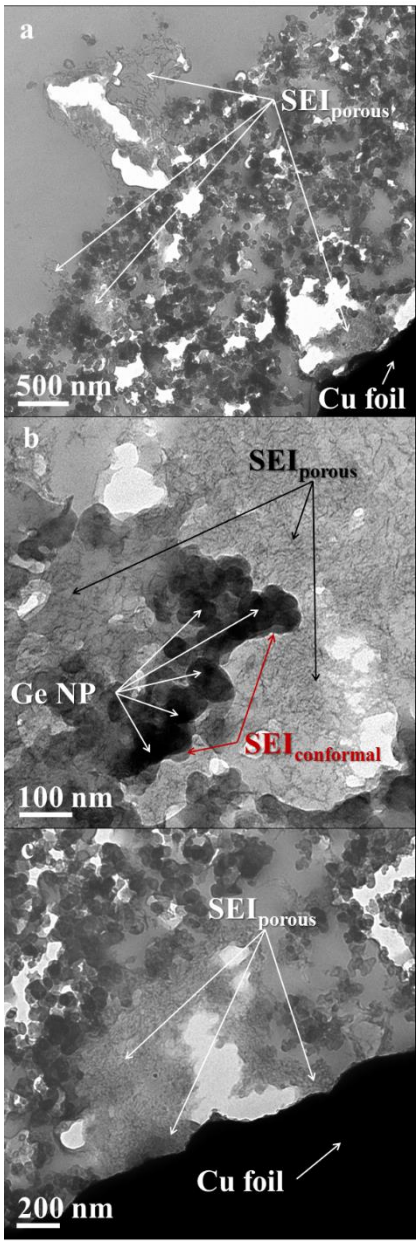

Figure 2.9: TEM cross-section of Ge nanoparticle electrode cycled 100 times at 1*C* (a) in the FEC/DEC electrolyte showing the cross-sectional architecture of the electrode film comprised of Ge nanoparticles, conductive additive Super-P Li and a porous SEI indicated by arrows, (b) in the EC/DMC electrolyte showing Ge nanoparticles in the electrode film surrounded by a roughly conformal coating of SEI that transitions into porous SEI and (c) in the FEC/DEC electrolyte showing porous SEI growth from the Cu foil current collector.

Due to the limited scope of a survey consisting of these TEM images which represent a section of less than 100 nm of the electrode film, we believe that the several sections imaged for this study are not necessarily representative of the entire film. What was observed indicated that the interior of the electrode cycled in the EC/DMC electrolyte differed in three significant ways from the electrode cycled in FEC/DEC. One, the porous SEI growths appeared to be of greater size and more densely formed in the electrode cycled in EC/DMC (Supplementary Information Figure SI.2.20). Two, there were larger agglomerations of Ge nanoparticles after cycling (Supplementary Information Figure SI.2.21). Three, large regions of fractured particles were observed in the electrode cycled in EC/DMC but not in the electrode cycled in FEC/DEC (Supplementary Information Figure SI.2.22).

High magnification SEM (Figure 2.7.k-l,n-o) shows that the morphology of the SEI film coating the conductive additive in the electrode is similar for both electrolytes tested. However, differences in cycling performance (Supplementary Information Figure SI.2.23) and impedance measured through these SEI films (Supplementary Information Figure SI.2.24) for the conductive additive were observed.

Surrounding the conductive additive particles in the electrode cycled in FEC/DEC, we observed unidentified spherical materials about 100-500 nm in diameter (Figure 2.7.i,l,o). Using EDX, these spherical materials were determined to be composed of material other than Ge. EDX mapping was attempted but the competing signal from other species nearby and below within this highly porous structure obscured the identity of this spherical material. These particles sometimes appeared smooth but more frequently were observed with an uneven and knobby surface (Supplementary Information Figure 2.SI.2.25 a-c).

Discussion of Cycling Performance

We observed that a Ge-based electrode employing FEC/DEC as the electrolyte has a high energy density and can cycle at high *C*-rates with high Coulombic efficiency for a long lifetime. The stable capacity along with near 100% Coulombic efficiency achieved through 500 cycles at 10*C* (16 A g^{-1}) constant current cycling recommends the Ge nanoparticle / FEC-based electrolyte combination as an attractive electrode suited for further study for optimizing its slurry composition and scaling up its mass loading. The performance of the electrode when tested at high discharge rates (10*C* or 20*C* discharge / 1*C* charge, Figure 2.2.c) and when tested for over 2,500 cycles at variable rates (1*C*, 5*C* and 10*C*, Figure 2.2.c) supports this recommendation.

We believe that the performance of this anode system could be improved in terms of capacity retention at high rates by using Ge nanoparticles of a narrower size distribution and of a smaller size. The Ge particles used in this research ranged from nano to micron sized (Supporting Information Figure SI.2.1) and consequently a fraction of the Ge particles were not fully lithiated at higher rates due to the limiting rate of Li bulk diffusion in the active material. Additionally, the applied current density per unit area of the electrode could be improved by increasing the mass fraction of the active material in the slurry and the mass loading. For example, we found electrode films made with 80 wt percent G nanoparticles cycled with minimal capacity fade (0.5 mAh g^{-1} per cycle) through 100 cycles at a rate of 1*C* (Supplementary Information Figure SI.2.2). Additionally, we found that an electrode made with 60 wt percent Ge nanoparticles achieved stable performance for 1000 cycles at 1*C* (Supporting Information Figure SI.2.7) with a mass loading several times higher than the anodes tested and discussed in the main paper. For this particular electrode, i.e., with 60 wt percent Ge nanoparticles, the 1000^{th} cycle capacity of 818 mAh g^{-1} (Coulombic efficiency, 99.7%) retained 93% of the 10^{th} cycle capacity. In contrast, the nominally

identical electrode cycled in EC/DMC retained less than 47% of its 10th cycle capacity after only 200 cycles.

Discussion of EIS and Differential Capacity Profile

The differential capacity profile for the Ge nanoparticle electrode cycled in FEC/DEC is consistent with the cycling data, both of which show the reversibility of this electrode system. The 1*C* profiles taken for the 200th and 700th cycles (Figure 2.5) are nearly identical, the difference between these being that the marginally lower capacity of the 700th cycle is reflected in the magnitudes of the Li insertion and extraction peaks.

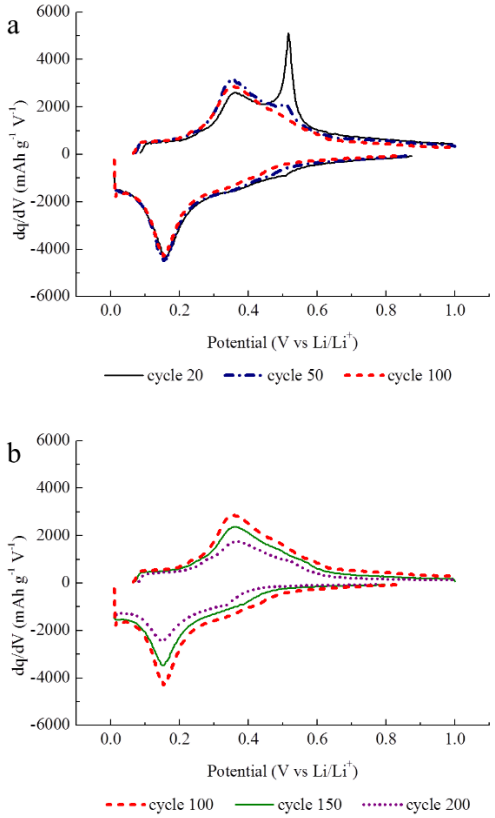

Figure 2.10: Differential capacity profiles for the Ge nanoparticle electrode cycled in EC/DMC at 1*C* (a) cycles 20, 50 and 100 and (b) cycles 100, 150 and 200.

The differential capacity profiles for the electrode cycled in EC/DMC is consistent with the cycling data, which shows the onset of capacity fade after about 20 cycles. During these first cycles for which there is no capacity fade, the Li insertion and extraction features of the differential capacity profile are essentially unchanged in both shape and magnitude. Coinciding with the capacity fade, the two Li extraction features change, with the feature at the higher potential disappearing while the feature at the lower potential grows in magnitude, both relatively in proportion to the disappearing peak and in absolute magnitude (Figure 2.10.a). The only shift in this peak is to a lower potential, signifying that less overpotential is required for the Li extraction. The EIS results showing the continuous decrease in total impedance through these 50 cycles supports the interpretation of these differential capacity profiles that the kinetics of the electrode system are improving (Figure 2.6). These results indicate that the thermodynamics of the electrode tested in EC/DMC change during these tens of cycles that coincide with the onset of capacity fade. When compared with the differential capacity profile of a similarly prepared electrode composed of GeO_2 nanoparticle, this progressive transformation in the EC-based Ge nanoparticle electrode differential capacity profiles may be explained as indicating the gradual oxidation of the Ge nanoparticle active material (Supplementary Information Figure SI.2.26).

After 100 cycles, the Li extraction peak initially observed above 500 mV has almost disappeared (Figure 2.10.a). During the subsequent 100 cycles (Figure 2.10.b), the changes in the differential capacity profile reflect the continuous capacity fade, with each of the Li insertion and extraction features decreasing in proportion. This behavior observed after 100 cycles fits the hypothesis which explains capacity fade in terms of either the general dislocation and dislodgement of regions of the film from the main body of the electrode and/or the electrical isolation of fractured particles when separated grains are coated with electrically insulating SEI on

their freshly exposed surfaces. As the amount of electrically connected Ge nanoparticles decreases, the amplitude of the differential capacity profile diminishes in proportion to the extent of capacity fade. Although the specific current density would then also increase in terms of the amount of electrically connected Ge nanoparticles, this does not result in peak shifts due to the excellent ionic conductivity of Li ions through the EC-derived SEI (as reported in the EIS results) and fast diffusion of Li through the bulk of the Ge nanoparticles.

The lower impedance through the SEI of the Ge nanoparticle electrode cycled in EC/DMC through the first 50 cycles at 1*C* conflicts with recent reports of an electrolyte survey (including FEC-based electrolytes) done by Aurbach's group[41] for a Si nanowire thin film electrode and by Lin, et al.,[42] for a slurry cast Si-based anode. In these reports, the ionic transport is improved through better Li^+ ion conducting SEI formed by FEC-based electrolytes, although this evolution towards diminished impedance is not reflected in the cycling data for Ge-based electrodes studied here which show stable performance for the electrode cycled in FEC/DEC and capacity fade for the electrode cycled in EC/DMC. This suggests that the impedance of transport through the surface films and related to charge transfer do not necessarily explain cycling performance data.

For both electrode systems, these EIS results coincide with the differential capacity profiles (Figure 2.4) in that these show that through 50 cycles at 1*C*, the primary Li insertion peak for the electrode cycled in EC/DMC is found at a higher potential (lower overpotential) than the same peak for the electrode cycled in FEC/DEC. Through 50 cycles, the decrease in impedance shown in the EIS for both electrode systems can be correlated with decreasing overpotentials required to reach this primary Li insertion peak for the electrode cycled in FEC/DEC but not for the electrode cycled in EC/DMC. For this electrode the primary Li insertion peak remains near 165 mV for cycles 10, 20 and 50. For Li extraction from these electrode systems, there is negligible difference

in the impedance spectra observed at 1000 mV, and these results correlate strongly with the minimal differences in Li extraction features for both the electrode cycled in EC/DMC and in FEC/DEC. There is no significant change in the EIS for the electrode cycled in EC/DMC which correlates to the large decrease in the size of the Li extraction feature near 515 mV for these cycles, which suggests that the reason for the observed capacity fade is not explained by the surface transport properties of this electrode system.

Discussion of High Rate and Long Cycle Life Performance

The cycling data for constant charge rate (1*C*) / variable high rate discharge testing show that Ge-based active materials tested using the FEC/DEC electrolyte are an appropriate choice for Li-ion batteries required for fast discharge applications. The nearly identical performance of electrodes tested at 10*C* and 20*C* discharge rates indicates that the charge rate, not the discharge rate, appears to be the significant limiting factor in the performance of this electrode for testing done at high current densities. We believe that this performance may be further improved not only by selecting Ge nanomaterials with an appropriate diffusion length for the rate desired but also by optimizing the electrolyte composition and separator membrane to support the rapid transport of Li^+ ions. This study used Ge nanoparticles with a size distribution far wider than was advertised for this commercially available product (see Supplementary Information Figure SI.2.1). As indicated above, the below-theoretical capacities reported in this study can be partially explained by the dimensions of the Ge active material used. The bulk diffusion rate of Li in Ge may limit electrode performance at higher *C*-rates leading to particles that are not fully lithiated. Smaller Ge particles, such as those used by Lee et al.,[16] or those otherwise designed with diffusion lengths appropriate for a specific range of *C*-rates would likely improve the capacity retention of this electrode system.

Discussion of SEM, TEM Characterization

The combined perspectives of SEM and cross-sectional TEM used in this study depicted the structure of the electrode film and provided a means to examine the structure of the cycled anode: the Ge nanoparticles, the conductive additive (Super-P Li) and the surrounding SEI. Although the type and extent of formation of the SEI in a negative electrode is considered crucial to understanding the electrode's cycling performance, we believe the TEM images shown herein are the first to reveal the nature and scope of growth of SEI within a cycled slurry cast electrode. Embedding the cycled electrode within epoxy, which is subsequently polymerized and hardened, preserves the chemical integrity of the electrode film and SEI from contaminating species formed when the sample is exposed to air. The structural integrity of the electrode film is also well preserved due to the hardened epoxy supporting the porous electrode architecture and because of the non-destructive nature of ultra-microtome sectioning. Using cross-sectional TEM, we observed what we believe are two types of SEI growth. One is a layered and more densely formed material, conformally surrounding the Ge nanoparticle (or conductive additive). The other observed variety of SEI developed off of both the electrically conductive particles and from the surface of the Cu foil current collector. Porous in nature, with fiber-like strands, we believe the structure of this SEI may be partially attributed to the motion of volumetric expansion and contraction of the Ge nanoparticles. Because of their microns-dimension and directional growth along an axis paralleling the gravitational rise of evolved gas bubbles (CO_2, H_2)[55-56] it may be that the evolved gas expands the SEI to the morphology observed.

Failure mode mechanisms, such as the extent of particle agglomeration and particle fracture are also indicated by TEM images. Here we observe evidence for both the agglomeration of active material nanoparticles (Supplementary Information Figure SI.2.21) and Ge particle fracturing

(Supplementary Information Figure SI.2.22). Due to the variety of sizes and shapes of the commercially used Ge nanopowder, the ability to contrast the changed morphology of the particle after several cycles with its uncycled condition is limited. With careful materials selection, and using image processing techniques to quantitatively assess the extent of particle agglomeration and fracture, a more comprehensive study of the cycled, slurry-cast electrode film may be done. Herein we demonstrate the first reported instance of cross-sectional TEM as a tool for characterizing the changes in the structure of the nanoparticle network and growth of SEI after cycling.

Conclusions

Ge nanoparticle based slurry cast electrodes were tested with PAA binder in 1M $LiPF_6$ EC/DMC or FEC/DEC electrolytes. The critical factor determining the cycling performance of the anode was determined to be the use of fluoroethylene carbonate (FEC) as a co-solvent in the electrolyte solution. For this FEC-based electrode system, we report long-term, high capacity/Coulombic efficiency and stable cycling results for a selection of high *C*-rate tests. Throughout a 2,500 cycle (alternating 200-cycle, variable high rate) test done at 1*C*, 5*C* and 10*C*, we found stable capacities/high Coulombic efficiencies near 1152 mAh g^{-1}/99.7%, 706 mAh g^{-1}/99.2% and 423 mAh g^{-1}/99.7%. Continuous testing at 10*C* showed a capacity near 700 mAh g^{-1} with an average Coulombic efficiency of 100% through 500 cycles. Capacities over 1000 mAh g^{-1} were observed when discharging the electrode at up to 20*C* while charging at 1*C* and a capacity of 425 mAh g^{-1} was achieved for a discharge rate of 50*C*. These results and our preliminary work for a similar electrode system with higher mass content and mass loadings (Supplementary Information Figures SI.2.2 and SI.2.7) successfully demonstrate that for the Ge-based, slurry cast electrode, the attractive properties of this Li-ion anode material – Li diffusion rate, electrical

conductivity and theoretical capacity – can be used to create an electrode system which is a candidate for optimization and scale-up based upon its performance in several of the significant battery parameters of interest: maximum specific power output, specific and volumetric energy densities, Coulombic efficiency and cycle life. These cycling improvements obtained by the use of the FEC-based electrolyte in a Ge-based electrode complements the recent progress in slurry cast Ge-based electrode research which has focused on improving performance through structural and chemical modifications to the structure of the active material. Differential capacity profiles provided evidence of the improved thermodynamic stability of the electrode system, which we suggest may be a result of the enhanced preservation of Ge active material by a FEC-derived SEI that stabilizes the electrode against oxidation. Through the use of cross-sectional TEM imaging, we characterize the evolution of the structure of the improved electrode cycled with the FEC-based electrolyte by considering the type and extent of SEI growth, particle agglomeration and fracturing within the cycled electrode film.

REFERENCES

1. J.B. Goodenough, Y. Kim, Chemistry of Materials, 22 (2009) 587-603.

2. L. Baggetto, E.J.M. Hensen, P.H.L. Notten, Electrochimica Acta, 55 (2010) 7074-7079.

3. X.H. Liu, S. Huang, S.T. Picraux, J. Li, T. Zhu, J.Y. Huang, Nano Letters, 11 (2011) 3991-3997.

4. D. Wang, Y.-L. Chang, Q. Wang, J. Cao, D.B. Farmer, R.G. Gordon, H. Dai, Journal of the American Chemical Society, 126 (2004) 11602-11611.

5. J. Graetz, C.C. Ahn, R. Yazami, B. Fultz, Journal of The Electrochemical Society, 151 (2004) A698-A702.

6. C.S. Fuller, J.C. Severiens, Physical Review, 96 (1954) 21-24.

7. M.-H. Park, Y. Cho, K. Kim, J. Kim, M. Liu, J. Cho, Angewandte Chemie International Edition, 50 (2011) 9647-9650.

8. R. Huggins, W. Nix, Ionics, 6 (2000) 57-63.

9. L. Baggetto, P.H.L. Notten, Journal of The Electrochemical Society, 156 (2009) A169-A175.

10. U. Kasavajjula, C. Wang, A.J. Appleby, Journal of Power Sources, 163 (2007) 1003-1039.

11. L.Y. Beaulieu, S.D. Beattie, T.D. Hatchard, J.R. Dahn, Journal of The Electrochemical Society, 150 (2003) A419-A424.

12. W.-J. Zhang, Journal of Power Sources, 196 (2011) 13-24.

13. H. Wu, Y. Cui, Nano Today, 7 (2012) 414-429.

14. J. Graetz, C.C. Ahn, R. Yazami, B. Fultz, J. Electrochem. Soc., 151 (2004) A698-A702.

15. J. Wang, N. Du, H. Zhang, J. Yu, D. Yang, Journal of Materials Chemistry, 22 (2012) 1511-1515.

16. H. Lee, M.G. Kim, C.H. Choi, Y.-K. Sun, C.S. Yoon, J. Cho, The Journal of Physical Chemistry B, 109 (2005) 20719-20723.

17. M.-H. Park, K. Kim, J. Kim, J. Cho, Advanced Materials, 22 (2010) 415-418.

18. M.-H. Seo, M. Park, K.T. Lee, K. Kim, J. Kim, J. Cho, Energy & Environmental Science, 4 (2011) 425-428.

19. A.M. Chockla, K. Klavetter, C.B. Mullins, B.A. Korgel, ACS Appl Mater Interfaces, (2012).

20. S. Yoon, C.-M. Park, H.-J. Sohn, Electrochemical and Solid-State Letters, 11 (2008) A42-A45.

21. D.-J. Xue, S. Xin, Y. Yan, K.-C. Jiang, Y.-X. Yin, Y.-G. Guo, L.-J. Wan, Journal of the American Chemical Society, 134 (2012) 2512-2515.

22. H. Lee, H. Kim, S.-G. Doo, J. Cho, J. Electrochem. Soc., 154 (2007) A343-A346.

23. G. Jo, I. Choi, H. Ahn, M.J. Park, Chemical Communications, 48 (2012) 3987-3989.

24. L.C. Yang, Q.S. Gao, L. Li, Y. Tang, Y.P. Wu, Electrochemistry Communications, 12 (2010) 418-421.

25. B. Wu, A. Heidelberg, J.J. Boland, Nat Mater, 4 (2005) 525-529.

26. L. Lu, M.L. Sui, K. Lu, Science, 287 (2000) 1463-1466.

27. C.K. Chan, X.F. Zhang, Y. Cui, Nano Letters, 8 (2007) 307-309.

28. C.K. Chan, H. Peng, G. Liu, K. McIlwrath, X.F. Zhang, R.A. Huggins, Y. Cui, Nat Nano, 3 (2008) 31-35.

29. A.S. Arico, P. Bruce, B. Scrosati, J.-M. Tarascon, W. van Schalkwijk, Nat Mater, 4 (2005) 366-377.

30. K.T. Lee, J. Cho, Nano Today, 6 (2011) 28-41.

31. R. Ruffo, S.S. Hong, C.K. Chan, R.A. Huggins, Y. Cui, The Journal of Physical Chemistry C, 113 (2009) 11390-11398.

32. H. Wu, G. Chan, J.W. Choi, I. Ryu, Y. Yao, M.T. McDowell, S.W. Lee, A. Jackson, Y. Yang, L. Hu, Y. Cui, Nat. Nanotechnol., 7 (2012) 310-315.

33. B. Hertzberg, A. Alexeev, G. Yushin, Journal of the American Chemical Society, 132 (2010) 8548-8549.

34. M.T. McDowell, S.W. Lee, I. Ryu, H. Wu, W.D. Nix, J.W. Choi, Y. Cui, Nano Letters, 11 (2011) 4018-4025.

35. H. Wu, G. Zheng, N. Liu, T.J. Carney, Y. Yang, Y. Cui, Nano Letters, 12 (2012) 904-909.

36. L. Hu, H. Wu, Y. Gao, A. Cao, H. Li, J. McDough, X. Xie, M. Zhou, Y. Cui, Advanced Energy Materials, 1 (2011) 523-527.

37. D. Wang, Z. Yang, F. Li, D. Liu, X. Wang, H. Yan, D. He, Materials Letters, 65 (2011) 1542-1544.

38. N.G. Rudawski, B.L. Darby, B.R. Yates, K.S. Jones, R.G. Elliman, A.A. Volinsky, Applied Physics Letters, 100 (2012) 083111-083114.

39. K.H. Seng, M.-H. Park, Z.P. Guo, H.K. Liu, J. Cho, Angewandte Chemie International Edition, 51 (2012) 5657-5661.

40. A.M. Chockla, K.C. Klavetter, C.B. Mullins, B.A. Korgel, ACS Appl Mater Interfaces, 4 (2012) 4658-4664.

41. V. Etacheri, O. Haik, Y. Goffer, G.A. Roberts, I.C. Stefan, R. Fasching, D. Aurbach, Langmuir, 28 (2011) 965-976.

42. Y.-M. Lin, K.C. Klavetter, P.R. Abel, N.C. Davy, J.L. Snider, A. Heller, C.B. Mullins, Chemical Communications, (2012).

43. H. Nakai, T. Kubota, A. Kita, A. Kawashima, Journal of The Electrochemical Society, 158 (2011) A798-A801.

44. N.-S. Choi, K.H. Yew, K.Y. Lee, M. Sung, H. Kim, S.-S. Kim, Journal of Power Sources, 161 (2006) 1254-1259.

45. V. Etacheri, U. Geiger, Y. Gofer, G.A. Roberts, I.C. Stefan, R. Fasching, D. Aurbach, Langmuir, 28 (2012) 6175-6184.

46. A. Magasinski, B. Zdyrko, I. Kovalenko, B. Hertzberg, R. Burtovyy, C.F. Huebner, T.F. Fuller, I. Luzinov, G. Yushin, ACS Applied Materials & Interfaces, 2 (2010) 3004-3010.

47. J.W. Choi, L. Hu, L. Cui, J.R. McDonough, Y. Cui, Journal of Power Sources, 195 (2010) 8311-8316.

48. A.M. Chockla, K.C. Klavetter, C.B. Mullins, B.A. Korgel, Chemistry of Materials, 24 (2012) 3738-3745.

49. J. Goodenough, J Solid State Electrochem, 16 (2012) 2019-2029.

50. D. Djian, F. Alloin, S. Martinet, H. Lignier, J.Y. Sanchez, Journal of Power Sources, 172 (2007) 416-421.

51. G.A. Umeda, E. Menke, M. Richard, K.L. Stamm, F. Wudl, B. Dunn, Journal of Materials Chemistry, 21 (2011) 1593-1599.

52. J.B. Goodenough, Y. Kim, Journal of Power Sources, 196 (2011) 6688-6694.

53. A.S. Jing Li, R. J. Sanderson, T. D. Hatchard, R. A. Dunlap, and J. R. Dahn, J. Electrochem. Soc., 156 (2009) A283-288.

54. J. Liu, A. Manthiram, Chemistry of Materials, 21 (2009) 1695-1707.

55. J.H. Seo, J. Park, G. Plett, A.M. Sastry, Electrochemical and Solid-State Letters, 13 (2010) A135-A137.

56. S.S. Zhang, Journal of Power Sources, 162 (2006) 1379-1394.

SUPPLEMENTARY INFORMATION

Experimental procedure for sectioning of cycled electrode for TEM imaging

The cycled electrode within a 2032 coin cell was removed in an Ar-filled glovebox (<0.1 ppm O_2) using plastic pliers (*I-V Products, Inc.*) so as to preserve the electrochemical properties of the delithiated electrode during disassembly. The electrode was transferred to a vial filled with DMC where it soaked overnight in order to dissolve Li-based salts. Inside the glovebox, small sections from the electrode, approximately 0.25 mm by 10 mm, were cut using a sterile razor blade and then placed into silicone embedding molds. 812 embedding resin (*Electron Microscopy Sciences*) was added to the molds which were subsequently transferred out of the glovebox and into an oven. The resin was polymerized for at least 48 hours at 60°C. The sample embedded in hardened epoxy was initially trimmed using a razor blade. The sample was then placed into the cutting arm of a Leica Ultracut UTC Ultramicrotome and a 47° diamond knife (*Dupont*) was used to produce a flat, trapezoidal face surrounding the sample (0.25 mm base length, 0.75 mm height). A 35° diamond knife (*DiATOME*) was used to slice several sections of 50-80 nm under ambient conditions. These slices floated off the diamond blade edge into a boat filled with filtered water and then collected onto Formvar coated, Cu-supported 300 mesh grids (*Electron Microscopy Services*).

Table SI.2.1: Cycling performance statistics for Ge nanoparticle electrode tested for 1,850 cycles at 1C, 5C and 10C in FEC/DEC electrolyte

Cycle Number	*C-rate*	*Capacity (mAh g^{-1})*	*Coulombic Efficiency (%)*	*Capacity / Capacity at cycle 10 (% of 1150 mAh g^{-1})*	*Capacity / Capacity of 10^{th} cycle for relevant C-rate series[*] (%)*
10	1*C*	1150	99.05 %	100 %	100 %
200	1*C*	1152	99.67 %	100 %	100 %
210	5*C*	667	99.24 %	58 %	100 %
400	5*C*	706	99.35 %	61 %	106 %
410	10*C*	389	99.44 %	34 %	100 %
600	10*C*	422	99.72 %	37 %	108 %
610	1*C*	1163	99.63 %	101 %	101 %
800	1*C*	1128	99.79 %	98 %	98 %
810	5*C*	664	99.11 %	58 %	100 %
1000	5*C*	642	99.38 %	56 %	96 %
1010	10*C*	385	99.82 %	33 %	99 %
1200	10*C*	417	99.63 %	36 %	107 %
1210	1*C*	1136	99.75 %	99 %	99 %
1400	1*C*	1092	99.76 %	95 %	95 %
1410	5*C*	654	99.19 %	57 %	98 %
1600	5*C*	631	99.36 %	55 %	95 %
1610	10*C*	384	99.67 %	33 %	99 %
1800	10*C*	407	99.47 %	35 %	105 %
1810	1*C*	1098	99.73 %	95 %	95 %
2500	1*C*	999	99.86 %	87 %	87 %

[*] The 10^{th} cycle capacities for the three series run at 1*C*, 5*C* and 10*C* are, respectively, (cycle 10), (cycle 210) and (cycle 410)

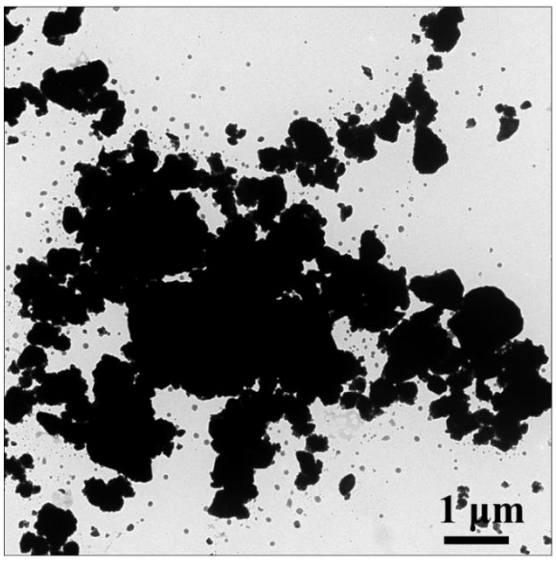

Figure SI.2.1: TEM of Ge nanoparticles purchased from American Elements

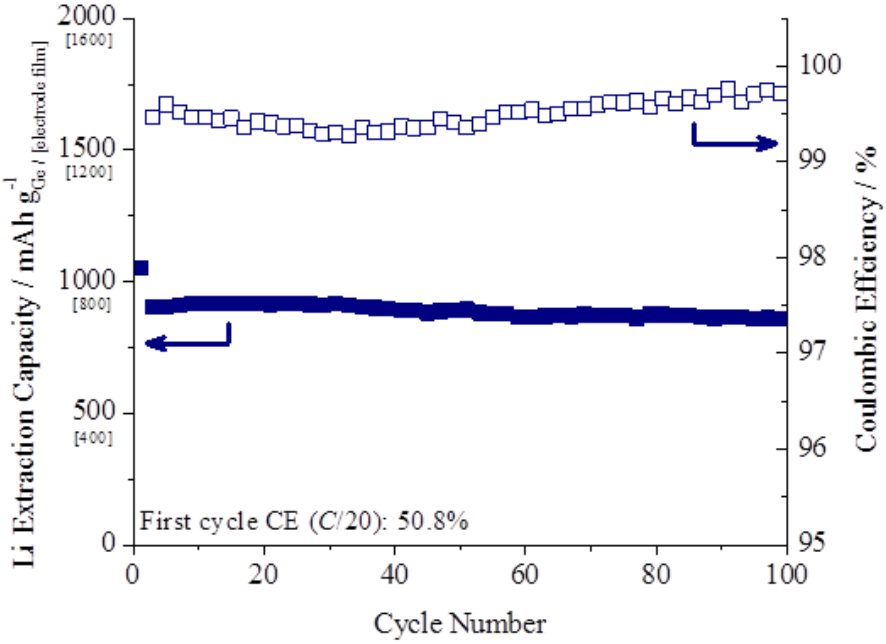

Figure SI.2.2: Cycling performance of a Ge nanoparticle based electrode tested in FEC:DEC electrolyte between 0.01 and 1 V at 1*C* following a first cycle *C*/20 conditioning cycle. The electrode composition is 80:10:10 Ge nanoparticle / PAA_{450kDa} / Super-P Li conductive additive

and the mass loading is 283 μg Ge nanoparticles per cm^2. Through 100 cycles at 1*C* (cycles 2-101), the capacity fade is from 900 to 852 mAh g^{-1}.

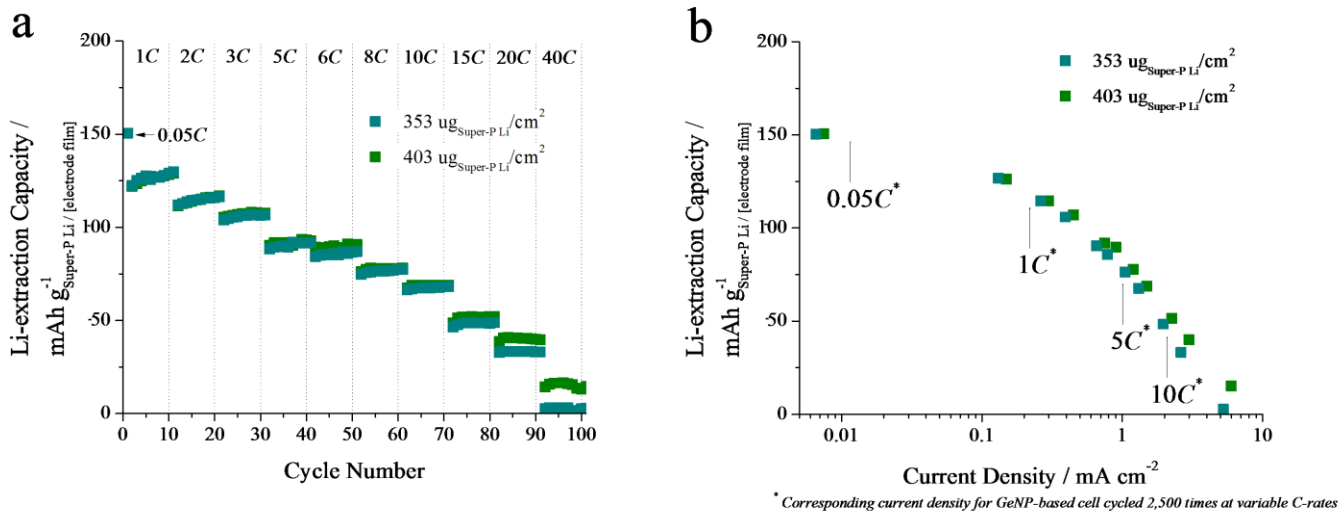

Figure SI.2.3: (a) Cycling performance of two nominally identical Super-P based electrodes tested in FEC:DEC electrolyte between 0.01 and 1V at variable *C*-rates following a first cycle *C*/20 conditioning cycle. The electrode composition is 80:20 Super-P Li / PAA_{450kDa}. (b) The result of the cycling performance for these electrodes shown in a plot of specific capacity as a function of applied current per area. The arrows indicate the current densities corresponding to the *C*/20, 1*C*, 5*C* and 10*C* rates at which the Ge nanoparticle based electrode tested for 2,500 cycles. For these current densities, the Super-P Li is estimated to contribute 145, 110, 70 and 40 mAh g^{-1} Super-P Li, respectively.

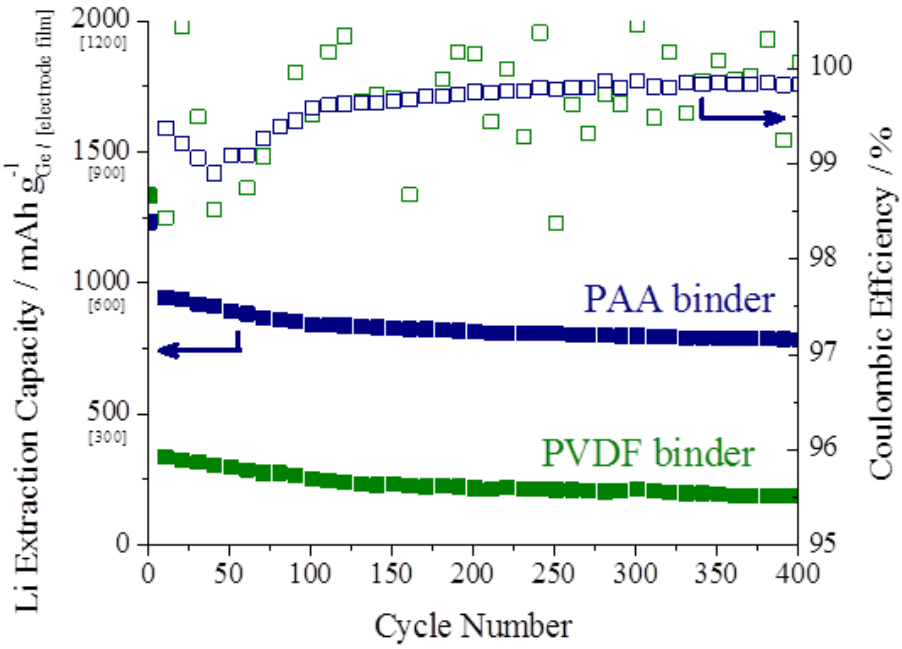

Figure SI.2.4: Cycling performance of a Ge nanoparticle based electrode tested in FEC:DEC electrolyte between 0.01 and 1 V at 1*C* for 400 cycles following a first cycle *C*/20 conditioning cycle. The electrode composition for the test of the PAA_{450kDa} binder is 66:11:22 Ge nanoparticle / PAA_{450kDa} / Super-P Li conductive additive and the mass loading is 285 µg Ge nanoparticles per cm^2. The electrode composition for the test of the PVDF binder is 60:20:20 Ge nanoparticle / PVDF / Super-P Li conductive additive and the mass loading is 258 µg Ge nanoparticles per cm^2.

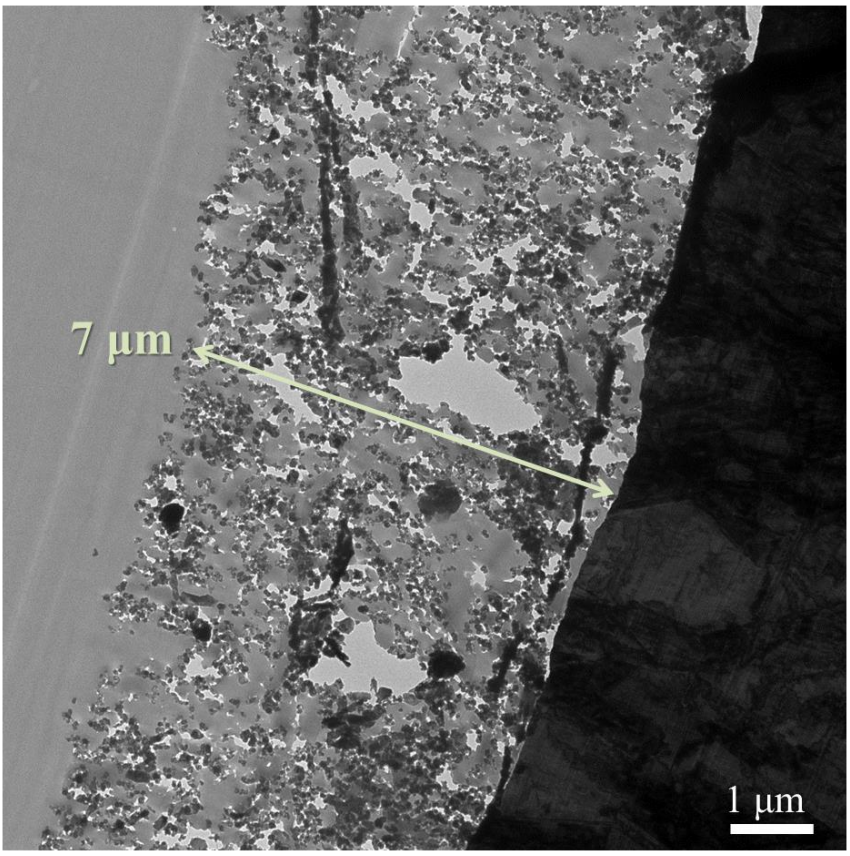

Figure SI.2.5: Cross-sectional TEM image of uncycled Ge nanoparticle electrode composed of 40:20:40 Ge nanoparticle / PAA_{450kDa} / Super-P Li conductive additive and the mass loading is 246 µg Ge nanoparticles per cm^2. The average thickness, rounded to the nearest tenth for several measurements, is 7.0 µm, leading to an estimated average electrode density of 350 mg of Ge nanoparticles per cm^3 (900 mg of electrode film material per cm^3).

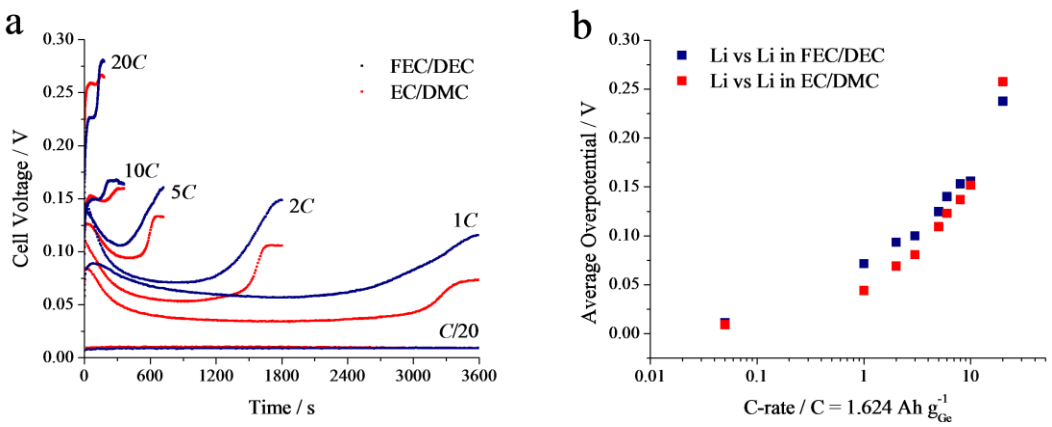

Figure SI.2.6: (a) The voltage profile of a Li vs Li coin cell tested in EC:DMC or FEC:DEC electrolyte as a function of time for one half of the 10th cycle of selected *C*-rates driving the stripping/plating for the cell. The test was run with one cycle conditioning cycle at a current density comparable to *C*/20 for a 500 μg electrode composed of 40 weight percent Ge nanoparticles followed by several 10 cycle sets of progressively higher current density testing: at 1*C*, 2*C*, 3*C*, 5*C*, 6*C*, 8*C*, 10*C*, and 20*C*. (b) The average overpotential required for stripping/plating Li as a function of *C*-rate (where the current density is set as if the electrode were 500 μg composed of 40 weight percent Ge nanoparticles) for Li vs Li cells cycled in EC:DMC or FEC:DEC.

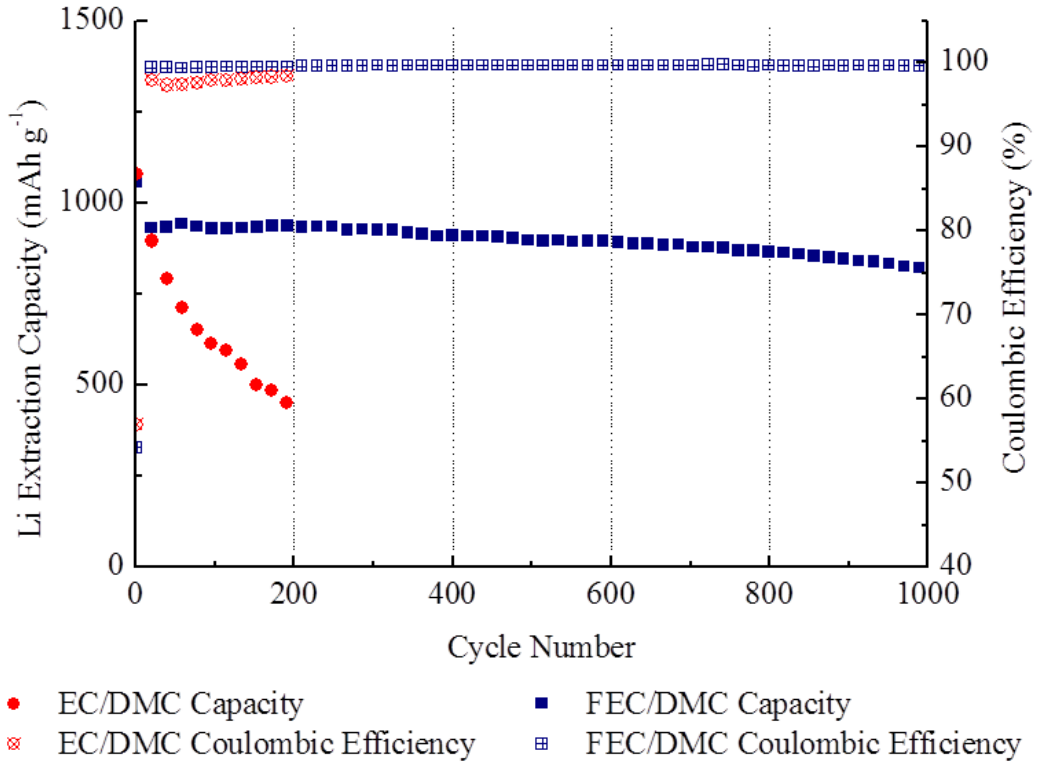

Figure SI.2.7: Cycling performance of a Ge nanoparticle based electrode tested in FEC:DMC or EC:DMC electrolyte between 0.01 and 1 V at 1*C* for up to 1000 cycles following a four cycle conditioning sequence of one cycle each at *C*/20, *C*/10, *C*/5 and *C*/2. The electrode composition for the test of the PAA_{450kDa} binder is 60:20:20 Ge nanoparticle / PAA_{250kDa} / Super-P Li conductive additive and the mass loading is 800 µg Ge nanoparticles per cm^2. The 1000^{th} cycle of the electrode cycled in FEC/DEC has a capacity of 818 mAh g^{-1} (Coulombic efficiency 99.7%) and retained 93% of the 10^{th} cycle capacity The lower capacity reflects the effect of using a slurry composition 60 wt percent Ge nanoparticles and, compared to the electrode tested in the main body of this paper, of using a higher mass loading of Ge nanoparticles on the electrodes of ~800 µg/cm^2 (total electrode mass loading near 1.3 mg).

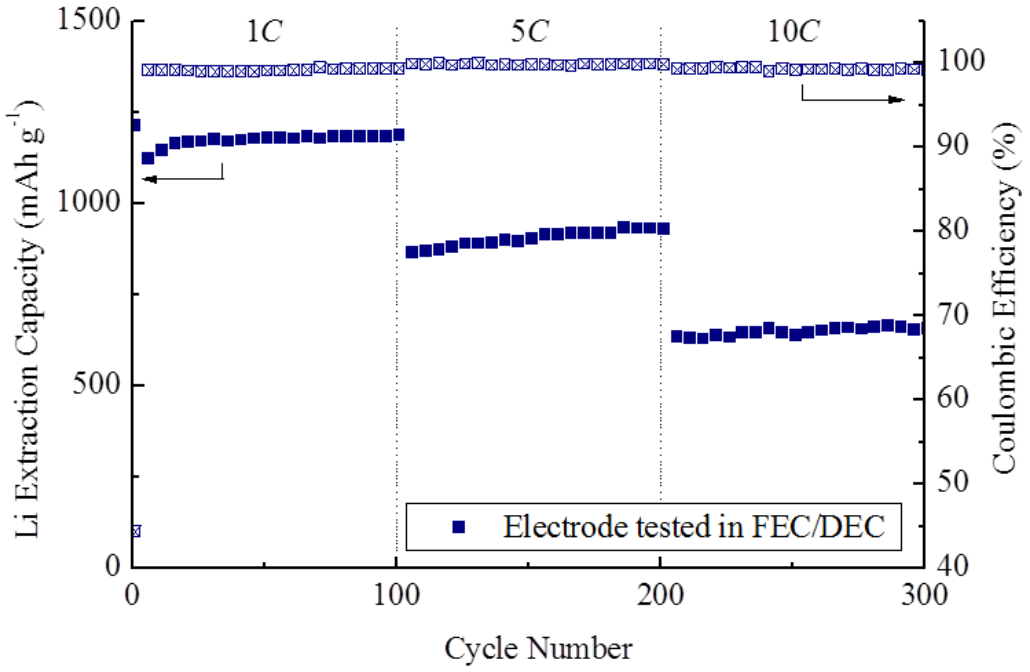

Figure SI.2.8: Cycling performance of Ge nanoparticle electrode tested for 100 cycle intervals at 1*C*, 5*C* and 10*C* in FEC/DEC electrolyte.

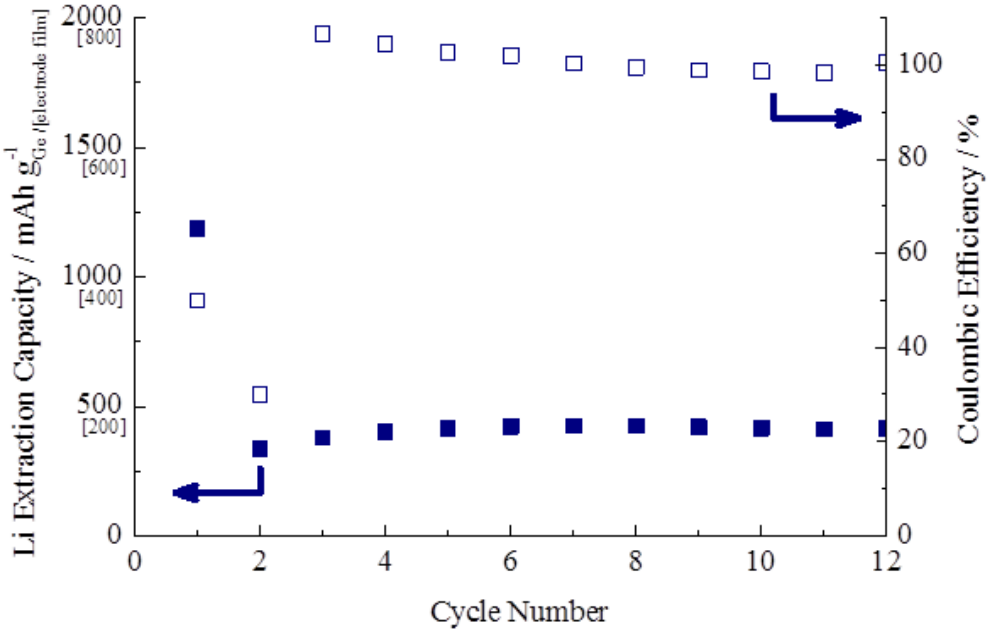

Figure SI.2.9: Cycling performance of Ge nanoparticle electrode in FEC/DEC at 50*C* discharge rate and 1*C* charge rate. Cycles after number 12 not shown because unusual behavior was observed during the subsequent 100 cycles during which the Li-extraction capacity continuously and increasingly exceeded the Li-insertion capacity.

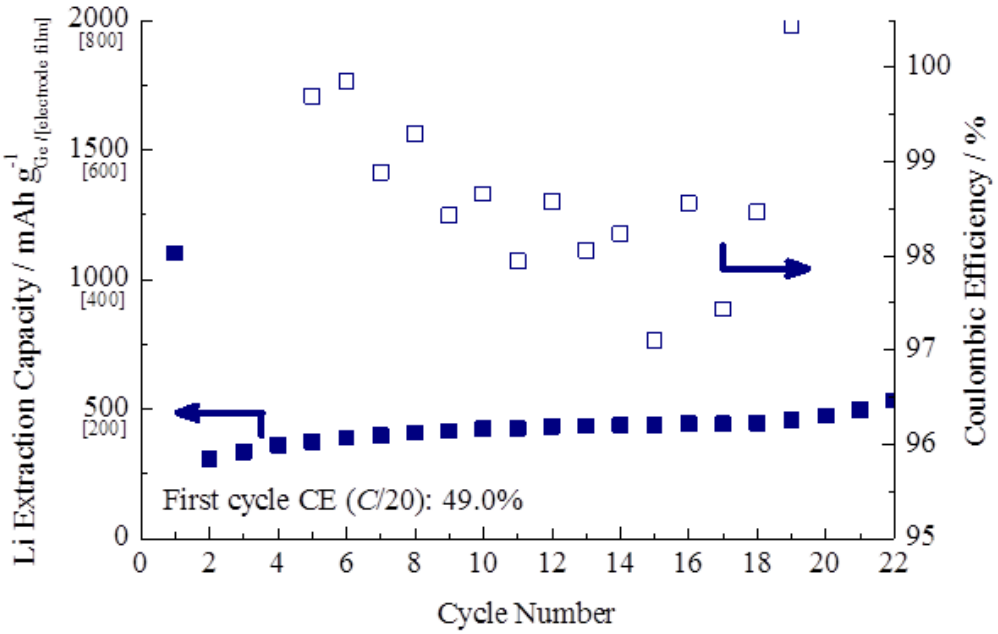

Figure SI.2.10: Cycling performance of Ge nanoparticle electrode in FEC/DEC at 50*C* discharge rate and 1*C* charge rate after treating Li foil with TEOS to inhibit dendritic growth during cycling. Cycles after number 22 not shown because unusual behavior was observed during the subsequent 100 cycles during which the Li-extraction capacity continuously and increasingly exceeded the Li-insertion capacity.

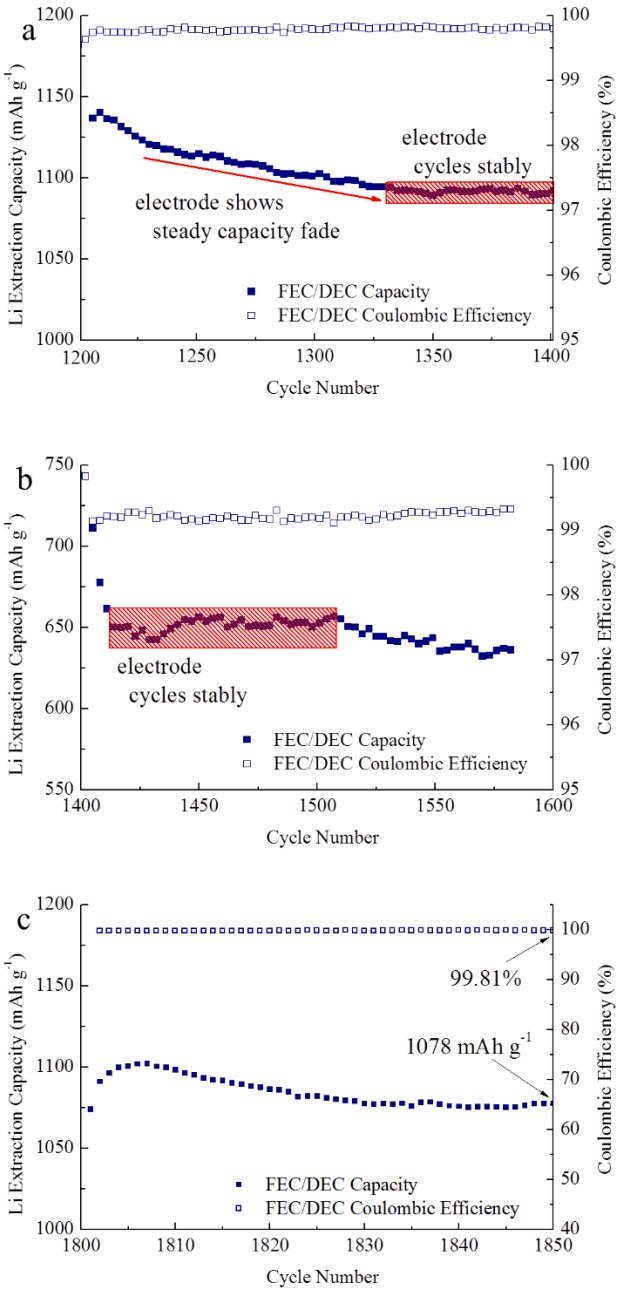

Figure SI.2.11: Stable cycling performance of Ge nanoparticle electrode in FEC/DEC during the (a) 1*C* (third iteration), (b) 5*C* (third iteration) and (c) 1*C* (forth iteration) of cycling during 1,850 cycle test.

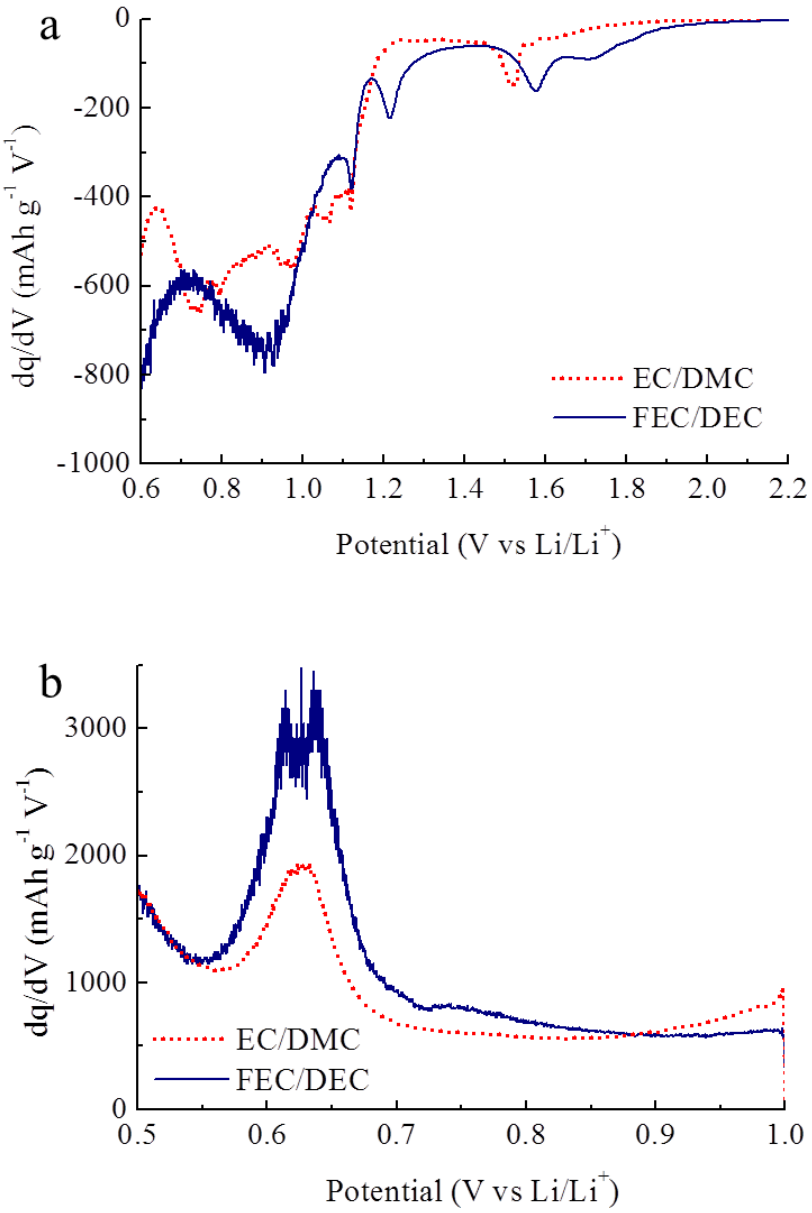

Figure SI.2.12: Differential capacity profile for the first cycle (a) lithium insertion and (b) lithium extraction for Ge nanoparticle electrodes cycled in EC/DMC (red-dotted line) and FEC/DEC (blue-solid line).

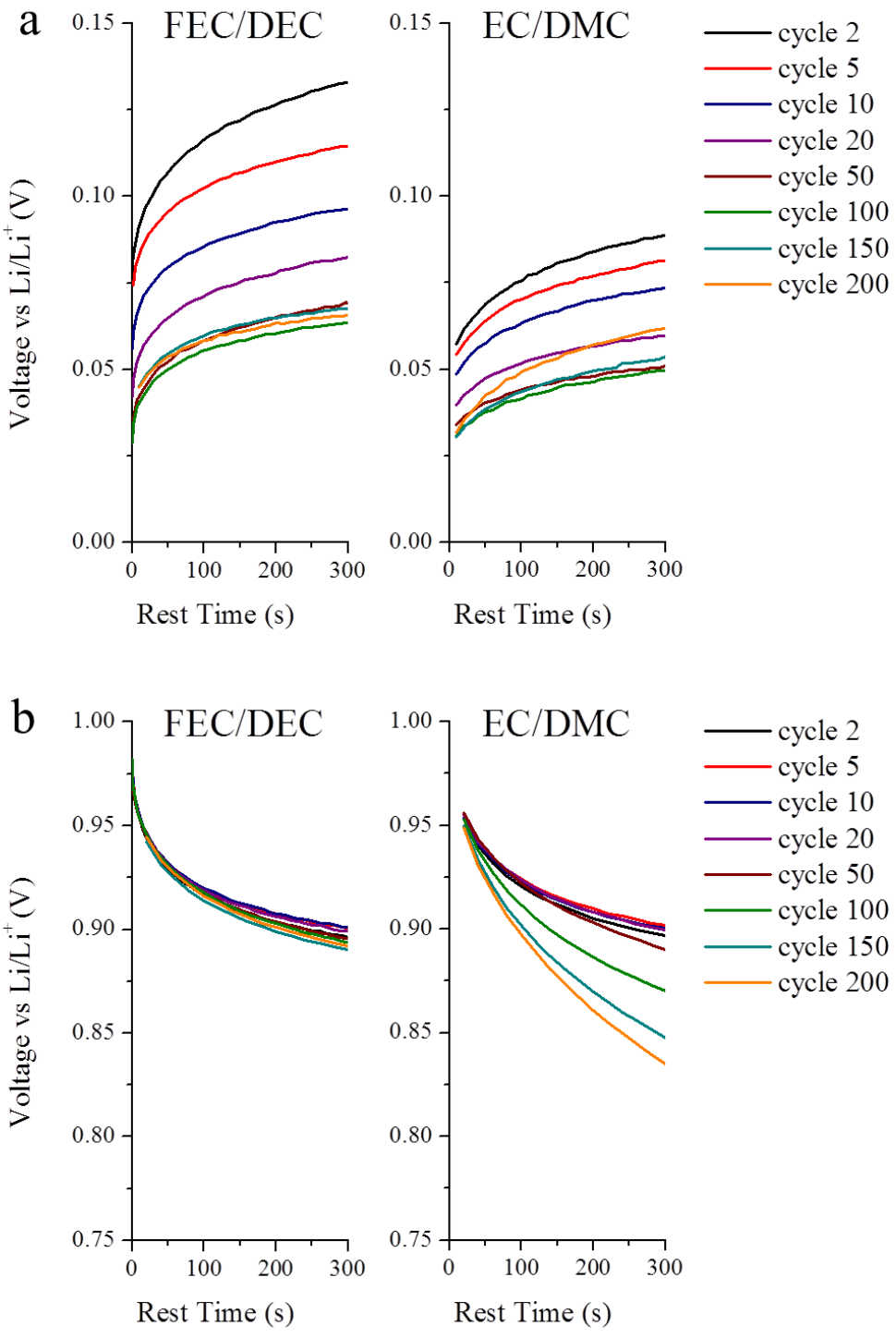

Figure SI.2.13: Relaxation current profiles for electrodes tested at 1*C* through 200 cycles in FEC/DEC (at left) or EC/DMC (at right) during rest period following (a) Li-insertion or (b) Li-extraction.

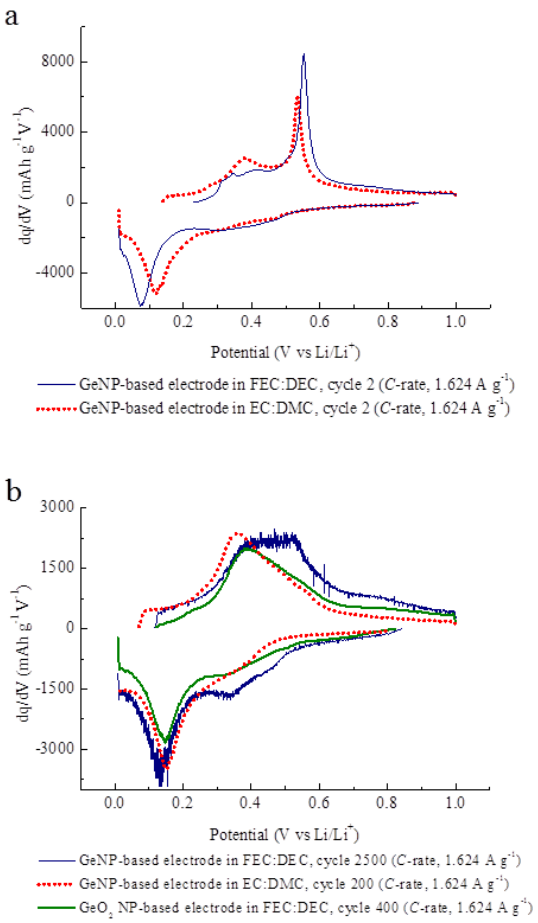

Figure SI.2.14: (a) Comparison of the differential capacity profiles of the Ge nanoparticle electrodes cycled in FEC:DEC (blue solid line) or EC:DMC (red dotted line) at cycle 2 (the first cycle tested at the rate of 1*C*), showing two clearly distinguishable Li-extraction features. (b) Overlay of the differential capacity profiles of the the Ge nanoparticle electrodes cycled in FEC:DEC (blue solid line) at cycle 2,500 (rate, 1*C*) or in EC:DMC (red dotted line) at cycle 200 (rate, 1*C*) compared to the differential capacity profile of a GeO_2 based electrode (60:20:20 GeO_2 nanoparticle / $PAA4_{50kDa}$ / Super-P Li conductive additive) cycled in FEC:DEC (green line) at cycle 400 (rate, 1*C*).

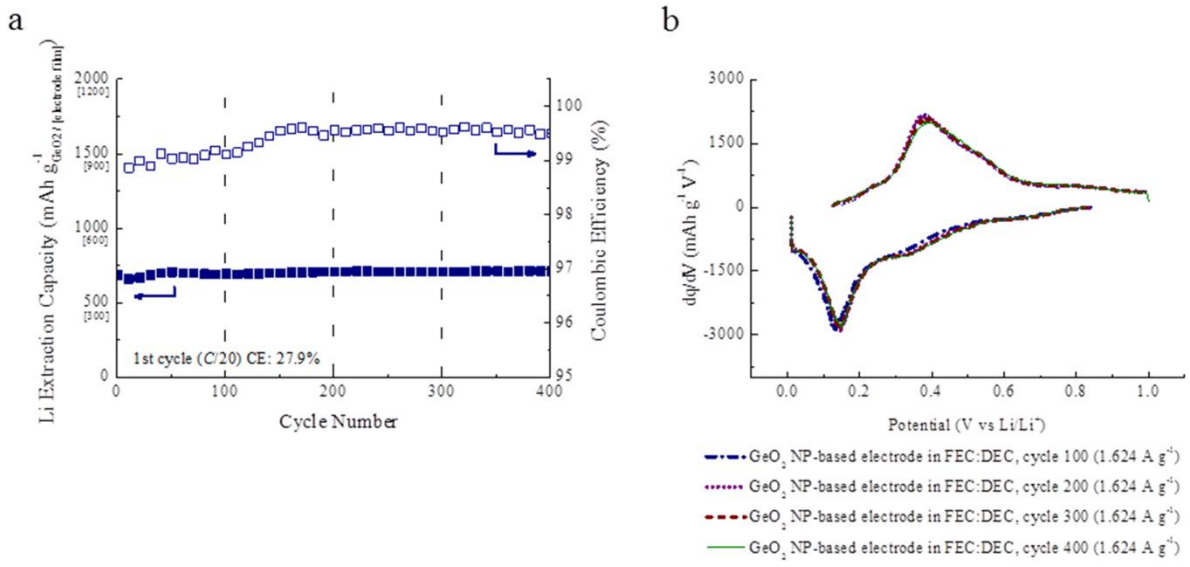

Figure SI.2.15: (a) Cycling performance of GeO_2 nanoparticle based electrodes tested in FEC:DEC electrolyte between 0.01 and 1V at 1*C* following a first cycle *C*/20 conditioning cycle. The electrode composition is 60:20:20 GeO_2 nanoparticle / PAA_{450kDA} / Super-P Li. (b) Overlay of the differential capacity profiles for the GeO_2 based electrode at cycles 100, 200, 300 and 400 (rate, 1*C*).

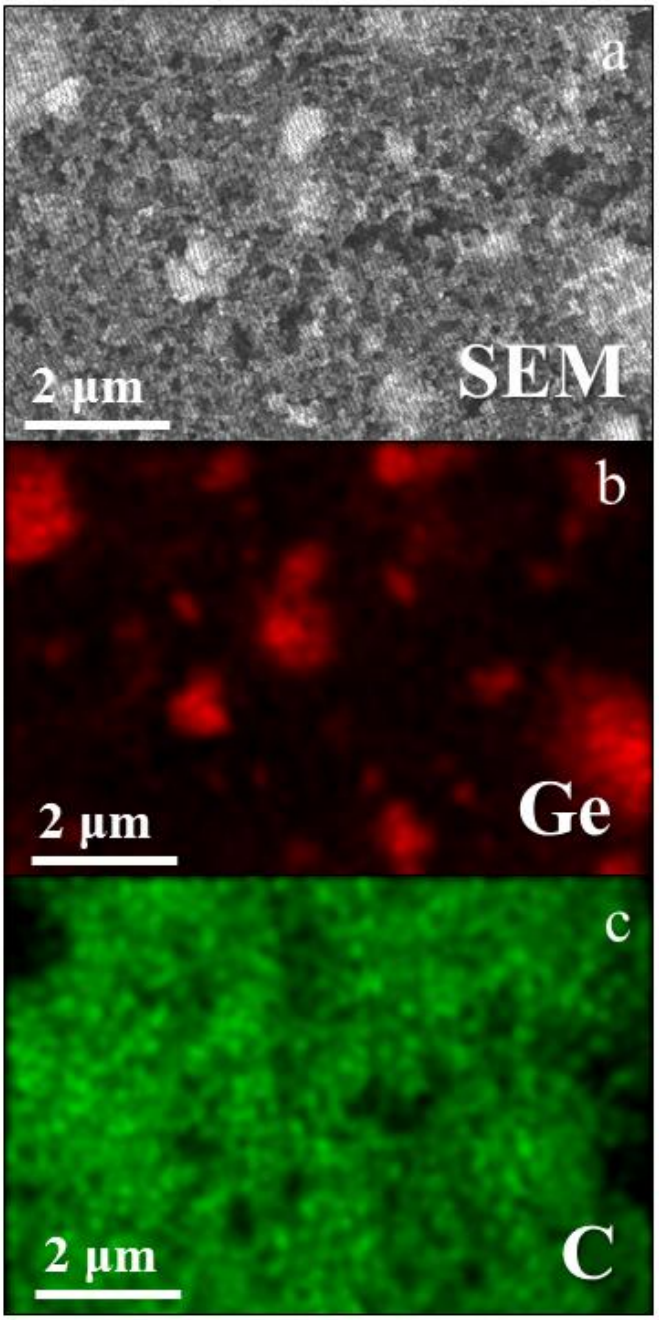

Figure SI.2.16: EDX mapping of Ge-based anode film (not cycled) showing (a) SEM and mapping of (b) germanium and (c) carbon.

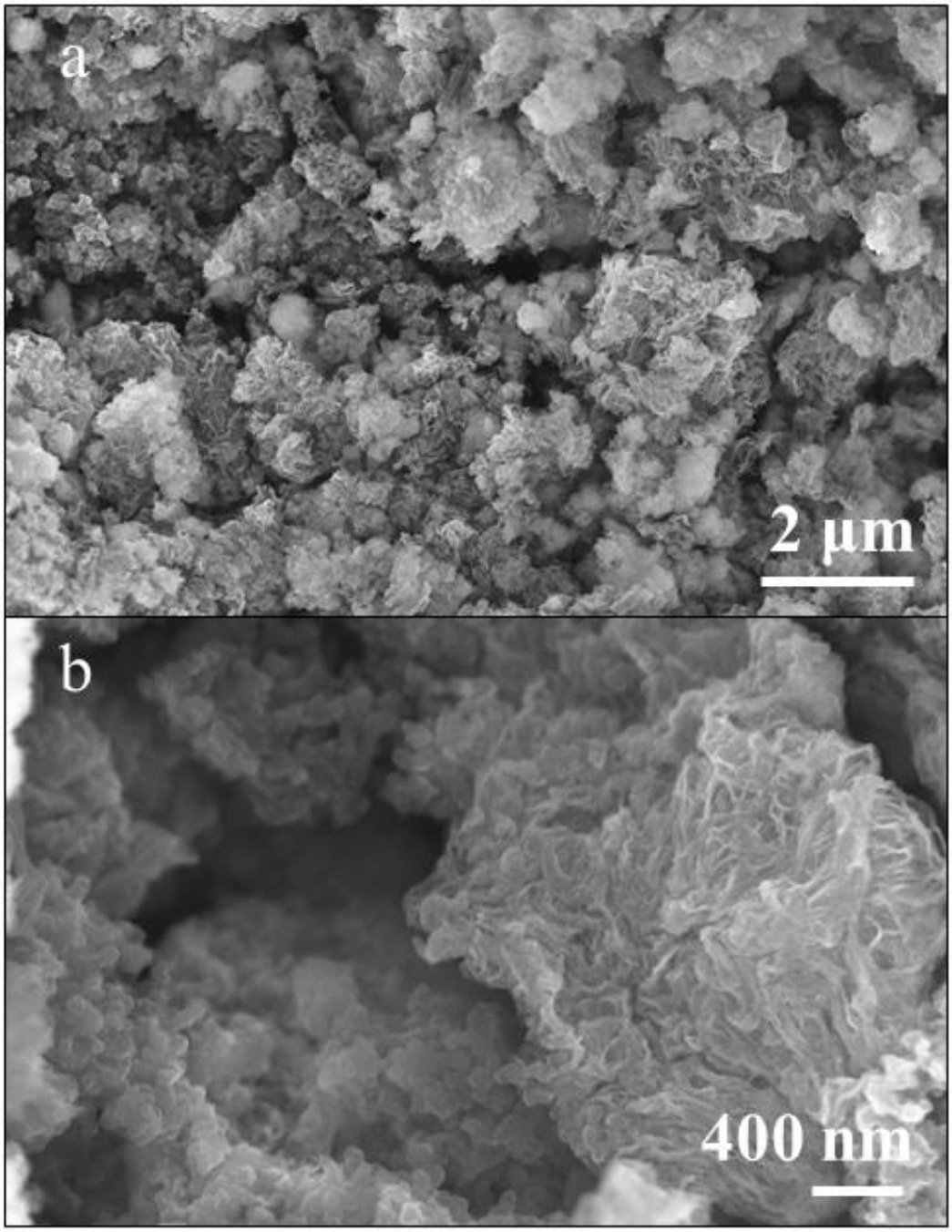

Figure SI.2.17: SEM of Ge nanoparticle electrode cycled 100 times at 1*C* in FEC/DEC showing (a) wide field view of electrode surface showing terraced SEI growths and (b) higher magnification view of SEI on Ge nanoparticles.

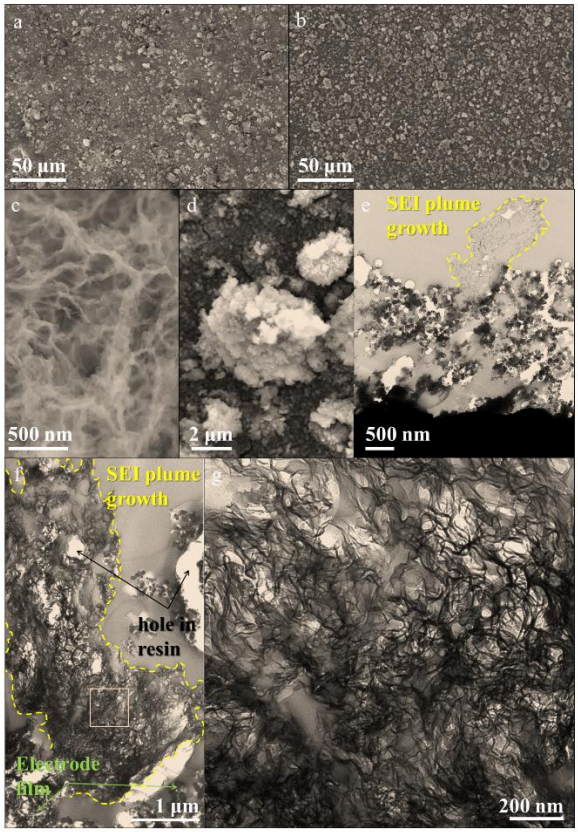

Figure SI.2.18: (a) SEM wide field view at 500x of electrode cycled 100 times at 1*C* in FEC/DEC. (b) SEM wide field view at 500x showing increase in SEI plume growths on surface of electrode cycled 700 times (200 cycles at 1*C*, 5*C* and 10*C* followed by 50 cycles at 5*C* and 1*C*) in FEC/DEC. (c) SEM of interior of plume growth on surface of electrode cycled 700 times (200 cycles at 1*C*, 5*C* and 10*C* followed by 50 cycles at 5*C* and 1*C*) in FEC/DEC. (d) SEM of plume growth on surface of electrode cycled 700 times (200 cycles at 1*C*, 5*C* and 10*C* followed by 50 cycles at 5*C* and 1*C*) in FEC/DEC. (e) TEM cross sectional view of plume growth on electrode cycled 100 times at 1*C* in FEC/DEC. (f) TEM cross section view with inset showing high magnification view of plume growth on electrode cycled 700 times (200 cycles at 1*C*, 5*C* and 10*C* followed by 50 cycles at 5*C* and 1*C*) in FEC/DEC. (g) High magnification view of SEI plume outlined by inset box in (f).

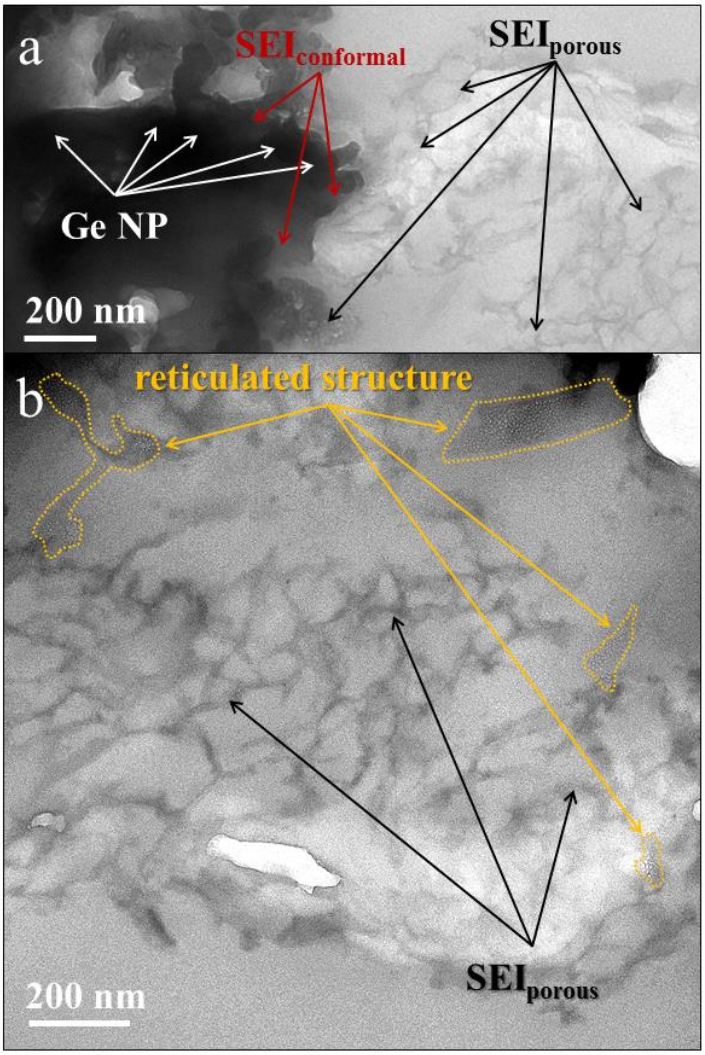

Figure SI.2.19: TEM cross-section of Ge nanoparticle electrode cycled 700 times (200 cycles at 1*C*, 5*C* and 10*C* followed by 50 cycles at 5*C* and 1*C*) in FEC/DEC showing (a) the more dense, roughly conformal SEI surrounding the Ge nanoparticles which transitions into a more porous structure and (b) high magnification TEM cross-section of porous SEI growth and an unspecified finely textured, reticulated honeycomb-like structure.

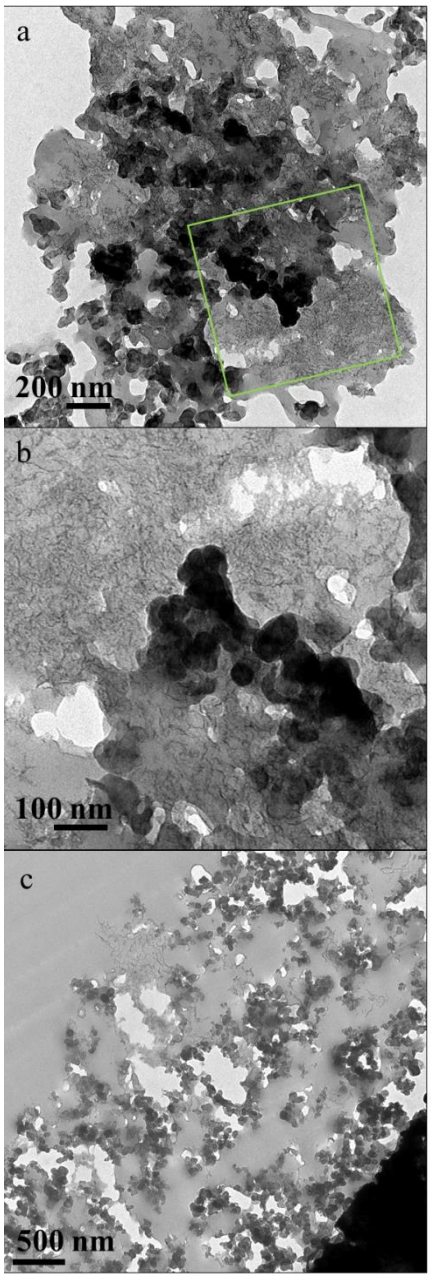

Figure SI.2.20: TEM cross-section showing the representative density of porous SEI observed in the Ge nanoparticle electrodes cycled 100 times at 1*C* in (a) EC/DMC, (b) magnified of green box in (a) and (c) less dense SEI in the electrode film cycled in FEC/DEC.

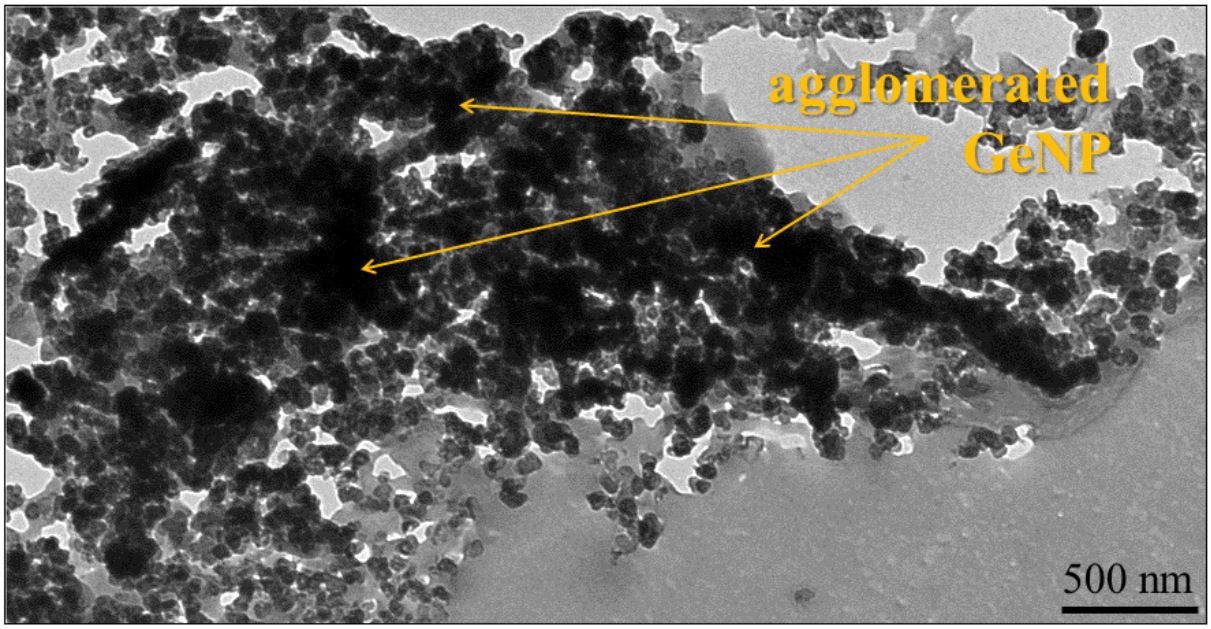

Figure SI.2.21: TEM cross-section showing the agglomerated Ge nanoparticles observed in the electrode cycled 100 times at 1*C* in EC/DMC.

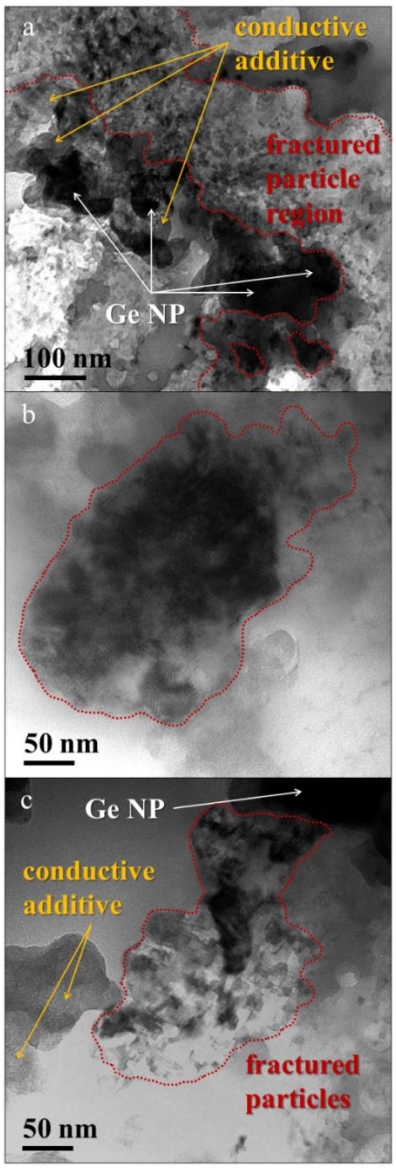

Figure SI.2.22: TEM cross-section showing fractured particles in electrode cycled 100 times at 1*C* in EC/DMC observed in the electrode. (a) Fractured particles surrounding Ge nanoparticles. (b) Ge nanoparticle partially broken into multiple grains. (c) Broken up Ge nanoparticle next to conductive additive and other Ge nanoparticles.

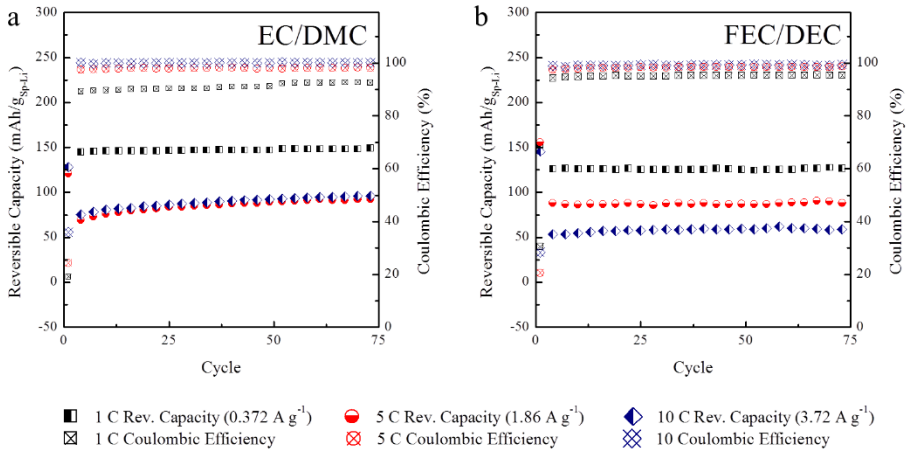

Figure SI.2.23: Cycling performance of conductive additive (Super-P Li) in 80/20 w/w percent Super-P Li/PAA$_{450kDa}$ film cycled in the (a) EC/DMC and (b) FEC/DEC electrolytes for 75 cycles at variable current densities (1*C* defined where C = 372 mAh g^{-1}).

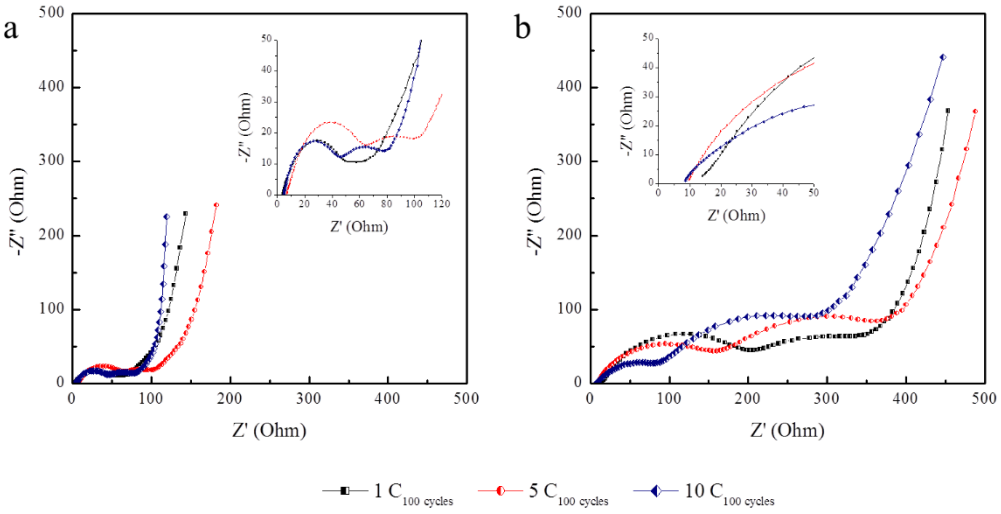

Figure SI.2.24: Electrochemical impedance spectroscopy measured at 1.0 V of conductive additive (Super-P Li) in 80/20 w/w percent Super-P Li/PAA$_{450kDa}$ film cycled in the (a) EC/DMC and (b) FEC/DEC electrolytes at variable current densities (1*C* defined where C = 372 mAh g^{-1}).

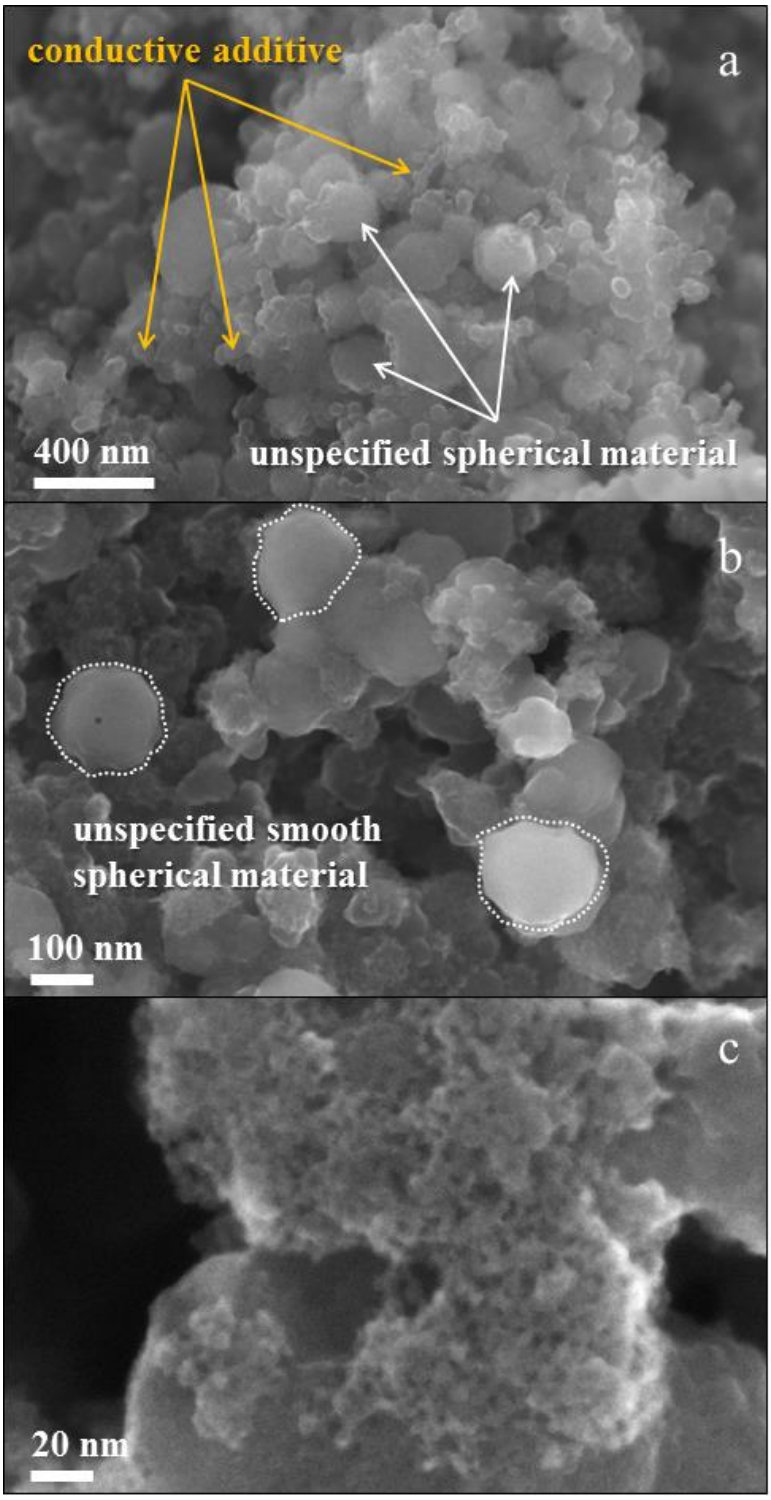

Figure SI.2.25: SEM of Ge nanoparticle electrode cycled 100 times at 1*C* in FEC/DEC showing (a) spherical materials, (b) smooth faced spherical materials and (c) high magnification image of the porous organic growth observed on the spherical materials.

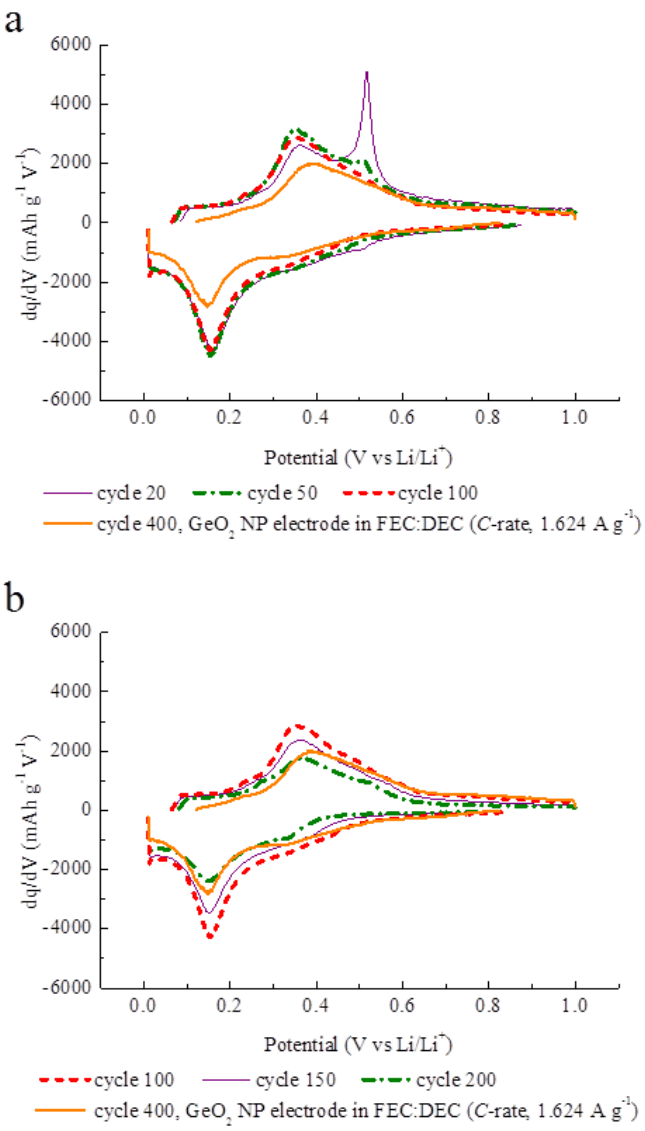

Figure SI.2.26: Differential capacity profiles for the Ge nanoparticle electrode cycled in EC/DMC at 1*C* (a) cycles 20, 50 and 100 compared with differential capacity profile of GeO_2 based electrode (cycle 400, rate 1*C*) and (b) cycles 100, 150 and 200 with differential capacity profile of GeO_2 based electrode (cycle 400, rate 1*C*).

NOTES ON STUDY

This study demonstrated - without intent and without knowledge during the experiment and its report - the efficacy of the FEC co-solvent in diminishing the growth of lithium dendrites, described as “plumes” in the study. Also, the co-solvent DFEC was tested in the course of this study, but was found to be inferior to FEC when used as a co-solvent substituting for EC and also as an additive of 5 weight percent (in comparison to FEC as an additive, this data also unpublished).

Chapter 3: A free-standing, flexible lithium-ion anode formed from an air-dried slurry cast of high tap density SnO_2, CMC polymer binder and Super-P Li[2]

INTRODUCTION

Flexible or free-standing electrodes for lithium ion batteries (LIB) that can be stretched, compressed and deformed are desired for use within the increasingly more compact framework of portable devices and powering an emerging class of stretchable, bendable electronics.[1,2] Commercial electrodes in standard lithium-ion batteries are currently constructed of a slurry cast electrode film adhered to a metal foil current collector. The bending or other deformation of this electrode design commonly results in degradation and sometimes delamination of the film, leading to increased resistance and loss of electrical connection.[3]

To attempt to avoid these issues, many electrode architectures designed without a metallic current collector have been devised. For a comprehensive survey of the state of this field of research, the reader is referred to three recently published review articles by Zhou et al.[4], Gwon et al.[5] and Hu and Sun[6]. The designs for electrodes made without a current collector may be generally characterized as belonging to one of two categories as defined by Hu and Sun[6]: i) flexible electrodes, which are formed by casting or depositing nanostructured active material onto a dually flexible and (typically) conductive substrate and ii) free-standing electrodes, which are films of

[2] The content in this chapter has been copied (with minor edits) from its original publication in the *Journal of Materials Chemistry A* in 2014.

homogenously integrated nanostructured active material and nanostructured carbon, such as carbon nanotubes (CNT), graphene or carbon fibers.

For flexible electrodes (category i), nanostructured active material is deposited (chemical[7,8,9] or physical[10,11] deposition, hydrothermal treatments[12], wet chemical deposition[13], sputtering[14]) or coated[15] upon a separately constructed flexible substrate. The substrate should be lightweight, strong and may be intrinsically conductive, or otherwise an initially non-conductive material (paper[15], membrane separator[16], Kimwipes[17]) may be made conductive by coatings. Flexible conductive substrates have been made from films of 1D or 2D carbons (such as CNT[18,19], carbon fibers[20], graphene[10,21,22], graphene foam[23]), 1D carbons embedded into polymer films[24,25], carbon cloth[12], nickel foam[26], *etc*. Several full batteries[15,10,17] have been developed using this approach and some electrodes with very high strength have been reported[9].

For free-standing electrodes (category ii), 1D or 2D carbons are combined with nanostructured active material (nanoparticles[8,13,27,28,29,30], nanofibers[31,32], nanowires[33,34,35], *etc.)* and the film is typically assembled by a vacuum filtration process. Although numerous high-performing free-standing electrodes have been reported, Hu and Sun cite the cost of nanostructured material syntheses and low-efficiency filtration process as significant barriers which might preclude transition from lab-scale development to scaled-up mass film production[6].

Recently, free-standing films resulting from using alternative binder materials have been demonstrated using micro-[36] or nano-fibrillated[37] carboxymethyl cellulose (CMC) as well as carboxymethyl cellulose fibers[38,39]. These have opened up an alternative (and possibly less expensive and energy intensive) route for creating free-standing electrodes.

Here we study a simple process for creating large areas of free-standing electrodes that avoids the need for vacuum filtration: we report electrodes cut from flexible, thin films formed from doctor-bladed slurries which delaminate from the substrate upon air-drying. The resulting films form within minutes of casting and are composed of commercially available micron-sized, high tap density SnO_2 particles and CMC 90-kDa polymer and can be made with CNT or Super-P Li (SP-Li) type carbon black particles. To the best of our knowledge, this is the first use of the commercially available polymer-form of CMC in a free-standing film.

Note that hereafter, films made using only CNT as the conductive additive are designated SnO_2/CNT and films made only using SP-Li as the conductive additive are designated SnO_2/SP-Li.

While the SnO_2/CNT electrode was measured to have a higher strength at break and lower electrical resistivity both before and after the folding and creasing of the electrode film (the recommended method of measuring the effect of flexing a film by rolling it around a thin rod[3] did not appear to be sufficient to test this surprisingly flexible film), the cycling performance of the SnO_2/SP-Li electrode exceeds that of the SnO_2/CNT electrode made with the orders-of-magnitude more expensive 1D carbon. In cycling tests conducted at 1*C* through 100 cycles or at variable *C*-rates up to 2*C*, the flexible SnO_2/SP-Li electrodes tested stably, while the SnO_2/CNT electrodes exhibited both lower as well as unstable and fading capacities in these same tests.

As the discovery of the self-delamination property of this electrode film was accidental, the selection of SnO_2 as the active material was made owing to ordinary design principles: SnO_2 is a potentially viable alternative anode active material that might be substituted for the commercially used graphite because of its (a) comparatively high theoretical capacity of 782 mAh g^{-1}, (b) relative abundance in concentrated ores[40], (c) viability for safe, rapid charging (without

severe risk of dendrite formation) due to the Li-alloying occurring at relatively high potentials vs the Li/Li^+ redox couple, (d) relatively low average discharge potential which allows for its use in a high voltage battery and (e) ability to cycle stably for many hundreds of cycles[41] despite undergoing a near 360% volumetric change[42] to accommodate Li-alloying/de-alloying.

To achieve areal capacities comparable to what is commercially available[43,44], the SnO_2/SP-Li electrode films (typical thicknesses of near or less than 5 μm) can be stacked to reach higher effective mass loadings. For a stack of electrodes made with between 7 to 10 films (film count was varied so as to achieve 4-4.5 mg-SnO_2 cm^{-2} loading), a 2.6 mAh cm^{-2} capacity was observed with 0.33 mA cm^{-2} current density (~*C*/12); 1.8 mAh cm^{-2} at 0.67 mA cm^{-2} (~*C*/6) and 0.9 mAh cm^{-2} at 1.0 mA cm^{-2} (~*C*/4). In addition to coin cell testing, this SnO_2/SP-Li electrode film was further studied in a flexed orientation to better understand the electrode behavior under conditions of intended use. In a home-built pouch cell, the electrode was folded and found to cycle stably for 20 cycles at 1*C* rate before slight capacity fade was observed.

Accompanying the potential advantages derived from the simple method of production and low cost of the conductive additive for this free-standing SnO_2/SP-Li electrode, we believe its flexible design may have particular application where space may be of concern such as in medical devices or wearable electronics, for the electrode's favorable cycling performance (in terms of capacity at variable rate, stability and coulombic efficiency results) is achieved with relatively high volumetric energy density owing to an absence of a current collector and the use of high tap density active material.

EXPERIMENTAL

Electrochemical testing. Electrodes were prepared by mixing microns-sized SnO_2 particles (*Alfa-44606,* SEM and TEM in S Figure 3.1 ESI†), CMC 90-kDa polymer binder (*Sigma*) and either Super-P Li (*Timcal,* \$0.00792 g^{-1}) or multi-walled carbon nanotubes (*NanoAmor*, 8-15 nm diameter, 10-50 μm length, \$6.00 g^{-1}) in a 3:1:1 weight ratio in deionized water. From SEM, we observed that the film volume is predominantly filled with conductive additive (S Figure 3.2 ESI†); this indicates that a higher content of active material would be possible to achieve in future optimization of the electrode composition. Also, we found that similar free-standing, flexible electrodes could be prepared using nanosized SnO_2 particles (*Sigma*, <100 nm S Figure 3.3 ESI†), but here we restricted our studies to electrode films made using micron sized particles which provide for higher volumetric energy density owing to a very high tap density[45] for the selected SnO_2 anode active material: 2.5 g cm^{-3} (*Quantachrome* Autotap).

The slurry mixture was cast onto copper foil (*MTI*, 10 μm) and left to air-dry. During the drying process, the films delaminated from the substrate into large, continuous free-standing sections. In an effort to improve the delamination process such that larger continuous regions of film formed, we attempted to cast upon a lower surface energy substrate (we selected Mylar, *McMaster Carr*). This change in substrate accordingly required lowering the surface tension of the slurry so that it wetted the surface upon casting. This wetting was achieved by using mixture of ethanol and water for the slurry and the delamination process was found to be most improved when the slurry was composed of 1 g solids, 4 g H_2O and 1.25 g EtOH (200 proof). Electrodes of $^7/_{16}$" diameter were punched from the film, vacuum-dried at room temperature and used as the negative electrode *vs* a lithium foil counter/reference electrode in a 2032 coin cell assembled in an Ar-filled glovebox (less than 3.2 ppm H_2O and less than 0.1 ppm O_2). *Celgard* 2400 (polyethylene) membrane was used as the separator with 1M $LiPF_6$ (*Sigma*) dissolved in 5 wt% FEC (*Solvay*

Fluor) in EC:DEC *(*co-solvents purchased individually from *Sigma* and mixed in a 1:1 volume % ratio) selected as the electrolyte. For anodes constituted of several films in a stack, a drop of electrolyte was added between each film in the stack.

Cycling tests using coin cells were performed on an Arbin BT-2043 or BT-2143 multichannel battery testing system. Charge (ion-insertion into the anode) and discharge (ion-extraction) was performed between 0.01 and 1.0 or 1.25 V vs the Li/Li^+ redox couple with the theoretical capacity defined as 782 mAh g^{-1} (1*C* = 0.782 A/g). For each cell, a conditioning cycle at *C*/20 was completed prior to testing.

Pouch cell testing was conducted inside a glovebox due to issues arising from O_2 and H_2O permeation through the polyethylene (PE) plastic bag used as the pouch. The flexible electrode and Li foil counter/reference electrode were connected to custom-cut copper 200-mesh leads (*TWP*) by applying slight pressure to the cell during testing. Electrolyte was added to the pouch before the pouch was closed using a *Food Saver* impulse sealer[46]. Galvanostatic testing with a conditioning cycle at *C*/20 followed by 1*C* testing was performed on the pouch cells using a *CH Instruments* potentiostat/galvanostat (608D).

Mechanical testing. Mechanical testing was performed using an Instron Microtensile tester model 5948 (*Instron*) with a 1kN load cell at a strain rate of 0.5 mm/min. Strips of each electrode film were cut into rectangular sections (approximate dimensions, ~2-3 mm in width by ~10-15 mm in length) with a razor to avoid tearing. Extensive observation of the length of the films' cut edges with a scanning electron microscope (SEM, *Zeiss Supra 40*) revealed no tears. Five or more successful tests were used to establish repeatability. Because of the thinness of the films, a caliper

was not suitable for measuring the film thickness. To establish the strength at break, this thickness measurement was made using SEM for two of the successful samples representative of the group of tests for both electrode film types: SnO_2/SP-Li and SnO_2/CNT. Ten images at 8,000x magnification (about 35 μm of film length in frame) were obtained, and using the software called *ImageJ*[47] the film cross-sectional area, film length and scale bar were measured in pixels and then the cross-sectional film area was divided by its length to find the average film thickness.

Resistivity measurements. The electrical resistivity of the films was measured using a four-point probe (Lucas 302) with a Keithly 220 programmable current source and a 127 □m tip radius (SP4-40-85-TC-5). The effect of folding and creasing the electrode film was determined by measuring the resistivity before and after (a) folding the film, (b) applying a weight to give a pressure of ~0.4 atm (the folded film was held between plastic covering and a weight was applied) and (c) unfolding the film and measuring resistivity with the probes oriented perpendicular to and across the fold. The film thicknesses were measured in the same manner as for mechanical testing.

Microscopy. Electron microscopy was performed using a scanning electron microscope (SEM, *Zeiss Supra 40*) and transmission electron microscope (TEM, *FEI Tecnai*) operated at 80 keV. For TEM, cross-sections of the electrode were prepared by use of an ultramicrotome as discussed in an earlier work.[48]

RESULTS

Electrochemical testing

The cycling performance of the free-standing SnO_2/SP-Li and SnO_2/CNT films was initially evaluated in a test through a series of *C*-rates from *C*/10 to 2*C* (Figure 3.1). Because of the tendency of Sn or SnO_2 based anodes to fail as a consequence of the Fe_2O_3 matrix degrading

at more oxidizing potentials (leading to Sn agglomeration into electrically isolated nanoclusters[49]), the upper voltage cut-off (UVC) for discharge was originally selected to be 1.0 V vs Li/Li^+, as recommended by Mohamedi et al.[50] This voltage boundary is appreciably higher than the potential suggested by Courtney and Dahn as to prevent Sn aggregation, although still below their recommended limit of ~1.3 V, the boundary beyond which damage to the Fe_2O_3 matrix may occur.[51]

For the SnO_2/CNT electrodes, unstable cycling performance was observed when discharging to the 1.0 V UVC, with rapid capacity fade evident beginning during the 1*C* testing sequence (cycles 31-40) in Figure 3.1. For the SnO_2/SP-Li electrodes, stable cycling performance was observed from *C*/10 to 2*C* rates, but with capacities lower than theoretical at even the low charge/discharge rate of *C*/20 (conditioning cycle) and *C*/10. The maximum observed capacity was near 600 mAh g^{-1}, suggesting that discharge completed only to the SnLi phase (the theoretical capacity corresponding to the SnLi phase is 178 mAh g^{-1}).[52]

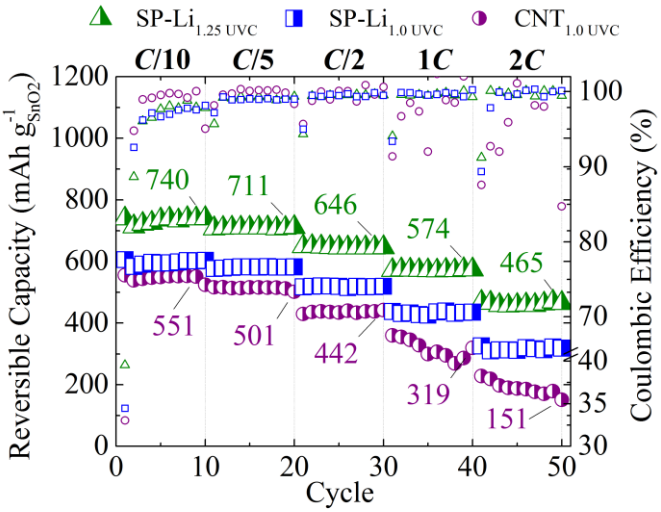

Figure 3.1. *C*-rate test of free-standing SnO_2/SP-Li electrodes (discharged to an upper voltage cut-off, UVC, of either 1.0 or 1.25 V vs Li/Li^+) or SnO_2/CNT electrodes (discharged to an UVC of 1.0 V). Prior to testing, a *C*/20 conditioning cycle was run.

For these SnO_2/SP-Li electrodes, the upper limit on discharge was then extended to 1.25 V, 1.5 V and 2.0 V in an effort to achieve full discharge and capacities nearer to the theoretical value for SnO_2 (782 mAh g^{-1}). With the UVC set at 2.0 V or at 1.5 V, we found unstable cycling performance, but improved capacities without sacrificing stability were observed with the UVC at 1.25 V. As shown by the voltage profiles in Figure 3.2, with this extended voltage window the capacity of the film was increased by 23 %, 22 %, 24 %, 32 % and 46 % at rates of *C*/10, *C*/5, *C*/2, 1*C* and 2*C*, respectively. By extending the UVC, the SnO_2/SP-Li electrodes also showed higher first cycle coulombic efficiencies – 39.6 % vs 34.5 % - although efficiencies recorded during cycling were similar.

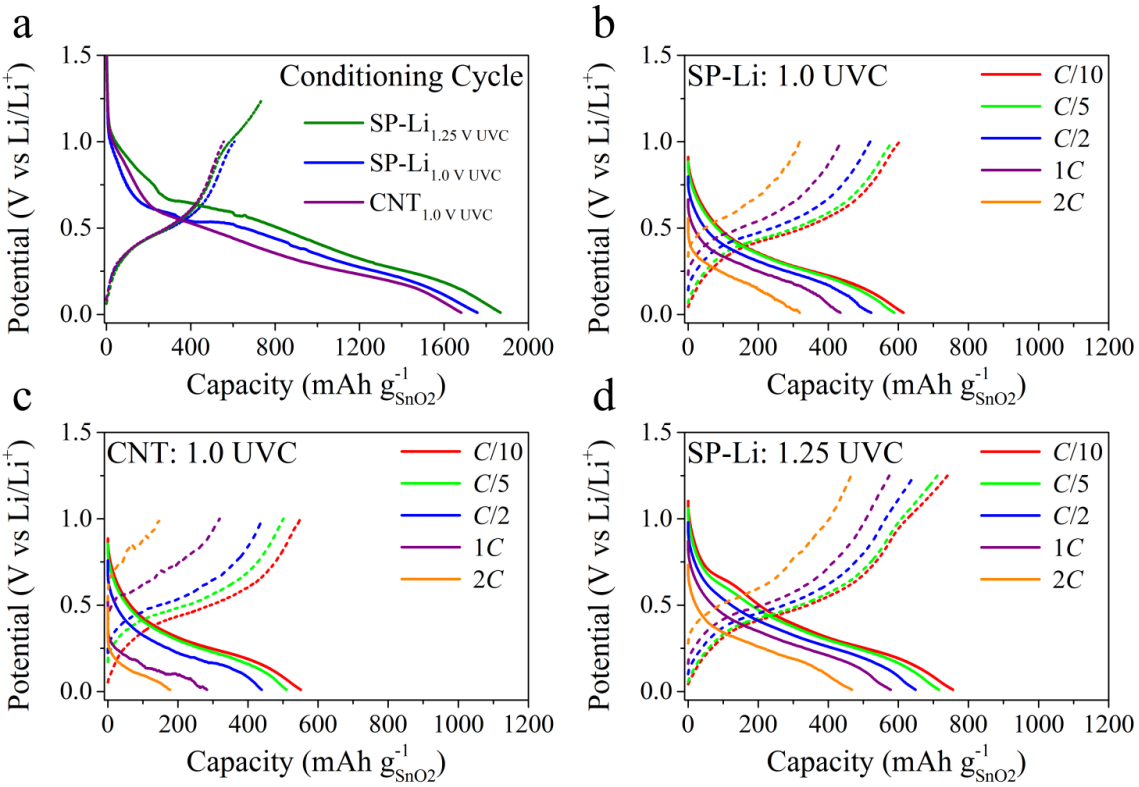

Figure 3.2. (a) The first cycle voltage profile and voltage profiles for each of the stages of *C*-rate testing for the SnO_2/SP-Li films, discharged to (b) 1.0 V vs Li/Li^+ or (d) 1.25 V vs Li/Li^+ and for the SnO_2/CNT films, discharged to 1.0 V vs Li/Li^+.

The SnO_2/SP-Li electrode cycled to the UVC of 1.25 V tested stably at a rate of 1*C* through 100 cycles (Figure 3.3). The reversible capacity (rising to 450 mAh g^{-1}) was lower than what was indicated by the *C*-rate tests, and this may be a consequence of the different testing conditions: a gradual increase in cycling rate *vs* a more abrupt polarization of the electrode arising from a larger increase in rate following the conditioning cycle. In this 1*C* test, SnO_2/CNT electrode cycled unstably after about 20 cycles, with erratic efficiencies between ~95 % and ~105 %, similar in performance to what was observed in the 1*C* sequence in *C*-rate tests.

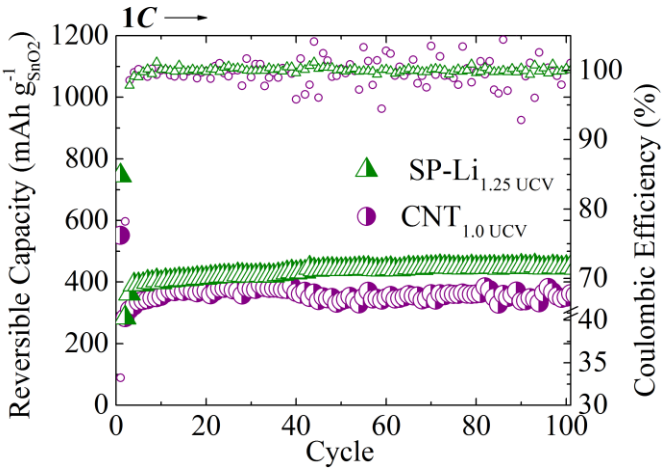

Figure 3.3. 1*C* testing of free-standing SnO_2/SP-Li films (discharged to an upper voltage cut-off of 1.25 V vs Li/Li^+) and SnO_2/CNT films (discharged to an upper voltage cut-off of 1.0 V). Prior to testing, a *C*/20 conditioning cycle was run.

In Figure 3.4, cycling performance is reported for a half cell in which several stacked SnO_2/SP-Li films rather than one single film are used as the anode. This is done to increase the energy density per unit "footprint", i.e., the areal capacity. For a selected active material particle, conventional slurry cast films may achieve higher areal capacities typically by increasing film thickness. However, with increasing thickness, the film becomes more resistive: there is a trade-off between energy density and power density (S Figure 3.4 ESI†) as a consequence of the limiting diffusion rate of the ion in the anode[53]. Also, with increasing thickness the conventional film's mechanical integrity decreases,[54] a consequence particularly significant for films which will be tightly wound such as in a jellyroll configuration. In high speed commercial processing, the electrode thickness is reported to be limited to 50 μm (mass loading of ~ 20 mg cm^{-2}) to avoid delamination.[55]

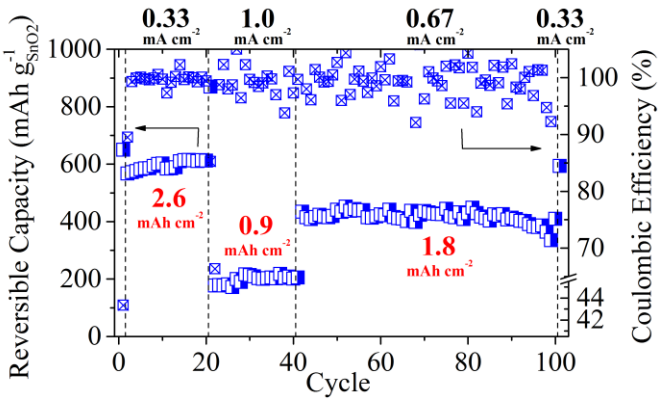

Figure 3.4. Variable rate (*C*/12, *C/4*, *C*/6, *C*/12) testing of stacked anode, comprised of nine SnO_2/SP-Li films stacked to provide higher areal capacity as a consequence of effective higher mass loading (4.2 mg SnO_2 cm^{-2}). Prior to testing, a *C*/20 conditioning cycle was run.

The thin, flexible electrodes tested here might be wound tightly to achieve higher areal capacities; however, as an alternative, an increased energy density may also be achieved by stacking several thin films which have no preferred orientation due to homogeneous mixing of the active materials, binder and conductive additive. The result is higher areal capacities achieved by higher mass loadings (4.2 mg SnO_2 cm^{-2}) at the cost of lower specific power: stable cycling with 2.6 mAh cm^{-2} capacity at 0.33 mA cm^{-2} (~*C*/12) rate, 0.9 mAh cm^{-2} capacity at 1.0 mA cm^{-2} (~*C*/4) rate, and slight capacity fade evident throughout a longer, 60-cycle test with 1.8 mAh cm^{-2} capacity at 0.67 mA cm^{-2} (~*C*/6) rate. When returned to a 0.33 mA cm^{-2} rate on its 101st cycle, the stacked anode retained 97 % of its maximum 0.33 mA cm^{-2} capacity observed during the initial 20 cycles of testing.

The result of cycling at the current density of 1.0 mA cm^{-2} appears to have irreversibly damaged the electrode because after the 20th cycle the coulombic efficiencies were scattered, ranging from ~95 % to 105 %. These are evidence of local, transient changes in resistance to charge

or discharge which might be attributable to the film degrading; changes or breaks in film-to-film contact cycle to cycle could explain this result.

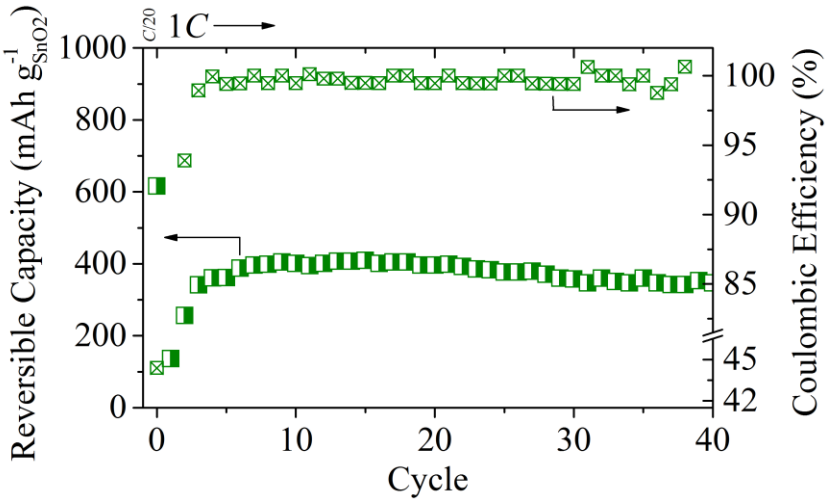

Figure 3.5. 1*C* testing of single film of SnO_2/SP-Li film in a flexed orientation: bent 180 degrees and compressed with binder clips. Prior to testing, a *C*/20 conditioning cycle was run.

To indicate the potential viability of the electrode when cycling in a severely flexed position, a single thin SnO_2/SP-Li film was tested in a bent orientation (180 degree fold, this orientation fixed with plates bounding the outside of the pouch held with binder clips) for 40 cycles at 1*C* rate (Figure 3.5). The electrode cycled stably at 1*C* for 20 cycles before slight capacity fade was observed along with increasing fluctuations in the coulombic efficiency.

Mechanical testing

or a semi-quantitative evaluation of the robustness of the free-standing films, the mechanical properties of tensile strength and elongation at break were measured for uncycled SnO_2/SP-Li and SnO_2/CNT films (Figure 3.6) as described in the experimental section. By using CNT rather than SP-Li, graphitic particles which form percolating, chain-like networks held together by Van der Waals forces, the strength at break of the film increased from an average of

near 13 MPa to near 33 MPa (Figure 3.6). The strain at break for all samples, SnO_2/CNT or SnO_2/SP-Li type films, was near 1.7%. By incorporating a higher molecular weight CMC binder, we believe improvement might be made for both of these properties. However, as currently constituted, the SnO_2/SP-Li film was found to be easy to handle and could tolerate folding/unfolding and flexing without noticeable damage.

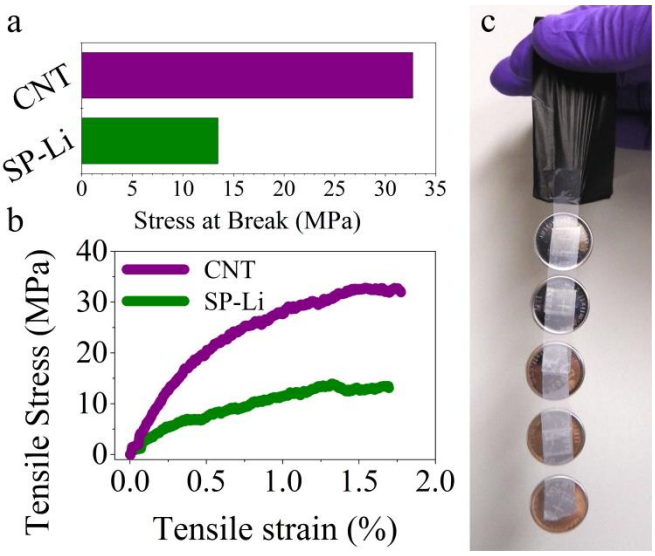

Figure 3.6. (a) Results representative of average of mechanical testing of uncycled SnO_2/SP-Li and SnO_2/CNT films with (b) raw data shown for representative tests. (c) Several 2032 assembled coin cells taped to edge of SnO_2/SP-Li film.

Electrical resistivity testing

To evaluate the degree to which flexing and folding affected the integrity of the film's electrically conductive network, uncycled films were measured using a four point probe before and after first folding the film, then applying pressure by placing a weight on top of the fold sandwiched between plastic and finally unfolding the film. This second, comparative measurement

was made in approximately the same location as the initial measurement and across (*i.e.* perpendicular to) the fold.

As shown in Figure 3.7, there was surprisingly little difference before and after this folding procedure, with an increase in resistivity of 6 % and 4 % for the SnO_2/SP-Li and SnO_2/CNT films, respectively, these changes within the margin of error determined by the standard deviation of the electrode thickness measurements described in the experimental section.

For context, we note that these resistivity measurements are on the same order of magnitude to the values reported by *TIMCAL* for $LiCoO_2$, $LiMn_2O_4$ and $LiNiO_2$ based electrodes slurry cast onto aluminum foil once the SP-Li concentration has passed the threshold for establishing an electrically percolating network[56].

Scanning electron microscopy (SEM)

It is not atypical for a slurry cast film to partially delaminate from the current collector, and this is generally a consequence of a pool of extra slurry drying into thicker films. However, this sort of delaminated film will generally crack into small pieces and readily fall apart. In contrast, for these SnO_2/SP-Li and SnO_2/CNT free-standing films reported here, a very thin film is the result of the delamination which occurs upon air-drying. The typical SnO_2/SP-Li (and SnO_2/ CNT) films were found to have a mass loading near 0.5 mg cm^{-2} with a thickness of about 5 μm (although films as thin as 2 μm were made).

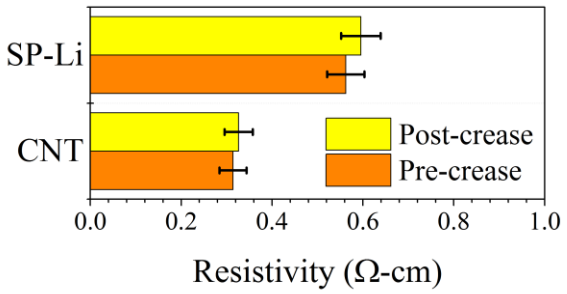

Figure 3.7. Electrical resistivity of SnO_2/SP-Li and SnO_2/CNT films established by four point probe measurements before and after (a) folding the film, (b) applying a weight to give a pressure of 0.4 atm – the folded film was held between plastic covering and a weight was applied – and (c) unfolding the film and measuring resistivity with the probes oriented perpendicular to and across the fold.

As shown in Figure 3.8, the morphology of the SnO_2/SP-Li film is noticeably smoother than that of the SnO_2/CNT film within which the CNT appear to agglomerate in clumps, a feature that is apparent from SEM taken with a top-down perspective (S Figure 3.2, ESI†). From the cross-sectional TEM (S Figure 3.5, ESI†), the nature of the film becomes more clear: the conductive additive – SP-Li or CNT – forms a thin boundary around the large particles. The SnO_2/SP-Li films appear significantly more porous than the SnO_2/CNT films, possibly explaining the poorer cycling performance for the SnO_2/CNT films: more tortuous pathways for solvated Li^+ ion transport through the anode equates to higher resistance and larger overpotentials required for each stage of charge and discharge. Extrapolating from these images, we suggest i) the use of a surfactant in addition to using probe sonication might better disperse the CNT, thereby improving this electrode's cycling performance and ii) that a mixture of CNT and SP-Li conductive additive in a film may enable better cycling performance. However, economic considerations may recommend a film made only using or at least primarily with the less expensive SP-Li.

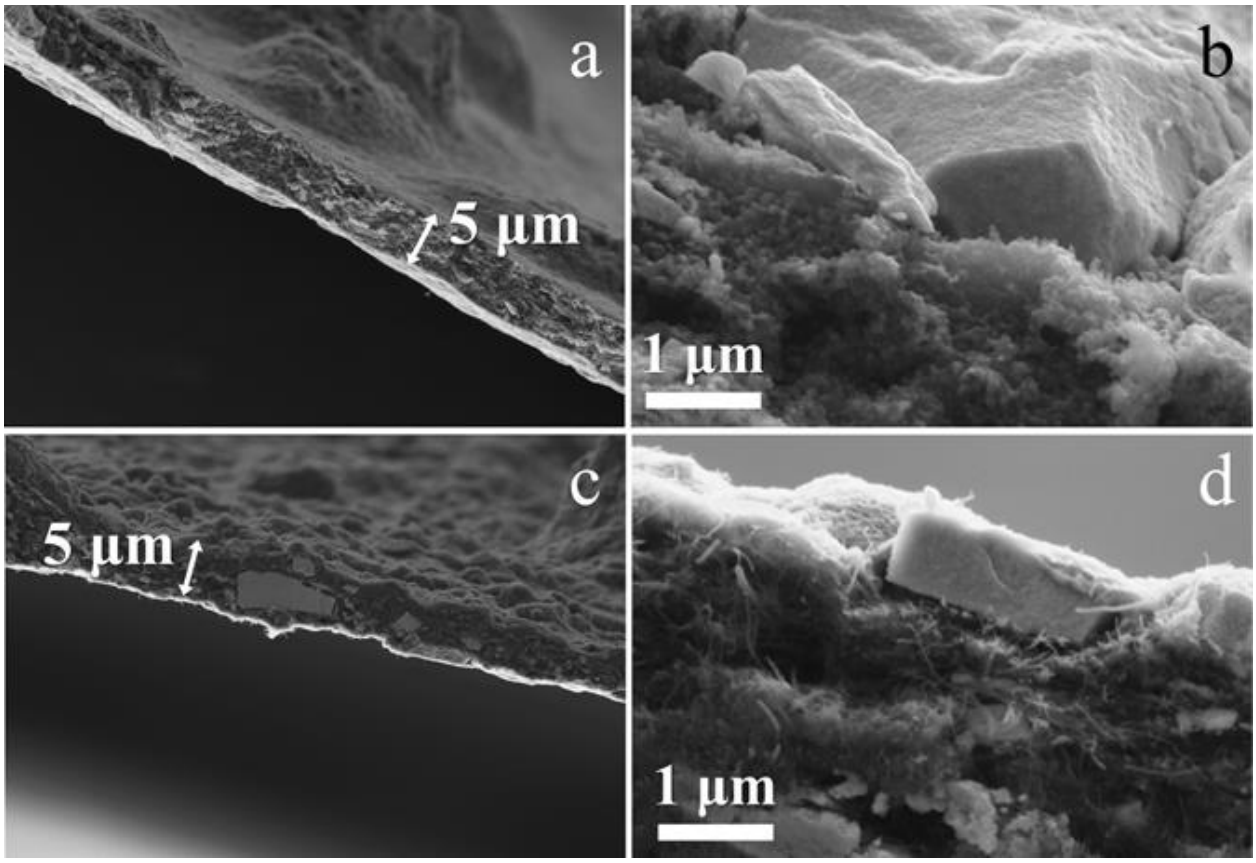

Figure 3.8. SEM images of the cross-sections of the SnO_2/SP-Li (a) – (b) and SnO_2/CNT (c) – (d) films at increasing magnification. The large bulges in the film are due to the microns-sized SnO_2 particles.

SEM images were recorded of the stacked electrode (cycling data in Figure 3.4) after it completed its 101st cycle. After cycling, the (then wetted) stacked films had compressed into one thick electrode which was found to be partially broken, fragile and damaged easily upon handling. When viewed with SEM, the majority of the film was obscured by SEI (S Figure 3.6a, ESI†) but under SEM magnification the originally layered, individual films which comprised the stacked anode could still be distinguished in some regions (S Figure 3.6b, ESI†).

Conclusions

A simple and direct method is reported for making free-standing electrode films composed of commercially available materials: microns-sized SnO_2 particles, CMC 90-kDa and Super-P Li conductive additive. An aqueous slurry of these materials can be cast onto a copper or other (Mylar, recommended) substrate and upon air-drying the film delaminates into large free-standing regions. The resulting SnO_2/SP-Li film is thin (~0.5mg cm^{-2} loading of active material for a film of ~5 □m thickness) with high energy density owing to the selection of high tap density (2.5 g cm^{-3}) active material. Before assembling into a coin cell, the film was found to be easy to handle and could be easily flexed as well as folded/unfolded. The mechanical properties of strength and strain at break of the uncycled film were measured to be 13 MPa and 1.7 %. With a four point probe, the electrical resistivity of an uncycled SnO_2/SP-Li film was 0.6 Ω-cm and this marginally increased (~6 %) after first folding the film, then creasing by applying ~0.4 atm pressure and finally unfolding.

In a 2032 coin cell, single, free-standing SnO_2/SP-Li films tested as the negative electrode *vs* lithium foil showed good stability and capacity retention of 74 % of theoretical capacity when tested at a 1*C* rate. By stacking several SnO_2/SP-Li films, the areal capacity of the anode could be increased and stable cycling was observed through 100 cycles: 2.6 mAh cm^{-2} capacity recorded at 0.33 mA cm^{-2} current density (~*C*/12); 0.9 mAh cm^{-2} at 1.0 mA cm^{-2} (~*C*/4) and 1.8 mAh cm^{-2} at 0.67 mA cm^{-2} (~*C*/6). To indicate the potential viability of the film when tested in a flexed orientation, cycle testing was conducted in a homemade pouch cell with the electrode folded 180 degrees. At 1*C* rate, the electrode cycled stably for 20 cycles before slight capacity fade was observed.

For free-standing or flexible electrodes, 1D or 2D carbons such as carbon nanotubes (CNT) or graphene are typically used to provide a bendable scaffolding which is both mechanically strong and electrically conductive. Here, CNT were substituted for the SP-Li conductive particles and

similar free-standing films were made and compared. With CNT, the electrode strength at break as well as the electronic conductivity increased but, despite this, the cycling performance of the electrodes made with the low-cost SP-Li carbon exceeds that of the electrodes made with orders-of-magnitude more expensive 1D carbon.

This free-standing SnO_2/SP-Li electrode film is noted for its simplicity of fabrication; flexibility; use of inexpensive Super-P Li conductive particles rather than more expensive 1D or 2D conductive carbons; use of a commonly available binder (carboxymethyl cellulose–90kDa); and, instead of nano-scale active material, high tap density microns-sized SnO_2.

REFERENCES

1. J. A. Rogers, T. Someya and Y. Huang, Science, 2010, 327, 1603-1607.

2. H. Nishide and K. Oyaizu, Science, 2008, 319, 737-738.

3. T. Marks, S. Trussler, A. J. Smith, D. Xiong and J. R. Dahn, Journal of The Electrochemical Society, 2011, 158, A51-A57.

4. G. Zhou, F. Li and H.-M. Cheng, Energy & Environmental Science, 2014, 7, 1307-1338.

5. H. Gwon, J. Hong, H. Kim, D.-H. Seo, S. Jeon and K. Kang, Energy & Environmental Science, 2014, 7, 538-551.

6. Y. Hu and X. Sun, Journal of Materials Chemistry A, 2014, DOI: 10.1039/c4ta00716f.

7. S. Li, Y. Luo, W. Lv, W. Yu, S. Wu, P. Hou, Q. Yang, Q. Meng, C. Liu and H.-M. Cheng, Advanced Energy Materials, 2011, 1, 486-490.

8. L.-F. Cui, L. Hu, J. W. Choi and Y. Cui, ACS Nano, 2010, 4, 3671-3678.

9. K. Evanoff, J. Benson, M. Schauer, I. Kovalenko, D. Lashmore, W. J. Ready and G. Yushin, ACS Nano, 2012, 6, 9837-9845.

10. H. Gwon, H.-S. Kim, K. U. Lee, D.-H. Seo, Y. C. Park, Y.-S. Lee, B. T. Ahn and K. Kang, Energy & Environmental Science, 2011, 4, 1277-1283.

11. S.-L. Chou, Y. Zhao, J.-Z. Wang, Z.-X. Chen, H.-K. Liu and S.-X. Dou, The Journal of Physical Chemistry C, 2010, 114, 15862-15867.

12. B. Liu, J. Zhang, X. Wang, G. Chen, D. Chen, C. Zhou and G. Shen, Nano Letters, 2012, 12, 3005-3011.

13. L. Noerochim, J.-Z. Wang, S.-L. Chou, D. Wexler and H.-K. Liu, Carbon, 2012, 50, 1289-1297.

14. M. Koo, K.-I. Park, S. H. Lee, M. Suh, D. Y. Jeon, J. W. Choi, K. Kang and K. J. Lee, Nano Letters, 2012, 12, 4810-4816.

15. L. Hu, H. Wu, F. La Mantia, Y. Yang and Y. Cui, ACS Nano, 2010, 4, 5843-5848.

16. X. Li, J. Yang, Y. Hu, J. Wang, Y. Li, M. Cai, R. Li and X. Sun, Journal of Materials Chemistry, 2012, 22, 18847-18853.

17. Q. Cheng, Z. Song, T. Ma, B. B. Smith, R. Tang, H. Yu, H. Jiang and C. K. Chan, Nano Letters, 2013, 13, 4969-4974.

18. H. Luo, Z. Shi, N. Li, Z. Gu and Q. Zhuang, Analytical Chemistry, 2001, 73, 915-920.

19. S. Y. Chew, S. H. Ng, J. Wang, P. Novák, F. Krumeich, S. L. Chou, J. Chen and H. K. Liu, Carbon, 2009, 47, 2976-2983.

20. A. K. Kercher, J. O. Kiggans and N. J. Dudney, Journal of The Electrochemical Society, 2010, 157, A1323-A1327.

21. C. Wang, D. Li, C. O. Too and G. G. Wallace, Chemistry of Materials, 2009, 21, 2604-2606.

22. L. Noerochim, J.-Z. Wang, D. Wexler, Z. Chao and H.-K. Liu, Journal of Power Sources, 2013, 228, 198-205.

23. N. Li, Z. Chen, W. Ren, F. Li and H.-M. Cheng, Proceedings of the National Academy of Sciences, 2012, 109, 17360-17365.

24. J. Chen, Y. Liu, A. I. Minett, C. Lynam, J. Wang and G. G. Wallace, Chemistry of Materials, 2007, 19, 3595-3597.

25. V. L. Pushparaj, M. M. Shaijumon, A. Kumar, S. Murugesan, L. Ci, R. Vajtai, R. J. Linhardt, O. Nalamasu and P. M. Ajayan, Proceedings of the National Academy of Sciences, 2007, 104, 13574-13577.

26. Y. Liu, K. Huang, Y. Fan, Q. Zhang, F. Sun, T. Gao, L. Yang and J. Zhong, Electrochimica Acta, 2013, 88, 766-771.

27. L. Yue, H. Zhong and L. Zhang, Electrochimica Acta, 2012, 76, 326-332.

28. J. K. Lee, K. B. Smith, C. M. Hayner and H. H. Kung, Chemical Communications, 2010, 46, 2025-2027.

29. X. Wang, X. Cao, L. Bourgeois, H. Guan, S. Chen, Y. Zhong, D.-M. Tang, H. Li, T. Zhai, L. Li, Y. Bando and D. Golberg, Advanced Functional Materials, 2012, 22, 2682-2690.

30. J. Liang, Y. Zhao, L. Guo and L. Li, ACS Appl. Mater. Interfaces, 2012, 4, 5742-5748.

31. X. Yang, K. Fan, Y. Zhu, J. Shen, X. Jiang, P. Zhao, S. Luan and C. Li, ACS Appl. Mater. Interfaces, 2013, 5, 997-1002.

32. P. Zhang, J. Qiu, Z. Zheng, G. Liu, M. Ling, W. Martens, H. Wang, H. Zhao and S. Zhang, Electrochimica Acta, 2013, 104, 41-47.

33. A. M. Chockla, J. T. Harris, V. A. Akhavan, T. D. Bogart, V. C. Holmberg, C. Steinhagen, C. B. Mullins, K. J. Stevenson and B. A. Korgel, Journal of the American Chemical Society, 2011, 133, 20914-20921.

34. Y. Qian, A. Vu, W. Smyrl and A. Stein, Journal of The Electrochemical Society, 2012, 159, A1135-A1140.

35. B. Wang, X. Li, B. Luo, Y. Jia and L. Zhi, Nanoscale, 2013, 5, 1470-1474.

36. L. Jabbour, C. Gerbaldi, D. Chaussy, E. Zeno, S. Bodoardo and D. Beneventi, J. Mater. Chem., 2010, 20, 7344-7347.

37. S. Leijonmarck, A. Cornell, G. Lindbergh and L. Waagberg, Nano Energy, DOI: 10.1016/j.nanoen.2013.02.002, Ahead of Print.

38. L. Jabbour, M. Destro, D. Chaussy, C. Gerbaldi, N. Penazzi, S. Bodoardo and D. Beneventi, Cellulose (Dordrecht, Neth.), 2013, 20, 571-582.

39. L. Jabbour, M. Destro, C. Gerbaldi, D. Chaussy, N. Penazzi and D. Beneventi, J. Mater. Chem., 2012, 22, 3227-3233.

40. , 2014.

41. N. Li, C. R. Martin and B. Scrosati, Electrochemical and Solid-State Letters, 2000, 3, 316-318.

42. C. Kim, M. Noh, M. Choi, J. Cho and B. Park, Chemistry of Materials, 2005, 17, 3297-3301.

43. L. Hu, J. W. Choi, Y. Yang, S. Jeong, F. La Mantia, L.-F. Cui and Y. Cui, Proceedings of the National Academy of Sciences, 2009, 106, 21490-21494.

44. B. A. Johnson and R. E. White, Journal of Power Sources, 1998, 70, 48-54.

45. D. Applestone and A. Manthiram, RSC Advances, 2012, 2, 5411-5417.

46. http://www.foodsaver.com/vacuum-sealers/FSFSSL2244-P00.html#start=10.

47. C. A. Schneider, W. S. Rasband and K. W. Eliceiri, Nat. Methods, 2012, 9, 671-675.

48. K. C. Klavetter, S. M. Wood, Y.-M. Lin, J. L. Snider, N. C. Davy, A. M. Chockla, D. K. Romanovicz, B. A. Korgel, J.-W. Lee, A. Heller and C. B. Mullins, Journal of Power Sources, 2013, 238, 123-136.

49. I. A. Courtney, W. R. McKinnon and J. R. Dahn, Journal of The Electrochemical Society, 1999, 146, 59-68.

50. M. Mohamedi, S.-J. Lee, D. Takahashi, M. Nishizawa, T. Itoh and I. Uchida, Electrochimica Acta, 2001, 46, 1161-1168.

51. I. A. Courtney and J. R. Dahn, Journal of The Electrochemical Society, 1997, 144, 2943-2948.

52. I. A. Courtney and J. R. Dahn, Journal of The Electrochemical Society, 1997, 144, 2045-2052.

53. M. Roberts, P. Johns, J. Owen, D. Brandell, K. Edstrom, G. El Enany, C. Guery, D. Golodnitsky, M. Lacey, C. Lecoeur, H. Mazor, E. Peled, E. Perre, M. M. Shaijumon, P. Simon and P.-L. Taberna, Journal of Materials Chemistry, 2011, 21, 9876-9890.

54. T. S. Arthur, D. J. Bates, N. Cirigliano, D. C. Johnson, P. Malati, J. M. Mosby, E. Perre, M. T. Rawls, A. L. Prieto and B. Dunn, MRS Bulletin, 2011, 36, 523-531.

55. L. Hu, F. La Mantia, H. Wu, X. Xie, J. McDonough, M. Pasta and Y. Cui, Advanced Energy Materials, 2011, 1, 1012-1017.

56. T. G. Carbon, TIMREX Graphite, ENSACO, SUPER P Li Carbon Black: Carbon powders for Lithium battery systems, http://www.timcal.com/scopi/group/timcal/timcal.nsf/pagesref/MCOA-7S6K2K/$File/Brochure_Carbon_Powders_for_Lithium_Battery_Systems.pdf.

SUPPLEMENTARY INFORMATION

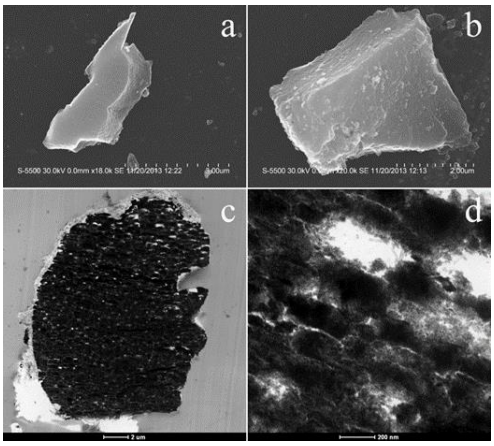

S Figure 3.1. SEM of SnO_2 particles (a) and (b). Cross-section TEM of particles in pristine film showing that the micron sized particle is the result of the sintering of nanoscale particles (c) and (d).

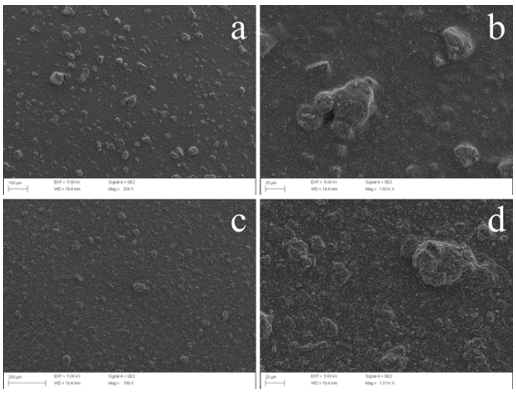

S Figure 3.2. SEM images at two levels of magnification showing uncycled electrodes in top down orientation featuring the surface of flexible electrode made using SP-Li conductive additive (a) – (b) and (c) – (d) with CNT. The large bulges in the film are the SnO_2 particles.

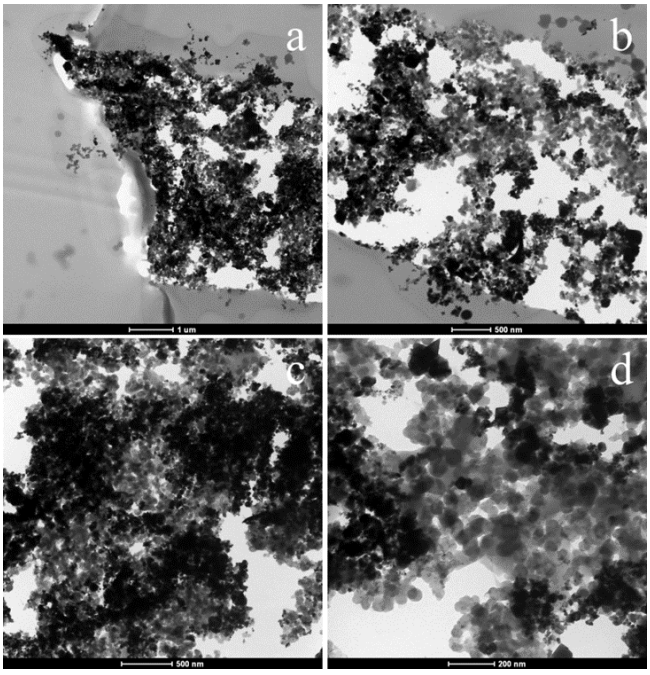

S Figure 3.3. TEM image of cross-section created by embedding electrode in resin and using an ultramicrotome to cut thin sections. This flexible electrode was created using low tap density, nanosized SnO_2 particles (*Sigma*, <100 nm). (a) – (d) Electrode shown at increasing magnification.

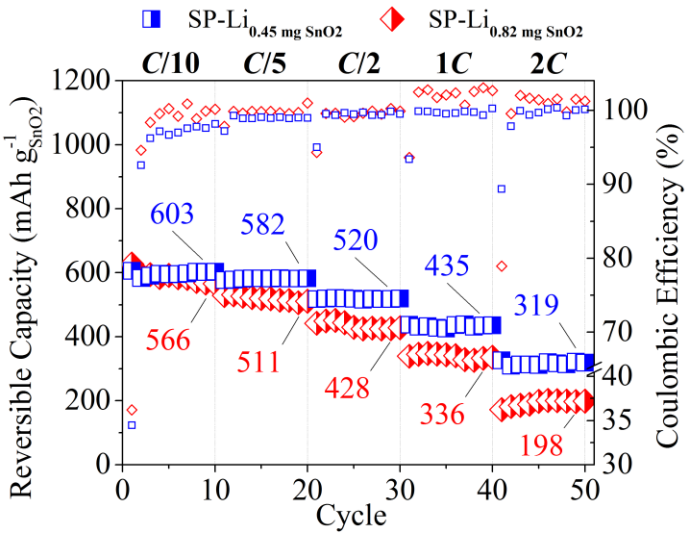

S Figure 3.4. C-rate test for electrode made with high tap density SnO_2 and SP-Li showing the effect of mass loading. The increase in mass loading results in higher resistance and lower capacities at faster rates.

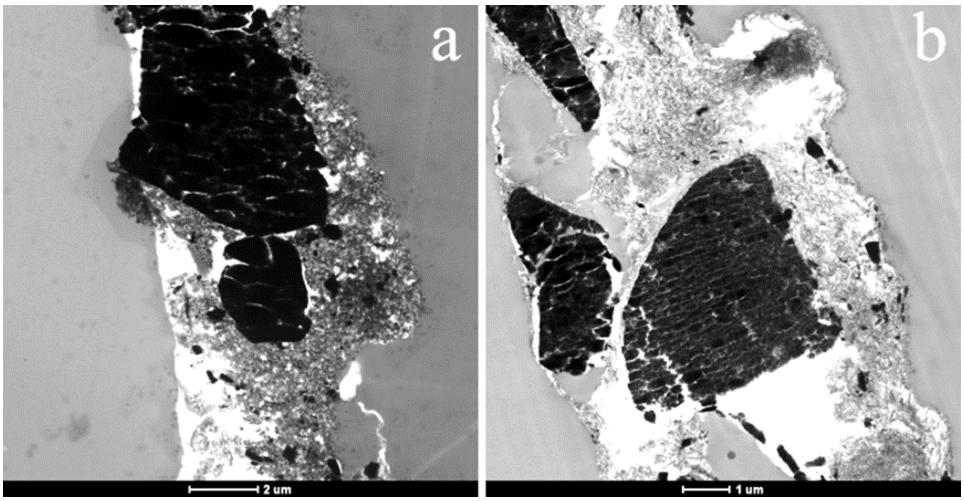

S Figure 3.5. TEM, cross-sections of uncycled electrode films made with high tap density SnO_2 and (a) SP-Li or (b) CNT conductive additive.

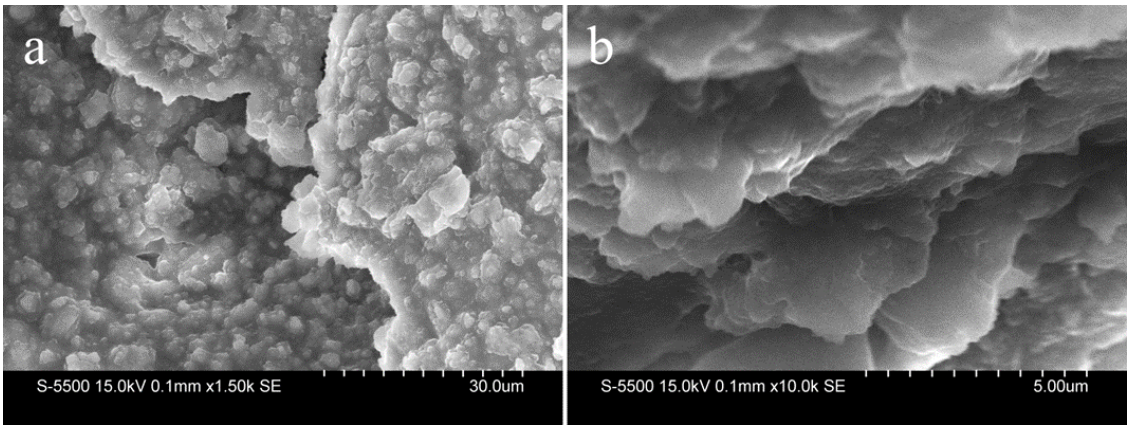

S Figure 3.6. SEM images of cycled stacked anode (made with nine stacked SP-Li films) in the discharged state after 101 cycles at variable rates (see Figure 3.4). The SEI coats the film surface. In (a) three films are visible at different heights and (b) is zoomed in on the edge of one of the films.

Citations

1. Kim, C.; Noh, M.; Choi, M.; Cho, J.; Park, B., Critical Size of a Nano SnO_2 Electrode for Li-Secondary Battery. *Chemistry of Materials* 2005, *17* (12), 3297-3301. http://dx.doi.org/10.1021/cm048003o

Chapter 4: Li- and Na-reduction products of *meso*-Co_3O_4 form high-rate, stably cycling battery anode materials[3]

INTRODUCTION

To charge to higher capacities at faster rates in lithium ion batteries, energy storage by a means other than intercalation into graphite is required. Graphite, the commonly used anode active material with a low practical capacity of near 360 mAh g^{-1}, charges at low potentials vs Li/Li^+ and so requires a relatively slow constant current, constant voltage charge method in order to avoid the hazard of electroplating of lithium and dendrite formation.

Potential rapidly charged anode materials being considered for rechargeable batteries include Li-reduced transition metal oxides that result in the formation of mixtures of transition metal, transition metal oxide and Li_2O. These anode materials charge to higher capacities at higher potentials *vs* the Li/Li^+ redox couple, resulting in a more safe charge at faster rates but with necessarily lower energy as a consequence of full discharge usually being achieved only by extending the discharge up to 3.0 V. Examples of such transition metal oxide anode materials include nanoparticles of Ni formed by Li-reduction of NiO[1], of Fe and FeO formed by Li-reduction of Fe_2O_3[2] and of Co and CoO by Li-reduction formed of Co_3O_4. Because of its theoretical capacity of 890 mAh g^{-1} (although with a relatively high discharge potential of near 2 V vs Li/Li^+), cobalt oxide has been pursued as an anode material and tested in a variety of morphologies – nanowire[3,4], nanorod[5,6], nanocage[7,8,9], leaf-like[10], *meso*-porous[11,12,13], platelet[14], hollow sphere[15], carbon-composite[16,17,18],

[3] The content in this chapter has been copied (with minor edits) from its original publication in the *Journal of Materials Chemistry A* in 2014.

micro/nano composite[19] – and high capacity retention at high rates has been obtained [10,12,13,15,16]. For this material in any of these forms tested, the onset of capacity fade at higher rates or during the course of cycling is commonly attributed to particle agglomeration leading to cobalt segregation into electrically isolated nanoscale domains, electrode crack formation and delamination from the current collector and/or SEI growth leading to increasing overpotentials.

From consideration of Co_3O_4 in nanowire and *meso*-porous morphologies, Bruce and coworkers[20] suggested that higher and more stable capacities for a cobalt oxide-based anode could be realized if a *meso*-porous particle could be found which retained its structure upon Li-reduction, avoiding Co aggregation and providing for reversible, fast Li-ion transport through the pores. In their study, the originally *meso*-porous Co_3O_4 was reduced to *meso*-porous CoO in the first cycle, but after 50 cycles the *meso*-porous structure was lost and significant capacity fade was observed. Recently, Xiao *et al.*[13] studied a low surface area (27 $m^2\ g^{-1}$) *meso*-porous Co_3O_4 reporting good rate capability and a very high 1600 mAh g^{-1} capacity which was retained after 100 cycles (at 100 mA g^{-1}). Also recently, Li *et al.*[11] reported full capacity retention (600 mAh g^{-1}) through 500 cycles at a rate of 500 mA g^{-1} with a *meso*-porous Co_3O_4 based anode, although their composite electrode required nearly an equal mass of graphene, a high content of a material with a cost 3-4 orders of magnitude higher than the commercially used carbon black conductive additive.

Here we report stable, high rate capacity cycling results of high surface area (367 $m^2\ g^{-1}$) *meso*-porous Co_3O_4 for Li and for Na ion half cells. The cycling performance is primarily attributed to the individual particles retaining their *meso*-porous structure upon repeated charging/discharging, as established by high-resolution transmission electron

micrography (TEM). With powder X-ray diffraction and selected area electron diffraction (SAED), we show that the cycled *meso*-porous particle lacks long range order but reverts upon discharge at highly oxidizing potentials to an inhomogeneous mixture of CoO and Co_3O_4.

Upon discovering the stable morphology of the active material particle in the electrodes, we attempted to improve the performance of the electrode by testing of alternative electrolyte formulations, as has been done for other lithium-ion battery anode materials.[21,22,23] Here, fluoroethylene carbonate (FEC) and chloroethylene carbonate (Cl-EC) as electrolyte co-solvents or additives allowed for higher capacity retention at high charge/discharge rates, increased coulombic efficiencies (CE), further improved cycling stability and decreased risk of internal shorting from dendrite formation. FEC was added because numerous reports have shown that it improves the calendar life and cycling performance of both Li- and Na-ion anodes, while Cl-EC was added because of its reported beneficial effect on improving coulombic efficiency[24], a metric for which some otherwise high-performing cobalt oxide-based anodes have performed poorly[10,15]. Employing FEC or Cl-EC, we survey alternative formulations to the conventional ethylene carbonate (EC) based electrolyte for cobalt oxide based electrodes. The advantages of the halogen-containing electrolytes over the conventional EC-based electrolyte include: (1) inhibited or eliminated cycling irregularities typical of long-term behaviour of electrodes tested with EC:DEC and (2) the lesser resistance to ion transport of the solid electrolyte interphases (SEIs) they form, as seen in the AC impedance spectra and X-ray photoelectron spectra (XPS) characterization of the SEIs.

EXPERIMENTAL

Materials. Synthesis of the *meso*-porous Co_3O_4 and the quality control evaluation done to verify its morphology, surface area and phase was performed as described elsewhere by Dahal *et al*.[25]

Electrochemical testing. An aqueous slurry of *meso*-porous Co_3O_4 (60 wt %), 90 kDa carboxymethyl cellulose (Sigma, 20 wt %) binder, and Super P Li conductive carbon (Timcal, 20 wt %) was slurry cast onto copper foil (MTI, 10 μm) and dried in a vacuum oven at 120 °C for at least 6 h. This film formed the working electrodes of CR 2032 coin-type cells and each electrode had a Co_3O_4 mass loading of 0.6-0.8 mg cm^{-2}. Scanning electron micrographs (SEM) of a typical electrode (uncycled), showing cross-section and distribution of active material and Super-P Li conductive additive are shown in Fig. S5..4.1a-b, ESI†.

The half cells were assembled in an argon-filled glovebox (O_2 less than 0.1 ppm, H_2O < 3.6 ppm) with Li foil (Alfa) or Na foil (Sigma) as the counter and reference electrode and Celgard 2400 polypropylene membrane as the separator. Additional testing performed on electrodes of composition 80:10:10 weight ratio had mass loadings of 0.9-1.0 mg cm^{-2} of active material. The electrolyte materials, ethylene carbonate (EC, Sigma), anhydrous diethyl carbonate (DEC, Sigma), chloroethylene carbonate (Cl-EC, TCI), fluoroethylene carbonate (FEC, Solvay Fluor) and $LiPF_6$ (BASF) were used as received. Electrolytes were preserved against moisture contamination by the addition of molecular sieves to the storage vials.

Electrochemical measurements were performed on an Arbin BT 2043 or BT 2143 multichannel battery testing system. Charge (ion-insertion into the anode) and discharge (ion-extraction) were performed between 0.01 and 3 V *vs* the Li/Li^+ or Na/Na^+ redox couple

with the theoretical capacity defined as 890 mAh g^{-1} (1*C* = 0.89 A/g). For each cell, a conditioning cycle at *C*/20 was done prior to testing.

AC impedance spectra were obtained from cells cycled at a conditioning *C*/20 rate followed by 10 cycles at a *C*/10 rate. On the tenth cycle at a *C*/10 rate, the cell was evaluated at two conditions: 1) after being charged at constant current (*C*/10) and held at constant voltage (100 mV, a voltage selected in order to avoid electroplating lithium) until the current dropped to below C/20 and 2) after being discharged to 3 V and then allowed to come to thermodynamic equilibrium after resting for greater than 12 h. The spectra were analysed in ZView (*Scribner Associates*)[26] and a best fit was made for the entire range of collected data (100k to 0.01 Hz, 5 mV perturbations).

Microscopy. Low-resolution transmission electron microscopy (LR-TEM) was performed for each of the electrode/electrolyte combinations using a FEI Tecnai Spirit BioTwin TEM operated at 80 kV to evaluate the condition of the *meso*-porous particle in its native electrode environment after preparation using an ultramicrotome sectioning procedure (as described elsewhere).[27] Select, additional imaging of these sectioned electrodes was done on a field emission JEOL 2010F TEM operated at 200 kV for higher resolution micrographs. Selected area electron diffraction (SAED) patterns were obtained from particles drop cast onto lacey carbon grids (*SPI*).

X-ray photoelectron spectroscopy (XPS). XPS measurements were conducted on electrodes that had been cycled to a fully discharged state, after ten cycles at a *C*/10 rate initiated by a *C*/20 conditioning cycle. This number of cycles was selected to allow for analysis of a fully formed SEI (the SEI primarily develops during the first 2-3 cycles as indicated by the CE) but to avoid micron-scale dendritic growths which were observed to

develop after many cycles. The cells were opened in the glovebox using plastic pliers (I-V Products) and the electrodes were placed into vials filled with DEC in order to wash off the residual $LiPF_6$ salt. The electrodes were transferred from the glovebox to the XPS analysis instrument (Kratos Axis Ultra) without exposure to air using a home-built delivery vessel (described elsewhere).[28]

The SEI surfaces were characterized utilizing a monochromatic Al *K*α X-ray source ($h\nu$ = 1486.5 eV) with and without the use of a charge neutralizer. The use of a charge neutralizer did not appreciably alter the shape and intensity of the spectra and the spectra collected without charge neutralization are therefore reported. The peak assignments of the XPS spectra collected for the Li-ion electrodes were calibrated to the C 1*s* sp^3 peak at 284.5 eV and checked by considering the resulting alignment of the F 1*s* LiF peak at 684.6 eV and P 2*p* P-O/P=O and P-F peaks at 134 eV and 136 eV, respectively.[29] The peak assignments for the Na-ion electrodes were similarly calibrated to the C 1*s* sp^3 peak at 284.5 eV and references for the Li-ion and Na-ion peak assignments are tabulated in S-Tables 4.1a-b, ESI†.

RESULTS AND DISCUSSION

The meso-porous particle

In this study we targeted a high surface area *meso*-porous mixed Co(II)-Co(III) oxide in an effort to improve the capacity retention of a cobalt oxide based lithium or sodium ion anode operated at high rates. As reported in the description of its synthesis,[25] this *meso*-porous structure exhibits a very high N_2 BET surface area of *ca.* 367 $m^2\ g^{-1}$. The material was prepared *via* a soft template synthesis using sacrificial surfactant templates to obtain SBA-15-like Co_3O_4; the material features *meso*-channels aligned parallel to the long axis

of the particle with regular, cylindrical-shaped pores with an average diameter measured to be 10.0 nm and wall thickness of 8.3 nm. This structure is suited to accommodate the volumetric change associated with charge and discharge as well as to enhance ion access to the active material by shortening diffusion lengths and by providing channels for more rapid liquid-phase ion transport into the bulk of the particle.

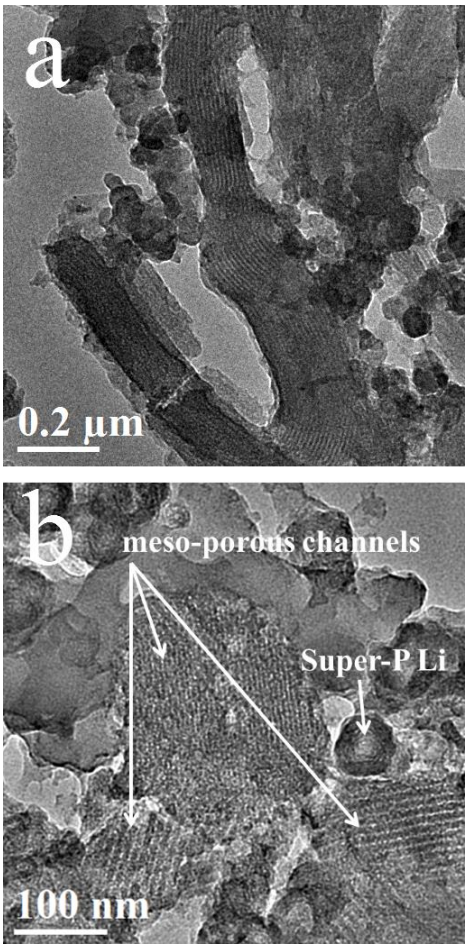

Fig. 4.1 TEM of ultramicrotomed cross-sections of electrodes in the discharged state after 250 cycles at 1*C* (a) showing the retention of the *meso*-porous channels in a few particles aligned parallel to the viewing plane and (b) indicating meso-porous particles and Super-P Li conductive additive particle.

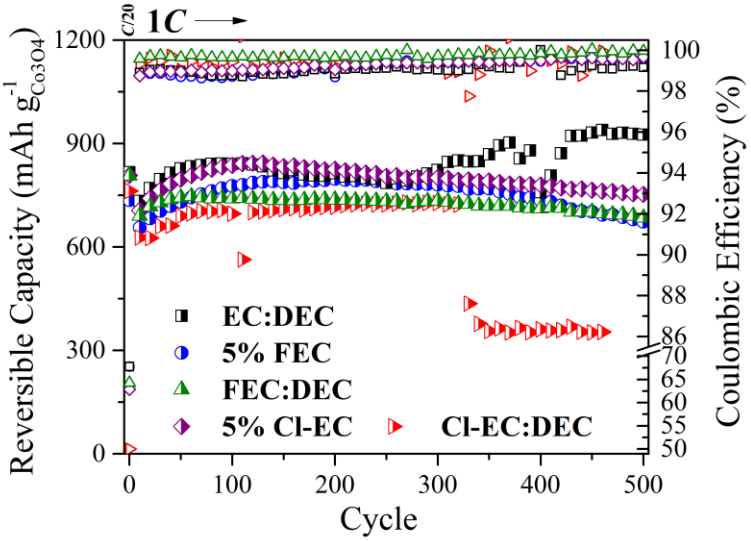

Fig. 4.2 Cycling test at 1*C* rate for 500 cycles following *C*/20 conditioning cycle in half cell of *meso*-porous Co_3O_4 based electrodes *vs* Li-foil with 1M $LiPF_6$ in EC:DEC, 5% FEC in EC:DEC, FEC:DEC, 5% Cl-EC in EC:DEC or Cl-EC:DEC electrolyte formulations.

The *meso*-porous particles studied here are promising for use in Li- or Na-ion batteries because their structure is preserved through many charge/discharge cycles despite the effects of energy storage via a conversion reaction. By means of XRD[30,31] and XPS[31] characterization, the conversion reaction has been shown to proceed by initially charging the mixed Co(II)-Co(III) oxide to $Li_xCo_3O_4$, then to CoO + Li_2O and finally to Co + Li_2O,[30] before discharging to give CoO.[20] However, the electrochemical charge after the CoO phase is reached occurs through amorphous phases (or through crystalline phases with only short-range order), limiting the extent to which these phase transitions can be currently described or, importantly, compared for cobalt oxide materials with varying morphologies. Currently, there exists no XRD data describing the subsequent discharge phase transitions except at a state of full discharge. This is significant, for after many cycles, the conventional explanation for capacity fade is that the Co formed during charging becomes segregated

into electrically isolated nanoclusters, as shown using TEM and SAED by Bruce's group in their study of *meso*-porous and nanowire-cluster cobalt oxide particles.[20] However, Kang *et al*.[31] found that through 100 cycles at a 1*C* rate, their Co_3O_4 based electrode cycled stably and that the particle discharged to a polycrystalline Co_3O_4 phase. By evaluating these contrasting reports, a possible indicator of the degree of cycling stability for a particular cobalt oxide morphology was considered be the condition of the morphology as well as the phase of the active material at full discharge.

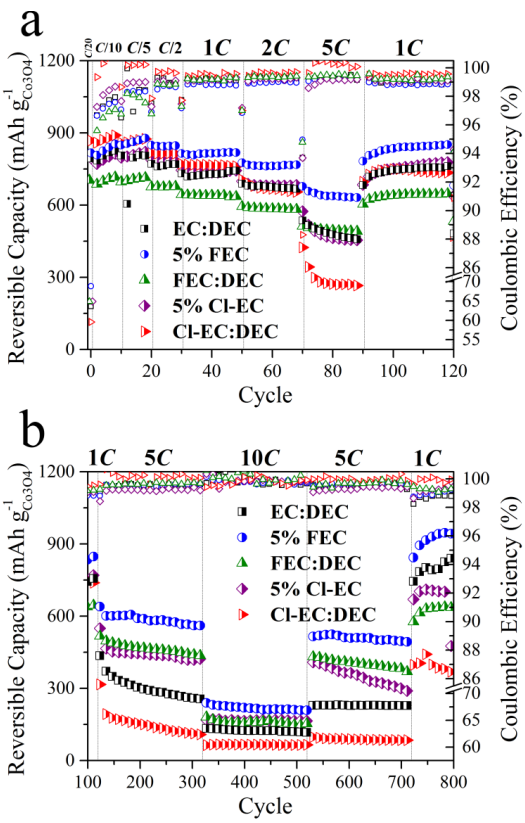

Fig. 4.3 Cycling test at *C*-rates from 0.1-10 through 800 cycles in half cell of *meso*-porous Co_3O_4 based electrodes *vs* Li-foil with 1M $LiPF_6$ in EC:DEC, 5% FEC in EC:DEC, FEC:DEC, 5% Cl-EC in EC:DEC or Cl-EC:DEC electrolyte formulations. Test results shown in (a) are continued in (b).

In our study we initially obtained TEM images of the ultramicrotomed cross-section of cycled electrodes (Fig 1, electrode tested in 5% FEC in EC:DEC electrolyte formulation) which surprisingly showed that the original meso-porous channels remained intact despite prolonged cycling (250 cycles testing at a 1*C* rate, Fig. S.4.2, ESI†). TEM of similarly cycled electrodes in the other electrolyte formulations are shown in Fig. S.4.3a-d, ESI†, and for each electrode/electrolyte combination tested, we find that the particles studied here retain their original *meso*-porous, channeled morphology.

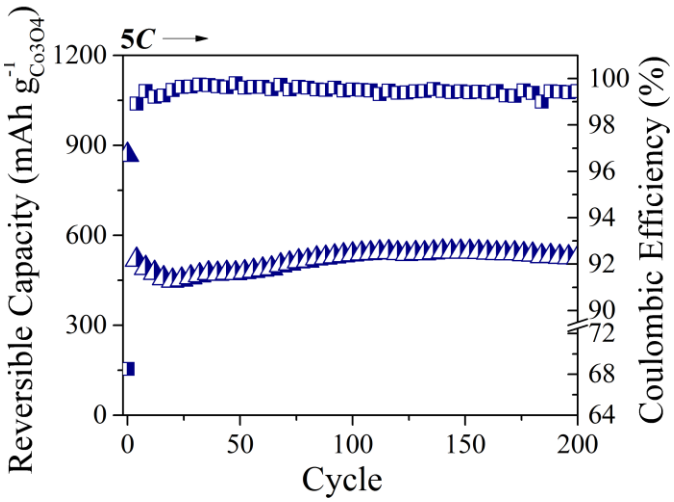

Fig. 4.4 Cycling test at 5*C* for 80% *meso*-porous Co_3O_4 (1.0 mg/cm^2 loading) / 10% Super-P Li / 10% CMC_{90kDa} electrode in 1M $LiPF_6$ in 5% FEC in EC:DEC electrolyte.

The preservation of the *meso*-porous morphology correlates with the reversible electrochemical cycling observed, and XRD was performed *ex-situ* to characterize the phase transitions responsible for stable cycling behavior. Surprisingly, at a full state of discharge after 10 cycles, no diffraction peaks were detected even with lengthy dwell times when performing characterization of the film upon the copper current collector or from a

powder sample removed from the tested film (done so as to avoid interfering signal from the copper substrate). When long-range order was found absent in the discharged *meso*-porous material (XRD pattern shown in Fig. S.4.4, ESI†), we endeavored to characterize the short-range structure by performing SAED. It was observed that upon discharge the *meso*-porous structure reverts to a generally amorphous material (Fig. S.4.5a-b, ESI) containing some CoO and Co_3O_4 nanocrystals. In Fig. S.4.5c-d, ESI, we find evidence for the existence of CoO which in this particular particle presents a nanocrystalline diffraction pattern with six-fold symmetry as observed due to its orientation along the <1 -1 1> zone axis.[32] However, after extensive searching, SAED showing the Co_3O_4 nanocrystalline phase was found to exist in other particles (Fig. S.4.5e-f, ESI†).

Upon finding that the discharged condition of the *meso*-porous particle could not be identified as a homogenous phase, we attempted to characterize the full extent of the phase transitions undergone throughout the charge/discharge process and for this constructed an *in-situ* coin cell similar to that reported by Rhodes et al.[33] The cell design described by Rhodes et al. was modified here in order to minimize x-ray attenuation through the copper-coated polyethylene terephthalate (PET, commercially known as Mylar) window. By considering the relative intensity of signal derived from comparable electrode films made using the *meso*-porous particles and using commercial nanopowder (*Sigma*, less than 50 nm), we found that the uncycled *meso*-porous particles were weakly crystalline. Accordingly, the x-ray permeable window was here constructed using a thinner PET disk (50 μm *vs* 125 μm) and the thermally evaporated copper coating was reduced from 600 nm to 200 nm thickness.

In-situ characterization of the *meso*-porous electrode was performed during its first cycle of charging *via* linear voltammetry at 0.05 mV/s. However, the negligible signal obtained during this characterization precluded identification of the phase transitions for the *meso*-porous particle based electrode. In contrast, from the *in-situ* spectra recorded from characterization of the more strongly crystalline nanopowder based electrode (Fig. S.4.6, ESI†), we observed a similar result to that of the findings of Larcher et al., showing that the cobalt oxide based electrode transitions through the CoO phase during initial charge and that subsequent electrochemical reactions proceed through amorphous phase transitions.

Li-ion cycling stability

The result of the retention of bulk *meso*-porous morphology of the active material is relatively stable cycling behavior with each five of the electrolyte formulations tested (Fig. 4.2). To minimize the coulombic inefficiencies leading to SEI build-up and comparatively poor capacity retention at high rates – common consequences[27,34,35] of pairing a conventional EC-based electrolyte with a non-graphite based anode – cycling tests were designed to probe the effect of pairing the *meso*-porous Co_3O_4-based electrode with electrolytes formulated with FEC or Cl-EC as additives or as co-solvent substitutes for EC.

In this study, the cycling tests performed on *meso*-porous Co_3O_4-based electrodes were designed to indicate the most advantageous electrolyte by comparative assessment of the metrics of stability, initial coulombic efficiency and coulombic efficiency over long lifetime – 500 cycles at 1*C* (Fig. 4.2) – and capacity retention at variable *C*-rates (Fig. 4.3a,b).

Although not commonly reported, the value of a prolonged stability test like that presented in Fig. 4.2 is that long-term stability trends which might not be easily recognized from short-term tests may be identified. While at least three electrodes were tested for each cycling test, we found that after the first hundred cycles of testing there were only certain combinations of electrode/electrolyte for which consistent performance was observed. For example, the electrodes tested in the FEC:DEC or 5% FEC in EC:DEC electrolyte formulations performed consistently, but deviations were observed in the performance of the electrodes tested in the other formulations. In the case of those electrodes tested in EC:DEC, these deviations may be ascribed the electroplating of lithium which is believed to unpredictably significantly impact cell cycling at some point after about the first couple hundred cycles. More on this point is discussed below.

In the case of the electrodes tested using Cl-EC as an additive, the onset of capacity fade is also variable. When using Cl-EC as a co-solvent, we observed that the cycling deviations arise in unpredictable cell failure, in which the capacity suddenly drops over the span of a several cycles, a symptom possibly due to a sudden rise in resistance to ion transport through what was found by AC impedance spectroscopy to be a high-impedance SEI. When only the first hundred cycles of testing were considered, these inconsistencies are obscured, preventing such analysis despite providing a more repeatable (albeit truncated) dataset.

We believe that data collected in a long-term cycling test, while containing deviations (some of which we do not understand) is important to report, particularly because the existence of inconsistencies in the testing of certain formulations of electrolyte

is powerful evidence indicating their ineffectiveness. Further, as will be discussed for the electrodes tested in EC:DEC, these inconsistencies can sometimes be attributed to electroplating of lithium, a serious safety hazard and one which does not necessarily present except during prolonged testing.

To illustrate the difference in perspective which would result from consideration of a shortened, 100-cycle test *vs* the 500-cycle dataset reported here, we observe that in the 1*C* test runs shown in Fig. 4.2, the maximum 1*C* capacity is found at near the 100th cycle for each of the 5 electrode/electrolyte combinations tested except for that with the FEC:DEC electrolyte. Upon extended testing at 1*C* through 500 cycles, the effects of the alternative electrolyte formulations are clearly observed. Through 325 cycles, the most stable cycling electrode was tested with the Cl-EC:DEC electrolyte: before its capacity unexpectedly fell to *c*. 350 mAh g^{-1} through a transition of several cycles, the capacity retention at 325 cycles was 98% of its maximum 1*C* capacity (and 94% of the *C*/20 conditioning cycle capacity). When tested at lower mass loadings (near 0.4 mg cm^{-2}), this electrode was found to perform stably through 500 cycles (Fig. S.4.7, ESI†), this attributable to the lower resistance through a thinner electrode. The FEC:DEC formulation best promoted stable cycling with capacity retention of 92% of its maximum 1*C* capacity (and 85% of the *C*/20 conditioning cycle capacity) with the highest average CE of 99.6%. These higher long-term efficiencies coincided with marginally lower initial, first cycle CE (for the conditioning cycle run at C/20) for which the EC:DEC and 5% FEC formulations led to the lowest irreversible losses (CE near 68%). The FEC:DEC and 5% Cl-EC formulations had first cycle CE's of about 65% and the highest irreversible losses were found when using the Cl-EC:DEC formulation: a first cycle CE of as low as 50%.

When Cl-EC was used as an additive, the cycling performance was comparatively improved, with reasonable capacity retention although lower CE (performance statistics provided in Table S4.2 ESI†). However, it was observed that the capacity fade onset for the electrode tested with this Cl-EC used as an additive could vary significantly, commencing after as soon as *c.* 150 cycles or delayed until after *c*. 300 cycles.

When testing with EC:DEC, it was found that the long-term electrode performance would eventually result in erratic performance (sometimes as early as after several cycles, but typically after a few hundred cycles), which we attribute to the electroplating of lithium (we believe as a consequence of buildup of the EC-derived SEI which impedes ion transport into the electrode active material) that is followed by abrupt rises in cell resistance (selected snap-shots of the voltage profiles for this are shown in Fig. S.4.8a ESI† along with other cycling tests showing erratic cycling behavior in Fig. S.4.8b-c ESI†).[36]

By analysis of the differential capacity profiles of the electrode tested in EC:DEC through this 500 cycle test, it can be shown that the stable cycling observed prior to the *ca*. 270th cycle correlates with a consistently repeated voltage profile during charge (Fig. S.4.9a-b ESI†). After the *ca*. 270th cycle, the capacity increases and this unusual behavior is accompanied by unstable capacities and coulombic efficiencies, recorded most obviously between cycles 300-450. By studying the voltage profiles (Fig. S.4.9c-d ESI†), this added capacity is found to derive from charge accomplished at very low voltages, plausibly the result of localized lithium plating on the surface of the anode. This finding is consistent with the increasingly noisy differential capacity profiles in the low voltage domains after the *ca*. 270th cycle: rather than a consistently decreasing cell potential difference which is typical of even charging, the cell after the *ca*. 270th cycle appears to charge unsteadily,

accomplishing a unit of charge with small, then large, then small changes in voltage. This behavior could be associated with localized lithium electroplating and dendrite growths arising from an increased tendency for ion accumulation on rather than transport through the higher impedance EC-derived SEI (further discussed in the section on AC impedance). For example, the drop observed in the voltage profile in the 400th cycle (Fig. S.4.9c-d ESI†) is indicative of how wide-spread electroplating of lithium could lead to a cell in which the voltage abnormally quickly drops to a near-zero potential difference *vs* the lithium foil counter electrode.

Li-ion cycling at variable C-rates

Because the discharge voltage curve of cobalt oxide-based anodes results in (a) a high average discharge potential near 2 V and (b) voltage discharge over a continuum of potentials rather than at one or two voltage plateaus, we believe that the most likely application of a developed anode technology made from this material would likely not be for electric vehicles but for low-voltage portable electronics similar to the target market of Sony's *Nexelion* battery.[37]

The *Nexelion* anode uses a Sn/Co alloy particle which, like cobalt oxide anode materials, delivers its discharge continuously throughout a range of nearly 2 V rather than on one or multiple narrowly defined voltage plateaus like graphite, silicon or tin based anodes.[37] The higher capacity and longer cycle lifetime of the *Nexelion* anode as well as its performance at variable high *C*-rates are important advantages: besides addressing the need to provide greater capacity than the graphite type anode, alternative anode materials such as the Nexelion anode (that discharge through a range of potentials) might be attractive

alternatives to graphite for use in low voltage electronics if these are able to charge at rapid rates.

In Fig. 4.3a-b, the capacity retention of the *meso*-porous Co_3O_4 electrode is shown at variable high rates up to 10*C*. The best performance was observed when using the 5% FEC in EC:DEC electrolyte: the electrode retained 100% of its conditioning cycle capacity after completing a 20 cycle series at 1*C* and 77% capacity retention after a series of 20 cycles at 5*C*. Eventually, after several cycles at 1*C* followed by a longer test of an additional 200 cycles at 5*C*, this capacity faded to 68% retention. After testing through 200 cycles at 10*C* rate and a third series of 200 cycles at 5*C*, the electrode performance stabilized with 60% retention. Then, upon returning to a 1*C* rate, the capacity recovered, recovering to a slightly higher (115% retention) capacity compared to the conditioning cycle capacity after a 100 cycle series (800 cycles total testing).

The results for using alternative electrolyte formulations for cobalt oxide-based anodes (statistics in Table S4.2a,b ESI†) can be evaluated in part by comparison to the results for the electrode cycled in the conventional EC:DEC which retained only 57% of its capacity after the first series (20 cycles) of testing at 5*C*. Typically, *C*-rate testing is conducted with intervals of 10 cycles at variable, progressively higher rates, concluding before 100 cycles of total testing. Here, the differences in electrode performance when tested with alternative electrolyte formulations become most notable only after the first hundred cycles. In the EC:DEC formulation, the electrode capacity exhibits significant fade when tested at a 5*C* rate for 200 cycles, from cycle numbers 120-319: at the end of this prolonged testing, the capacity retention is only 32% (vs the 68% retention for the electrode tested in the formulation employing FEC as additive). This retention may be attributed to

the effect of the electrolyte, because we observed that after the testing reverted to a 1*C* rate after 720 cycles, the initial capacity was retained (106% retention), indicating that (a) that the electrode remained laminated to the current collector and (b) that the initial population of active material was still accessible for charge/discharge.

The comparative improvements made when using FEC:DEC, which retained 70% of its capacity after the 20 cycle 5*C* series and still 62% after the subsequent, extended 200 cycle series, were impressive gains compared to the results obtained when using EC:DEC. However, the actual capacity retention in FEC:DEC at high rates was consistently low when compared to the results when using FEC as an additive (*e.g.*, after the first 20 cycle initial 5*C* series, the capacity for the electrode in 5% FEC in EC:DEC was 631 mAh g^{-1} vs 490 mAh g^{-1} with FEC:DEC). The cycling results in terms of capacity retention and stability when using Cl-EC as an additive or co-solvent were comparatively poor, suggesting that this formulation results in a high-impedance ion transport barrier which restricts application to moderate rates of near 1*C* or lower for this electrode. When using Cl-EC as co-solvent, we believe that this high-impedance SEI is responsible for the unpredictable cell failures during long-term testing: after the impedance to ion transport increases beyond a certain limit, regions of the electrode may become inaccessible for future charging/discharging as the ions accumulate on or within the interphase rather than permeating through.

After these tests, the 5% FEC in EC:DEC electrolyte was selected for evaluation in a long-term, variable high *C*-rate test with an electrode made with higher active material composition (80% Co_3O_4 / 10% Super-P Li / 10% CMC) on an electrode of higher mass loading (1 mg cm^{-2}) in an effort to better assess the viability of the particle for use in a future anode. Similar to what was observed when using the lower content active material

electrode (60% weight Co_3O_4), the high rate performance at 5*C* was relatively stable: after 200 cycles at 5*C*, the capacity retention was 525 mAh g^{-1}, 95% of the maximum 5*C* capacity and 59% of the theoretical 890 mAh/g (Fig. 4.4).

Through an additional 300 cycles at 5*C* (Fig. S.4.10a ESI†), the capacity declined to 334 mAh g^{-1}, 60% of its 5*C* maximum value. After cycling stably with low capacity (~130 mAh/g) at 10*C*, the electrode tested at 5*C* for an additional 500 cycles and its capacity declined slightly to 273 mAh g^{-1}, 50% of its 5*C* maximum. Then, upon returning to 1*C* rate, the electrode capacity recovered, cycling stably for 100 cycles to 962 mAh g^{-1}, 111% of its conditioning cycle capacity.

From this result, we attribute the gradual decline in capacity experienced during the 1,000 cycles of 5*C* testing to a rate limiting step during the ion transport. Despite this electrode being composed of 50% less conductive additive and binder, these cycling results – particularly the recovery of capacity after reverting to 1*C* rate after 1500 cycles – indicate the electrode performance did not suffer due to issues pertaining to electrode electrical conductivity or film delamination. Because of evidence indicating that these particles retained their morphology and because of the stable capacities observed during the first couple hundred cycles of this test, we believe that persistent irreversible reactions leading to an increasing thickness of SEI is responsible for the capacity decline observed. Indeed, the primary deficiency of the 5% FEC in EC:DEC formulation when compared to the next best alternative, FEC:DEC, is that the CE are lower, by an average of 0.5% during the 500 cycles of 1*C* testing.

In an effort to avoid increasing SEI growth and irreversible losses of Li ions, we experimented with a lower voltage cut-off potential, originally set at 10 mV. In the literature reporting on cobalt oxide-based anodes, the lower voltage cut-off potential is set at 5 or 10 mV in order to maximize charge capacity, particularly at high rates when kinetic limitations manifest. However, this choice of lower voltage cut-off does not reconcile with the selection of cobalt oxide as a safer alternative to graphite for an anode active material: besides its higher capacity, cobalt oxide, like other transition metal oxide materials, is a possible candidate for replacing the graphite electrode because it may allow for safer charging, without the hazard of electroplating and dendrite growth. The primary charging reactions (the reader is referred to detailed discussion of differential capacity profiles in ESI†) occur near 1.5 and 1.0 V (at 1*C* rate), which is far above the Li/Li^+ redox potential. In theory, a higher potential for the lower voltage cut-off when cycling cobalt oxide based anodes would allow for both complete charging of the active material (although perhaps not of the polymeric gel-like layer) and elimination of the hazard of electroplating and dendritic growths which contribute to irreversible losses and increasing SEI growth. This hypothesis was examined after the 1,500 variable high *C*-rate test when the cell returned to 1*C* rate testing. In (Fig. S.4.10b ESI†) we observe that the average CE for this electrode cycled to 10 mV (cycles 1501-1600) at 1*C* was 98.35%, but when the lower voltage cut-off was raised to 100 mV, the average CE increased to 99.22% (cycles 1601-1650).

The decrease in side reactions was accompanied by diminished capacity, from an average of 932 mAh g^{-1} to 826 mAh g^{-1}. By adjusting the lower voltage cut-off potential, capacity decreased (by 106 mAh g^{-1}) but, significantly, irreversible losses were decreased by 60%, from 15.4 to 6.4 mAh g^{-1}. Adjustment of the lower voltage cut-off to 150 mV

resulted in further attenuation of capacity to an average of 754 mAh g^{-1} and of irreversible losses to 4.2 mAh g^{-1} (corresponding to an average CE of 99.45%).

AC impedance spectroscopy

AC impedance spectroscopy was used to characterize the influence of the FEC or Cl-EC electrolyte formulations compared to a standard EC-based electrolyte on the impedance of Li-ion transport. The differences in cycling performance recorded when using the five electrolyte formulations can be analyzed in semi-quantitative terms by comparing their effect on the common steps of ion transport: bulk ion transport in the electrolyte, ion de-solvation (charge transfer), transport through the SEI and diffusion in the active material. The AC impedance spectra were collected at states of full charge (Fig. 4.5a) and discharge (Fig. 4.5b) after ten slow cycles at *C*/10 so that the effect of a fully developed SEI would be characterized, and the data was fitted to an equivalent circuit (Fig. S.4.11a ESI†) commonly used to identify the impedance of these four transport steps in porous electrodes.[38]

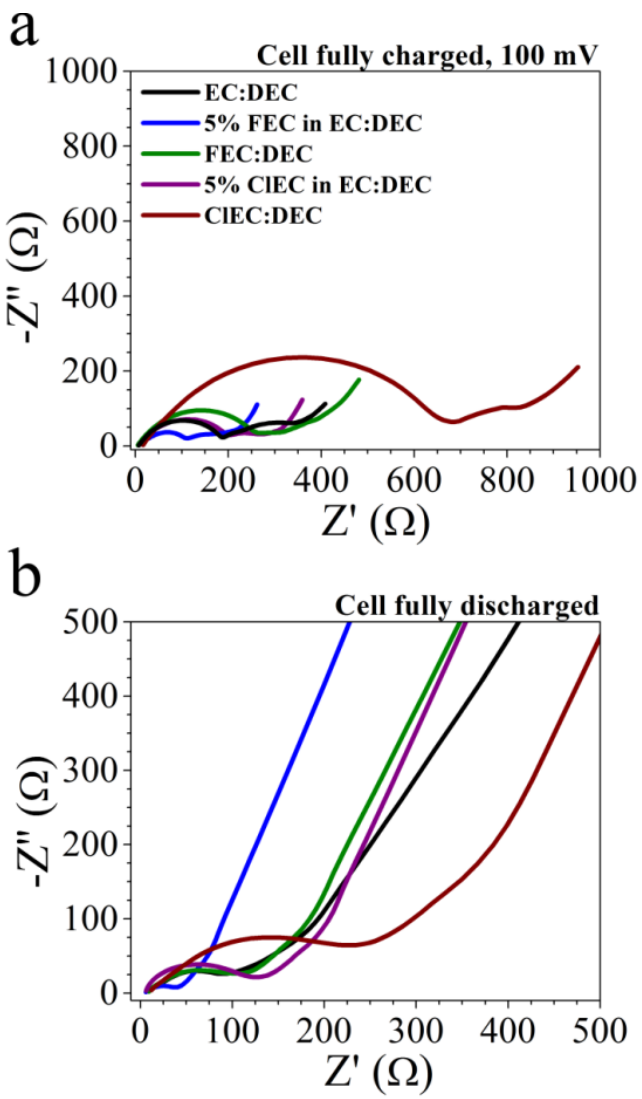

Fig. 4.5 AC impedance spectroscopy on *meso*-porous based Co_3O_4 electrodes at the fully charged and discharged state in the 10th cycle of *C*/10 testing in half cells with EC:DEC, 5% FEC in EC:DEC, FEC:DEC, 5% Cl-EC in EC:DEC or Cl-EC:DEC electrolyte solvent formulations.

The use of FEC or Cl-EC as additives or co-solvents was shown to have a significant effect on the activation energy required for de-solvation of the ion, the resistance to transport through the SEI and, surprisingly, also upon diffusion in the active material. The use of FEC or Cl-EC as electrolyte additives was expected to modify the SEI and the rate of ion transport through the interphase because these carbonates reduce more easily than

EC: the energy of the lowest unoccupied molecular orbital (LUMO) for EC is 0.81 eV, compared to 0.37 eV for FEC and –0.43 eV for Cl-EC.[39] When FEC or Cl-EC was substituted for EC and used as a co-solvent, it was expected that there would also be a decrease in the resistance to charge transfer during de-solvation of the ion due to the lower binding energy of these carbonates to Li^+ in its solvation sheath.[39]

What we found from the AC impedance testing supported the results of our cycling tests, providing semi-quantitative analysis showing how the Li-ion transport is improved or impeded by the different electrolyte formulations. A comparison of the resistance to four transport steps for the electrode at full state of charge is shown in Fig. S.4.11b ESI† (listed values provided in Table S4.4 ESI†).

The AC impedance spectra serve to indicate the physical basis for why the nominally identical electrodes perform so differently when cycled in alternative electrolytes. For the best capacity retention at high *C*-rate testing, FEC was used as an electrolyte additive. The use of this additive resulted in a modified SEI with only ~60% of the resistance to ion transport of the SEI derived from EC. This decrease in impedance through the SEI was accompanied by a decrease in the activation energy required for de-solvation of the ion. With this electrolyte formulation, the ion is exclusively solvated by EC[39,40] and so the decrease in resistance to this charge transfer step is attributed to the modified SEI stabilizing the de-solvation process.

While the use of FEC as a co-solvent resulted in a SEI with greater resistance (~50% more) to ion migration, this electrolyte formulation resulted in further attenuation in the charge transfer resistance (greater than 90%), attributable to the interwoven effects of diminished Li^+/FEC bond energy in the solvation sheath and the surface chemistry of the

SEI that facilitates de-solvation. The comparatively lower capacities (particularly at higher C-rates as recorded for electrodes tested in electrolytes with FEC as co-solvent rather than additive) are attributed to the higher resistance to ion transport through the SEI. The difference in transport rates might be ascribed to a combination of effects deriving from the chemistry and morphology of the SEI; the surface chemistry of these FEC-derived interphases (as well as those formed by Cl-EC containing electrolytes) was studied by XPS and these results are discussed further below.

The most stable cycling performance over 500 cycles testing at a rate of 1*C* was achieved using the FEC:DEC electrolyte but its use did not allow for as high of capacity retention at faster charge/discharge rates. This may be attributed to the comparatively greater resistance to ion migration through the exclusively-FEC derived SEI: 230% of the resistance for the 5% FEC in EC:DEC derived SEI. For the electrode cycled in Cl-EC:DEC, we observed far slower transport through the SEI and also in the particle bulk, as indicated by fitting the low-frequency data to a Warburg impedance element or, more specifically, the component of this element which describes diffusion length and diffusion rate (Fig. S.4.11c ESI†). By using Cl-EC as an additive, the resistance to ion transport was comparable to what was found for the electrode cycled in EC:DEC and, as similar to what was observed when using FEC as an additive, the resistance to charge transfer was diminished. However, while the use of Cl-EC as an additive did increase the capacities recorded (particularly at higher rates) the cycling performance was not stable. Interestingly, good stability – 102% capacity retention *vs* the 10^{th} cycle capacity – was observed for a meso-porous Co_3O_4 electrode tested with an electrolyte formulation of Cl-EC:FEC:DEC

(1:1:2, volume %) through up to 1,000 cycles at 1*C* rate but with relatively poor, sub-99% CE (Fig. S.4.12 ESI†).

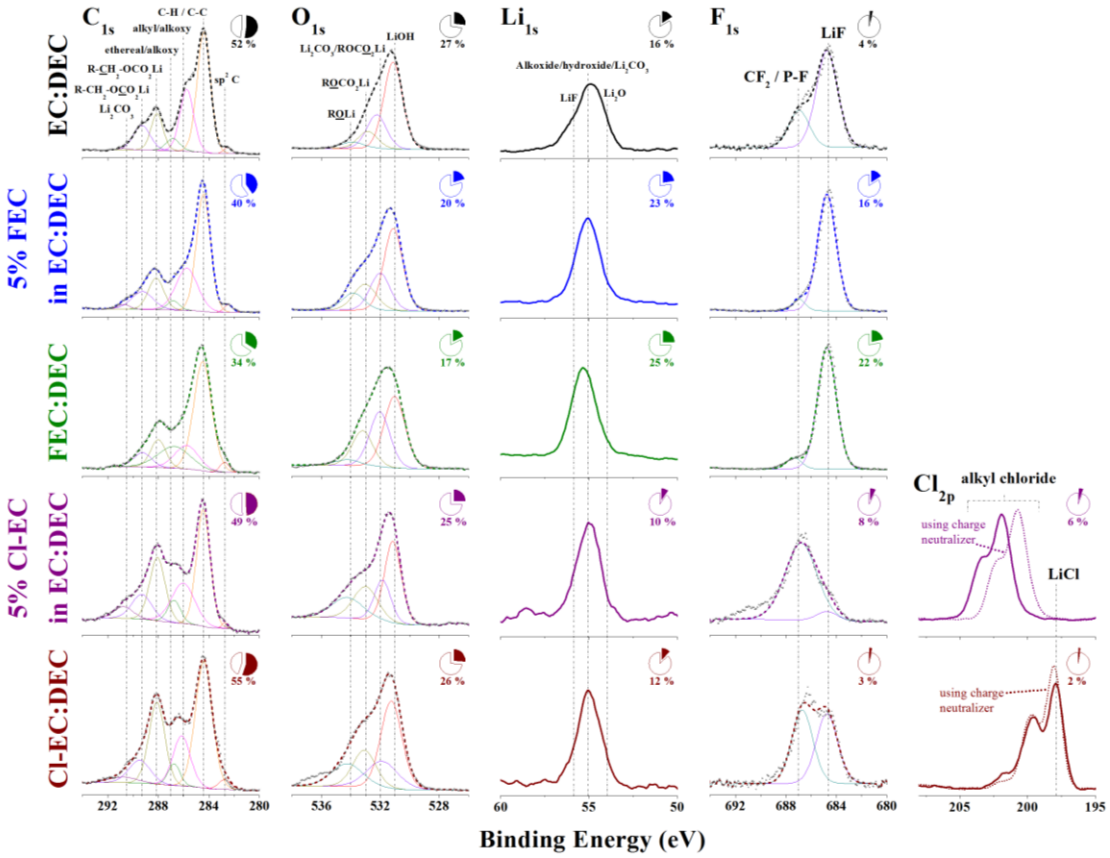

Fig. 4.6 XPS of SEI of the discharged anode after the 10th cycle of *C*/10 testing for each of the five electrolyte formulations evaluated. Species assignments are indicated by text and elemental composition is noted by the pie chart adjoining each regional spectra.

XPS characterization of Li-ion SEI

XPS investigation of the SEI formed on the electrodes cycled 10 times at *C*/10 to their discharged state was conducted to complement the findings from AC impedance spectroscopy, which showed that resistance to ion transport (*via* migration through the SEI and de-solvation of the ion) is a function of SEI. Survey spectra and regional spectra (Fig. 4.6) were obtained to allow for a detailed analysis of the species present within the SEI.

The method used to correct the spectra to account for charging and the references to the species assignments is found in the Experimental section. No signal was detected from the Co 2*p* region for any sample, indicating that the SEI thickness exceeded the *ca.* 10 nm thickness from which XPS signal is derived.

The SEI for the standard case – the SEI derived from the EC:DEC formulation – is dominated by C, O and Li signal (52, 27 and 16 atomic %, respectively), with only 4% F and less than 1 % P (these last elements derived from the reduction of the molten salt anion, PF_6^-). Several peaks can be deconvoluted from the C 1*s* and O 1*s* regional spectra, indicating this SEI is constituted of lithium hydroxide and of carbon species with mainly lower degrees of oxidation, principally sp^3 C-C and C-H and alkyl/alkoxide species (the percentage distribution of the C 1s spectra is provided in Fig. S.4.13 ESI†) with a lesser amount of lithium alkyl-carbonate species. A portion of the alkyl/alkoxy signal is attributable to the carboxymethyl cellulose binder,[41] which is believed to be present within the bounds of the SEI interphase.

By including FEC as an additive, the chemistry of the SEI is significantly enriched by lithium fluoride. The F elemental composition is increased from 4 to 16 %, the overwhelming majority of which is found in lithium fluoride, a species which can be formed by the reactions of PF_5 and PF_6^- with Li, but in this instance is predominately generated by the decomposition of FEC. It has been reported that in the absence of EC, there is a more pronounced reduction of the PF_6^- ion[42] but for this electrolyte formulated with FEC only as an additive, this rationale does not apply. The correlation of increased concentration of LiF in the SEI and stable electrode cycling has been reported many times

but the causation – how this species improves performance – remains restricted to informed speculation.[43]

Some reports link LiF to the formation of a thinner SEI which allows for more rapid ion transport as a consequence of its dimension.[22] Other reports suggest that a LiF-rich SEI is better able to withstand the volumetric changes which fracture an EC-derived SEI.[34] Based upon the results from AC impedance, we suggest another explanation: that with increasing LiF content, lithium ions are drawn more closely to and into the SEI, facilitating the ion desolvation process, as has been recently shown in a study employing atomistic modeling by Jorn et al.[44] Whether LiF is responsible for facilitating de-solvation as indicated by the experimental evidence, there appears to be a limit to its utility in improving overall ion transport; although the resistance to desolvation further diminishes with increase in content of LiF in the SEI found when using the FEC:DEC electrolyte formulation, the resistance to ion transport through the SEI increases markedly.

This resistance to transport is borne out in the cycling performance, particularly at higher *C*-rates, yet besides the already noted increase in LiF content, there is marginal difference in the regional spectra for the SEI derived from the electrolyte employing FEC as an additive or co-solvent. Measurements of the SEI morphology, the use of high-resolution XPS with careful depth profiling or evaluation of the SEI formed after cycling at higher rates may provide better insight into what distinguishes these SEI layers.

For the electrodes cycled in Cl-EC based formulations, there was a small uptake of Cl into the SEI (interestingly, more uptake for the formulation with Cl-EC as an additive) which differentiated its composition from that derived from EC:DEC or those using FEC. The most striking difference in the content of the Cl-EC derived SEIs was the relative

amount of carbon, particularly lithium alkyl-carbonate and lithium carbonate species. From the fitting parameters imposed according to the results of prior works[29,42,45,46] focused on studying the reduction of electrolyte solvents and the composition of the SEI, we assigned the peaks representative of the content of the several carbon species. Notably, the lithium alkyl-carbonate and lithium carbonate species constituted about 25% of the SEI formed from the EC:DEC formulation but were over 35% for the Cl-EC formulations.

The rise in carbon-containing species came with an expected decrease in fluorine content but an unexpected decrease in lithium content, falling to near 10%. Taken with the AC impedance results, we believe that the higher content of carbonate species and lower content of lithium fluoride (or chloride) is responsible for the higher resistance of ion transport through the SEI, which was particularly evident for the Cl-EC:DEC formulation. It should be noted that the use of the charge neutralizer was employed for analysis of all regions due to the highly shifted chlorine signal for the SEI formed from 5% Cl-EC in EC:DEC. The dominant signal from the compensated spectra obtained using the charge neutralizer shows an oxidized chlorine containing species at near 200 eV which we were unable to confidently assign.

Evaluation of meso-Co_3O_4 for Na-ion batteries

The viability of *meso*-porous Co_3O_4 for use in a future Na-ion battery was examined with the same electrochemical tests and characterization performed for the Li-ion electrodes. These results complement and expand upon a recent communication reported by Rahman *et al*.,[47] indicating that Co_3O_4 is a potential candidate for use sodium ion battery anodes and also supporting their finding that the theoretical capacity of this active material is 447 mAh g^{-1} *vs* Na. By assuming a charge mechanism analogous to the conversion

reaction with lithium, Klein *et al*. previously calculated that the sodium ion theoretical capacity remains 890 mAh g^{-1} with the free energy of formation of the Co + Na_2O (fully charged) phase formed at 0.84 V *vs* Na/Na^+.[48] However, in experiments, we find that even at low rates the reversible capacity of the electrode appears to be limited to only around half the theoretical value, near 445 mAh g^{-1}, in agreement with the finding of Rahman *et al*. This low capacity may be due to excessive cell internal resistance, for the differential capacity profile (Fig. S.4.18 ESI†) indicates that the sodium charge/discharge reaction proceeds analogously to that of the lithium cell. Experiments are underway to verify the theoretical capacity by characterizing the mechanism of charge and discharge by means of *in-situ* Raman spectroscopy and *in-situ* XRD characterization. However, we believe that the mechanism proposed by Rahman *et al*. is more consistent with the cycling performance for the *meso*-porous particles tested here. Like Rahman *et al*., we find that at low *C*-rates the electrode discharges reversibly to near 445 mAh g^{-1} but the more practically useful capacity at the relatively slow rate of 1*C* (0.89 A g^{-1}) was found to decrease to near 175 mAh g^{-1} using the best electrolyte formulations, 5% FEC in EC:DEC and FEC:DEC.

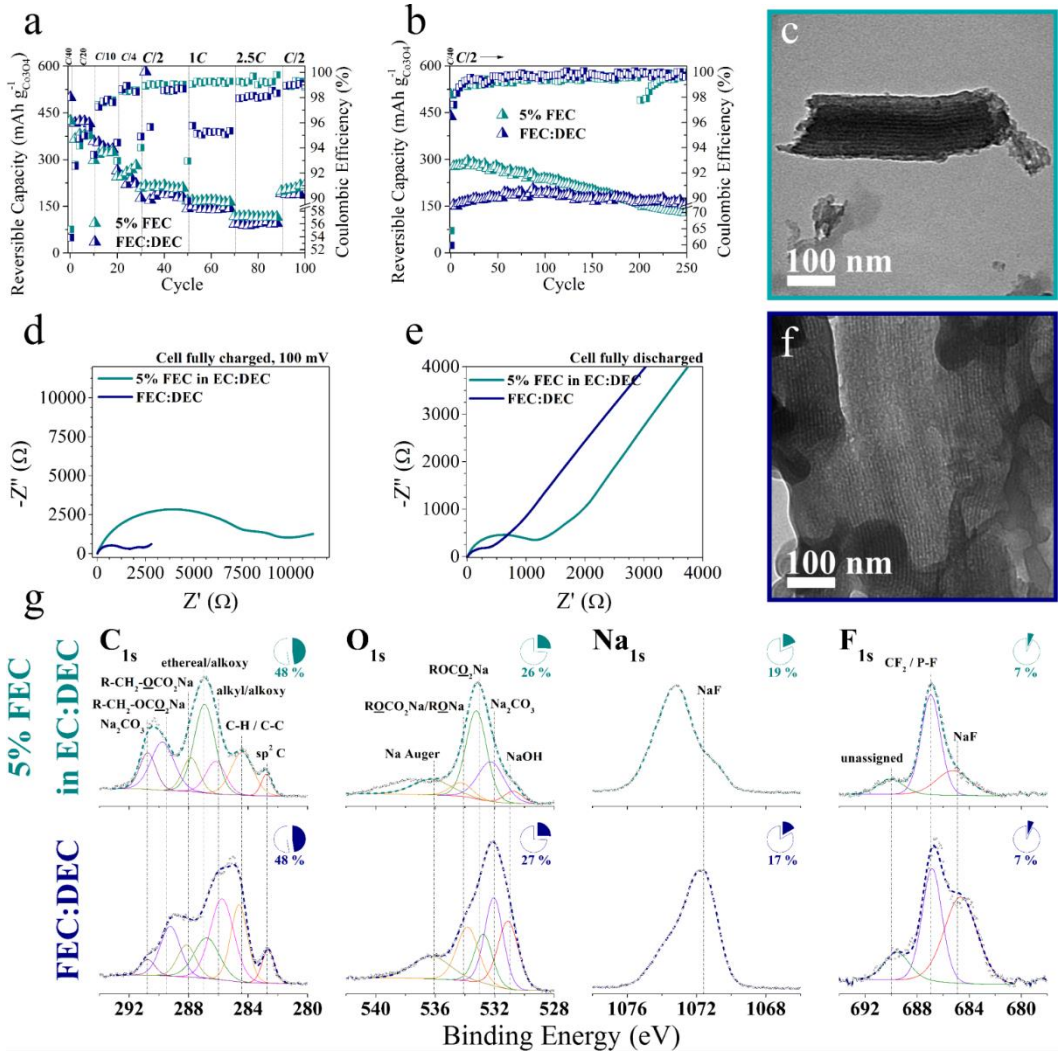

Fig. 4.7 Characterization of meso-porous Co_3O_4 when used as the active material for a Na-ion half cell, tested with two electrolyte formulations: 1M $NaPF_6$ in 5% FEC in EC:DEC and FEC:DEC. Electrochemical testing conducted (a) at variable *C*-rates and (b) to evaluate cycling stability at *C*/2 (0.445 mA/g) rate. AC impedance spectroscopy conducted at (a) fully charged and (b) discharged states in the 10th cycle of a *C*/20 test. After 250 cycles testing at *C*/2 rate, TEM done on ultramicrotomed sections of electrodes in discharged state showing meso-porous channels intact: (c) cycled in 5% FEC in EC:DEC and (f) cycled in FEC:DEC. XPS characterization of SEI formed in the discharged state for each electrode/electrolyte combination after the ten cycles testing at *C*/20 rate.

In this electrolyte survey, the EC:DEC formulation was omitted owing to its comparatively poor performance in several recent studies of Na-ion anode materials[49,50], while the majority of the coin cells tested with the Cl-EC:DEC and 5% Cl-EC in EC:DEC formulations were found to consistently fail after several cycles owing to internal shorting, likely a consequence of rapid sodium dendrite formation arising from poorly formed and/or high impedance SEIs, a problem which affected in lesser degree the Li-ion cells tested with analogous formulations.

In a variable rate test (Fig. 4.7a), the capacity retention for the electrode was similar using either of the FEC-type electrolyte formulations: at a rate of *C*/2 (455 mA g^{-1}), the retention was only 23% of the theoretical capacity (890 mAh g^{-1}) for the electrode in the 5% FEC formulation and 20% in the FEC:DEC formulation. However, in terms of stability (Fig. 4.7b), the electrode tested in FEC:DEC performed significantly better. At near 200 cycles, the electrodes provided near the same capacity, although the electrode tested in FEC:DEC retained 80% of its maximum 204 mAh g^{-1} capacity found during testing at *C*/2 (445 mA g^{-1}) through 200 cycles (and retained 75% capacity through 250 cycles) while the electrode cycled in 5% FEC retained only 53% through 200 cycles (44% through 250 cycles). The first cycle CE for the electrode tested in FEC:DEC was near 64%, slightly higher than the 60% value found for the 5% FEC formulation. The average CE during the first 200 cycles at *C*/2 (445 mA g^{-1}) was 99.7% when using FEC:DEC and a significantly lower 99.2% when using 5% FEC.

Irrespective of the electrolyte formulation used, the *meso*-porosity was retained as with the electrodes tested in lithium-ion cells; after 250 cycles at *C*/2, TEM was used to

characterize ultramicrotomed sections of the electrodes in their full discharged state and the *meso*-porous channels were observed to be intact (Fig. 4.7c,f).

The differences in the cycling performance between the electrodes tested in the different electrolyte formulations as well as those differences in performance between electrodes tested with lithium *vs* sodium ions may be explained in part by the results of AC impedance spectroscopy taken after ten slow cycles at *C*/20 rate. Considering the electrode in its fully charged state (Fig. 4.7d), the impedance for the sodium ion electrodes is 1-2 orders of magnitude greater than that for lithium ion electrodes. The result of using FEC as a co-solvent rather than as an additive diminished the resistance to transport through the SEI by a factor of 6 and the charge transfer resistance by a factor of 2. (Tabulated values from fitted results found in Table S4.5 ESI†.)

As for the electrodes tested in lithium-ion cells, we attribute the differences in cycling performance – these derived in large measure from the ionic transport properties of the electrode system – to the chemistry and morphology of the SEI. The SEI formed on electrodes tested in sodium ion cells was characterized by XPS. In Fig. 4.7g, the regional spectra for the dominant elements is shown (the P signal is not shown as it accounted for about 1 atomic % in each SEI).

Compared to the SEI derived from lithium-ion salts, these SEI are constituted of a greater content of ether/alkoxy and carbonate species carbon species. As with the SEI derived from the Cl-EC:DEC formulation for the lithium-ion cell, the increased population of carbonates, alkyl-carbonates and ethers can be correlated to increased impedance to ion transport through the SEI and resistance to desolvation.

Following the parameters imposed according to the results of prior research into the Na-ion SEI,[51,52] the content of the various carbon species was found for these sodium-ion cell SEIs (Fig. S.4.14 ESI†). The content of alkyl carbonates/carbonates for the SEI derived from the 5% FEC formulation was near 70% while only 43% for the SEI derived when FEC was employed as a co-solvent. While the presence of carbonate species appears to correlate with SEI in poorer performing cells, the increased content of NaF in the FEC:DEC derived SEI was observed to correlate with the more facile ion transport, this is possibly due to an analogous rationale to what has been suggested for the lithium-ion cell SEIs: the NaF species more strongly attracts the ion, facilitating its desolvation into the SEI.

Conclusions

The voltage characteristics of the cobalt oxide based anode recommend its consideration for use in low power portable electronics and other applications which might benefit from higher capacities and faster charge rates (at higher and therefore more safe voltages). We believe that the potential viability of a cobalt oxide-based anode is derived in part from progress in semiconductor technology that has led to the development of low voltage circuit architectures targeted toward extending battery life. For a recently developed model which optimizes via consideration of battery discharge and delay product, the desired V_{dd} was found to be 0.9 V for a simulation run for supply voltages ranging from 0.8-1.6 V for a VLSI circuit with 0.35u CMOS type transistors.[53]

Therefore, despite operating over a continuum of voltages, the low voltage requirements of modern semiconductors could allow for the possibility of a cobalt oxide based anode: when paired with a lithium cobalt oxide cathode, the average battery discharge potential at a C/10 rate is near 2.5 V: the average *meso*-porous cobalt oxide anode discharge

potential at a C/10 rate vs Li/Li^+ is 1.68 V, and the average lithium cobalt oxide cathode charge potential at C/10 rate vs Li/Li^+ is near 4.2 V.[54]

With the stable structure of high surface area *meso*-porous Co_3O_4 particles in a conventional slurry cast electrode cycled using 1 M $LiPF_6$ in a mixture of 5 wt% FEC in (1:1 vol%) EC/DEC, we report good capacity retention at high rates: 77% retention at 5*C* and after testing through 800 cycles at variable *C*-rates, 115% capacity retention with stable cycling upon return to 1*C* rate. For highest capacity retention and coulombic efficiency over a calendar life test of 500 cycles at 1*C*, the co-solvent mixture of (1:1 vol%) FEC:DEC is preferred: 92% capacity retention with an average CE of 99.6%.

The stable cycling even up to high rates that was observed in these tests may be attributed to a combination of factors: (a) the retention of the *meso*-porous structure that facilitates 1D ion transport down the *meso*-pores and appears to allow these particles to avoid the progressive segregation of Co into electrically isolated clusters as has been found previously and (b) the selection of alternative electrolyte formulations which form SEI with lower impedance to ion migration across the electrolyte/electrode interphase and which also facilitate ion desolvation, perhaps due to an increased content of ion-fluoride species which have been shown to have this effect in a recent atomistic modeling study.

The commonly used EC-based formulation (here a 1:1 vol% EC:DEC formulation is used) is not recommended due to worse cycling stability, retention at high *C*-rates, coulombic efficiency and, notably, safety concerns arising from a tendency for cells cycled with this electrolyte formulation to cycle irregularly (arising from abrupt cell resistance increases) after hundreds of cycles of testing.

In Na-ion testing, the potential for a *meso*-porous cobalt oxide based anode was demonstrated, with stable cycling performance and near 100% coulombic efficiencies observed at variable *C*-rates and during a 250 cycle test at 445 mA g^{-1} (*C*/2) rate. For best cycling stability, the electrolyte survey done here recommends the use of the 1M $NaPF_6$ in 1:1 (vol%) FEC:DEC formulation. Further, the experimental capacities reported here support the recent finding by Rahman *et al*. that an alternative mechanism exists for Co_3O_4 when charging/discharging *vs* Na, resulting in a theoretical capacity of 447 mAh g^{-1}.

REFERENCES

1. X.-J. Zhu, J. Hu, H.-L. Dai, L. Ding and L. Jiang, Electrochimica Acta, 2012, 64, 23-28.

2. X. Huang, H. Yu, J. Chen, Z. Lu, R. Yazami and H. H. Hng, Advanced Materials, 2014, DOI: 10.1002/adma.201304467, n/a-n/a.

3. J. Chen, X.-h. Xia, J.-p. Tu, Q.-q. Xiong, Y.-X. Yu, X.-l. Wang and C.-d. Gu, Journal of Materials Chemistry, 2012, 22, 15056-15061.

4. K. T. Nam, D.-W. Kim, P. J. Yoo, C.-Y. Chiang, N. Meethong, P. T. Hammond, Y.-M. Chiang and A. M. Belcher, Science, 2006, 312, 885-888.

5. Z. Hui, W. Jianbo, Z. Chuanxin, M. Xiangyang, D. Ning, T. Jiangping and Y. Deren, Nanotechnology, 2008, 19, 035711.

6. W. Mei, J. Huang, L. Zhu, Z. Ye, Y. Mai and J. Tu, Journal of Materials Chemistry, 2012, 22, 9315-9321.

7. L. Hu, N. Yan, Q. Chen, P. Zhang, H. Zhong, X. Zheng, Y. Li and X. Hu, Chemistry – A European Journal, 2012, 18, 8971-8977.

8. X. Wang, L. Yu, X.-L. Wu, F. Yuan, Y.-G. Guo, Y. Ma and J. Yao, The Journal of Physical Chemistry C, 2009, 113, 15553-15558.

9. N. Yan, L. Hu, Y. Li, Y. Wang, H. Zhong, X. Hu, X. Kong and Q. Chen, The Journal of Physical Chemistry C, 2012, 116, 7227-7235.

10. Y. Fu, X. Li, X. Sun, X. Wang, D. Liu and D. He, Journal of Materials Chemistry, 2012, 22, 17429-17431.

11. L. Li, G. Zhou, X.-Y. Shan, S. Pei, F. Li and H.-M. Cheng, Journal of Power Sources, 2014, 255, 52-58.

12. Y. Li, B. Tan and Y. Wu, Nano Letters, 2007, 8, 265-270.

13. Y. Xiao, C. Hu and M. Cao, Journal of Power Sources, 2014, 247, 49-56.

14. Y. Lu, Y. Wang, Y. Zou, Z. Jiao, B. Zhao, Y. He and M. Wu, Electrochemistry Communications, 2010, 12, 101-105.

15. X. Rui, H. Tan, D. Sim, W. Liu, C. Xu, H. H. Hng, R. Yazami, T. M. Lim and Q. Yan, Journal of Power Sources, 2013, 222, 97-102.

16. J. Sun, H. Liu, X. Chen, D. G. Evans and W. Yang, Nanoscale, 2013, 5, 7564-7571.

17. Z.-S. Wu, W. Ren, L. Wen, L. Gao, J. Zhao, Z. Chen, G. Zhou, F. Li and H.-M. Cheng, ACS Nano, 2010, 4, 3187-3194.

18. L. Zhan, Y. Wang, W. Qiao, L. Ling and S. Yang, Electrochimica Acta, 2012, 78, 440-445.

19. B. Zhang, Y. Zhang, Z. Miao, T. Wu, Z. Zhang and X. Yang, J. Power Sources, 2014, 248, 289-295.

20. K. M. Shaju, F. Jiao, A. Debart and P. G. Bruce, Physical Chemistry Chemical Physics, 2007, 9, 1837-1842.

21. N.-S. Choi, K. H. Yew, K. Y. Lee, M. Sung, H. Kim and S.-S. Kim, Journal of Power Sources, 2006, 161, 1254-1259.

22. H. Nakai, T. Kubota, A. Kita and A. Kawashima, Journal of The Electrochemical Society, 2011, 158, A798-A801.

23. A. M. Chockla, K. C. Klavetter, C. B. Mullins and B. A. Korgel, ACS Applied Materials & Interfaces, 2012, 4, 4658-4664.

24. Z. X. Shu, R. S. McMillan, J. J. Murray and I. J. Davidson, Journal of The Electrochemical Society, 1996, 143, 2230-2235.

25. N. Dahal, I. A. Ibarra and S. M. Humphrey, Journal of Materials Chemistry, 2012, 22, 12675-12681.

26. http://www.scribner.com/.

27. K. C. Klavetter, S. M. Wood, Y.-M. Lin, J. L. Snider, N. C. Davy, A. M. Chockla, D. K. Romanovicz, B. A. Korgel, J.-W. Lee, A. Heller and C. B. Mullins, Journal of Power Sources, 2013, 238, 123-136.

28. P. R. Abel, Y.-M. Lin, H. Celio, A. Heller and C. B. Mullins, ACS Nano, 2012, 6, 2506-2516.

29. S. Malmgren, K. Ciosek, M. Hahlin, T. Gustafsson, M. Gorgoi, H. Rensmo and K. Edström, Electrochimica Acta, 2013, 97, 23-32.

30. D. Larcher, G. Sudant, J.-B. Leriche, Y. Chabre and J.-M. Tarascon, Journal of The Electrochemical Society, 2002, 149, A234-A241.

31. Y.-M. Kang, M.-S. Song, J.-H. Kim, H.-S. Kim, M.-S. Park, J.-Y. Lee, H. K. Liu and S. X. Dou, Electrochimica Acta, 2005, 50, 3667-3673.

32. J. M. Zuo and J. C. Mabon, Microsc Microanal, 2004, 10.

33. K. Rhodes, M. Kirkham, R. Meisner, C. M. Parish, N. Dudney and C. Daniel, Review of Scientific Instruments, 2011, 82, 075107-075107-075107.

34. Y.-M. Lin, K. C. Klavetter, P. R. Abel, N. C. Davy, J. L. Snider, A. Heller and C. B. Mullins, Chemical Communications, 2012, 48, 7268-7270.

35. Y.-M. Lin, K. C. Klavetter, A. Heller and C. B. Mullins, The Journal of Physical Chemistry Letters, 2013, 4, 999-1004.

36. P. C. Howlett, D. R. MacFarlane and A. F. Hollenkamp, J. Power Sources, 2003, 114, 277-284.

37. D. Foster, J. Wolfenstine, J. Read and J. L. Allen, Performance of Sony's Alloy Based Li-ion Battery, S. a. E. D. Directorate Report ARL-TN-0319, Army Research Laboratory, Army Research Laboratory, 2008.

38. J. Liu and A. Manthiram, Chemistry of Materials, 2009, 21, 1695-1707.

39. M. H. Park, Y. S. Lee, H. Lee and Y.-K. Han, J. Power Sources, 2011, 196, 5109-5114.

40. K. Xu, Y. Lam, S. S. Zhang, T. R. Jow and T. B. Curtis, The Journal of Physical Chemistry C, 2007, 111, 7411-7421.

41. N. Pahimanolis, A. Salminen, P. Penttilä, J. Korhonen, L.-S. Johansson, J. Ruokolainen, R. Serimaa and J. Seppälä, Cellulose, 2013, 20, 1459-1468.

42. V. Etacheri, O. Haik, Y. Goffer, G. A. Roberts, I. C. Stefan, R. Fasching and D. Aurbach, Langmuir, 2011, 28, 965-976.

43. M.-J. Chun, H. Park, S. Park and N.-S. Choi, RSC Advances, 2013, 3, 21320-21325.

44. R. Jorn, R. Kumar, D. P. Abraham and G. A. Voth, The Journal of Physical Chemistry C, 2013, 117, 3747-3761.

45. A. M. Andersson and K. Edström, Journal of The Electrochemical Society, 2001, 148, A1100-A1109.

46. S. Chattopadhyay, A. L. Lipson, H. J. Karmel, J. D. Emery, T. T. Fister, P. A. Fenter, M. C. Hersam and M. J. Bedzyk, Chemistry of Materials, 2012, 24, 3038-3043.

47. M. M. Rahman, A. M. Glushenkov, T. Ramireddy and Y. Chen, Chemical Communications, 2014, 50, 5057-5060.

48. F. Klein, B. Jache, A. Bhide and P. Adelhelm, Physical Chemistry Chemical Physics, 2013, 15, 15876-15887.

49. P. R. Abel, Y.-M. Lin, T. de Souza, C.-Y. Chou, A. Gupta, J. B. Goodenough, G. S. Hwang, A. Heller and C. B. Mullins, The Journal of Physical Chemistry C, 2013, 117, 18885-18890.

50. D. Y. W. Yu, P. V. Prikhodchenko, C. W. Mason, S. K. Batabyal, J. Gun, S. Sladkevich, A. G. Medvedev and O. Lev, Nat Commun, 2013, 4, 2922.

51. S. Komaba, W. Murata, T. Ishikawa, N. Yabuuchi, T. Ozeki, T. Nakayama, A. Ogata, K. Gotoh and K. Fujiwara, Advanced Functional Materials, 2011, 21, 3859-3867.

52. S. Komaba, T. Ishikawa, N. Yabuuchi, W. Murata, A. Ito and Y. Ohsawa, ACS Applied Materials & Interfaces, 2011, 3, 4165-4168.

53. M. Pedram and Q. Wu, presented in part at the Proceedings of the 36th annual ACM/IEEE Design Automation Conference, New Orleans, Louisiana, USA, 1999.

54. Lithium Batteries: Science and Technology, Springer, 2003.

SUPPLEMENTARY INFORMATION

1. SEM of un-cycled electrode

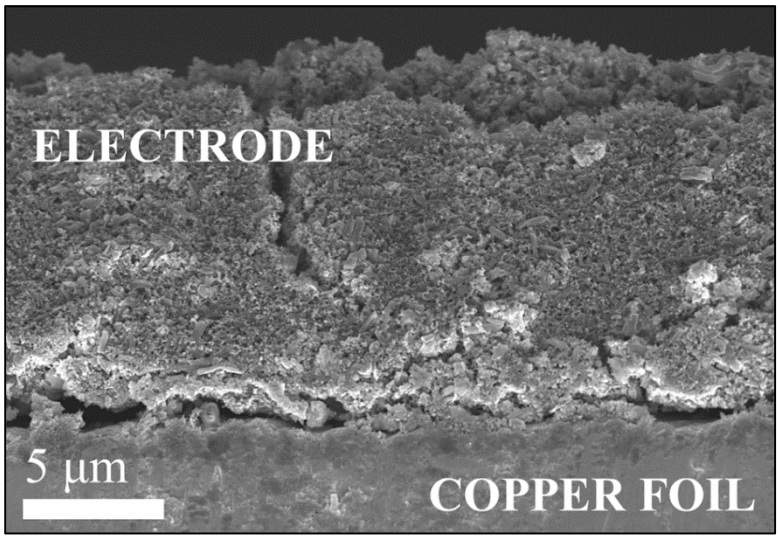

Fig. S.4.1a. SEM cross-sectional image of un-cycled meso-porous Co_3O_4 based electrode on copper foil current collector.

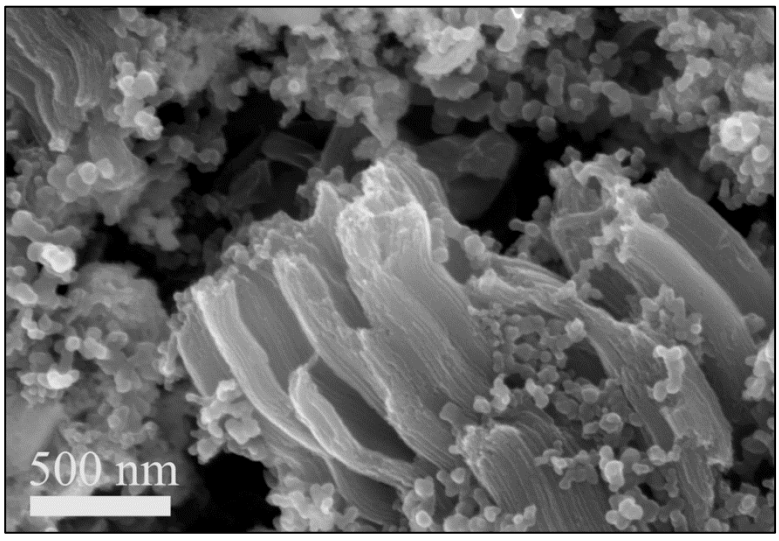

Fig. S.4.1b. SEM cross-sectional image of un-cycled meso-porous Co_3O_4 based electrode showing meso-porous material surrounded by Super-P Li conductive additive.

1. X-ray photoelectron spectroscopy (XPS) characterization and analysis procedure

XPS analysis of SEI surface of cycled electrodes

The peak assignments for the XPS spectra were described in the experimental section. The peak assignments used for analysing the spectra of SEI formed upon lithium ion anodes are summarized in the tables below. Our interpretation of the data is that it represents the surface of a SEI which extends beyond the depth of characterization for XPS (estimated to be ~10 nm) because no cobalt signal was observed.

Table S4.1a. Regional assignments for species constituting the Li-ion derived SEIs.

Region	Species	Binding Energy	Ref.	Binding energy	FWHM Range	Lineshape
C 1s	sp^2 C in graphitic C	282.5	[1]	282.5±0.25	0 - 2	GL(30)
	C-H, C-C	284.5	[1]	284.5±0.1	0 - 2	GL(30)
	alkyl and alkoxy	285-287	[2]	286±0.25	0 - 3	GL(30)
	ethereal, alkoxy	286-288	[2]	287±0.25	0 - 3	GL(30)
	R-CH_2-OCO_2-Li	287.7-	[3]	288±0.25	0 - 2	GL(30)
	R-CH_2-OCO_2-Li	289.2-	[3]	289.5±0.25	0 - 2	GL(30)
	Li_2CO_3	290.5-	[4]	291±0.25	0 - 3	GL(30)
O 1s	LiOH	531	[2, 5]	530.8±0.25	0 - 2.5	GL(30)
	$ROCO_2Li$ / Li_2CO_3	532	[6]	531.8±0.25	0 - 2.5	GL(30)
	$ROCO_2Li$	533	[6]	533.2±0.25	0 - 2.5	GL(30)
	ROLi	534	[6]	534.5±0.25	0 - 2.5	GL(30)
Li 1s	LiF	56	[2]	not fitted		
	Li_2CO_3	55.5	[2]	not fitted		
	alkoxide, hydroxide	55.5	[2]	not fitted		
	Li_2O	54	[2]	not fitted		
F 1s	LiF	685	[2]	685±0.25	0 - 2	GL(30)
	P-F, CF_2	687.2-	[1]	687.2±0.25*	0 - 3	GL(30)
				*±0.5 for Cl-EC based electrolytes		
P 2p	$LiPF_6$	138	[3]	not fitted		
Cl 2p	LiCl	198.5-6	[7]	not fitted		GL(30)
	CH3Cl	200.8	[8]	not fitted		GL(30)

The peak assignments for Na-ion derived SEI were similarly aligned and assigned.

Table S4.1b. Regional assignments for species constituting the Ni-ion derived SEIs.

Region	Species	Binding Energy (eV)	Ref.	Binding energy	FWHM Range	Lineshape
C 1s	sp^2 C in graphitic C	282.5	[1]	282.5±0.25	0 - 2	GL(30)
	C-H, C-C	284.5	[1]	284.5±0.1	0 - 2	GL(30)
	alkyl and alkoxy	285-287	[2]	286±0.25	0 - 3	GL(30)
	ethereal, alkoxy	286-288	[2]	287±0.25	0 - 3	GL(30)
	R-CH_2-OCO_2-Na	287.7-288.2	[3]	288±0.25	0 - 2	GL(30)
	R-CH_2-OCO_2-Na	289.2-290.2	[3]	289.5±0.25	0 - 2	GL(30)
	Na_2CO_3	290.5-291.5	[4]	291±0.25	0 - 3	GL(30)
O 1s	NaOH	531		531±0.25	0 - 2.5	GL(30)
	Na_2CO_3	532	[6]	532±0.25	0 - 2.5	GL(30)
	$ROCO_2Na$	533	[6]	533±0.25	0 - 2.5	GL(30)
	$ROCO_2Na$/RONa	534	[6]	534±0.25	0 - 2.5	GL(30)
	Na KLL Auger	536	[9]	536±0.25	0 - 3	GL(30)
Na 1s	NaF	1071-1072.5	[10,11]	not fitted		
F 1s	NaF	686.6	[12, 2]	685.7±0.25	0 - 3	GL(30)
	PF6-	688.8	[12]	687.9±0.25	0 - 3	GL(30)
	C-F	691	[12]	687.9±0.25	0 - 3	GL(30)

Evaluation of the meso-porous Co_3O_4 particle

A 250 cycle test at 1*C* was conducted in with nominally identical electrodes tested in alternative electrolyte formulations. The slight aberration in cycling results and coulombic efficiencies at cycle 200 is due to the cell being stopped and restarted.

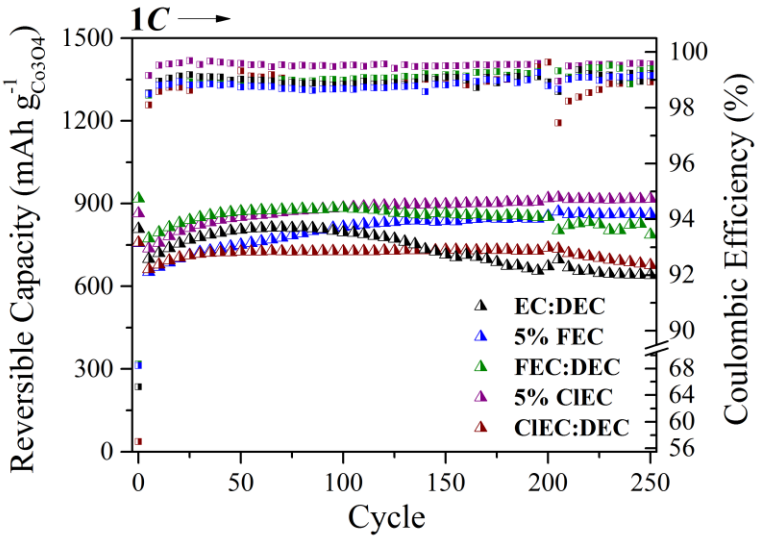

Fig. S.4.2. 250 cycle test in lithium-ion cell at 1C after conditioning cycle at C/20 for nominally identical electrodes cycled in 5 different electrolyte formulations (indicated in legend).

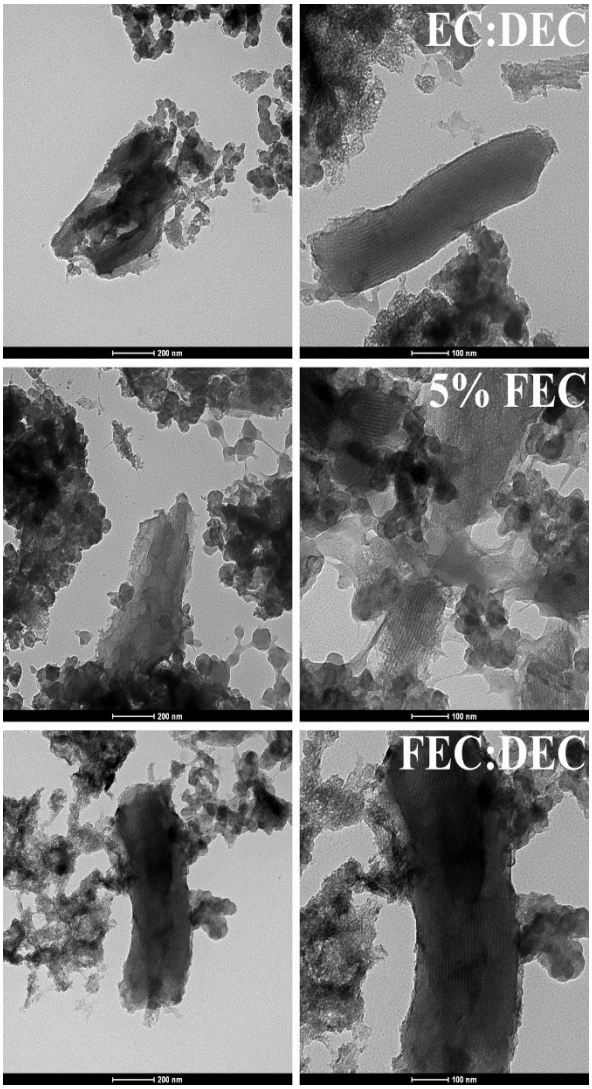

Fig. S.4.3a. TEM at 2 magnifications of (ultramicrotomed) sections of electrode in fully discharged state after 250 cycles testing at 1C rate. The *meso*-porous channels are observed to remain intact. Here, electrodes cycled in 1M $LiPF_6$ in EC:DEC, 5% FEC in EC:DEC or FEC:DEC shown.

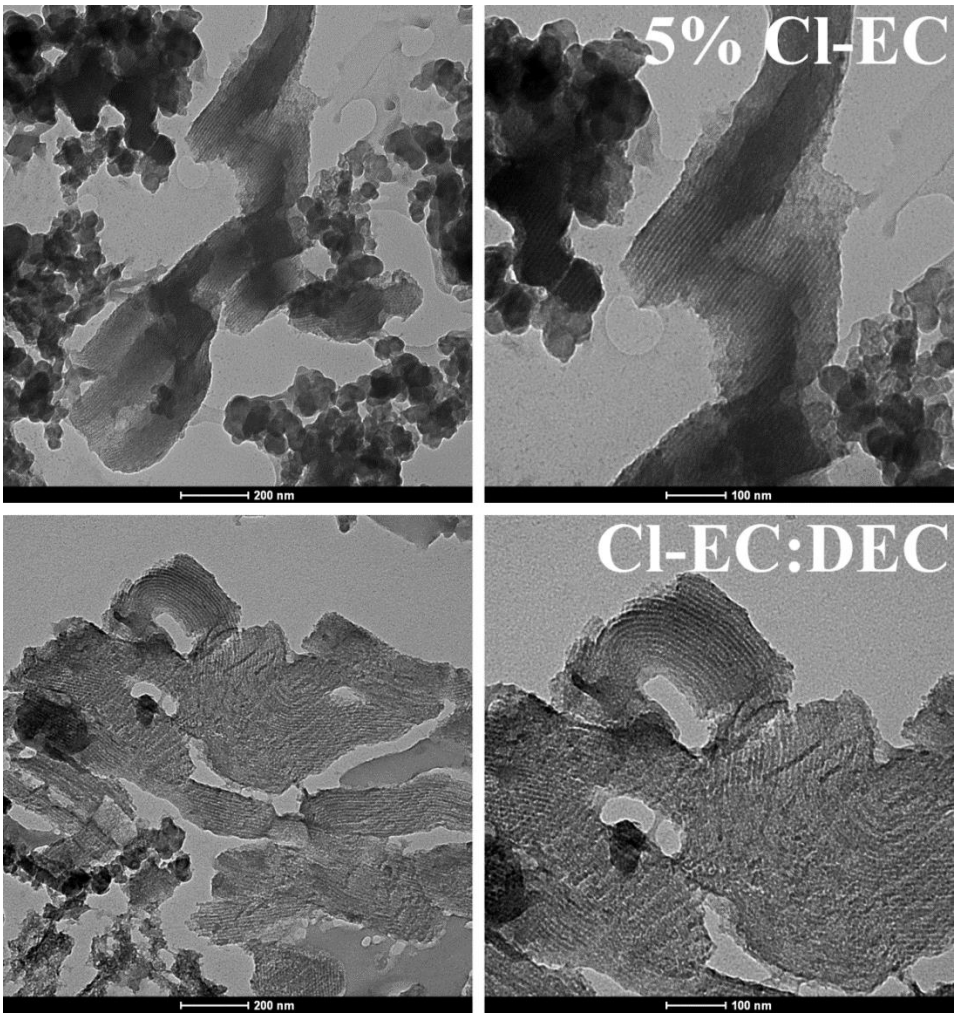

Fig. S.4.3b. TEM at 2 magnifications of (ultramicrotomed) sections of electrode in fully discharged state after 250 cycles testing at 1C rate. The *meso*-porous channels are observed to remain intact. Here, electrodes cycled in 1M $LiPF_6$ in 5% Cl-EC in EC:DEC or Cl-EC:DEC shown.

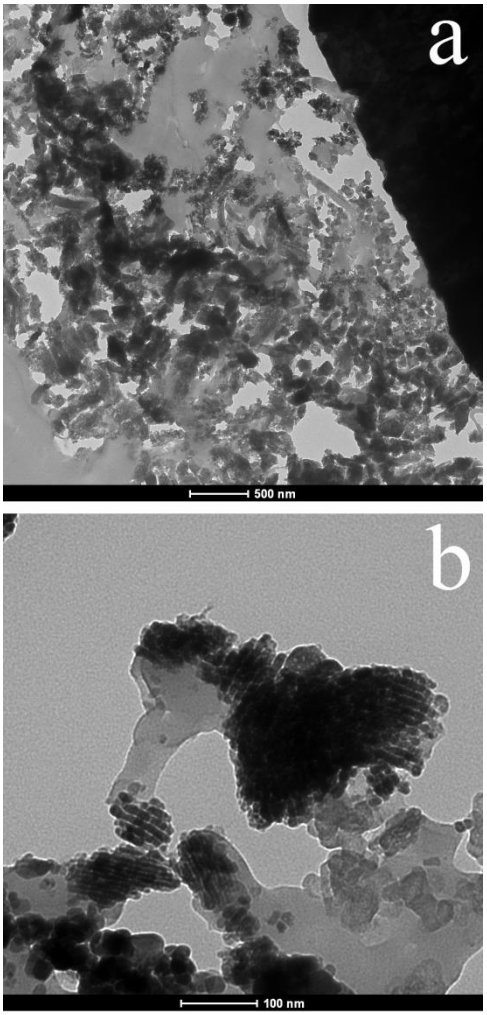

Fig. S.4.3c. TEM of (ultramicrotomed) sections of un-cycled electrode showing (a) wide-field view of electrode and copper foil current collector (black, top right corner) and (b) *meso*-porous particle with channels in plane of view.

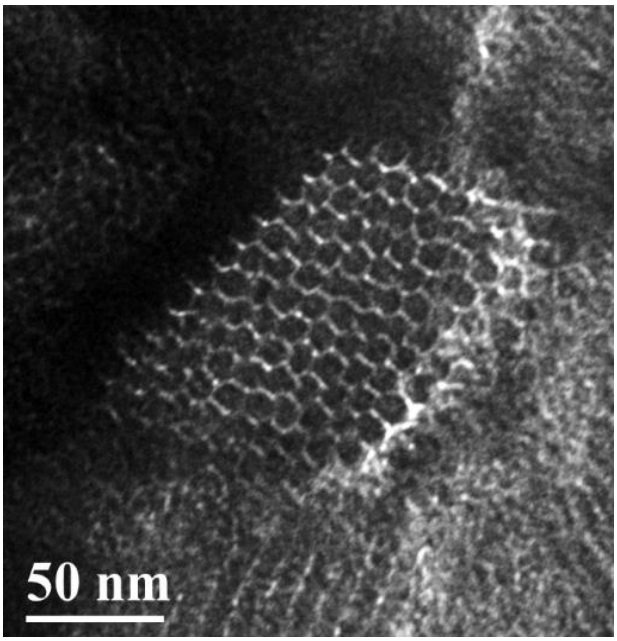

Fig. S.4.3d. TEM of (ultramicrotomed) section of electrode in fully discharged state after 250 cycles at 1C rate in 1 M $LiPF_6$ in 5% FEC in EC:DEC electrolyte formulation. The material in this frame appears to be structured in a manner unlike the anticipated *meso*-porous arrangement and was observed in only a few locations during the several hours of TEM characterization performed. This structure is not considered representative of the bulk of the *meso*-porous particles as it was observed in only a very small fraction of the electrode. Based upon consideration of the many images taken during TEM and SEM characterization, we suggest that this structure may be possibly explained by: (i) a small fraction of the synthesized *meso*-porous Co_3O_4 material forming nanorod clusters, (ii) the *meso*-porous channels being largely filled as a result of the active material swelling as it experienced volumetric changes during charge and discharge or (iii) that the channel walls "ball-up" into what appears to be a string of beads when the particle is cut at a particular, transverse angle (during ultramicrotoming).

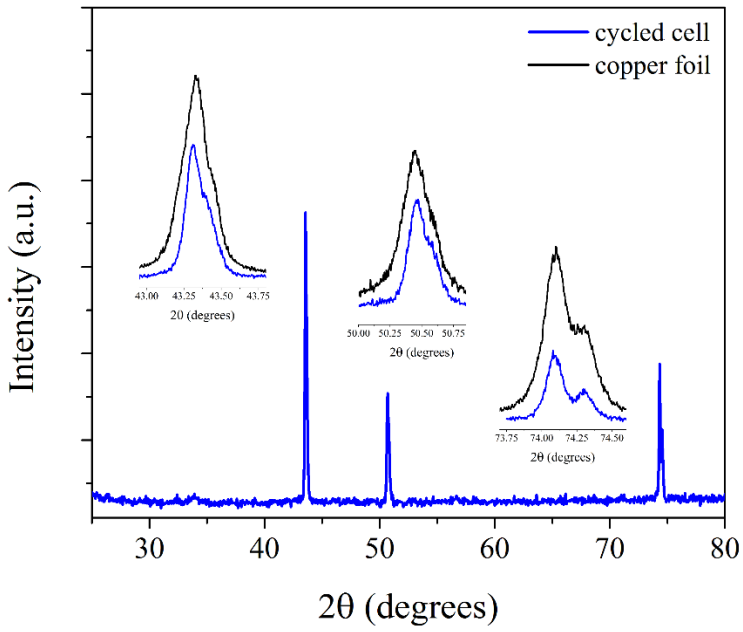

Fig. S.4.4. XRD of cycled electrode in discharged state after 500 cycles at 1*C* in lithium ion cell with 5% FEC in EC:DEC electrolyte formulation. The peaks observed are due to the copper substrate of the electrode and the splitting is a result of the difference in the k-alpha 1 and k-alpha 2 Cu energies. Inset on the Fig. are comparisons of higher resolution diffraction patterns obtained from selected 2-theta domains, comparing the signal electrode to a pristine piece of the copper foil current collector. Patterns taken on similarly cycled anode material removed from the Cu current collector showed no features, confirming the result shown here.

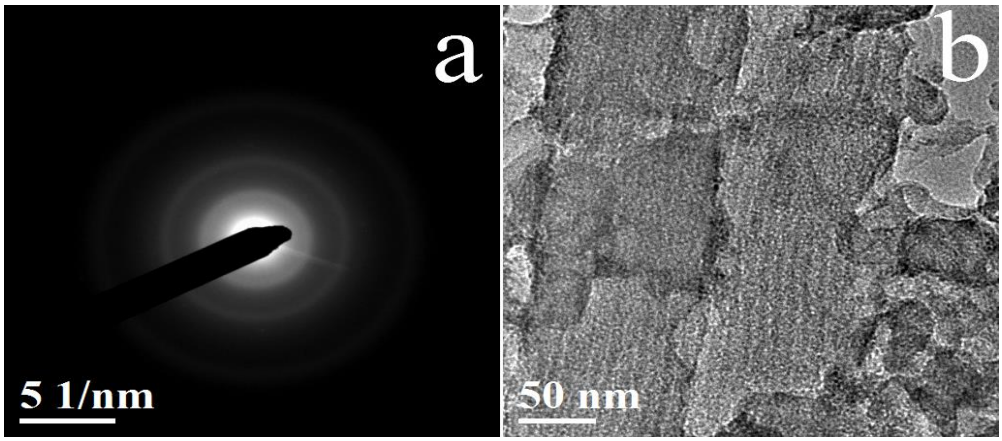

Fig. S.4.5a,b. (a) SAED pattern and (b) corresponding particle with amorphous structure.

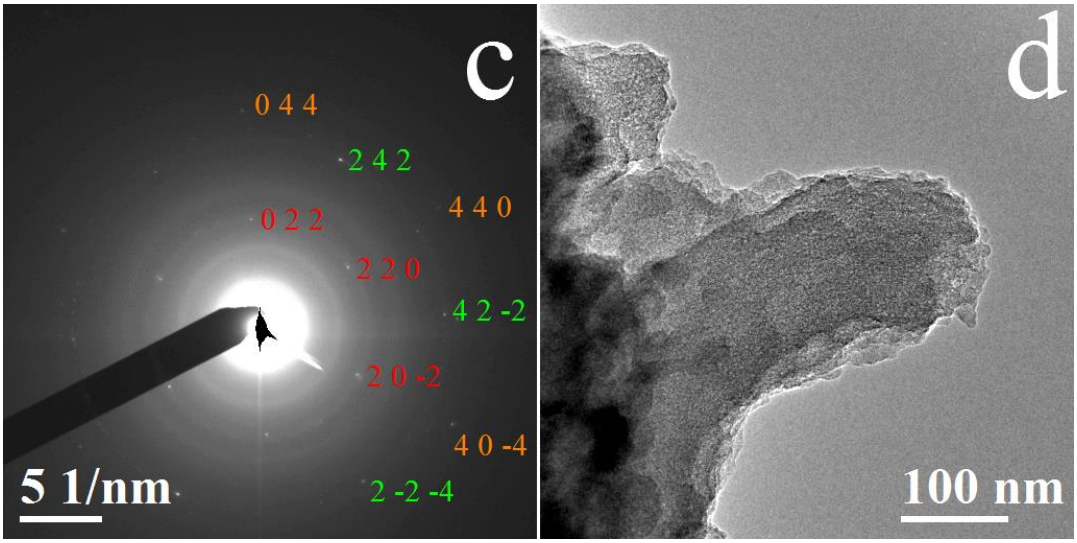

Fig. S.4.5c,d. (c) SAED pattern and (d) corresponding particle with CoO structure indicated by six-fold symmetry along the 1 -1 1 zone axis.

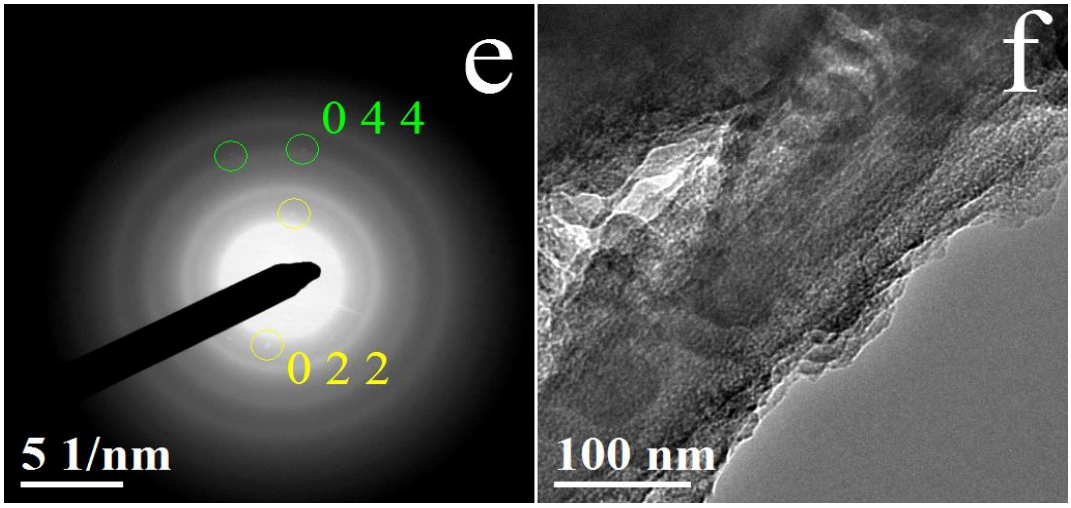

Fig. S.4.5e,f. SAED of electrode showing Co_3O_4 phase in discharged state after 250 cycles at 1*C* rate testing in 5% FEC in EC:DEC electrolyte. (e) the diffraction spots obtained for the material in (f) correspond to the Co_3O_4 phase: despite the few diffraction spots able to be recorded, the 0 2 2 ring is good evidence for the existence of this phase, for these diffraction spots are at a reciprocal distance far removed from that of any other cobalt oxide phase d-spacing.

a

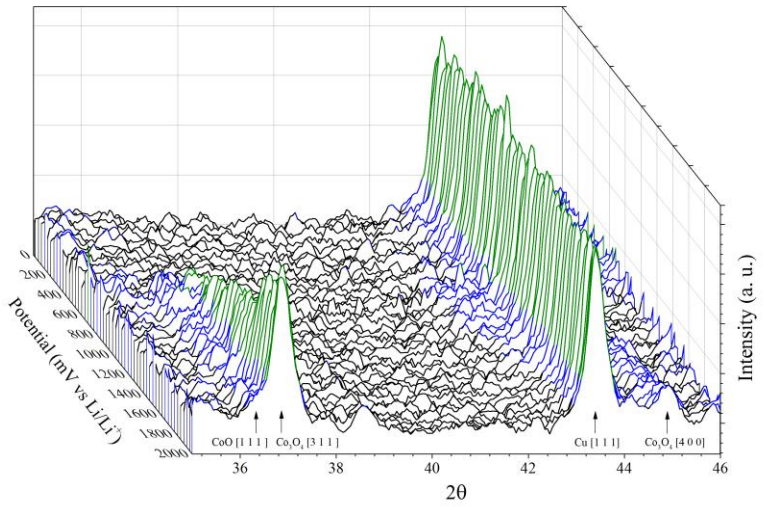

b

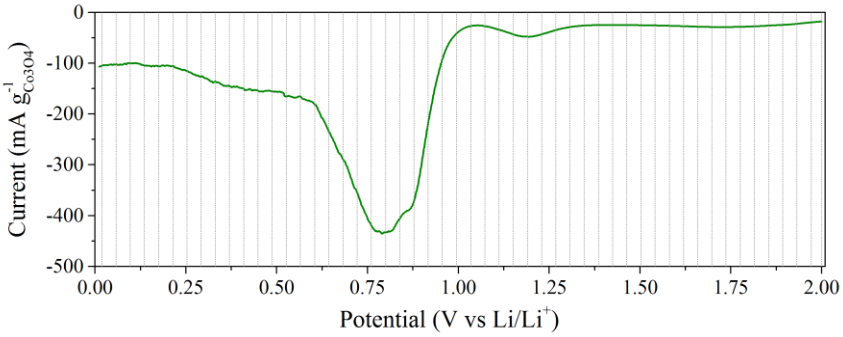

Fig. S.4.6a,b. (a) *in-situ* XRD pattern collected for the charge (*via* linear voltammetry) of an electrode composed of 80/10/10 nanopowder Co_3O_4 (Sigma, less than 50 nm), CMC_{90kDa} and Super-P Li in a modified 2032 coin cell. The test was conducted using Phillips X'PERT scanning 35-46 degrees 2θ with 2.5 second dwell on 0.05 degree 2θ step size. (b) The linear voltammetry was conducted at 0.05 mV/s from 2.0 to 0.01 V and the start of each XRD scan is indicated by dotted lines. Similar testing done on the *meso*-porous electrodes were inconclusive, owing to very weak crystalline signal from the active material.

Table S4.2a Capacities and capacity retention for 1*C* rate test of Li-ion half cells through 500 cycles

Electrolyte	C/20	1C, 500th cycle	Max. 1C capacity	% retention of *C*/20 capacity, 1C 500th cycle	% retention of max 1C	1st cycle CE	average CE at 1C
EC:DEC*	816	925	843	113%	110%	65.8	99.3
5% FEC in EC:DEC	736	673	800	91%	84%	67.7	99.1
FEC:DEC	807	685	748	85%	92%	64.3	99.6
5% Cl-EC in ClEC:DEC	808	752	845	93%	89%	62.9	99.3
	762	n/a	730	n/a	n/a	50.0	n/a

* irregular, repeated abrupt increases in cell resistance resulted in unstable cycling performance

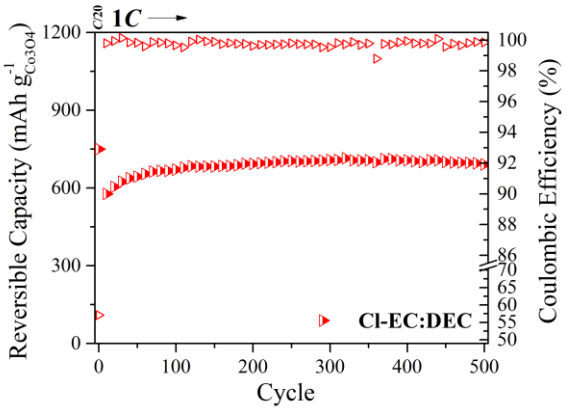

Fig. S.4.7. Cycling test at 1*C* rate for 500 cycles following *C*/20 conditioning cycle in half cell of *meso*-porous Co_3O_4 based electrodes *vs* Li-foil with 1M $LiPF_6$ in Cl-EC:DEC electrolyte formulation. The mass loading of the cell is reduced (0.45 mg cm^{-2}) compared to the typical electrode tested in this study.

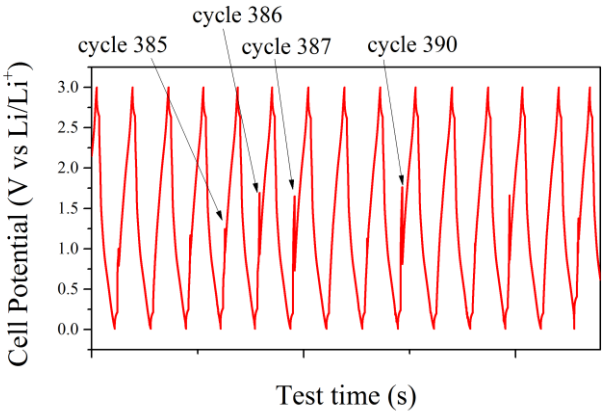

Fig. S.4.8a. Voltage profile showing voltage spikes for cell tested in 1M $LiPF_6$ in EC:DEC for 500 cycle test at 1*C* rate.

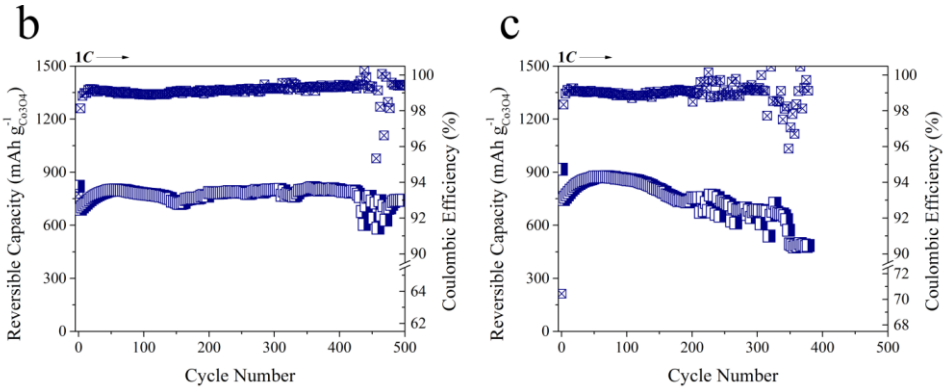

Fig. S.4.8b,c. Erratic cycling behaviour exhibited by *meso*-porous electrodes tested in 1M $LiPF_6$ in EC:DEC electrolyte during 1*C* test for 500 cycles indicating dendritic formations.

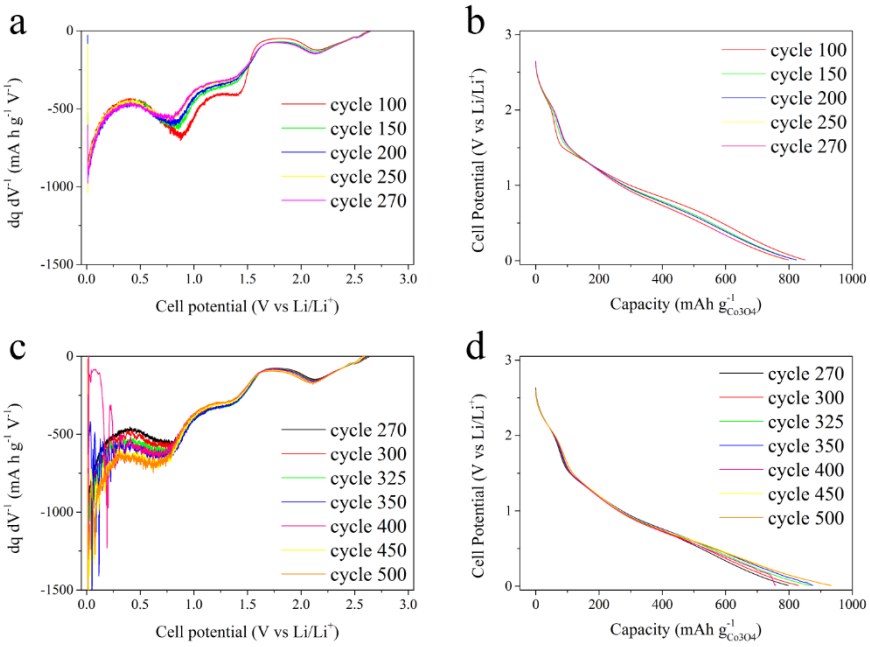

Fig. S.4.9. Electrochemical data for the electrode tested in the 1M $LiPF_6$ in EC:DEC electrolyte for 500 cycles at 1*C* rate. (a), (c) differential capacity profiles and (b), (d) corresponding voltage profiles for the lithiation half-cycle grouped according to before and after the *ca*. 270th cycle, after which unusual cycling behaviour was observed (e.g. increasing capacity, unstable capacities and coulombic efficiencies).

Table S4.3a. Capacities for *C*-rate test of Li-ion half cells through 800 cycles at variable rates

	(capacity in mAh/g at end of rate test series)							
Electrolyte	C/20	C/10	1C	5C	5C (319^{th} cycle)	10C (519^{th} cycle)	5C (719^{th} cycles)	1C (800^{th} cycle)
EC:DEC	793	806	744	454	255	117	229	839
5% FEC in EC:DEC	817	861	820	631	558	209	492	941
FEC:DEC	703	721	636	490	435	153	367	634
5% Cl-EC in	790	818	745	454	418	165	286	518
ClEC:DEC	867	896	762	264	107	65	84	365

Table S4.3b. Capacity retention as percent of C/20 conditioning cycle for for *C*-rate test of Li-ion half cells through 800 cycles at variable rates

	(capacity in mAh/g at end of rate test series)							
Electrolyte	C/20	C/10	1C	5C	5C (319^{th} cycle)	10C (519^{th} cycle)	5C (719^{th} cycles)	1C (800^{th} cycle)
EC:DEC	100%	102%	94%	57%	32%	15%	29%	106%
5% FEC in EC:DEC	100%	105%	100	77%	68%	26%	60%	115%
FEC:DEC	100%	103%	90%	70%	62%	22%	52%	90%
5% Cl-EC in	100%	104%	94%	57%	53%	21%	36%	66%
ClEC:DEC	100%	103%	88%	30%	12%	7%	10%	42%

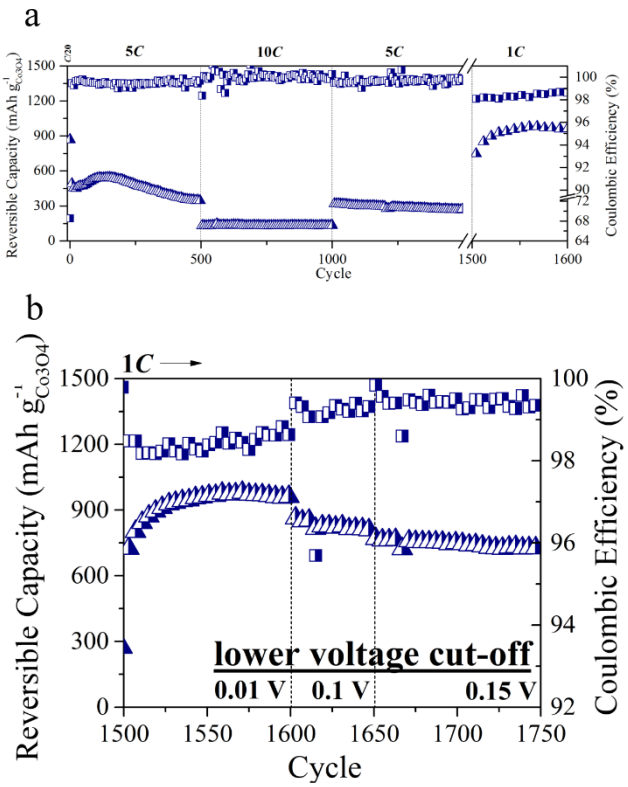

Fig. S.4.10. Cycling test of 80% meso-porous Co_3O_4 (1.0 mg/cm^2 loading) / 10% Super-P Li / 10% CMC_{90kDa} electrode in 1M $LiPF_6$ in 5% FEC in EC:DEC electrolyte. (a) Variable high rate test at 5*C*, 10*C* and 5*C* for 500 cycles each followed by 1*C*. (b) Cycling at 1*C* rate to different lower voltage cut-offs.

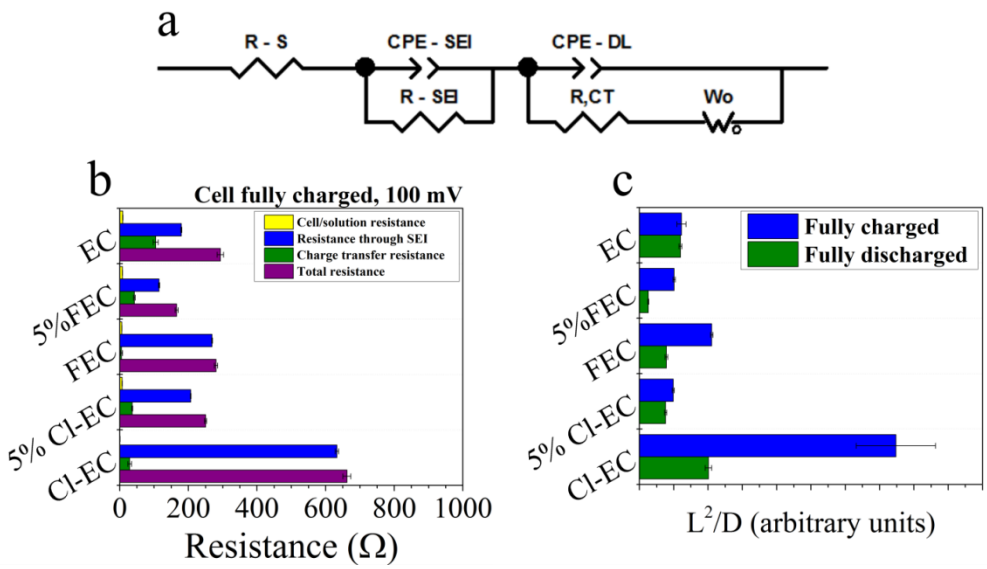

Fig. S.4.11. (a) Equivalent circuit used to model AC impedance spectra. (b) Bar graph indicating contribution to resistance from each circuit resistor when cell is at state of full charge. (c) Bar graph indicating the magnitude of the diffusion term extracted from the Warburg impedance element for the electrode in its fully charged and discharged states.

Table S4.4. AC impedance values given as percent of the resistance through each element of the spectra obtained for the electrode tested in the EC:DEC electrolyte

Electrolyte	R_{SEI}, 100 mV	R_{ct}, 100 mV	L^2/D, 100 mV	L^2/D, discharged
5% FEC in EC:DEC	64%	41%	83%	22%
FEC:DEC	150%	5%	172%	66%
5% Cl-EC in EC:DEC	115%	35%	81%	64%
Cl-EC:DEC	353%	28%	609%	168%

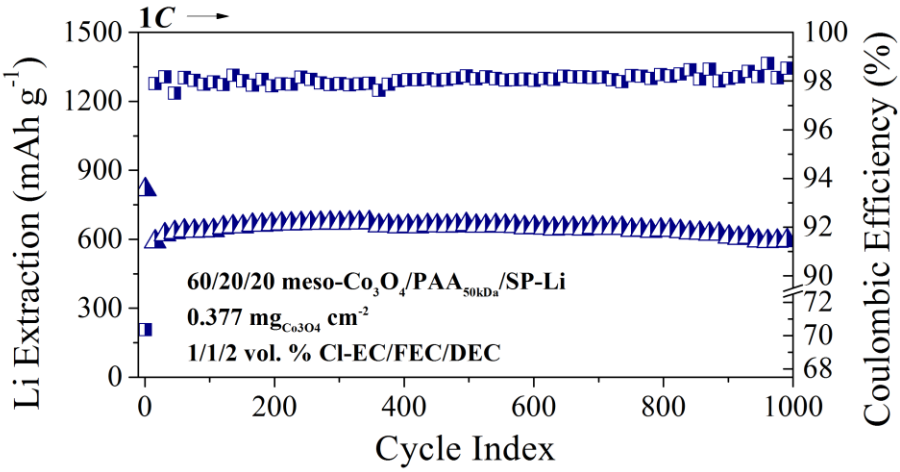

Fig. S.4.12. Cycling performance of lithium ion electrode tested through 1000 cycles at 1C in hybrid electrolyte of 1/1/2 volume percent Cl-EC/FEC/DEC. Electrode composition was 60 % meso-porous Co_3O_4, 20% Super-P Li and 20% PAA_{50kDa}.

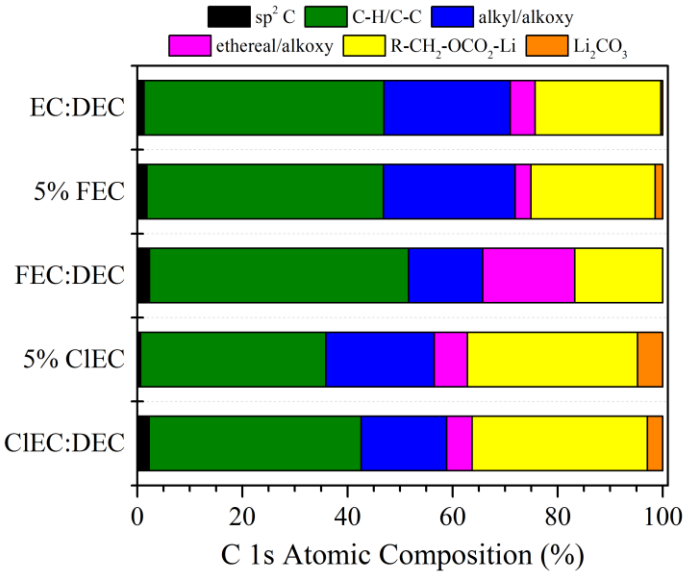

Fig. S.4.13. Species composition in the C 1s region for each of the SEIs derived from Li-ion half-cell testing with the 5 electrolytes evaluated.

Table S4.5. AC Impedance Table (Resistances for Na-ion cells) for electrodes at state of full charge in cycle 10 (*C*/20 rate testing)

Electrolyte	R_{SEI}, 100 mV (Ω)	R_{ct}, 100 mV (Ω)
5% FEC in EC:DEC	7241 ± 132	3055 ± 208
FEC:DEC	1367 ± 33	1510 ± 86

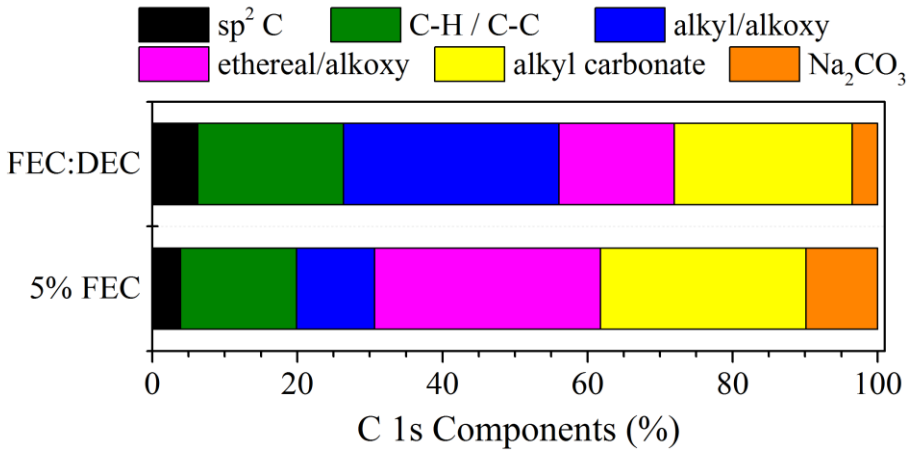

Fig. S.4.14. Species composition in the C 1s region for each of the SEIs derived from Na-ion half cell testing with the 2 electrolytes evaluated.

Discussion of differential capacity profiles

*Li-ion cells.*Differential capacity profiles illustrate the phase transitions and thereby indicate the mechanism by which the active material charges with and discharges lithium (or sodium). The peaks typically represent phase transitions or other reactions; depending on the kinetics of the reaction or phase transition, the potential of these peaks will occur at some overpotential beyond the theoretical energy of formation. The primary practical value of these profiles for this study is in their identification the majority of the discharge occurring at high potentials (average near 2 V) vs the Li/Li^+ redox couple. By inspection of a capacity vs. cycle number plot, the electrode performance appears stable and has the advantages of relatively good retention of capacity at high rates. However, this capacity is discharged at relatively high potentials, meaning that the energy quality is low. As a consequence, there is limited application of this active material; for example, we believe that it is unlikely that cobalt oxide would be attractive for use in electric vehicles or power tools, because both technologies require high voltage batteries.

In the first cycle differential capacity profile, there are 5 observed features during charge, the first of which (between 1.7 – 2.0 V) represents part of the charge which is irreversibly lost to SEI formation (labeled I in Fig. S.4.12a ESI†). For the electrolytes containing Cl-EC, the SEI formation begins above 2 V and appears to further develop in a second reaction near 1.3 V while for the electrolytes containing FEC the SEI formation begins nearer 1.7 V. Initial SEI formation from the EC:DEC electrolyte also appeared to begin near 1.7 V. The charging of the Co_3O_4 is observed to occur at near 1.2 V (labeled II in Fig. S.4.12a ESI†), this voltage being previously reported as the potential at which the mixed valence cobalt oxide forms Li_2O and CoO ($Li_xCo_3O_4$ has been reported, but only for very slow charge rates).[13] The magnitude of this feature is difficult to determine because it

appears to be convoluted (particularly in the case of the electrodes tested with an electrolyte containing Cl-EC) with an irreversible feature that possibly signifies a second phase of development of the SEI simultaneously as the Co_3O_4 matrix is distorted and its volume marginally increases.

At near 1.1 V, a two phase reaction occurs (labeled III in Fig. S.4.12a ESI†); the corresponding chemistry may follow the traditionally accepted reaction pathway in which CoO is further reduced to Co metal in a matrix of lithia, but the accumulated charge after this feature (at 0.9 V) is only around 650-700 mAh/g, not nearly the theoretical capacity. Although more difficult to isolate, there is another feature (labeled IV in Fig. S.4.12a ESI†) which would likely be ascribed to the reaction of lithium and the active material at near 0.7 V before a final and large feature (labeled V in Fig. S.4.12a ESI†) appears, beginning at near 0.5 V. This large feature, V, represents almost exactly 1/3 of the entire capacity charged during this initial conditioning cycle. Feature V might represent the potential at which the bulk of the irreversible reactions occur (the irreversible capacities for the electrodes are near 500 mAh/g), the charging of the polymer gel often cited as a reason for why some cobalt oxide electrodes have higher than expected capacities[14], the continuation of the lithiation of the active material or some combination of these.

Upon consideration of the contribution of this same feature to the charge capacity in subsequent cycling, we believe that feature V in the conditioning cycle marks the potential at which approximately half of the irreversible losses occur. This is estimated by evaluating the difference in capacities of (a) the extent of the contribution of feature V to the reversible capacity in cycle 100 (between 140-200 mAh/g or near 20% of the reversible capacity) and (b) the capacity of feature V in the conditioning cycle (between 350-425 mAh/g or nearly

33% of the reversible capacity). A small portion of the reversible storage of lithium accomplished in this low potential results is weakly held and readily discharges, signified by the linear portion of the discharge profile commencing at 70 mV and continuing up through about 1.0 V. At near 1.5 V, a slight feature is observed, perhaps corresponding to the phase transition during charge denoted as feature IV. Then, at near 2.0 V the majority of the discharge occurs; feature VIII, assigned to represent the delithiation of the lithia and the reformation of a mixture of CoO and Co_3O_4 (as observed by SAED), estimated to begin at about 1.75 V, accounts for about 55% of the reversible capacity in each electrode/electrolyte combination. As a practical consequence of the majority of the discharge chemistry occurring at these relatively high potentials, the quality of energy delivered by a hypothetical future battery implementing a cobalt-oxide based anode would necessarily be low.

In the 1C testing done after the conditioning cycle, the differential capacity profile indicates the existence of a multi-step mechanism beyond the commonly accepted direct transition between a charged phase of lithia surrounding cobalt metal nanoparticles and a mixture of cobalt oxides in the discharged state. There is a small charge accomplished at a high potential of near 2.2 V before two features in sequence are observed at 1.4 V and 0.85 V. Similar to the profile from the conditioning charge, an incomplete feature begins at a low potential (shifted slightly, attributable to greater overpotential required for charging at the faster rate of 1 C). Because this feature does not present as a peak, even at low charge rates for which kinetics should not prevent the full lithiation of the material, we believe this feature does not represent a phase transition but, instead, an accumulation of charge possibly in the polymer as has been suggested previously.[14] However, it is difficult to

accurately interpret these differential capacity profiles, particularly with an incomplete understanding of the nature of phase transitions occurring at the lower potentials of charge. *In-situ* XRD has been employed by Larcher et al.[13] but this technique only allows for analysis of the initial charging of Co_3O_4. SAED analysis has indicated the formation of Co nanoparticles[15,16] but this technique is inherently limited due to the small length scale of characterization. A technique such as Raman, capable of assessing the bonding of elements so as to clarify the extent of the degradation of the original mixed valence cobalt oxide structure, may help clarify the condition of the electrode at higher states of charge.

By the 500th cycle of 1 C testing, a difference is observed in the shapes of the differential capacity profiles (Fig. S.4.13 ESI†), with a greater proportion of the discharge occurring in the discharge feature at near 1.5 V *vs* at 2.2 V (except, interestingly, in the case of the electrode cycled in 5% FEC in EC:DEC). The loss in capacity for the electrodes not forming dendrites (the electrode cycled in EC:DEC showed signs of dendritic growths in several cycles after about cycle 300) may be attributed to the attenuation of this feature, originally representing the potential at which most of the de-lithiation occurred.

When comparing the differential capacity profiles at variable *C*-rates (Fig. S.4.14 ESI†), the effect of internal cell resistance becomes apparent, as the features in the profile are decreased, although not significantly shifted. For example, the increase in rate from 2 *C* to 5 *C* (cycle 69 vs cycle 89) results in an approximate increase of 100 mV in overpotential required to reach the two dominate features in charging. In the case of a silicon electrode, this increase in rate would more significantly shift the potentials at which the charge chemistry occurred, resulting in lower capacity as a consequence of the poor kinetics associated with the charge reaction.[17] Here, this shift is not seen, although the lower

capacity is evident, particularly for the electrodes tested in electrolyte formulations besides 5% FEC in EC:DEC. From this, we believe that the reason for lower capacity is linked to increased cell resistance attributable to issues arising from ion transport during charge transfer and transport across the electrode/electrolyte interface. As this interface thickness increases, the attenuation of the charge and discharge features similarly increases (differential profile for cycle 700 at 5 *C* in Fig. S.4.14 ESI†). However, when the rate is lowered (to 1 *C*, Fig. S.4.14 ESI†), the SEI and/or charge transfer steps are no longer limiting and full capacity is achieved in the case of the electrodes tested in 5% FEC in EC:DEC, FEC:DEC and EC:DEC.

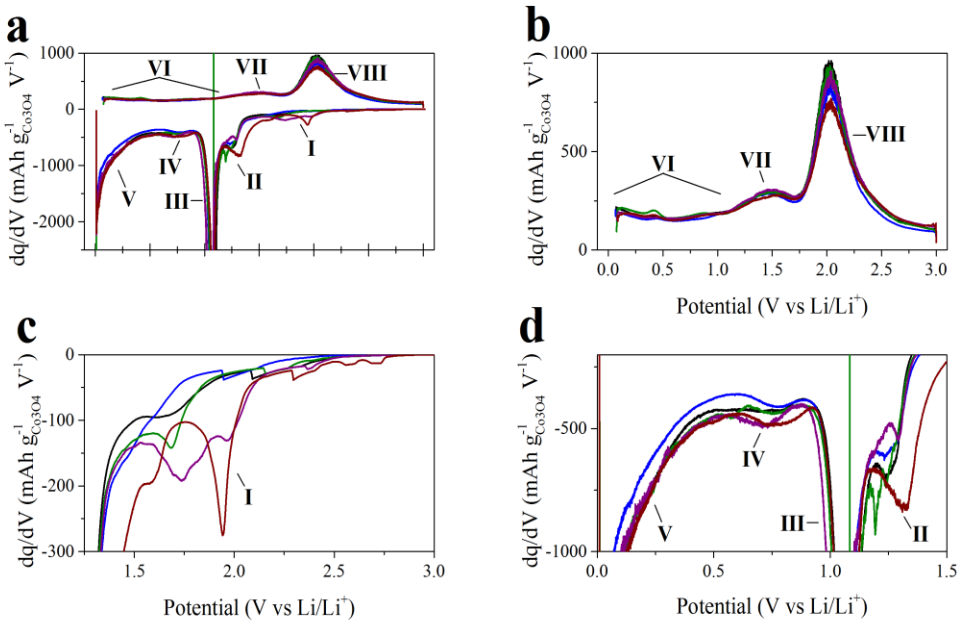

Fig. S.4.15. (a) Differential capacity profile for Li-ion half cells for conditioning cycle (carried out at *C*/20) rate before 500 cycle test at 1*C* rate. (b) Focus on the discharge side

of the profile with (c) and (d) indicating in detail the charge profile. Black line corresponds to EC:DEC electrolyte formulation, blue line to 5% FEC in EC:DEC, green line to FEC:DEC, purple line to 5% Cl-EC in EC:DEC and red line to Cl-EC:DEC.

Table S4.6a. Significant values for differential capacity profiles of the conditioning cycle for Li-ion half cells.

cycle 1	full charge capacity	full discharge capacity	irreversible losses	% capacity after 550 mV, charge	% discharge capacity after 1.75 V
EC:DEC	1205	816	389	34%	56%
5% FEC	1087	736	351	32%	55%
FEC	1255	807	448	32%	56%
5% ClEC	1285	808	477	32%	57%
ClEC	1313	750	563	32%	55%

Table S4.6b. Significant values for differential capacity profiles of the 100th cycle (at 1*C* rate) for Li-ion half cells following the conditioning cycle described in S Table 6a.

cycle 100	full charge capacity	full discharge capacity	irreversible losses	% capacity after 350 mV, charge
EC:DEC	851	840	11	23%
5% FEC	787	777	10	24%
FEC	743	740	3	19%
5% ClEC	845	836	9	23%
ClEC	673	670	3	21%

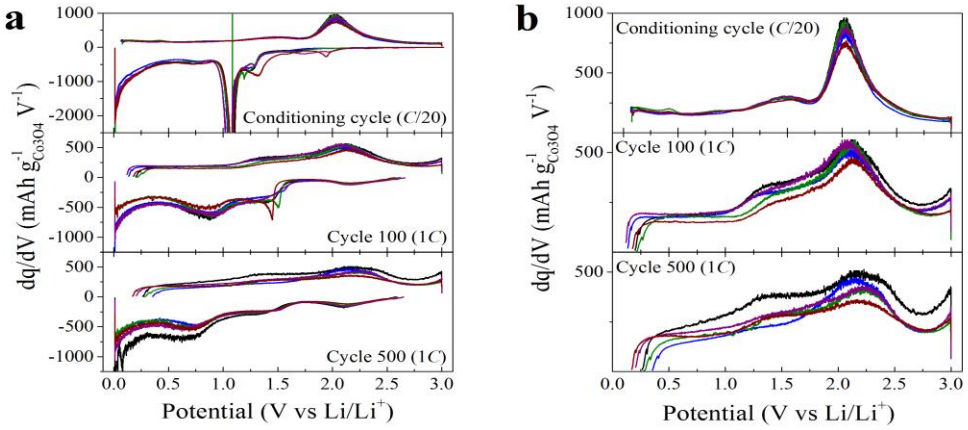

Fig. S.4.16. (a) Differential capacity profiles at cycles 0 (conditioning cycle), 100 and 500 for Li-ion half cells tested at 1*C* rate after *C*/20 conditioning cycle. (b) Profile only of discharge for cycles shown in (a). Black line corresponds to EC:DEC electrolyte formulation, blue line to 5% FEC in EC:DEC, green line to FEC:DEC, purple line to 5% Cl-EC in EC:DEC and red line to Cl-EC:DEC.

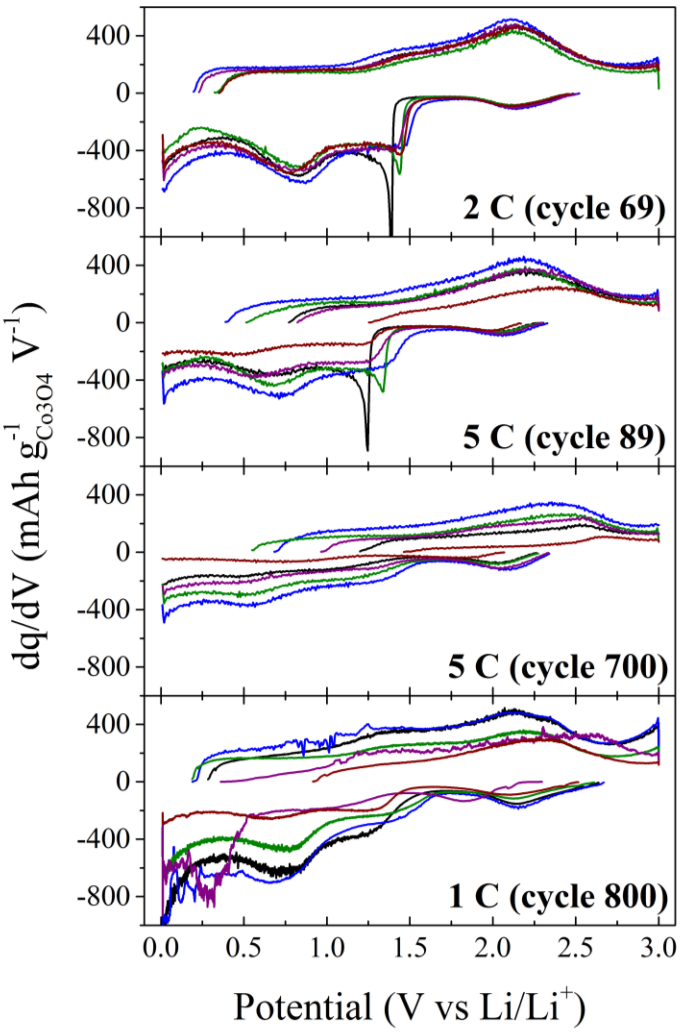
400
0
-400
-800
2 C (cycle 69)
5 C (cycle 89)
5 C (cycle 700)
1 C (cycle 800)
0.0
0.5
1.0
1.5
2.0
2.5
3.0
dq/dV (mAh g$^{-1}_{Co3O4}$ V^{-1})
Potential (V vs Li/Li^{+})

Fig. S.4.17. Differential capacity profiles at selected cycles during extended *C*-rate test. Black line corresponds to EC:DEC electrolyte formulation, blue line to 5% FEC in EC:DEC, green line to FEC:DEC, purple line to 5% Cl-EC in EC:DEC and red line to Cl-EC:DEC.

Na-ion cells. Partly as a consequence of the potential difference between the Li/Li^+ and Na/Na^+ redox couples (-3.04 V vs -2.714 V, respectively) and the free energy of formation of Li_2O and Na_2O, the charging and discharging of the Na-ion meso-porous Co_3O_4 half-cell proceeds at lower potentials than for the analogous reaction with Li: for the more stably performing electrode tested in FEC:DEC, the average potential of charge (cycle 100, 0.5 *C* rate) is 550 mV and the average potential of discharge is 1.58 V. By comparison, after 100 cycles at 1 *C* rate in FEC:DEC electrolyte in the lithium-ion cell, the average potentials of charge/discharge are 900 mV/1.76 V. Like with the lithium-ion cell, there are two dominant features in the (post conditioning cycle) differential charge profile for the Na-ion cell (Fig. S.4.15 ESI†) followed by an incomplete feature which might be attributable to charge storage in the polymer gel layer at low potentials. The multiple (three discernable) discharge features likewise coincide with what was observed for the lithium-ion cells. However, in the Na-ion cell, there is no high voltage feature such as what is found near 2.2 V (charge) for the lithium ion cell (Fig. S.4.14 ESI†).

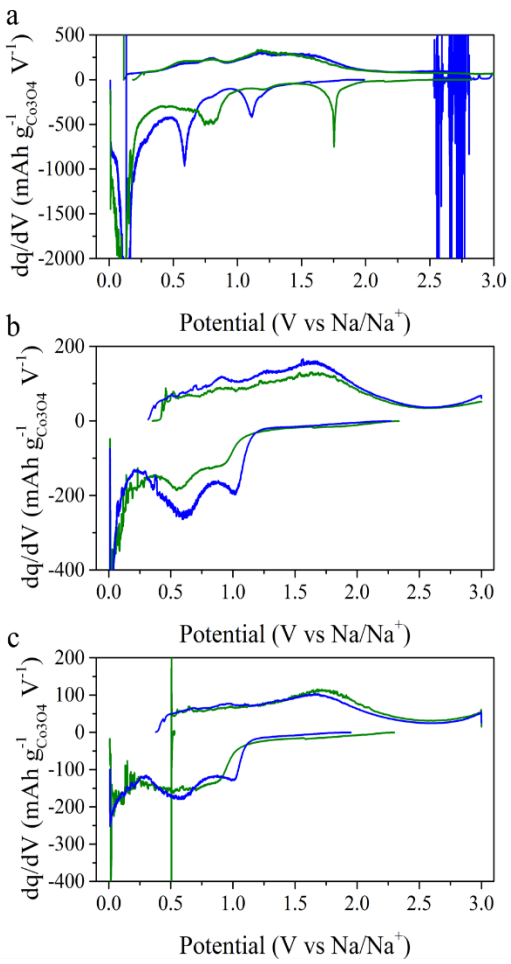

Fig. S.4.18. Differential capacity profiles at selected cycles during 250 cycle 0.5*C* test for Na-ion cells. Blue line corresponds to 5% FEC in EC:DEC electrolyte formulation, green line to FEC:DEC. (a) conditioning cycle at 0.025 *C*, (b) cycle 100 at 0.5 *C* and (c) cycle 200 at 0.5 *C*.

References for ESI

1. S. Malmgren, K. Ciosek, M. Hahlin, T. Gustafsson, M. Gorgoi, H. Rensmo and K. Edström, *Electrochimica Acta*, 2013, 97, 23-32.
2. V. Etacheri, O. Haik, Y. Goffer, G. A. Roberts, I. C. Stefan, R. Fasching and D. Aurbach, *Langmuir*, 2011, 28, 965-976.
3. A. M. Andersson and K. Edström, *Journal of The Electrochemical Society*, 2001, 148, A1100-A1109.
4. S. Chattopadhyay, A. L. Lipson, H. J. Karmel, J. D. Emery, T. T. Fister, P. A. Fenter, M. C. Hersam and M. J. Bedzyk, *Chemistry of Materials*, 2012, 24, 3038-3043.
5. K. Tasaki, A. Goldberg, J.-J. Lian, M. Walker, A. Timmons and S. J. Harris, *Journal of The Electrochemical Society*, 2009, 156, A1019-A1027.
6. S. Komaba, W. Murata, T. Ishikawa, N. Yabuuchi, T. Ozeki, T. Nakayama, A. Ogata, K. Gotoh and K. Fujiwara, *Advanced Functional Materials*, 2011, 21, 3859-3867.
7. W. E. Morgan, J. R. Van Wazer and W. J. Stec, *Journal of the American Chemical Society*, 1973, 95, 751-755.
8. X. L. Zhou, F. Solymosi, P. M. Blass, K. C. Cannon and J. M. White, *Surface Science*, 1989, 219, 294-316.
9. A. Mekki, D. Holland, C. F. McConville and M. Salim, *Journal of Non-Crystalline Solids*, 1996, 208, 267-276.
10. S. H. and M. Soma, *J. Chem. Soc. Faraday Trans.*, 1985, 81, 485.
11. W. C.D., *Discuss. Faraday Soc.*, 1975, 60, 291.

12. W. Liu, H. Li, J.-Y. Xie and Z.-W. Fu, *ACS Applied Materials & Interfaces*, 2014, 6, 2209-2212.

13. D. Larcher, G. Sudant, J.-B. Leriche, Y. Chabre and J.-M. Tarascon, *Journal of The Electrochemical Society*, 2002, 149, A234-A241.

14. S. Laruelle, S. Grugeon, P. Poizot, M. Dolle, L. Dupont and J. M. Tarascon, *J. Electrochem. Soc.*, 2002, 149, A627-A634.

15. K. M. Shaju, F. Jiao, A. Debart and P. G. Bruce, *Physical Chemistry Chemical Physics*, 2007, 9, 1837-1842.

16. Y.-M. Kang, M.-S. Song, J.-H. Kim, H.-S. Kim, M.-S. Park, J.-Y. Lee, H. K. Liu and S. X. Dou, *Electrochimica Acta*, 2005, 50, 3667-3673.

17. A. M. Chockla, T. D. Bogart, C. M. Hessel, K. C. Klavetter, C. B. Mullins and B. A. Korgel, *The Journal of Physical Chemistry C*, 2012, 116, 18079-18086.

Chapter 5: High tap density microparticles of selenium-doped germanium as a high efficiency, stable cycling lithium-ion battery anode material[4]

INTRODUCTION

The development of Li-ion cells with higher energy densities may be achieved using alloy-type anode materials[1] rather than graphite in the negative electrode. Prominent amongst graphite alternatives are Si-based alloys. These have been studied in academia[2,3,4,5,6,7,8] and developed commercially[9,10] due to the material's abundance, low voltage and the high volumetric capacity of lithiated Si, 2213 Ah/L for $Li_{15}Si_4$.[9] Ge-based alloys are similar low-voltage and high volumetric capacity materials (2158 Ah/L for $Li_{15}Ge_4$)[9] and have been studied owing to faster bulk Li diffusion and higher electrical conductivity *vs* Si.[11,12]

To be commercially relevant, it is necessary although not sufficient that such negative electrode materials are cast into films with high volumetric energy density and cycle stably without limiting the lower potential experienced by the anode.[9, 13] To achieve these results, the negative electrode active material should be a particle capable of withstanding massive strain, with high tap density and low specific surface area so as to minimize irreversible losses of lithium on the first as well as subsequent cycles.

Here we report that slurry cast films comprising μm-sized particles of Ge cycle stably and with high efficiency when Se-doped to $Ge_{0.9}Se_{0.1}$. This sub-stoichiometric alloy is the optimized

[4] The content in this chapter has been copied (with minor edits) from its original publication in the *Journal of Materials Chemistry A* in 2015.

result of a previously reported combinatorial study of $Ge_{1-x}Se_x$ thin film negative electrodes.[14] In that combinatorial study, $Ge_{0.9}Se_{0.1}$ was observed to rapidly and stably lithiate/delithiate and with high efficiency to full depth of discharge at 50*C* for 1000 cycles. The cycling result was attributed to the Se-reduction products forming an inactive phase that buffered the volumetric expansion of the Ge active phase and provided for an order of magnitude faster Li diffusion *vs* in control films of pure Ge.

In this report, we compare the performance of μm-sized particles of $Ge_{0.9}Se_{0.1}$ and pure Ge formed by quenching the respective melts and then jet milling, a milling method suited for contamination-free and rapid, commercial-scale production of Li-ion battery particles.[15] Fitting with studies indicating that nanostructuring is required to alleviate the massive strain associated with Li (de)alloying,[16,17,18,19,20] the control, pure Ge particle is shown to fracture upon cycling, resulting in film delamination, severe capacity fade and low efficiency. In contrast, the Se-doped Ge particle provides for stable, high efficiency performance through hundreds of cycles. This result coincides with what was found for the thin film format of $Ge_{0.9}Se_{0.1}$ and we similarly attribute the improved electrochemical behaviour to the formation in the $Ge_{0.9}Se_{0.1}$ particle of a highly Li-permeable amorphous Li-Se-Ge inactive phase that effectively buffers the Li (de)alloying in the particle's Ge active phase.

This success using the active/inactive phase design is consistent with the principles recommended in [1] and the performance reported for several Si-based μm-sized particles.[4,9,21,22] For Ge-based materials, good performance has been reported for porous, μm-sized particles composed of nm-sized Ge in oxide[23] or carbon[24] matrices but μm-sized Ge-based particle alloys have received less attention: recently, in [25] high rate performance was observed for an active/active phase Ge/Sn composite made by a high-throughput melt-spinning process.

RESULTS AND DISCUSSION

The μm-sized $Ge_{0.9}Se_{0.1}$ particles of this study were formed as follows: a 9:1 atomic ratio Ge and Se mixture was melted in an evacuated quartz ampoule placed in a continuously rocked tube furnace, forming a single liquid phase.[26] The liquid phase was rapidly quenched by dropping the hot ampoule in water (for experimental details, see the ESI). The pieces were manually collected and crushed in a mortar. The resulting coarse powder was then jet milled to μm-sized particles. Jet milling was selected because it is a widely used, high-throughput process that can be scaled to commercial production levels,[15] is clean owing to milling done by high velocity particle on particle contact and provides for a narrower particle size distribution than ball milling.[27] The pure μm-sized Ge particles were similarly made.

The pure Ge and $Ge_{0.9}Se_{0.1}$ powders had similar 1.8 g cm^{-3} tap densities and particle sizes (Fig. S5.1†). Powder x-ray diffraction patterns (XRD) of the $Ge_{0.9}Se_{0.1}$ and the pure Ge particles (Fig. S5.2†) showed that they were crystalline, the $Ge_{0.9}Se_{0.1}$ comprised of Ge and GeSe phases. Energy dispersive x-ray spectroscopy (EDS) confirmed the purities of the pure Ge and the $Ge_{0.9}Se_{0.1}$ particles and the homogeneity of distribution of Se in the $Ge_{0.9}Se_{0.1}$ particles. Both quantitative EDS line-scans and qualitative EDS mapping of $Ge_{0.9}Se_{0.1}$ showed that Ge and Se were well mixed (Fig. S5.3†). Neither the pure Ge nor the $Ge_{0.9}Se_{0.1}$ particles were contaminated in the jet milling process (Fig. S5.4†).

The pure Ge or $Ge_{0.9}Se_{0.1}$ loading of the slurry-cast electrodes was ~0.6 mg cm^{-2}. The films comprised 80:10:10 w:w:w pure Ge or $Ge_{0.9}Se_{0.1}$: Super P carbon: carboxymethylcellulose. The

electrodes were tested in 2032 coin cells, where the second electrode was lithium metal foil. As in the cells of Abel et al.[19] the electrolyte was 1M $LiPF_6$ in 1:1 v:v fluoroethylene carbonate and diethyl carbonate.

Galvanostatic charge-discharge cycling was conducted in the 10 mV to 1.5 V range to evaluate deep discharge performance. In the discharge (de-lithiation) branch of the first (conditioning) cycle, the pure Ge electrode was observed to achieve less than theoretical capacity and a 92% coulombic efficiency. The $Ge_{0.9}Se_{0.1}$ electrode reached near theoretical capacity in the discharge branch of the initial conditioning cycle and a coulombic efficiency of 86%, this value expected in light of the formation of a stable SEI and of the reduction of Se. In the differential capacity profile for the initial charge of the $Ge_{0.9}Se_{0.1}$ based electrode (Fig. S5.5†), an irreversible reduction feature at 1.0 V vs Li/Li^+ is observed and attributed to the reduction of Se. Previously in [28] this feature was ascribed to the irreversible formation of Li_2Se, but our measurements (described below) show instead that a glassy Li-Se-Ge containing phase is likely formed. Following the irreversible reduction of Se, the voltage profiles of the $Ge_{0.9}Se_{0.1}$ based electrode coincide with those for the pure Ge based electrodes (Fig. S5.5†), indicating that only Ge is active in the Li (de)alloying during cycling.

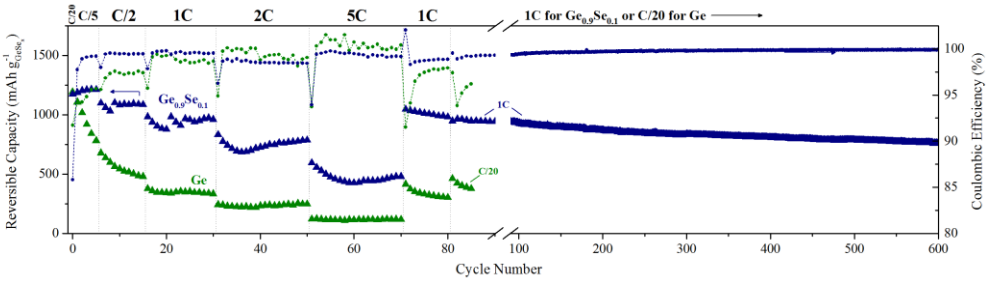

Fig. 5.1 Galvanostatic deep discharge cycling of the micro-sized particles of pure Ge- (green data) or $Ge_{0.9}Se_{0.1}$-based (blue data) electrodes showing performance at variable *C*-rates through 80 cycles following a conditioning cycle at *C*/20. After 80 cycles, the pure Ge-based electrode was tested at *C*/20 for five cycles so as to measure the fraction of electrochemically active material remaining: *c*. 32%. The $Ge_{0.9}Se_{0.1}$-based electrode was tested at 1*C* for 920 additional cycles to assess its long-term stability: the average capacity fade was 0.3 mAh g^{-1} per cycle and the average efficiency was 99.9%.

Fig. 5.1 shows the capacities retained after cycling at various *C*-rates, each data series reproduced with at least four different cells (Fig. S5.6†). Following a conditioning cycle at C/20 rate, the electrodes were cycled five times at *C*/5 rate; the pure Ge electrode lost 35% of its capacity, while the $Ge_{0.9}Se_{0.1}$ electrode gained 3%. When the *C*-rate was increased, the performance of the pure Ge electrode deteriorated while the $Ge_{0.9}Se_{0.1}$ cycled stably. At the conclusion of the 80-cycle variable *C*-rate test of Fig. 1, the pure Ge electrode was re-tested at a slow *C*/20 rate. It retained a capacity of only 378 mAh g^{-1}, 32% of its initial C/20 rate capacity. In contrast, when the $Ge_{0.9}Se_{0.1}$ electrode was returned after the 80 cycle variable *C*-rate test to 1*C* rate, its 1 Ah g^{-1} capacity initially exceeded that measured at a 1*C* rate in cycles 16-30. During the next 920 cycles at 1*C* rate, the capacity of the $Ge_{0.9}Se_{0.1}$ electrode faded at a rate of *c*. 0.3 mAh g^{-1} $cycle^{-1}$, and the electrode an efficiency of 99.7% and increasing to 99.9 % in cycles 400-1000. The cell coulombic inefficiency per hour[29] is plotted in Fig. S5.6†.

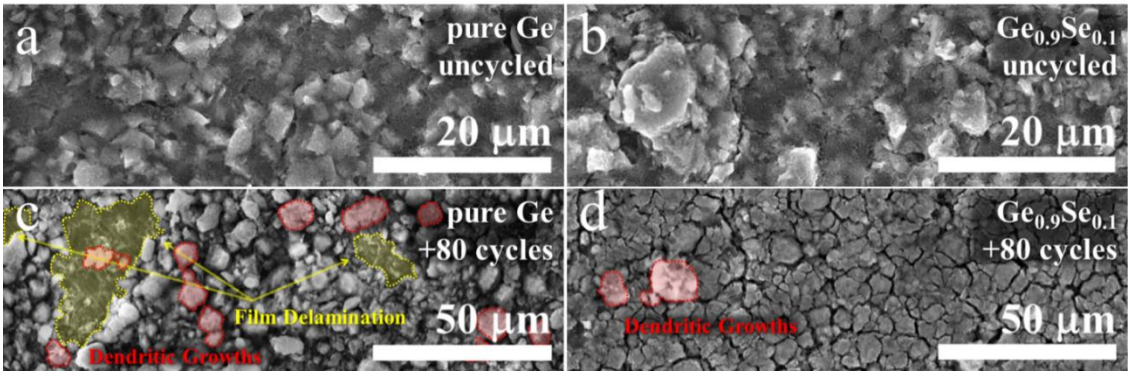

Fig. 5.2 SEM of uncycled (a) pure Ge-based and (b) $Ge_{0.9}Se_{0.1}$-based electrodes. *Ex-situ* SEM after the 80 cycle variable *C*-rate test characterizing the charged (shown in ESI†) and discharged state of the (c) pure Ge-based and (d) $Ge_{0.9}Se_{0.1}$-based electrodes. The yellow dashed line in *c* outlines the regions of unambiguous film delamination. No evidence of delamination was found in observation of the $Ge_{0.9}Se_{0.1}$-based films. The red dashed line in *d* outlines some of the few dendritic growths observed. The red dashed line outlines several of the multitude of dendritic growths observed upon the pure Ge-based electrode *c*.

The scanning electron micrographs (SEM) of the pure Ge and the $Ge_{0.9}Se_{0.1}$ electrodes taken before the 80 cycle variable *C*-rate test (Fig. 5.2a,b) were similar; but after the test, the film of the Ge electrode was observed to be partially delaminated. The delamination was visible to the naked eye. SEM and the EDS of the pure Ge electrode (Fig. 5.2c, Fig. S5.7-10†) showed that the film was covered with Li-dendrites, identified by their shape[30] and by their chemical composition, which was high in O, F, C and P, all elements of the electrolyte. Lithium dendrite growth is not unexpected, considering that less than 1/3rd of the originally electrochemically active pure Ge active material remained; because the current density passing through the remaining pure Ge particles increases, the overpotential increases and metallic, potentially dendritic, lithium is electrodeposited. In contrast, the surface of the $Ge_{0.9}Se_{0.1}$ electrodes remained smooth,

comparatively free of observable dendrites (Fig. 5.2d and Fig. S5.9-10†). A striking change in the cycled $Ge_{0.9}Se_{0.1}$ electrodes was the clustering of conductive additive/binder around their $Ge_{0.9}Se_{0.1}$ particles. Unlike the pure Ge film, the $Ge_{0.9}Se_{0.1}$ film did not delaminate in the 80-cycle variable rate test.

High resolution transmission electron micrographs (HR-TEM) and high angle annular dark field scanning transmission electron micrographs (HAADF-STEM) of ultramicrotome sectioned electrodes (Fig. 5.3a-f and Fig. 5.4a-f) taken after their 80 cycle variable *C*-rate test provided information about the particle interiors as well as their edge regions.

At low magnification, large pieces of the cycled (de-lithiated) pure Ge particle were observed (Fig. 5.3b). The SAED and fast Fourier transform (FFT) of their HR-TEM (Fig. S5.11†) showed domains of polycrystalline Ge. The irregular perimeter of the cycled Ge particles indicated the effects of anisotropic volume change: initially formed with block-like faces, the Ge particles deformed during their cycling, their edges becoming stretched and fractured. Additional evidence of the disruptive effect of repeated strain of the pure Ge particles was found in their interior which was distorted into a material appearing sponge-like with a network of pores of variable size. Nano-scale pores have been reported earlier for cycled Ge nanowires which did not fracture at their smaller size.[31,32,33]

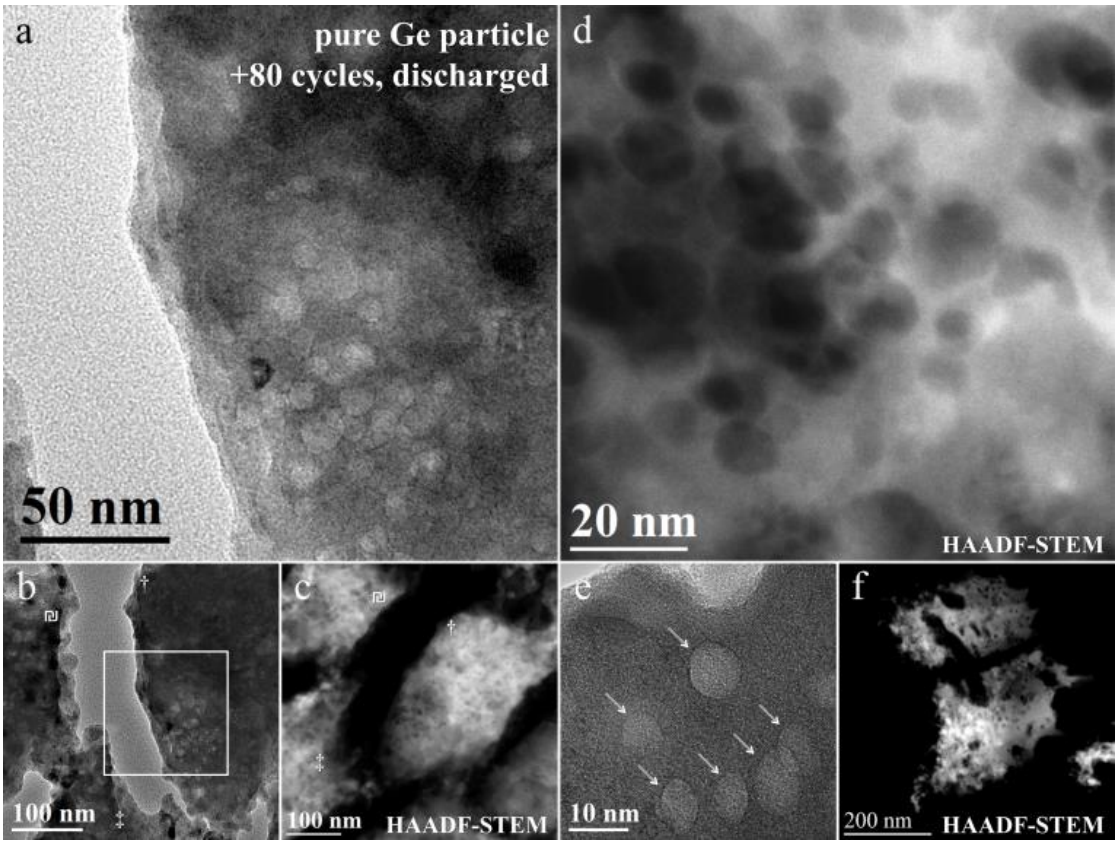

Fig. 5.3 Ultramicrotome-sectioned particles of undoped Ge in the discharged state after 80 cycles of different *C*-rates. (a) TEM showing the spongy, cavity-ridden interior. (b) TEM showing a distorted particle edge from (a). (c) HAADF-STEM of *a* and *b* particles showing the porous interior of particles and their torn edges. (d) HAADF-STEM of *c* at high magnification showing cavities in the interior of a cycled undoped Ge particle. (e) HR-TEM of pores (indicated by arrows) in the interior of an undoped Ge particle with crystalline Ge domains. (f) HAADF-STEM of an undoped Ge particle showing distortion and particle fracture.

Fig. 5.3c,d shows HAADF-STEM images of the same particle imaged with TEM (Fig. 5.3a,b). These HAADF-STEM images along with that of a different particle (Fig. 5.3f) more clearly define the interior structure of the cavities. By recording intensity as a linear function of material thickness (generally constant owing to the ultramicrotome sectioning) and by an

exponential function of the atomic number (~Z^2), the view of carbonaceous clutter near and upon the Ge particle can be suppressed with focus given to the structure of the higher-Z active material. In these HAADF-STEM images and in the several others provided with HR-TEM (Fig. 5.3f and in the ESI† in Fig. S5.12†), the partial cavities located at the surface of the particles appear to be precursors of the disconnected Ge fragments proximal to the particles.

In contrast, HR-TEM of the cycled (de-lithiated) $Ge_{0.9}Se_{0.1}$ particles (Fig. 5.4a-f) show retention of the block-like faces of the initial, jet milled material, and formation of a heterogeneous network of crystalline Ge clusters, surrounded by the Se-containing amorphous phase. Consistent with the stability exhibited in the electrochemical data and the integrity of the cycled film as observed by SEM, the cycled $Ge_{0.9}Se_{0.1}$ particle was observed to remain intact, but comprising a glassy Se-containing phase embedded within a network of Ge nano-crystals. Fig. 5.4e shows crystallite and amorphous regions found in the interior of a representative particle. In the discharged state, the Ge inclusions are nano-crystallites identified with local fast Fourier transform (FFT) analysis based upon reflections corresponding to the relatively intense signal from the Ge (111) and (022) planes (Fig. S5.13†). The thickness of the ultramicrotomed section (*c.* 50 nm) is here an order of magnitude greater than the typical crystallite size. Consequently, the observation of crystallites depends upon the focal plane selected.

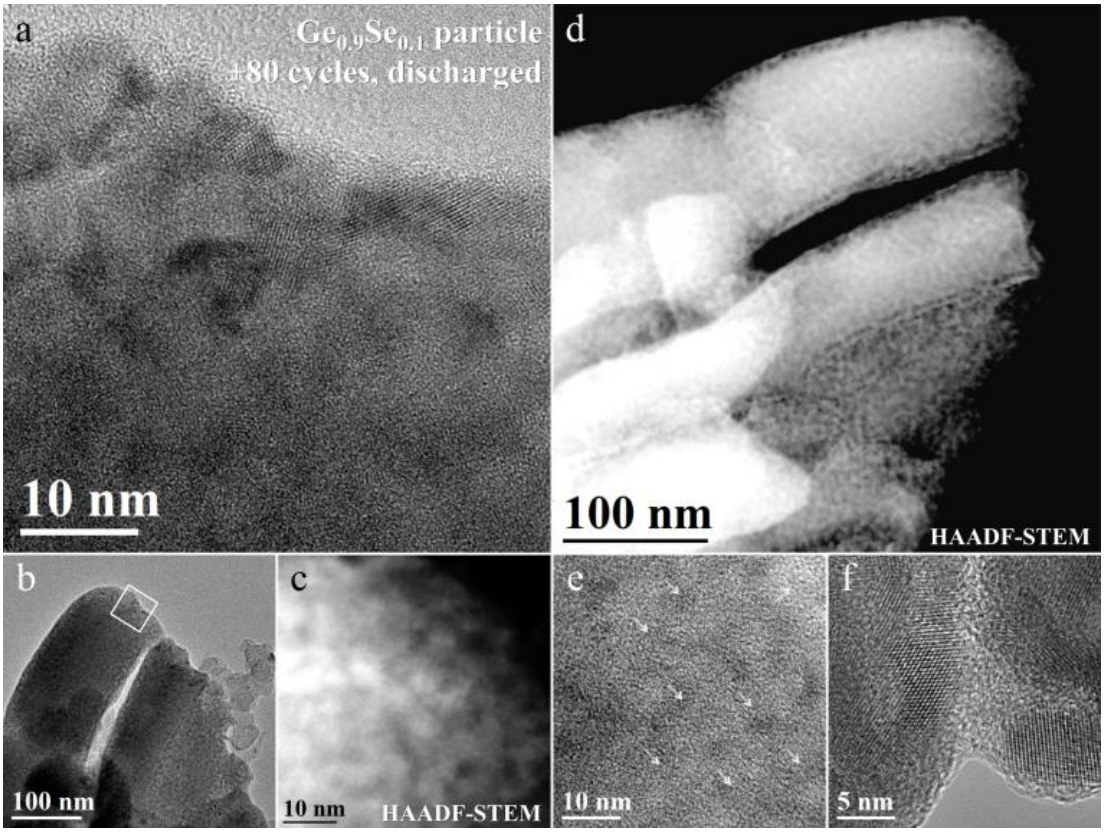

Fig. 5.4 Ultramicrotomed sectioned particles of $Ge_{0.9}Se_{0.1}$ in the discharged state after 80 cycles of different *C*-rates. (a) HR-TEM of a particle edge showing that the cycled $Ge_{0.9}Se_{0.1}$ is a continuous material with nano-scale Ge crystallites enveloped by an amorphous phase. (b) Lower magnification TEM with white box indicating region shown in *a.* (c) HAADF-STEM showing two phases: densely packed Ge crystallites enveloped by an amorphous phase. (d) HAADF-STEM of the *a*, *b* and *c* particle. (e) HR-TEM of the interior of a $Ge_{0.9}Se_{0.1}$ particle. The white arrows point to Ge crystallites. (f) HR-TEM showing the crystallites embedded in the amorphous phase.

With selected area electron diffraction (SAED), all crystal structures within entire $Ge_{0.9}Se_{0.1}$ particle pieces are identified and only Ge reflections were observed (Fig. S5.14†). For the initial charging of the $Ge_{0.9}Se_{0.1}$, we had anticipated the irreversible formation of Li_2Se (a crystalline material) as had been reported in a recent study on germanium selenide materials.[28] In

the absence of reflections identifying Li_2Se, the reduced product of the Se component of $Ge_{0.9}Se_{0.1}$ was determined to be contained in the amorphous phase, for with EDS mapping we observed that Se was homogeneously distributed within the $Ge_{0.9}Se_{0.1}$ particles (Fig. S5.15†). As Li_2Se is the thermodynamically stable possibility for a combination of only Li and Se, we conclude that irreversible reduction of Se forms a more complex species, including Ge: a glassy Li-Se-Ge phase distributed throughout the network of active Ge inclusions (Ge crystallites in the discharged material, additional images provided in Fig. S5.16†).

We hypothesize that this amorphous phase is a superionically conductive Li-Ge-Se glass[34] studied in the past as a potential solid electrolyte. The rate of bulk-diffusion of lithium has been estimated by electrochemical impedance spectroscopy (EIS) with the low frequency data points fitted to a Warburg impedance element.[35] These impedance data are consistent with a Li-diffusion coefficient in the cycled $Ge_{0.9}Se_{0.1}$ that is magnitudes of order higher than in undoped Ge (Fig. S5.17†).

We are now pursuing a full study of the diffusion coefficient with comprehensive EIS and potentiostatic intermittent titration characterization (PITT) based on the method described by Drozhzhin et. al. [36] Because of the seemingly regular distribution of nanoscale Ge inclusions (shown more clearly in the HAADF-STEM images, Fig. 5.4c-d) and the Se-containing amorphous phase, we are still working to confidently identify the composition of the Se-containing inactive phase using EDS and electron energy loss spectroscopy (EELS). With *in-situ* XRD and Raman characterization of the $Ge_{0.9}Se_{0.1}$ electrode phase transitions during galvanostatic cycling, we intend to more fully describe the genesis and effect of the active/inactive mixed phases.

Conclusions

We report that the inclusion of a sub-stoichiometric ratio of Se in Ge to form a $Ge_{0.9}Se_{0.1}$ alloy enables stable and high efficiency galvanostatic cycling of the material in μm-sized particles tested in a slurry cast electrode.

With HR-TEM, HAADF-STEM and SAED we found that the $Ge_{0.9}Se_{0.1}$ forms a network of Ge inclusions amidst an amorphous Se-containing inactive phase during the course of cycling. We believe this inactive phase is responsible for alleviating strain and enhancing the rate of Li diffusion. While our previous thin film combinatorial study[14] that surveyed various $Ge_{1-x}Se_x$ combinations identified the $Ge_{0.9}Se_{0.1}$ stoichiometry as optimal, we believe that those results may only indicate the general range of stoichiometries for which micro-scale particles of $Ge_{1-x}Se_x$ are stabilized against particle fracture: the stable cycling performance achieved here may manifest with an even lower Se dopant content for micro-scale particles. In contrast, electrodes made from similarly prepared undoped Ge μm-sized particles of the same morphology exhibit rapid capacity fade, low coulombic efficiency, film delamination and accelerated lithium dendrite growth.

REFERENCES

1. M. N. Obrovac, L. Christensen, D. B. Le and J. R. Dahn, Journal of The Electrochemical Society, 2007, 154, A849-A855.

2. M. A. Al-Maghrabi, J. Suzuki, R. J. Sanderson, V. L. Chevrier, R. A. Dunlap and J. R. Dahn, Journal of The Electrochemical Society, 2013, 160, A1587-A1593.

3. M. Gauthier, D. Reyter, D. Mazouzi, P. Moreau, D. Guyomard, B. Lestriez and L. Roué, Journal of Power Sources, 2014, 256, 32-36.

4. S.-O. Kim and A. Manthiram, Journal of Materials Chemistry A, 2014, DOI: 10.1039/c4ta06113f.

5. N. Liu, Z. Lu, J. Zhao, M. T. McDowell, H.-W. Lee, W. Zhao and Y. Cui, Nat Nano, 2014, 9, 187-192.

6. M. N. Obrovac and L. J. Krause, Journal of The Electrochemical Society, 2007, 154, A103-A108.

7. J. Song, S. Chen, M. Zhou, T. Xu, D. Lv, M. L. Gordin, T. Long, M. Melnyk and D. Wang, Journal of Materials Chemistry A, 2014, 2, 1257-1262.

8. M. Wu, J. E. C. Sabisch, X. Song, A. M. Minor, V. S. Battaglia and G. Liu, Nano Letters, 2013, 13, 5397-5402.

9. V. L. Chevrier, L. Liu, D. B. Le, J. Lund, B. Molla, K. Reimer, L. J. Krause, L. D. Jensen, E. Figgemeier and K. W. Eberman, Journal of The Electrochemical Society, 2014, 161, A783-A791.

10. Nexeon, Nexeon Technology Overview, http://www.nexeon.co.uk/technology-2/.

11. J. Graetz, C. C. Ahn, R. Yazami and B. Fultz, Journal of The Electrochemical Society, 2004, 151, A698-A702.

12. C.-Y. Chou and G. S. Hwang, Journal of Power Sources, 2014, 263, 252-258.

13. A. J. Smith, J. C. Burns, S. Trussler and J. R. Dahn, Journal of The Electrochemical Society, 2010, 157, A196-A202.

14. P. R. Abel, K. C. Klavetter, A. Heller and C. B. Mullins, The Journal of Physical Chemistry C, 2014, 118, 17407-17412.

15. Jet Pulverizer Works to Commercialize Emerging Lithium-Ion Battery Technology, http://www.jetpulverizer.com/news-and-events/article01.php, 2009.

16. M. T. McDowell, S. W. Lee, J. T. Harris, B. A. Korgel, C. Wang, W. D. Nix and Y. Cui, Nano Letters, 2013, 13, 758-764.

17. M. T. McDowell, I. Ryu, S. W. Lee, C. Wang, W. D. Nix and Y. Cui, Advanced Materials, 2012, 24, 6034-6041.

18. S.-C. Chao, Y.-F. Song, C.-C. Wang, H.-S. Sheu, H.-C. Wu and N.-L. Wu, The Journal of Physical Chemistry C, 2011, 115, 22040-22047.

19. S.-C. Chao, Y.-C. Yen, Y.-F. Song, Y.-M. Chen, H.-C. Wu and N.-L. Wu, Electrochemistry Communications, 2010, 12, 234-237.

20. W. Liang, H. Yang, F. Fan, Y. Liu, X. H. Liu, J. Y. Huang, T. Zhu and S. Zhang, ACS Nano, 2013, 7, 3427-3433.

21. Z. Du, R. A. Dunlap and M. N. Obrovac, Journal of The Electrochemical Society, 2014, 161, A1698-A1705.

22. X. Zhao, R. A. Dunlap and M. N. Obrovac, Journal of The Electrochemical Society, 2014, 161, A1976-A1980.

23. X.-L. Wang, W.-Q. Han, H. Chen, J. Bai, T. A. Tyson, X.-Q. Yu, X.-J. Wang and X.-Q. Yang, Journal of the American Chemical Society, 2011, 133, 20692-20695.

24. D. T. Ngo, R. S. Kalubarme, H. T. T. Le, J. G. Fisher, C.-N. Park, I.-D. Kim and C.-J. Park, Advanced Functional Materials, 2014, 24, 5291-5298.

25. S. Fan, L. Y. Lim, Y. Y. Tay, S. S. Pramana, X. Rui, M. K. Samani, Q. Yan, B. K. Tay, M. F. Toney and H. H. Hng, Journal of Materials Chemistry A, 2013, 1, 14577-14585.

26. L. Ross and M. Bourgon, Canadian Journal of Chemistry, 1969, 47, 2555-2559.

27. Frequently Asked Questions, http://www.jetpulverizer.com/faq.php#link-7, 2014.

28. H. S. Im, Y. R. Lim, Y. J. Cho, J. Park, E. H. Cha and H. S. Kang, The Journal of Physical Chemistry C, 2014, 118, 21884-21888.

29. D. Y. Wang and J. R. Dahn, Journal of The Electrochemical Society, 2014, 161, A1890-A1897.

30. K. C. Klavetter, S. M. Wood, Y.-M. Lin, J. L. Snider, N. C. Davy, A. M. Chockla, D. K. Romanovicz, B. A. Korgel, J.-W. Lee, A. Heller and C. B. Mullins, Journal of Power Sources, 2013, 238, 123-136.

31. X. H. Liu, S. Huang, S. T. Picraux, J. Li, T. Zhu and J. Y. Huang, Nano Letters, 2011, 11, 3991-3997.

32. T. Kennedy, E. Mullane, H. Geaney, M. Osiak, C. O'Dwyer and K. M. Ryan, Nano Letters, 2014, 14, 716-723.

33. E. Mullane, T. Kennedy, H. Geaney and K. M. Ryan, ACS Applied Materials & Interfaces, 2014, 6, 18800-18807.

34. S. Kikkawa, T. Miyai and M. Koizumi, Solid State Ionics, 1988, 28–30, Part 1, 743-746.

35. Y. H. Rho and K. Kanamura, Journal of Solid State Chemistry, 2004, 177, 2094-2100.

36. O. A. Drozhzhin, M. A. Vorotyntsev, S. R. Maduar, N. R. Khasanova, A. M. Abakumov and E. V. Antipov, Electrochimica Acta, 2013, 89, 262-269.

SUPPLEMENTARY INFORMATION

Materials and Methods

Synthesis of $Ge_{0.9}Se_{0.1}$ and pure Ge. In a typical synthesis of $Ge_{0.9}Se_{0.1}$, 4.46 g Ge (Lesker, 99.999% pure, 3-6 mm pieces) and 0.54 g Se (Lesker, 99.999% pure, 1-3 mm pieces) were set inside quartz ampoule (GM Associates, Inc., 8mm ID, 12 mm OD) previously cleaned (by rinsing with acetone and drying) and sealed at one end. The ampoule was evacuated to 10^{-6} torr and carefully sealed *c*. 12 cm from its end. The ampoule was then heated to 1100°C at 5°C min^{-1} and held at 1100°C for 48 h inside a quartz tube continuously rotated in a tube furnace (Lindberg Blue M, single zone). The continuous rotation was achieved using a home-built rotational tube drive and gently rocked the ampoules, promoting the mixing of Ge and Se as suggested by the study done by Ross and Bourgon.[1] The synthesis temperature of 1100°C was selected so as to form a single liquid phase of $Ge_{0.9}Se_{0.1}$. Rapid quenching was performed by dropping the ampoule into a room temperature water bath. Approximately 10 seconds or less elapsed between when the ampoule was directly in the furnace hot zone and when the ampoule was fully submerged under water. After allowing the ampoule to fully cool, the ampoule was scored and opened: a slight "pop" was heard upon opening which verified that the ampoule was properly sealed and held vacuum during the high temperature mixing synthesis. Note on safety: on one occasion, the ampoule may have been improperly sealed and when it was opened without allowing for its contents to fully cool, the odor of rotted eggs was detected, indicating the presence of the very hazardous H_2Se gas. The synthesis of the pure Ge was performed in a similar way, except that the ampoule contained only Ge pieces, the ampoule was scaled to a longer length to

accommodate 25 g of Ge and the hold time at 1100°C was limited to 12 h because there was no need to mix the ampoule contents.

Production of microsized particles. The contents of the ampoules were carefully removed and then quickly crushed into roughly uniform pieces by pestle and mortar. This material was fed into a jet mill (Glen Mills, Jet-O-Mizer Model 00) operated at 100 psi feed pressure, 80 psi pusher pressure and with N_2 as the feed and pusher gas. The rate of feed was *c.* 0.25-0.5 g min^{-1} and managed using a vibratory feeder fitted with a custom 3D printed part designed to regulate particle flow rate. Greater than 80 percent yield was obtained using a home-built collection apparatus. Because the particle size distribution of jet milled materials is a function of the material properties, the initial size distribution of the material and the feed rate, the material was processed twice. The first run processed feed material of comparatively wide particle size distribution made from coarse crushing with a pestle and mortar. The design of the jet mill only allows product particles of below a certain size to escape the milling chamber and for Ge-type materials this size is *c.* 10 microns at the largest. Thus, for the second run of processing, the feed material was of a relatively narrow size distribution. The total time for processing was about 20-40 minutes per run with about 20 minutes required to carefully retrieve the powder from the home-built collection apparatus.

The advantages of jet milling. Jet milling is a commercially used process already employed for production of lithium-ion battery (LIB) materials. Importantly, jet milling is a process which can be easily scaled from lab processing (several grams per hour) to commercial processing (many tons per hour). Jet milling has several advantages:[5] one, it

allows for contamination-free product as the grinding is done by particle on particle collision. For this reason, high purity materials such as those used in the pharmaceutical, electronics and battery materials industries. Two, the particle size and size distribution can be controlled. In this study, we report on particles of an average size of about 2-3 microns and with SEM (Fig. S1†) we observed, as expected, a low content of fines, small particles which are common in ball milled materials. However, with expertise and custom-tuning of the mill (particularly the feed rate), the particle size can be lowered by up to an order of magnitude and the size distribution can be narrowed. For example, the Jet Pulverizer Company developed a jet mill process in 2009[6] to create high-purity lithium titanate oxide of less than 300 nm average size. Should we find in subsequent studies that solid state diffusion of lithium is the limiting factor in the $Ge_{0.9}Se_{0.1}$ particles tested in this study, then we might anticipate that the electrochemical performance of a 300 nm sized $Ge_{0.9}Se_{0.1}$ particle could be improved by more than a magnitude of order, retaining 80% capacity at 10*C* or more rather than at 1*C* as demonstrated in Fig. 1. Note: Jet milling units such as the one used in this study can be rented on a month-to-month basis rather than purchased outright and are simple enough for undergraduate research assistants to set up and operate.

Particle characterization. (Fig. S5.1-4) Tap density measurements on the $Ge_{0.9}Se_{0.1}$ and the pure Ge powders (after the jet milling process described above) were performed using a Quantachrome AT–4 Autotap machine. Powder XRD measurements were performed using a Rikagu MiniFlex 600 (Fig. S2†). SEM characterization was performed using a Hitachi S5500 SEM/STEM at 30kV and 20 μA on powders dispersed by bath sonication in ethanol and dropped onto lacey carbon TEM grids (SPI Supplies). EDS measurements were performed using the STEM mode on the Hitachi S5500. The particles

of $Ge_{0.9}Se_{0.1}$ and pure Ge were found to be uncontaminated by the quartz ampoule, the jet mill (316 stainless steel) and with negligible oxygen content (Fig. S4†). EDS spectra, line scans and mapping were performed on the $Ge_{0.9}Se_{0.1}$ particles to assess the degree of mixing of the Ge and Se. The EDS line scans for the $Ge_{0.9}Se_{0.1}$ particles are composed of thousands of discrete measurements of elemental composition. These data are plotted in a histogram (Fig. S3†) alongside a representative EDS mapping of several particles. A bimodal distribution was observed with the majority of the material characterized as the desired $Ge_{0.9}Se_{0.1}$ mixture and a minority of the material characterized as a GeSe-like material, slightly rich in Ge, $Ge_{0.6}Se_{0.4}$. Owing to the large dimension of the particles characterized, only several seconds of EDS signal collection were necessary to achieve a stable spectra, helping to minimize the error associated with this measurement technique.

Electrochemical testing by galvanostatic cycling. (Fig. S5.5-6) A typical slurry was composed of 0.8 g active material (pure Ge or $Ge_{0.9}Se_{0.1}$ particles), 0.1 g Super P Li conductive additive (Timcal) and 0.1 g carboxymethyl cellulose (Sigma, 90 kDa, pre-dissolved in water) in water. Mixing was done in two stages: first using an IKA ULTRA-TURRAX tube drive homogenizer and second using a probe sonicator (QSonica microtip, pulses at 20 percent amplitude, 1 s on, 1 s off for 20 min) with the slurry container cooled by a water bath. The slurry was cast on 10 □m thick Cu foil (MTI), allowed to air dry and then dried overnight under vacuum at 100°C. Electrodes were punched with a 7/16 inch diameter and measured to 0.01 mg (Mettler Toledo). In an Ar-filled glovebox (MBRAUN, H_2O and O_2 less than 0.1 ppm), 2032 coin cells were constructed using Celgard 2400 membrane separators, 0.75 mm thick Li foil (Alfa) and 1M $LiPF_6$ (BASF) in 1:1 (volume ratio) FEC (Solvay):DEC (Alfa, 99.9% anhydrous). Cells were allowed to rest for at least 6 hours prior to commencing room temperature (*c.* 25°C) galvanostatic

testing on an Arbin BT 2043 with a voltage window of 10 mV to 1.5 V. Each test began with an initial cycle at *C*/20 to condition the electrode. The pure Ge-based electrodes were tested using 1,384 mAh g^{-1} as the theoretical capacity. The $Ge_{0.9}Se_{0.1}$ electrodes were tested using 1,205 mAh g^{-1} as the theoretical capacity because only Ge is active within the voltage range used. Plots of cycling performance as shown with capacity measured specific to the weight of the active material, either pure Ge or $Ge_{0.9}Se_{0.1}$. Eight electrodes of similar mass loading (0.54-0.70 mg cm^{-2}) were tested to indicate the performance of the pure Ge particles (Fig. S5.5c,f†). Fifteen electrodes of similar mass loading (0.54-0.67 mg cm^{-2}) were tested to indicate the performance of the $Ge_{0.9}Se_{0.1}$ particles (Fig. S5.5a-b,d-e†). Five of the 15 $Ge_{0.9}Se_{0.1}$ electrodes were cycled to show an additional 100 cycles at 1*C* following the 80 cycle variable *C*-rate test and three of these five electrodes were cycled an additional 320 cycles for a total of 500 cycles of testing. All cell testing indicated good repeatability of the electrode performance. For the plot of galvanostatic cycling performance in the communication (Fig. 5.1), electrodes of about average performance were selected as representative of the other cell data and the pure Ge based electrode had a mass loading of 0.54 mg cm^{-2} and the $Ge_{0.9}Se_{0.1}$ electrode had a mass loading of 0.58 mg cm^{-2}. First cycle voltage profiles for the pure Ge and the $Ge_{0.9}Se_{0.1}$ particles are shown in Fig. S5.6†.

Scanning electron microscopy (SEM). (Fig. S5.7-10) SEM was conducted to examine the change in condition of the electrodes made with either pure Ge or $Ge_{0.9}Se_{0.1}$ active material before and after cycling. In this study, the pristine (uncycled) electrodes were compared with cycled electrodes in the charged or discharged state following the 80 cycle variable *C*-rate test. The cycled electrodes were carefully removed from the 2032 coin cells by gently prying open one end of the 2032 cell using a pair of plastic pliers (I-V Products). The electrodes were then rinsed in DEC (Alfa) to remove the $LiPF_6$ before being dried. The electrodes were exposed to air for several

minutes before entry into the SEM. This is not believed to impact the morphology of the film. Note: a few solvents (acetic acid based, hydrochloric acid based) were employed in unsuccessful attempts to remove the SEI to expose the active material beneath without doing obvious damage to the film. Shown below are additional SEM and EDS of the pure Ge-based and the $Ge_{0.9}Se_{0.1}$-based electrodes in the pristine state, +80 cycles in charged state and +80 cycles in discharged state.

Transmission electron microscopy (TEM). (Fig. S5.11-16) TEM on a JEOL 2010F was conducted to examine the change in condition of the particles within the electrodes made with either pure Ge or $Ge_{0.9}Se_{0.1}$ active material before and after cycling. In this study, the electrodes were examined in the discharged state following the 80 cycle variable *C*-rate test. The cycled electrodes were carefully removed from the 2032 coin cells by gently prying open one end of the 2032 cell using a pair of plastic pliers (I-V Products) inside the Ar-filled glovebox. The electrodes were then rinsed in DEC (Alfa) to remove the $LiPF_6$ before being dried inside the Ar-filled glovebox. A razor blade was used to cut a sliver of the electrode *c*. 1 cm long by 0.25 mm thick which was set into a silicone mould. While still inside the Ar-filled glovebox, resin (812, Electron Microscopy Supplies) was poured around the suspended sliver of electrode and the resin was allowed to harden at 90°C for 48 h. The resin-embedded electrode sliver was then sectioned by ultramicrotome. The thickness of the sections cut by diamond knife edge (DiATOME) was set to *c*. 50 nm and a lacey carbon grid (SPI Supplies) was used to catch the sections while floating on water. It is likely that the exposure of the outside of the section to water and air chemically contaminated the sample. To what extent is unknown. However, it is our belief that this is the most efficient and least contaminating method available to provide insight into the interior of the cycled electrode, particularly for this study which focuses upon the structural changes in the particles

which are unlikely to be noticeably altered by exposure to water or air. We further note that in a previous study, this method successfully allowed for viewing of dendrites[2], indicating that the resin safely preserves the material which is not directly exposed to the air or water. Lastly, we found that the large, micro-sized particles studied here were observed to often crack, possibly due to the cut made by the diamond knife, something which we sometimes observed in the course of a previous study[7].

High angle annular dark field (HAADF) scanning transmission electron microscopy (STEM). (Fig. S5.11-16) A STEM beam of 1 nm was employed for HAADF-STEM images and EDS analysis of the sectioned electrodes. This technique is suited for providing more clear insight into the interior structure of the particles studied. By resolving signal as a function of thickness of sample (assumed constant due to the sectioning technique employed for sample preparation), density and atomic number (Z) of material (signal intensity scales as a function of about Z^2, the carbonaceous polymer/SEI/conductive additive can be effectively masked. High contrast (bright/white signal) indicates regions of high density/high Z. Additionally, this technique enabled study of the phase segregation in the $Ge_{0.9}Se_{0.1}$ because of the high signal given from the crystalline (high density) nano-inclusions of Ge (high Z) surrounding the amorphous (lower density) Ge-Se-Li containing phase.

*Electrochemical impedance spectroscopy (EIS)***.** (Fig. S5.17) EIS was performed on a ChI 608D from 100 kHz to 0.01 Hz with 5 mV perturbation. The spectra were collected at a state of full discharge at open circuit potential on 2032 cells tested through the 80 cycle variable *C*-rate test. The low frequency data was analysed by fitting to a Warburg impedance element. The available electrochemically active surface area, *a*, was estimated by (i) assuming the electroactive

material remaining was indicated by the 1C capacity, (ii) assuming that the average particle size was 2 microns in diameter and (iii) assuming spherical particles. Alternatively, by assuming the electrochemically active surface area was the electrode geometric area, a similar difference in diffusion coefficient values would be obtained. The differential potential to differential change in *x*, the amount of Li in the Li_xGe phase, was obtained using the voltage profile of the 80^{th} cycle in the variable *C*-rate test. The slope of the voltage profile near full discharge is relatively constant. Given these assumptions, the difference in the diffusion coefficients was estimated and found to be orders of magnitude different, as might be indicated by the different slopes of the low frequency EIS data: *c.* 10^{-11} cm^2 s^{-1} for the cycled $Ge_{0.9}Se_{0.1}$ and *c.* 10^{-16} cm^2 s^{-1} for the cycled pure Ge.

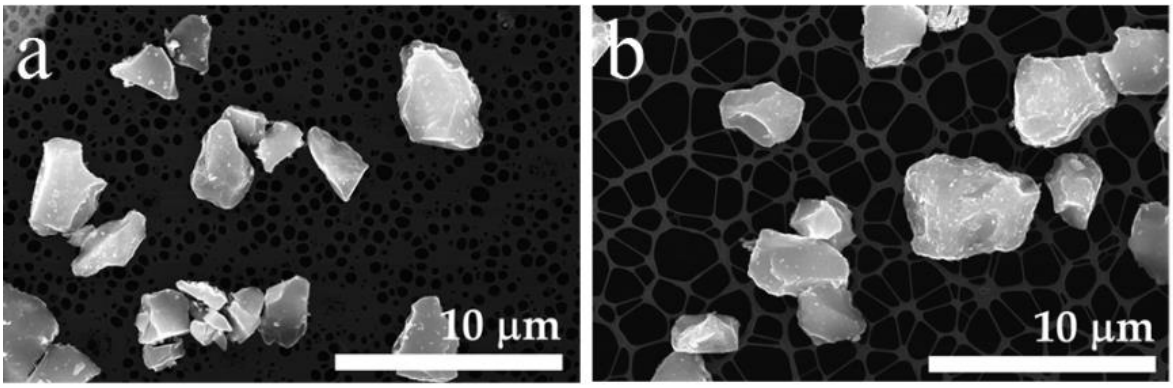

Fig. S5.1. (a) Pure Ge micro-sized particles produced from jet milling. (b) $Ge_{0.9}Se_{0.1}$ micro-sized particles produced from jet milling.

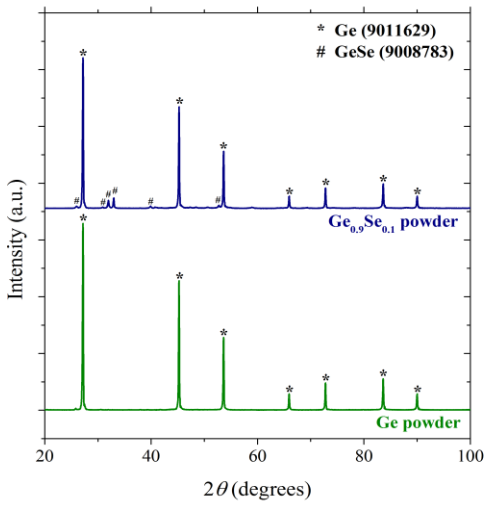

Fig. S5.2. Powder XRD of (a) $Ge_{0.9}Se_{0.1}$ micro-sized particles produced from jet milling and (b) pure Ge micro-sized particles produced from jet milling.

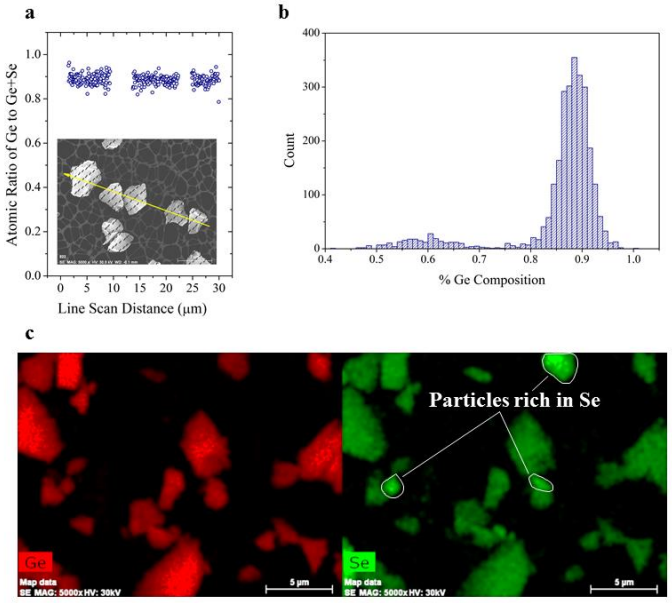

Fig. S5.3. (a) Typical EDS line scan of $Ge_{0.9}Se_{0.1}$ particles after jet milling showing EDS line path and the corresponding elemental ratio of Ge to Ge+Se recorded. (b) Histogram reflecting thousands of discrete EDS point measurements analysed as a ratio of Ge to Ge+Se. A bimodal distribution is observed, with the majority of the material reflecting the desired $Ge_{0.9}Se_{0.1}$ composition and a minority reflecting a GeSe-like phase, slightly rich in Ge. (c) Typical EDS map confirming that the majority of the particles are in the desired $Ge_{0.9}Se_{0.1}$ mixture and that a minority of particles are Se-rich.

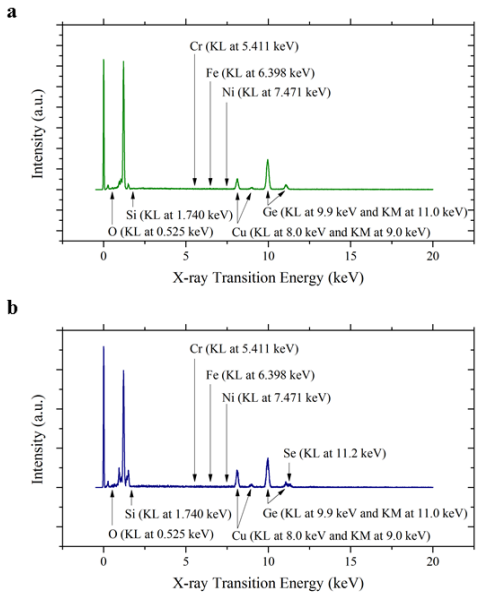

Fig. S5.4. Typical EDS spectrum characterizing many particles of (a) pure Ge and (b) $Ge_{0.9}Se_{0.1}$ particles. Arrows are drawn to indicate the locations of the dominant x-ray transition energies for the desired elements, Ge or Ge and Se, as well as for potential contaminants. Contamination from the ampoule was not found as indicated by the absence of Si; contamination from the jet milling process was not found as indicated by the absence of Cr, Fe and Ni; and contamination from oxidation was negligible as indicated by the nearly undetectable O signal.

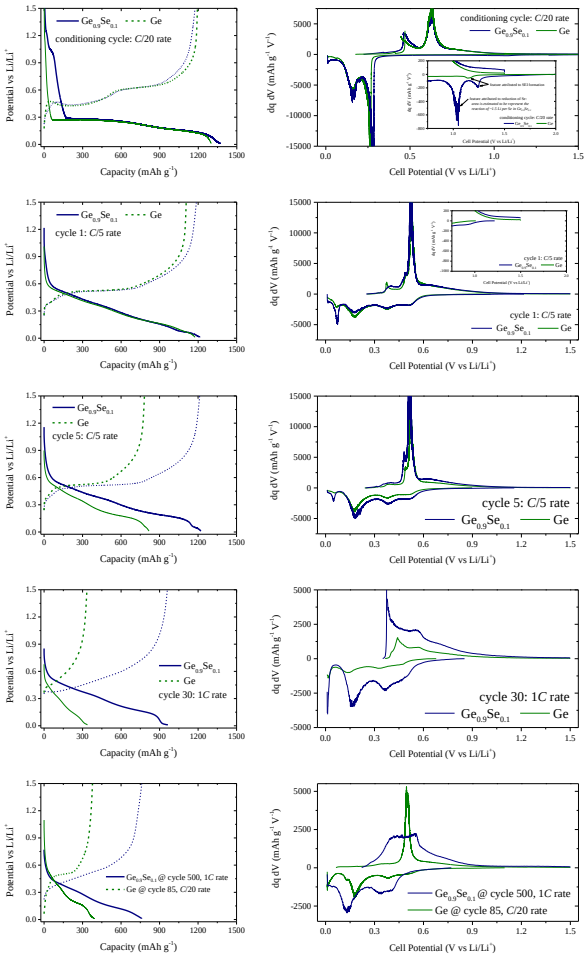

Fig. S5.5. Voltage profiles and corresponding differential capacity profiles for the pure Ge and the $Ge_{0.9}Se_{0.1}$ based electrodes. Shown above are the conditioning cycle, 1st cycle (at *C*/5 rate), 5th cycle (at *C*/5 rate), 30th cycle (at 1*C* rate), and 500th cycle ($Ge_{0.9}Se_{0.1}$ at 1*C* rate) or 85th cycle (pure Ge at *C*/20 rate). For the conditioning cycle, there is a lower capacity and larger irreversible loss in the $Ge_{0.9}Se_{0.1}$-based electrode due to the irreversible reaction of Li with Se (shown in inset graph to the differential capacity profile) which is not seen subsequently. The reaction pathway for the $Ge_{0.9}Se_{0.1}$ appears nearly identical to that for the pure Ge, indicating that the Se reduces into an inactive phase.

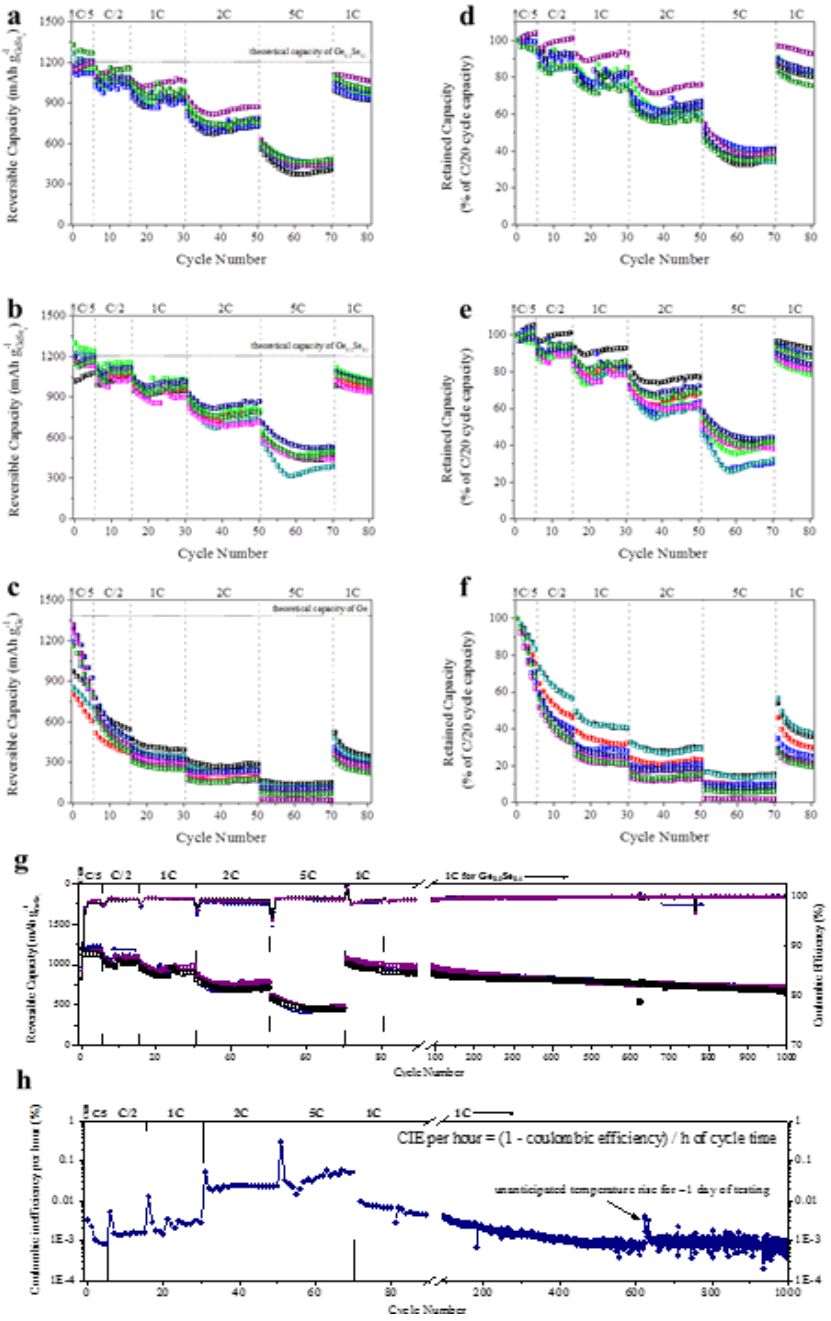

Fig. S5.6. Galvanostatic cycling performance of cells showing repeatability of data shown in Fig. 1 of the communication. Specific capacity *vs* cycle number for $Ge_{0.9}Se_{0.1}$ cells (15 total) shown in (a) and (b) and corresponding graphs (d) and (e) of the capacity retention measured as a percent of the first cycle discharge (Li-extraction) capacity when testing was done at *C*/20. Specific capacity *vs* cycle number for the pure Ge cells (8 total) shown in (c) and corresponding

graph (f) of the capacity retention measured as a percent of the first cycle discharge (Li-extraction) capacity when testing was done at *C*/20. Figure (g) shows the repeatability of the three $Ge_{0.9}Se_{0.1}$ cells tested until 500 cycles. (h) The coulombic inefficiency per hour (CIE/h) of cycle time for the $Ge_{0.9}Se_{0.1}$ electrode result shown in Fig. 1. The data is limited by the accuracy of the Arbin battery tester used which we estimate measures the coulombic efficiency to an accuracy of *c*. 0.1 percent. For a point of reference, the reader is referred to one of Dahn's recent studies[3] of commercial graphite-based batteries for which the CIE/h of cycle time is at least two orders of magnitude lower (10^{-5} CIE/h) than what is observed for the $Ge_{0.9}Se_{0.1}$ based electrode studied here.

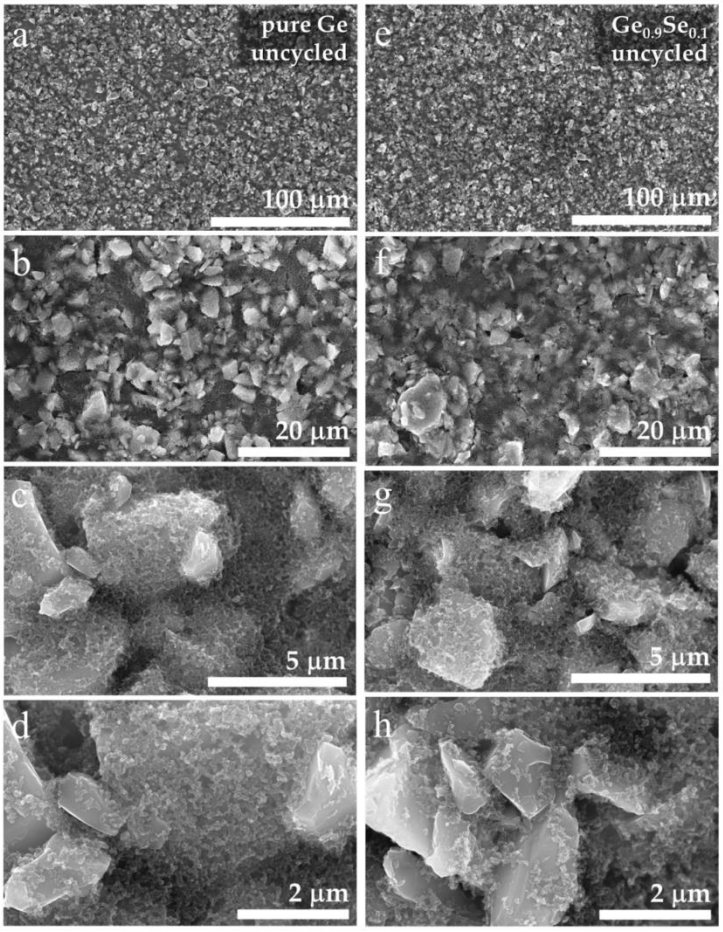

Fig. S5.7. SEM of pristine (uncycled) electrodes made using the pure Ge (a-d) or $Ge_{0.9}Se_{0.1}$ (e-h) as the active material. The electrodes appear indistinguishable with similar particle size and degree of mixing and spacing of the larger, micro-sized active material particles and the smaller, conductive additive particles.

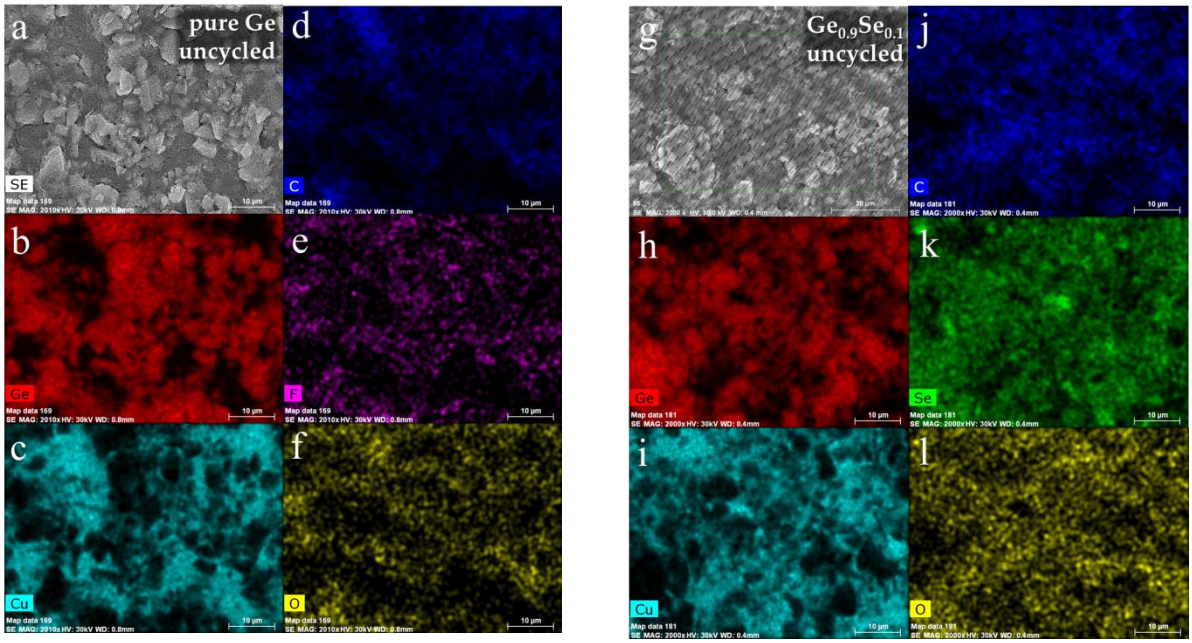

Fig. S5.8. EDS mapping of pristine (uncycled) electrodes made using the pure Ge (a-f) or $Ge_{0.9}Se_{0.1}$ (g-l) as the active material. The electrodes appear indistinguishable with similar degree of mixing. Using Castaing's formula, the analysis depth (for Ge or $Ge_{0.1}Se_{0.1}$) is estimated to be less than 4 μm for the beam conditions (30kV).

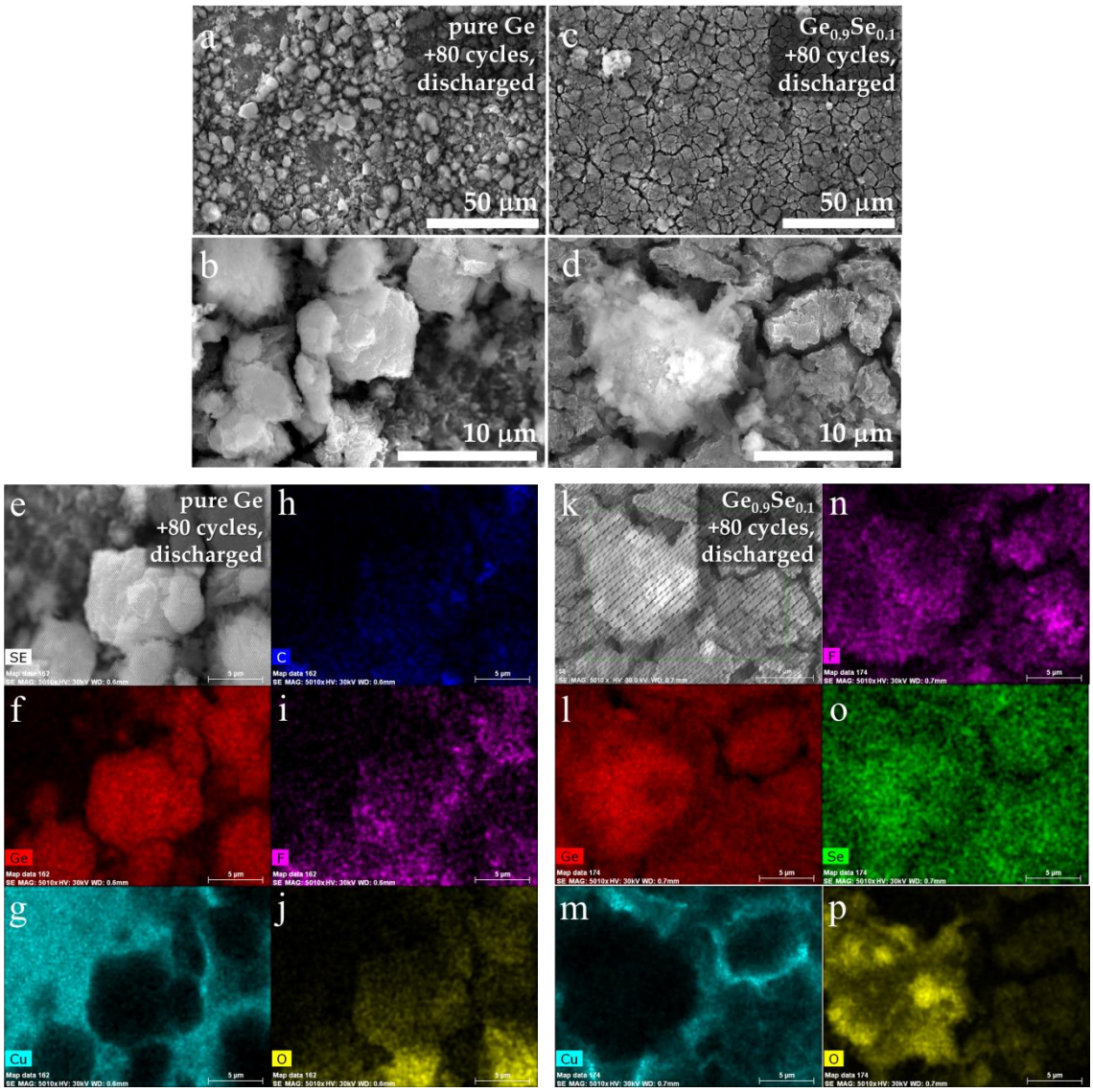

Fig. S5.9. SEM and EDS mapping of cycled electrodes (+80 cycles, after the variable *C*-rate test, discharged state) with the pure Ge (SEM: a-b, EDS: e-j) or $Ge_{0.9}Se_{0.1}$ (SEM: c-d, EDS:k-p) as the active material. The EDS mapping for the cycled (discharged) pure Ge based electrode (e-j) shows a region which shows the border of delaminated film, clearly indicated by the EDS signal for the Ge (active material) and the Cu (substrate). The cycled film is covered in SEI and also in dendritic growths, these characterized by their structure (similar to what has been reported previously[2]) and high content of O which would be present in the decomposition species formed on the highly

reactive lithium metal surfaces. The EDS mapping for the cycled (discharged) $Ge_{0.9}Se_{0.1}$ based electrode (k-p) focuses upon one of the few dendritic growths observed on this film and is similarly identified by a particularly high O signal. As expected, the major dendritic growths are typically found on top of active material, indicating a local "hot zone" where the flux of lithium exceeds the rate at which it can transport into and react within the active material.

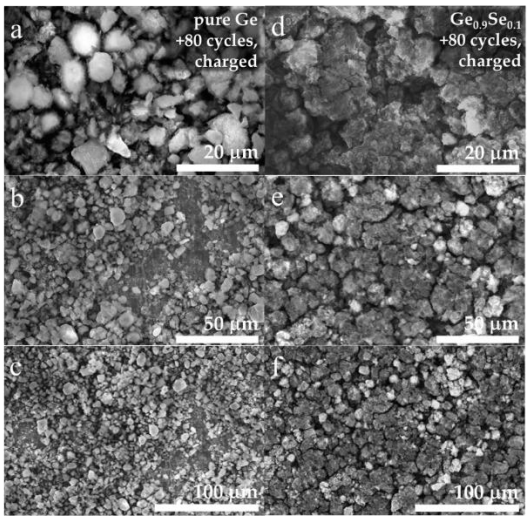

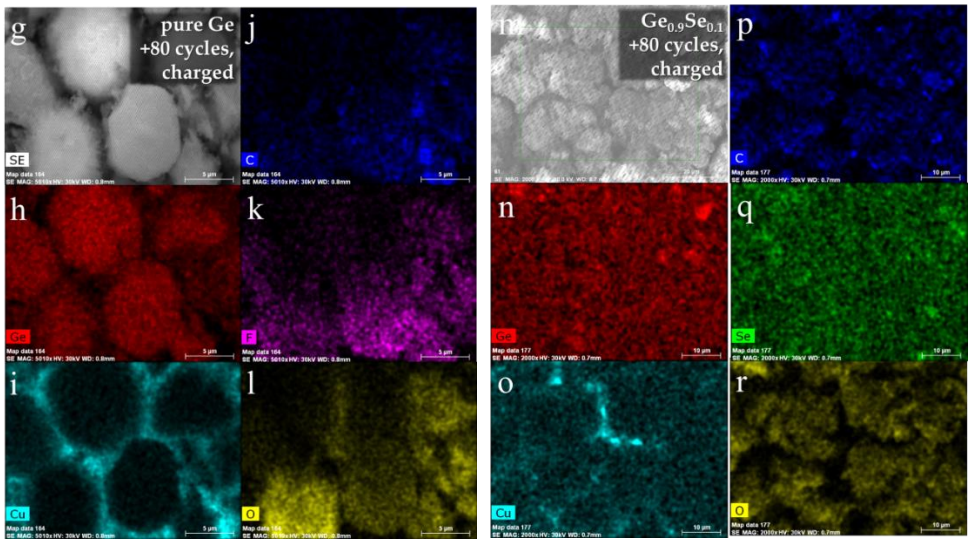

Fig. S5.10. SEM and EDS mapping of cycled electrodes (+80 cycles, after the variable *C*-rate test, charged state) with the pure Ge (SEM: a-c, EDS: g-l) or $Ge_{0.9}Se_{0.1}$ (SEM: d-f, EDS:m-r) as the active material. The cycled pure Ge based electrodes show significant film delamination and significantly more dendritic growths (growing out of the pure Ge particles). The EDS mapping for the cycled (charged) pure Ge based electrode (g-l) shows a region with some Ge particles covered in dendritic growths and some comparatively clean of dendritic growths. The EDS mapping for the cycled (charged) $Ge_{0.9}Se_{0.1}$ based electrode (m-r) shows that there are more dendritic growths observable in the charged state than in the discharged state.

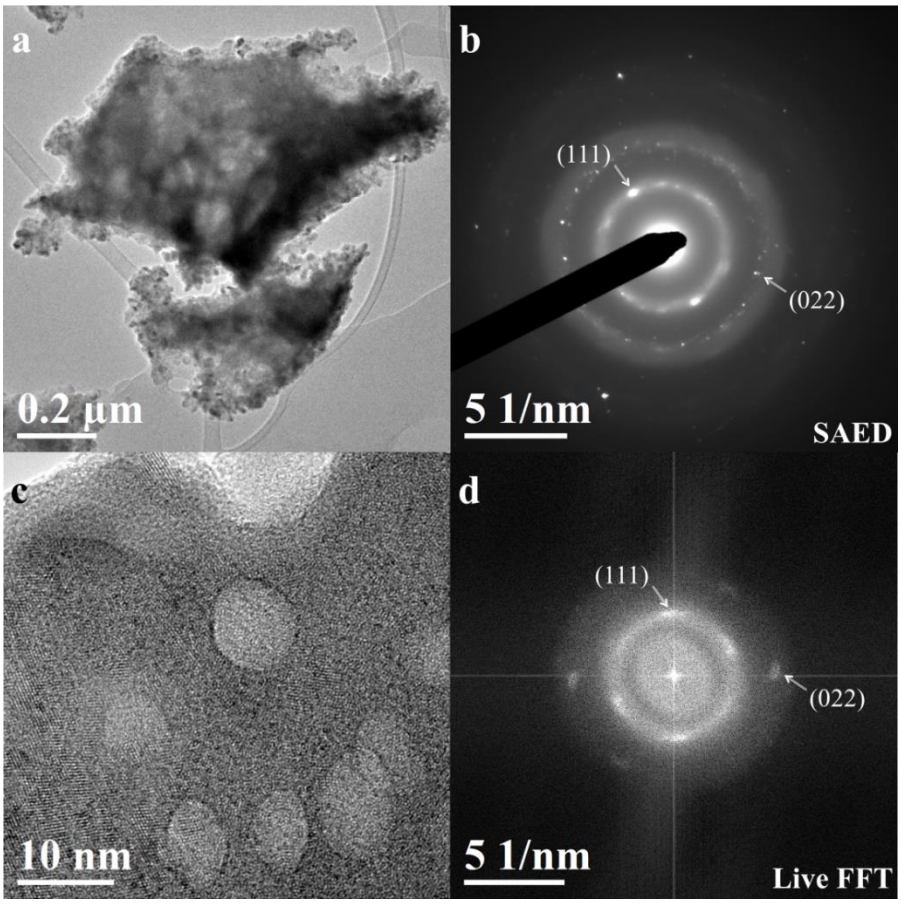

Fig. S5.11. *Ex-situ* TEM of ultramicrotome sectioned cycled (discharged) pure Ge-based electrode after the 80 cycle variable *C*-rate test. (a) TEM of Ge particle and (b) corresponding selected area electron diffraction pattern (SAED). The prominent reflections form rings corresponding to the dominant (111) and (022) planes of Ge. The small area shown in the HR-TEM image (c) cannot be observed exclusively by SAED given restrictions on the aperture size but from FFT (d) it is found that the crystalline structure visually apparent is also Ge.

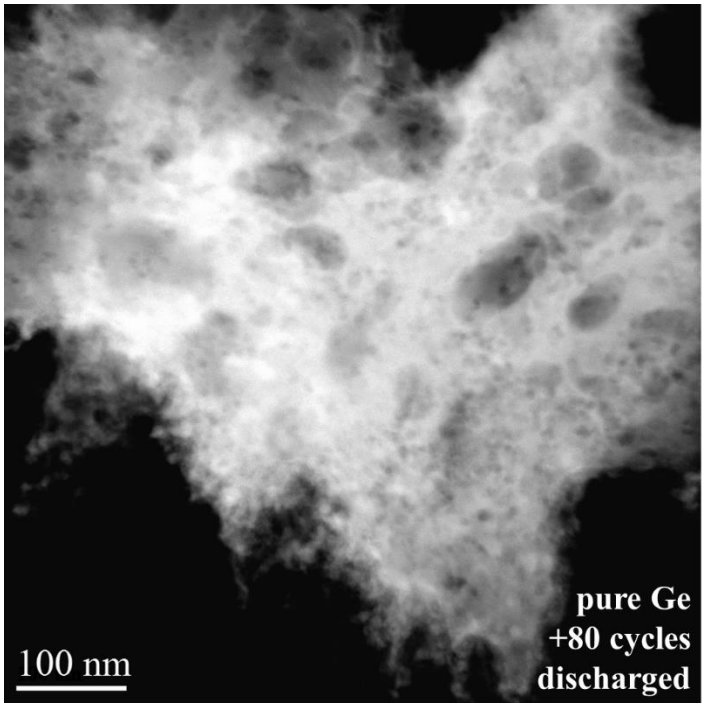

Fig. S5.12a. HAADF-STEM of a Ge particle from the pure Ge-based electrode in its discharged state after 80 cycles of variable *C*-rate testing. Note that the edges of the particle appear torn and fractured. There are several locations on the edge (perimeter) of the particle which appear to be half of a cavity, the hole-like structure observed throughout the interior of the particle.

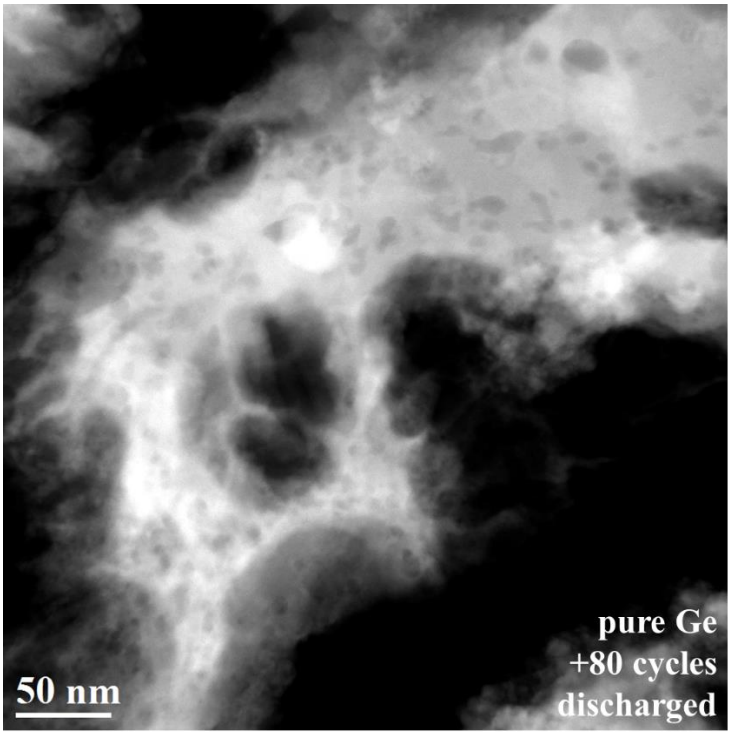

Fig. S5.12b. HAADF-STEM of a Ge particle from the pure Ge-based electrode in its discharged state after 80 cycles of variable *C*-rate testing. Note that the edges of the particle appear torn and fractured. There are several locations on the edge (perimeter) of the particle which appear to be half of a cavity, the hole-like structure observed throughout the interior of the particle.

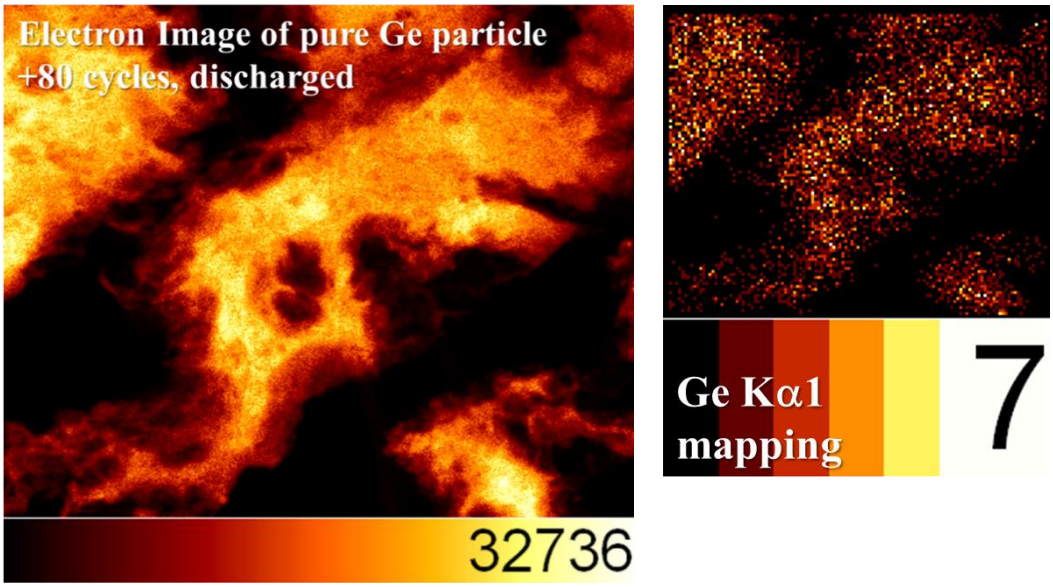

Fig. S5.12h. EDS mapping of a Ge particle from the pure Ge-based electrode in its discharged state after 80 cycles of variable *C*-rate testing. The mapping was done to further verify the identity of the particle being characterized by HR-TEM and/or HAADF-STEM. The electron image from the mapping is shown at left and the Ge Kα1 mapping is shown at right. Because the EDS detector does not have a drift corrector, similar mappings could not be performed at higher-magnifications.

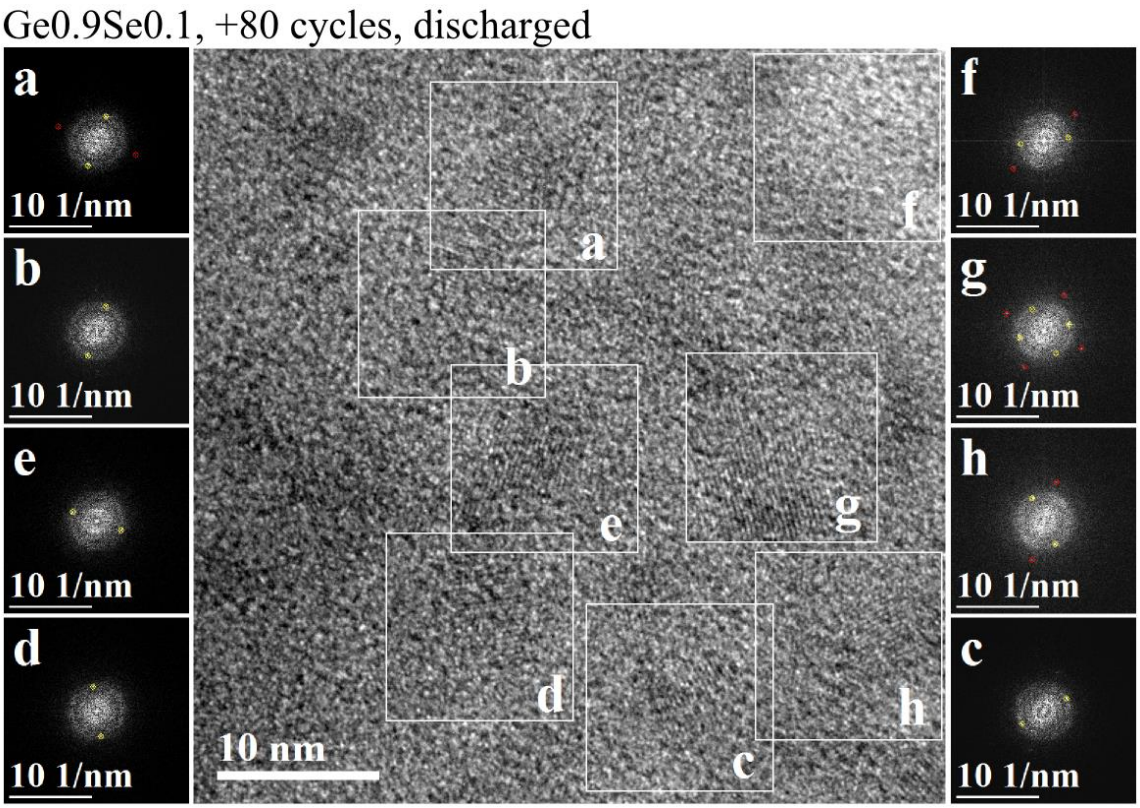

Fig. S5.13. FFT analysis of HR-TEM image of interior of $Ge_{0.9}Se_{0.1}$ particle in discharged state after 80 cycle variable *C*-rate test. The FFT resolution is sufficient to identify only several out of all the visible crystallite regions in the image. The cycled material appears to be a network of nano-inclusions of Ge (crystalline in the discharged state) surrounded by an amorphous material.

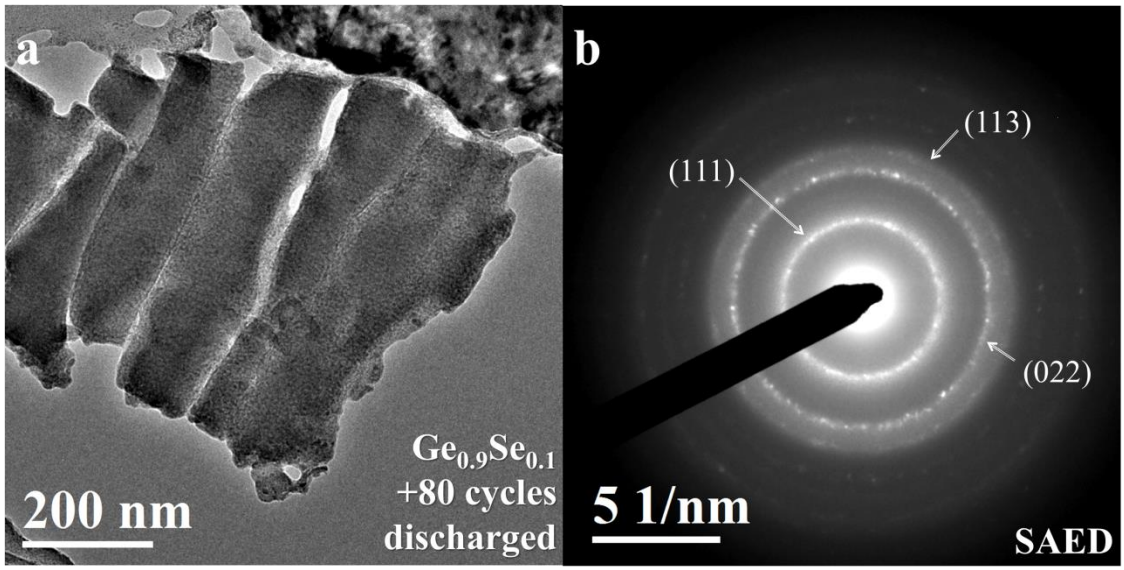

Fig. S5.14. SAED analysis of HR-TEM image of $Ge_{0.9}Se_{0.1}$ particles in discharged state after 80 cycle variable *C*-rate test. Only reflections (rings, indicating polycrystalline material) for Ge planes are observed in the SAED. Surprisingly, no other reflections are visible, indicating that the Se in the particle is within an amorphous phase rather than in crystalline Li_2Se.

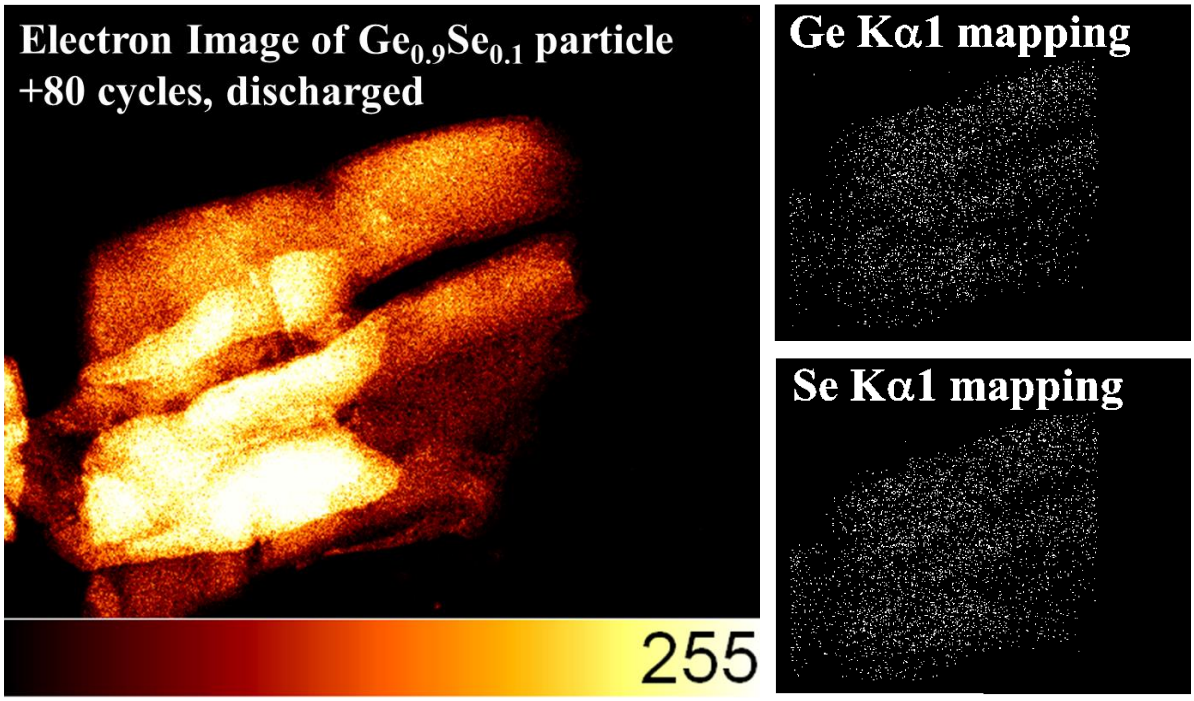

Fig. S5.15. EDS mapping of a $Ge_{0.9}Se_{0.1}$ particle from the $Ge_{0.9}Se_{0.1}$-based electrode in its discharged state after 80 cycles of variable *C*-rate testing. The mapping was done to further verify the identity of the particle being characterized by HR-TEM and/or HAADF-STEM. The electron image from the mapping is shown at left and the Ge Kα1 and Se Kα1 mapping is shown at right. Because the EDS detector does not have a drift corrector, similar mappings could not be performed at higher-magnifications. However, the mapping and EDS spectra are sufficient to show that there is Se present in the particle. Useful quantitative analysis was precluded by the condition of the detector (not calibrated).

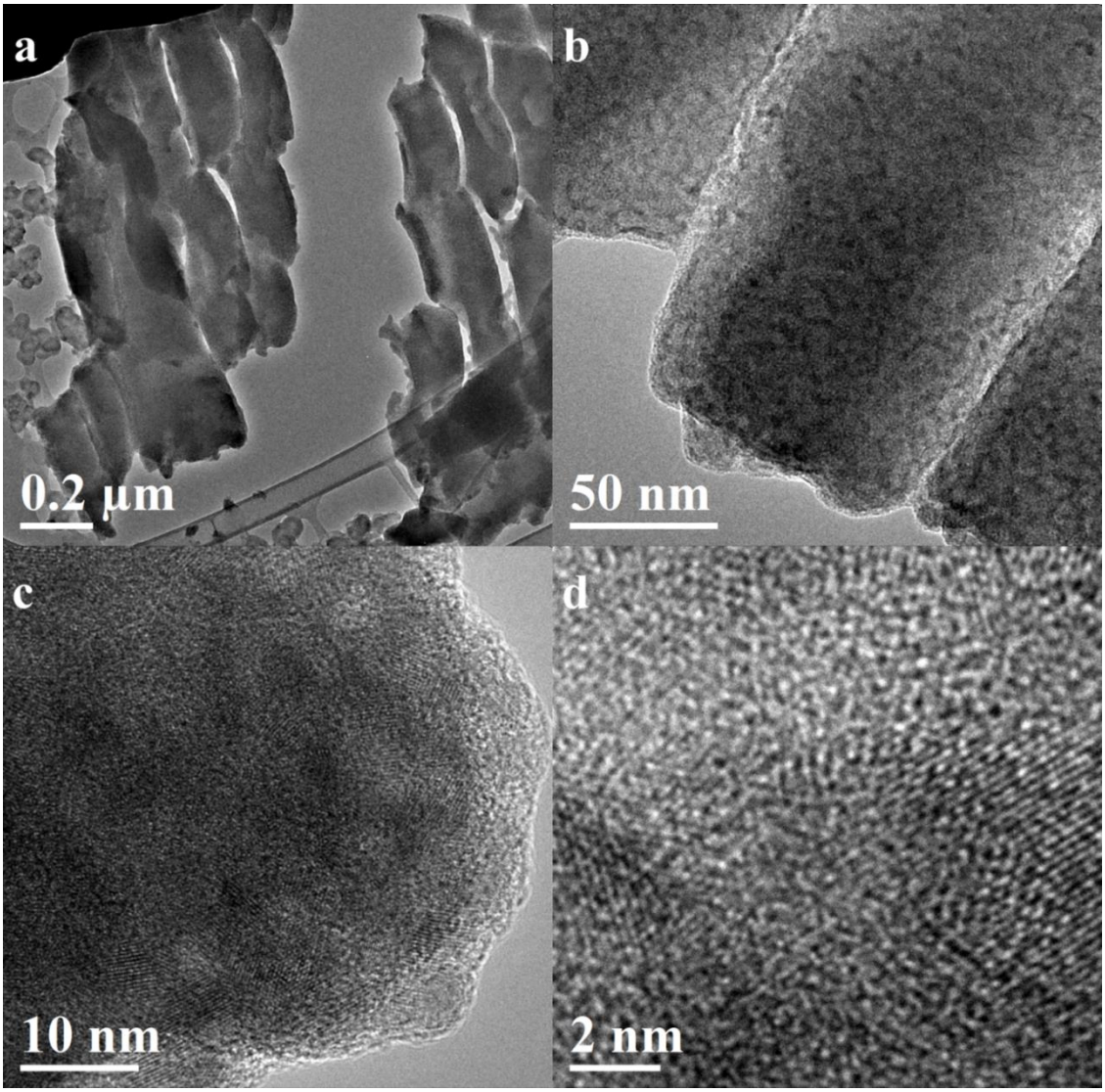

Fig. S5.16. HR-TEM of a $Ge_{0.9}Se_{0.1}$ particle from the $Ge_{0.9}Se_{0.1}$-based electrode in its discharged state after 80 cycles of variable *C*-rate testing. Note that the edges of the particle appear to be relatively intact and have comparatively smooth edges, suggesting that the particles did not fracture. In (a) there may be evidence to suggest that the particles cleanly break, but because this seems to occur along parallel lines we believe this may be an artefact of the ultramicrotome sectioning technique. Within the particle, there are no pores or cavities and at progressively higher magnifications the network of nano-crystallite inclusions of Ge around small veins of an amorphous material are observed.

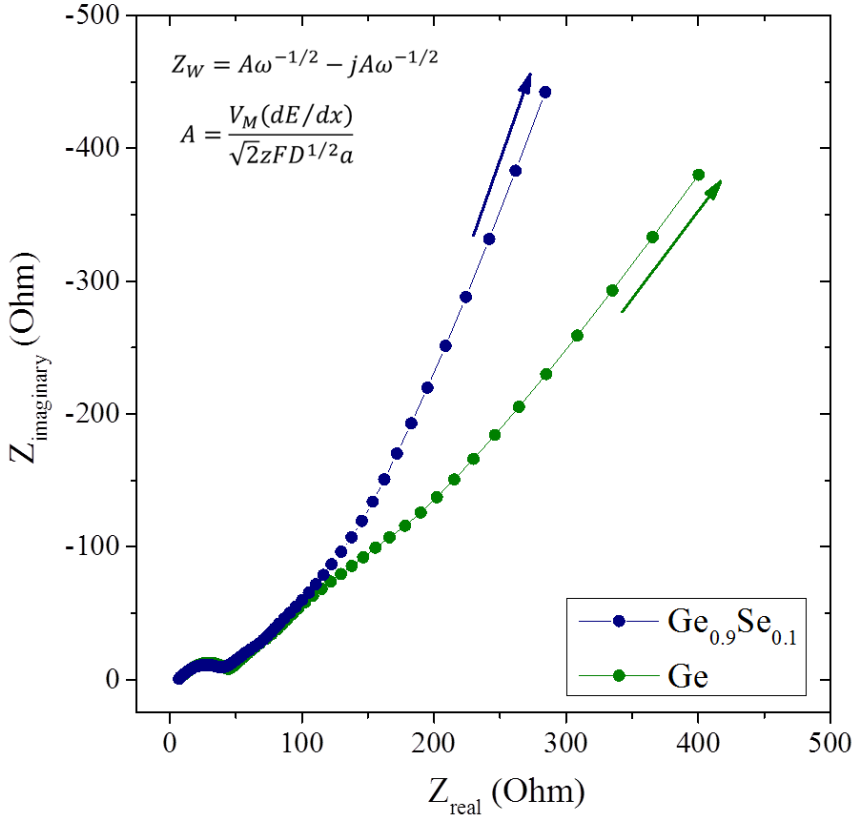

Fig. S5.17. EIS performed from 100 kHz to 0.01 Hz at open circuit potential on the pure Ge-based and the $Ge_{0.9}Se_{0.1}$-based electrodes at a state of full discharge following the 80 cycle variable *C*-rate test.

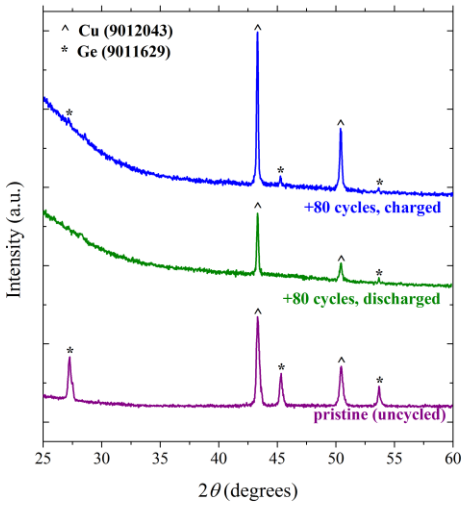

Fig. S5.18. *Ex-situ* XRD (Rikagu Microflex 600) of pristine and cycled pure Ge based or $Ge_{0.9}Se_{0.1}$ based electrodes in the charged and discharged state after the 80-cycle variable *C*-rate test. Due to the nature of the experiment, two nominally identical electrodes (with very similar galvanostatic cycling performance) were used, one for the pattern of the charged electrode and one for the pattern of the discharged electrode. Interestingly, for the cycled pure Ge based electrode, a Ge pattern is observed for both the charged and discharged electrode. Although it is possible that the discharged electrode reverts into polycrystalline domains large enough to be identifiable by XRD, we believe that this pattern from the discharged state is more likely attributable to electrochemically disconnected, discharged pure Ge active material. With higher degree of confidence, we attribute the Ge pattern observed in the charged pure Ge based electrode to this phenomenon. In contrast, there is no Ge pattern observed in the charged or discharged $Ge_{0.9}Se_{0.1}$ based electrodes. This indicates that the nanocrystallites of Ge characterized in the discharged electrode by HR-TEM, SAED and FFT are possibly too small or not strongly crystalline enough to form a clear XRD pattern. This odd behaviour has been observed previously in a similar study[4] which employed D-

STEM, a powerful electron microscopy technique which enables the collection of an electron diffraction pattern from a point on the sample only 2 nm in diameter.

References

1. Ross, L.; Bourgon, M., Germanium-selenium phase diagram. Can. J. Chem. 1969, 47 (Copyright (C) 2014 American Chemical Society (ACS). All Rights Reserved.), 2555-9. http://dx.doi.org/10.1139/v69-422

2. Klavetter, K. C.; Wood, S. M.; Lin, Y.-M.; Snider, J. L.; Davy, N. C.; Chockla, A. M.; Romanovicz, D. K.; Korgel, B. A.; Lee, J.-W.; Heller, A.; Mullins, C. B., A high-rate germanium-particle slurry cast Li-ion anode with high Coulombic efficiency and long cycle life. Journal of Power Sources 2013, 238 (0), 123-136. http://dx.doi.org/http://dx.doi.org/10.1016/j.jpowsour.2013.02.091

3. Wang, D. Y.; Dahn, J. R., A High Precision Study of Electrolyte Additive Combinations Containing Vinylene Carbonate, Ethylene Sulfate, Tris(trimethylsilyl) Phosphate and Tris(trimethylsilyl) Phosphite in Li[Ni1/3Mn1/3Co1/3]O2/Graphite Pouch Cells. Journal of The Electrochemical Society 2014, 161 (12), A1890-A1897. http://dx.doi.org/10.1149/2.0841412jes

4. Abel, P. R.; Klavetter, K. C.; Jarvis, K.; Heller, A.; Mullins, C. B., Sub-stoichiometric germanium sulfide thin-films as a high-rate lithium storage material. Journal of Materials Chemistry A 2014, 2 (44), 19011-19018. http://dx.doi.org/10.1039/c4ta04496g

5. Frequently Asked Questions. http://www.jetpulverizer.com/faq.php#link-7.

6. JET PULVERIZER WORKS TO COMMERCIALIZE EMERGING

LITHIUM-ION BATTERY TECHNOLOGY. http://www.jetpulverizer.com/news-and-events/article01.php.

7. Klavetter, K. C.; Snider, J. L.; de Souza, J. P.; Tu, H.; Cell, T. H.; Cho, J. H.; Ellison, C. J.; Heller, A.; Mullins, C. B., A free-standing, flexible lithium-ion anode formed from an air-dried slurry cast of high tap density SnO2, CMC polymer binder and Super-P Li. Journal of Materials Chemistry A 2014, 2 (35), 14459-14467. http://dx.doi.org/10.1039/c4ta03201b

Chapter 6: Conclusion

Overview of Completed Work

The completed work presented in this dissertation has achieved the following:

1. [Chapters 2-5] Demonstrated the efficacy of fluoroethylene carbonate (FEC) solvent in improving through a stable solid electrolyte interphase (SEI) by the cycling performance of four anodes. For Ge particles of nano to micron size, SnO_2 micron sized particles, mesoporous Co_3O_4 micron sized particles and micron sized $Ge_{0.9}Se_{0.1}$ particles, stable cycling for hundreds to thousands of cycles was demonstrated.
2. [Chapter 2] TEM imaging of ultramicrotomed cross sections of resin embedded, cycled electrodes revealed that FEC inhibited dendritic lithium growth on Ge particles.
3. [Chapter 5] The e-beam evaporation grown thin film $Ge_{0.9}Se_{0.1}$ anode anode was made into a high tap density particle anode.
4. [Chapter 5] Determined from cycling data supported by HAADF-STEM how a small atomic fraction of inactive Se in a micron sized Ge particle prevents fracture of the particle.

Ongoing and Future Work

There exist four ongoing projects that can be discussed at this time to varying degrees of specificity and one proposed project to be conducted in collaboration with Sandia National Laboratories.

1. Effect of current density on the electrodeposition of lithium

Lithium metal as an anode material in lithium ion batteries provides for high density charge storage (3860 mA h g^{-1}) at low voltages. For this reason, the lithium metal anode is critical to the design of Li-S or Li-air concept battery chemistries proposed for use in powering long-range electric vehicles.

However, the lithium metal anode cannot be safely or efficiently operated. During charge, Li^+ ions electrodeposit as adatoms unevenly, forming dendritic structures that can unpredictably cause internal short circuiting and sometimes thermal runaway. The high specific surface area lithium growths also prevent long-term cycling because the battery electrolyte species irreversibly reduce upon the exposed surfaces of the very electropositive lithium metal, depleting the battery's supply of both electrolyte species and lithium.

Parameters affecting dendrite growth include the chemistry of the electrolyte and the operating conditions which determine the nucleation density, electrode polarization (depletion of Li ions from the electrolyte at high current density) and surface energy of the growing nuclei. Strategies developed for reducing and controlling the formation of dendritic growths include: use of high modulus barriers[3,4,5,6], designing the electrolyte to increase the Li^+ transference number[7,8], modification of the lithium metal/solid electrolyte interphase/electrolyte interface[9,10,11] to increase or regulate[12] the rate of cathodic charge transfer and adopting to the Li-ion system classic electroplating deposition techniques such as pulsed charging.

An assumption implicit in some of these strategies for mitigating dendrite growth is that the high degree of electrode polarization resultant from application of high current density necessarily results in enhanced growth rate of dendrites. Here we apply nucleation theory[13,14] to show that by promoting nucleation, high current densities can reduce dendritic growth.[15,16,17] We also show in coin cell testing that by brief application of high current density prior to DC charging

at current densities relevant for future Li/S and Li/air concept batteries, the electrode surface can be conditioned such that the coulombic cycling efficiency is greatly improved.

REFERENCES

1. Cohen, Y. S.; Cohen, Y.; Aurbach, D., Micromorphological Studies of Lithium Electrodes in Alkyl Carbonate Solutions Using in Situ Atomic Force Microscopy. *The Journal of Physical Chemistry B* **2000,** *104* (51), 12282-12291.

2. Rosso, M.; Gobron, T.; Brissot, C.; Chazalviel, J. N.; Lascaud, S., Onset of dendritic growth in lithium/polymer cells. *Journal of Power Sources* **2001,** *97–98* (0), 804-806.

3. Zheng, G.; Lee, S. W.; Liang, Z.; Lee, H.-W.; Yan, K.; Yao, H.; Wang, H.; Li, W.; Chu, S.; Cui, Y., Interconnected hollow carbon nanospheres for stable lithium metal anodes. *Nat Nano* **2014,** *advance online publication*.

4. Verma, P.; Maire, P.; Novák, P., A review of the features and analyses of the solid electrolyte interphase in Li-ion batteries. *Electrochimica Acta* **2010,** *55* (22), 6332-6341.

5. Khurana, R.; Schaefer, J. L.; Archer, L. A.; Coates, G. W., Suppression of Lithium Dendrite Growth Using Cross-Linked Polyethylene/Poly(ethylene oxide) Electrolytes: A New Approach for Practical Lithium-Metal Polymer Batteries. *Journal of the American Chemical Society* **2014,** *136* (20), 7395-7402.

6. Umeda, G. A.; Menke, E.; Richard, M.; Stamm, K. L.; Wudl, F.; Dunn, B., Protection of lithium metal surfaces using tetraethoxysilane. *Journal of Materials Chemistry* **2011,** *21* (5), 1593-1599.

7. Suo, L.; Hu, Y.-S.; Li, H.; Armand, M.; Chen, L., A new class of Solvent-in-Salt electrolyte for high-energy rechargeable metallic lithium batteries. *Nat Commun* **2013,** *4*, 1481.

8. Qian, J.; Henderson, W. A.; Xu, W.; Bhattacharya, P.; Engelhard, M.; Borodin, O.; Zhang, J.-G., High rate and stable cycling of lithium metal anode. *Nat Commun* **2015,** *6*.

9. Lu, Y.; Tu, Z.; Archer, L. A., Stable lithium electrodeposition in liquid and nanoporous solid electrolytes. *Nat Mater* **2014,** *13* (10), 961-969.

10. Goodman, J. K. S.; Kohl, P. A., Effect of Alkali and Alkaline Earth Metal Salts on Suppression of Lithium Dendrites. *Journal of The Electrochemical Society* **2014,** *161* (9), D418-D424.

11. Miao, R.; Yang, J.; Feng, X.; Jia, H.; Wang, J.; Nuli, Y., Novel dual-salts electrolyte solution for dendrite-free lithium-metal based rechargeable batteries with high cycle reversibility. *Journal of Power Sources* **2014,** *271* (0), 291-297.

12. Ding, F.; Xu, W.; Chen, X.; Zhang, J.; Shao, Y.; Engelhard, M. H.; Zhang, Y.; Blake, T. A.; Graff, G. L.; Liu, X.; Zhang, J.-G., Effects of Cesium Cations in Lithium Deposition via Self-Healing Electrostatic Shield Mechanism. *The Journal of Physical Chemistry C* **2014,** *118* (8), 4043-4049.

13. Popov, K.; Djokic, S.; Grugur, B., *Fundamental Aspects of Electrometallurgy*. Kluwer Academic Publishers: New York, 2002.

14. Ely, D. R.; García, R. E., Heterogeneous Nucleation and Growth of Lithium Electrodeposits on Negative Electrodes. *Journal of The Electrochemical Society* **2013,** *160* (4), A662-A668.

15. Sano, H.; Sakaebe, H.; Senoh, H.; Matsumoto, H., Effect of Current Density on Morphology of Lithium Electrodeposited in Ionic Liquid-Based Electrolytes. *Journal of The Electrochemical Society* **2014,** *161* (9), A1236-A1240.

16. Nishikawa, K.; Mori, T.; Nishida, T.; Fukunaka, Y.; Rosso, M., Li dendrite growth and Li+ ionic mass transfer phenomenon. *Journal of Electroanalytical Chemistry* **2011,** *661* (1), 84-89.

17. Nishida, T.; Nishikawa, K.; Rosso, M.; Fukunaka, Y., Optical observation of Li dendrite growth in ionic liquid. *Electrochimica Acta* **2013,** *100* (0), 333-341.

2. The Mechanism of Lithium Dendrite Growth in 1M $LiPF_6$ in EC:DEC

The mechanism of lithium dendrite growth in the electrolyte composed of $LiPF_6$ dissolved to 1M in ethylene carbonate and diethyl carbonate has not yet been identified. There currently exist conflicting reports of growth from dendritic tips, from kinks or defects or from the base of the dendritic structure. Here we identify the growth mechanism for the lithium dendrite by resolving in high spatial resolution with ToF-SIMS the distribution of ^{6}Li electrodeposited upon a pre-existing ^{nat}Li dendritic growth. These results are complemented by *in-situ* optical observation of lithium dendritic growth. To the best of our knowledge, these are the first *in-situ* optical observations conducted using reconstructed 3D imaging technology.

3. The Physical Basis for the Electrochemical Voltage Spike Observed During Testing of Li-Ion Cells

The occurrence of a transient, high resistance event during the charge or discharge of a lithium-ion battery cell has not yet been correlated with a physical event. Here, using *in-situ* optical microscopy, we identify the basis for this voltage spike and suggest a chemical additive to suppress the frequency of voltage spikes during electrochemical testing.

4. Three Dimensional Current Collectors for High Energy Density Li-Ion Battery Electrodes

The typical thickness of the commercial Li-ion battery electrode film is limited so as to avoid film delamination and increases in ohmic resistance.[1,2] For thick electrodes, the larger

overpotentials required for lithium (de)insertion are attributable to a combination of longer ionic diffusion paths[3] and resistance for electronic transport through long-chain, percolating conductive additive networks originating at the current collector surface.[4] These factors require restricting the capacity stored per unit area of electrode to 2-4 mA h cm^{-2}, provided by an active material loading of *c.* 10 mg cm^{-2} for anodes and *c.* 25 mg cm^{-2} for cathodes.[5,6]

For electrodes – especially anodes – tested in academic research labs, the typical loading of active materials is small and resulting in an areal capacity and energy density that is a small fraction of what is available from commercial batteries.[7]

To allow for more clear identification of the potential comparative advantages of advanced Li-ion battery materials being studied – *e.g.*, improvements in capacity, capacity retention at high charge/discharge rates or over long-lifetime tests, coulombic efficiency – the electrodes tested should be loaded to an extent that provides for an areal capacity equal to or exceeding a commercial standard.[7] Otherwise, the degree to which the measured performance for a low-loaded electrode indicates potential performance in a scaled-up film cannot be predicted. One reason for this is that there remains debate about the extent to which the active particle population during lithium (de)insertion is attributable to limitations arising from ionic, electronic or solid state lithium transport. [1,3,8,9,10]

For some electrodes, particularly those composed of low tap-density active material particles, it may not be possible to form a securely adhered film at a thickness great enough to provide for areal capacities equal to commercial electrodes. For all electrodes, increases in film thickness due to higher mass loading of particles results in higher resistance from some combination of limitations in electronic and ionic transport, particularly for anodes when solid electrolyte interphase (SEI) coverage grows between particles across the film surface.[11]

Accordingly, for the traditional electrode film cast upon a metal foil substrate, there exist *i)* a limit to energy density due to both film thickness restrictions as well as the space/weight required for the foil current collector and *ii)* a trade-off for which increases in energy density are offset by disproportionate decreases in power density.

To enable testing of higher mass loading electrodes and attempt to de-couple this inverted and non-linear relationship between energy and power density, alternative substrate designs and materials have been studied: metal foams,[12,13,14] carbon fabrics[15] and meshes of graphene-like or carbon nanotube materials,[16] porous carbons,[17] templated micro-structured substrates,[18,19] and nano-structured arrays devised by micro-machining and other methods.[20,21]

Here we demonstrate with commercially produced $LiFePO_4$ a high energy density electrode formed upon a novel, inexpensive 3D current collector.

REFERENCES

1. Lu, W.; Jansen, A.; Dees, D.; Nelson, P.; Veselka, N. R.; Henriksen, G., High-energy electrode investigation for plug-in hybrid electric vehicles. *Journal of Power Sources* **2011,** *196* (3), 1537-1540.

2. Wood Iii, D. L.; Li, J.; Daniel, C., Prospects for reducing the processing cost of lithium ion batteries. *Journal of Power Sources* **2015,** *275* (0), 234-242.

3. Zheng, H.; Li, J.; Song, X.; Liu, G.; Battaglia, V. S., A comprehensive understanding of electrode thickness effects on the electrochemical performances of Li-ion battery cathodes. *Electrochimica Acta* **2012,** *71* (0), 258-265.

4. Li, Y.; El Gabaly, F.; Ferguson, T. R.; Smith, R. B.; Bartelt, N. C.; Sugar, J. D.; Fenton, K. R.; Cogswell, D. A.; Kilcoyne, A. L. D.; Tyliszczak, T.; Bazant, M. Z.; Chueh, W. C., Current-induced transition from particle-by-particle to concurrent intercalation in phase-separating battery electrodes. *Nat Mater* **2014,** *13* (12), 1149-1156.

5. Johnson, B. A.; White, R. E., Characterization of commercially available lithium-ion batteries. *Journal of Power Sources* **1998,** *70* (1), 48-54.

6. Aurbach, D.; Markovsky, B.; Rodkin, A.; Cojocaru, M.; Levi, E.; Kim, H.-J., An analysis of rechargeable lithium-ion batteries after prolonged cycling. *Electrochimica Acta* **2002,** *47* (12), 1899-1911.

7. Gogotsi, Y.; Simon, P., True Performance Metrics in Electrochemical Energy Storage. *Science* **2011,** *334* (6058), 917-918.

8. He, Y.; Downing, R. G.; Wang, H., 3D mapping of lithium in battery electrodes using neutron activation. *Journal of Power Sources* **2015,** *287* (0), 226-230.

9. Whittingham, M. S., Ultimate Limits to Intercalation Reactions for Lithium Batteries. *Chemical Reviews* **2014,** *114* (23), 11414-11443.

10. Strobridge, F. C.; Orvananos, B.; Croft, M.; Yu, H.-C.; Robert, R.; Liu, H.; Zhong, Z.; Connolley, T.; Drakopoulos, M.; Thornton, K.; Grey, C. P., Mapping the Inhomogeneous

Electrochemical Reaction Through Porous LiFePO4-Electrodes in a Standard Coin Cell Battery. *Chemistry of Materials* **2015,** *27* (7), 2374-2386.

11. Burns, J. C.; Kassam, A.; Sinha, N. N.; Downie, L. E.; Solnickova, L.; Way, B. M.; Dahn, J. R., Predicting and Extending the Lifetime of Li-Ion Batteries. *Journal of The Electrochemical Society* **2013,** *160* (9), A1451-A1456.

12. Qiu, H.; Zeng, L.; Lan, T.; Ding, X.; Wei, M., In situ synthesis of GeO2/reduced graphene oxide composite on Ni foam substrate as a binder-free anode for high-capacity lithium-ion batteries. *J. Mater. Chem. A* **2015,** *3* (Copyright (C) 2015 American Chemical Society (ACS). All Rights Reserved.), 1619-1623.

13. Poetz, S.; Fuchsbichler, B.; Schmuck, M.; Koller, S., Development of a 3d current collector for the positive electrode in lithium-ion batteries. *J. Appl. Electrochem.* **2014,** *44* (Copyright (C) 2015 American Chemical Society (ACS). All Rights Reserved.), 989-994.

14. Um, J. H.; Park, H.; Cho, Y.-H.; Glazer, M. P. B.; Dunand, D. C.; Choe, H.; Sung, Y.-E., 3D interconnected SnO2-coated Cu foam as a high-performance anode for lithium-ion battery applications. *RSC Advances* **2014,** *4* (101), 58059-58063.

15. Hu, L.; La Mantia, F.; Wu, H.; Xie, X.; McDonough, J.; Pasta, M.; Cui, Y., Lithium-Ion Textile Batteries with Large Areal Mass Loading. *Advanced Energy Materials* **2011,** *1* (6), 1012-1017.

16. Hu, Y.; Sun, X., Flexible rechargeable lithium ion batteries: advances and challenges in materials and process technologies. *Journal of Materials Chemistry A* **2014,** *2* (28), 10712-10738.

17. Han, S.; Wu, D.; Li, S.; Zhang, F.; Feng, X., Porous Graphene Materials for Advanced Electrochemical Energy Storage and Conversion Devices. *Advanced Materials* **2014,** *26* (6), 849-864.

18. Hang, T.; Nara, H.; Yokoshima, T.; Momma, T.; Osaka, T., Silicon composite thick film electrodeposited on a nickel micro-nanocones hierarchical structured current collector for lithium batteries. *Journal of Power Sources* **2013,** *222* (0), 503-509.

19. Hang, T.; Mukoyama, D.; Nara, H.; Yokoshima, T.; Momma, T.; Li, M.; Osaka, T., Electrochemical impedance analysis of electrodeposited Si–O–C composite thick film on Cu

microcones-arrayed current collector for lithium ion battery anode. *Journal of Power Sources* **2014,** *256* (0), 226-232.

20. Arthur, T. S.; Bates, D. J.; Cirigliano, N.; Johnson, D. C.; Malati, P.; Mosby, J. M.; Perre, E.; Rawls, M. T.; Prieto, A. L.; Dunn, B., Three-dimensional electrodes and battery architectures. *MRS Bulletin* **2011,** *36* (07), 523-531.

21. Long, J. W.; Dunn, B.; Rolison, D. R.; White, H. S., Three-Dimensional Battery Architectures. *Chemical Reviews* **2004,** *104* (10), 4463-4492.

5. PROPOSED PROJECT: NANOPOROUS CARBON FOR INTERCALATION OF Mg^{++} IONS

Existing Mg^{++} ion chemistries for high voltage - greater than 3V - batteries require electrolytes that are incompatible with most metal oxide cathode materials because of slow insertion kinetics and/or side reactions with solution species. Therefore, it is strongly desirable to select simpler electrolytes (using solvents such as PC and AN and salts such as $Mg(TFSI)_2$ and $Mg(ClO_4)_2$) that are simultaneously a) compatible with high voltage cathodes, b) composed of solvents with wider windows of electrochemical stability and c) use salts that are simpler, more stable and permit faster desolvation, i.e., charge/discharge rates. As the adoption of these simpler electrolytes does not permit the use of Mg metal as the battery anode due to decomposition reactions on the Mg metal surface which form of a Mg^{++} blocking surface film, an alternative charge storage material would be required. Ideally, this material would be analogous to the graphite used in commercial Li^{+} ion batteries, allowing for fast charge/discharge via the mechanism of ion intercalation. Heretofore, no such material has been identified and only slow charge/discharge Mg-alloying type anode materials requiring solid-state Mg diffusion (Sn, Bi) have been studied.

Mg^{++} intercalation is different in kind than that of Li^{+} in graphite, because solvent species accompany the Mg^{++}. Accordingly, the dimension and charge of the partially solvated Mg^{++} is dependent upon the chemistry of the electrolyte. The Mg^{++} charge storage material must therefore be designed with a tunable and narrowly defined porosity to simultaneously accommodate Mg^{++} charge storage and maximize energy density. Control of these critical material properties can be achieved for an electrochemically stable nanoporous carbon (NPC) material formed by pulsed laser deposition. It is proposed to identify the critical porosity required for Mg^{++} intercalation from several electrolytes.

Bibliography

A. Al-Maghrabi, J. Suzuki, R. J. Sanderson, V. L. Chevrier, R. A. Dunlap and J. R. Dahn, Journal of The Electrochemical Society, 2013, 160, A1587-A1593.

A. Courtney and J. R. Dahn, Journal of The Electrochemical Society, 1997, 144, 2943-2948.

A. Courtney and J. R. Dahn, Journal of The Electrochemical Society, 1997, 144, 2045-2052.

A. Courtney, W. R. McKinnon and J. R. Dahn, Journal of The Electrochemical Society, 1999, 146, 59-68.

A. Drozhzhin, M. A. Vorotyntsev, S. R. Maduar, N. R. Khasanova, A. M. Abakumov and E. V. Antipov, Electrochimica Acta, 2013, 89, 262-269.

A. Johnson and R. E. White, Journal of Power Sources, 1998, 70, 48-54.

A. Rogers, T. Someya and Y. Huang, Science, 2010, 327, 1603-1607.

A. Schneider, W. S. Rasband and K. W. Eliceiri, Nat. Methods, 2012, 9, 671-675.

A.M. Chockla, K. Klavetter, C.B. Mullins, B.A. Korgel, ACS Appl Mater Interfaces, (2012).

A.M. Chockla, K.C. Klavetter, C.B. Mullins, B.A. Korgel, ACS Appl Mater Interfaces, 4 (2012) 4658-4664.

A.M. Chockla, K.C. Klavetter, C.B. Mullins, B.A. Korgel, Chemistry of Materials, 24 (2012) 3738-3745.

A.S. Arico, P. Bruce, B. Scrosati, J.-M. Tarascon, W. van Schalkwijk, Nat Mater, 4 (2005) 366-377.

A.S. Jing Li, R. J. Sanderson, T. D. Hatchard, R. A. Dunlap, and J. R. Dahn, J. Electrochem. Soc., 156 (2009) A283-288.

Applestone and A. Manthiram, RSC Advances, 2012, 2, 5411-5417.

Arthur, T. S.; Bates, D. J.; Cirigliano, N.; Johnson, D. C.; Malati, P.; Mosby, J. M.; Perre, E.; Rawls, M. T.; Prieto, A. L.; Dunn, B., Three-dimensional electrodes and battery architectures. *MRS Bulletin* **2011,** *36* (07), 523-531.

Aurbach, D.; Markovsky, B.; Rodkin, A.; Cojocaru, M.; Levi, E.; Kim, H.-J., An analysis of rechargeable lithium-ion batteries after prolonged cycling. *Electrochimica Acta* **2002,** *47* (12), 1899-1911.

Baggetto, E.J.M. Hensen, P.H.L. Notten, Electrochimica Acta, 55 (2010) 7074-7079.

Baggetto, P.H.L. Notten, Journal of The Electrochemical Society, 156 (2009) A169-A175.

Burns, J. C.; Kassam, A.; Sinha, N. N.; Downie, L. E.; Solnickova, L.; Way, B. M.; Dahn, J. R., Predicting and Extending the Lifetime of Li-Ion Batteries. *Journal of The Electrochemical Society* **2013,** *160* (9), A1451-A1456.

C. Howlett, D. R. MacFarlane and A. F. Hollenkamp, J. Power Sources, 2003, 114, 277-

C. Klavetter, S. M. Wood, Y.-M. Lin, J. L. Snider, N. C. Davy, A. M. Chockla, D. K. Romanovicz, B. A. Korgel, J.-W. Lee, A. Heller and C. B. Mullins, Journal of Power Sources, 2013, 238, 123-136.

C. Klavetter, S. M. Wood, Y.-M. Lin, J. L. Snider, N. C. Davy, A. M. Chockla, D. K. Romanovicz, B. A. Korgel, J.-W. Lee, A. Heller and C. B. Mullins, Journal of Power Sources, 2013, 238, 123-136.

C.K. Chan, H. Peng, G. Liu, K. McIlwrath, X.F. Zhang, R.A. Huggins, Y. Cui, Nat Nano, 3 (2008) 31-35.

C.K. Chan, X.F. Zhang, Y. Cui, Nano Letters, 8 (2007) 307-309.

C.S. Fuller, J.C. Severiens, Physical Review, 96 (1954) 21-24.

C.-Y. Chou and G. S. Hwang, Journal of Power Sources, 2014, 263, 252-258.

Chattopadhyay, A. L. Lipson, H. J. Karmel, J. D. Emery, T. T. Fister, P. A. Fenter, M. C. Hersam and M. J. Bedzyk, Chemistry of Materials, 2012, 24, 3038-3043.

Chen, X.-h. Xia, J.-p. Tu, Q.-q. Xiong, Y.-X. Yu, X.-l. Wang and C.-d. Gu, Journal of Materials Chemistry, 2012, 22, 15056-15061.

Cheng, Z. Song, T. Ma, B. B. Smith, R. Tang, H. Yu, H. Jiang and C. K. Chan, Nano Letters, 2013, 13, 4969-4974.

Cohen, Y. S.; Cohen, Y.; Aurbach, D., Micromorphological Studies of Lithium Electrodes in Alkyl Carbonate Solutions Using in Situ Atomic Force Microscopy. *The Journal of Physical Chemistry B* **2000,** *104* (51), 12282-12291.

D. Larcher, G. Sudant, J.-B. Leriche, Y. Chabre and J.-M. Tarascon, Journal of The Electrochemical Society, 2002, 149, A234-A241.

D. T. Ngo, R. S. Kalubarme, H. T. T. Le, J. G. Fisher, C.-N. Park, I.-D. Kim and C.-J. Park, Advanced Functional Materials, 2014, 24, 5291-5298.

D. Wang, Y.-L. Chang, Q. Wang, J. Cao, D.B. Farmer, R.G. Gordon, H. Dai, Journal of the American Chemical Society, 126 (2004) 11602-11611.

D. Wang, Z. Yang, F. Li, D. Liu, X. Wang, H. Yan, D. He, Materials Letters, 65 (2011) 1542-1544.

D. Y. W. Yu, P. V. Prikhodchenko, C. W. Mason, S. K. Batabyal, J. Gun, S. Sladkevich, A. G. Medvedev and O. Lev, Nat Commun, 2013, 4, 2922.

D. Y. Wang and J. R. Dahn, Journal of The Electrochemical Society, 2014, 161, A1890-A1897.

D.-J. Xue, S. Xin, Y. Yan, K.-C. Jiang, Y.-X. Yin, Y.-G. Guo, L.-J. Wan, Journal of the American Chemical Society, 134 (2012) 2512-2515.

Dahal, I. A. Ibarra and S. M. Humphrey, Journal of Materials Chemistry, 2012, 22, 12675-12681.

Ding, F.; Xu, W.; Chen, X.; Zhang, J.; Shao, Y.; Engelhard, M. H.; Zhang, Y.; Blake, T. A.; Graff, G. L.; Liu, X.; Zhang, J.-G., Effects of Cesium Cations in Lithium Deposition via Self-Healing Electrostatic Shield Mechanism. *The Journal of Physical Chemistry C* **2014,** *118* (8), 4043-4049.

Djian, F. Alloin, S. Martinet, H. Lignier, J.Y. Sanchez, Journal of Power Sources, 172 (2007) 416-421.

Du, R. A. Dunlap and M. N. Obrovac, Journal of The Electrochemical Society, 2014, 161, A1698-A1705.

Ely, D. R.; García, R. E., Heterogeneous Nucleation and Growth of Lithium Electrodeposits on Negative Electrodes. *Journal of The Electrochemical Society* **2013,** *160* (4), A662-A668.

Etacheri, O. Haik, Y. Goffer, G. A. Roberts, I. C. Stefan, R. Fasching and D. Aurbach, Langmuir, 2011, 28, 965-976.

Etacheri, O. Haik, Y. Goffer, G.A. Roberts, I.C. Stefan, R. Fasching, D. Aurbach, Langmuir, 28 (2011) 965-976.

Etacheri, U. Geiger, Y. Gofer, G.A. Roberts, I.C. Stefan, R. Fasching, D. Aurbach, Langmuir, 28 (2012) 6175-6184.

Fan, L. Y. Lim, Y. Y. Tay, S. S. Pramana, X. Rui, M. K. Samani, Q. Yan, B. K. Tay, M. F. Toney and H. H. Hng, Journal of Materials Chemistry A, 2013, 1, 14577-14585.

Foster, J. Wolfenstine, J. Read and J. L. Allen, Performance of Sony's Alloy Based Li-ion Battery, S. a. E. D. Directorate Report ARL-TN-0319, Army Research Laboratory, Army Research Laboratory, 2008.

Frequently Asked Questions, http://www.jetpulverizer.com/faq.php#link-7, 2014.

Fu, X. Li, X. Sun, X. Wang, D. Liu and D. He, Journal of Materials Chemistry, 2012, 22, 17429-17431.

G. Carbon, TIMREX Graphite, ENSACO, SUPER P Li Carbon Black: Carbon powders for Lithium battery systems,

G. Crabtree, AIP Conference Proceedings, 2015, 112.

G.A. Umeda, E. Menke, M. Richard, K.L. Stamm, F. Wudl, B. Dunn, Journal of Materials Chemistry, 21 (2011) 1593-1599.

Gauthier, D. Reyter, D. Mazouzi, P. Moreau, D. Guyomard, B. Lestriez and L. Roué, Journal of Power Sources, 2014, 256, 32-36.

Gogotsi, Y.; Simon, P., True Performance Metrics in Electrochemical Energy Storage. *Science* **2011,** *334* (6058), 917-918.

Goodman, J. K. S.; Kohl, P. A., Effect of Alkali and Alkaline Earth Metal Salts on Suppression of Lithium Dendrites. *Journal of The Electrochemical Society* **2014,** *161* (9), D418-D424.

Gwon, H.-S. Kim, K. U. Lee, D.-H. Seo, Y. C. Park, Y.-S. Lee, B. T. Ahn and K. Kang, Energy & Environmental Science, 2011, 4, 1277-1283.

Gwon, J. Hong, H. Kim, D.-H. Seo, S. Jeon and K. Kang, Energy & Environmental Science, 2014, 7, 538-551.

H. Liu, S. Huang, S. T. Picraux, J. Li, T. Zhu and J. Y. Huang, Nano Letters, 2011, 11, 3991-3997.

H. Luo, Z. Shi, N. Li, Z. Gu and Q. Zhuang, Analytical Chemistry, 2001, 73, 915-920.

H. Nakai, T. Kubota, A. Kita and A. Kawashima, Journal of The Electrochemical Society, 2011, 158, A798-A801.

H. Nakai, T. Kubota, A. Kita, A. Kawashima, Journal of The Electrochemical Society, 158 (2011) A798-A801.

H. Nishide and K. Oyaizu, Science, 2008, 319, 737-738.

H. Rho and K. Kanamura, Journal of Solid State Chemistry, 2004, 177, 2094-2100.

H. S. Im, Y. R. Lim, Y. J. Cho, J. Park, E. H. Cha and H. S. Kang, The Journal of Physical Chemistry C, 2014, 118, 21884-21888.

H. Wu, G. Chan, J.W. Choi, I. Ryu, Y. Yao, M.T. McDowell, S.W. Lee, A. Jackson, Y. Yang, L. Hu, Y. Cui, Nat. Nanotechnol., 7 (2012) 310-315.

H. Wu, G. Zheng, N. Liu, T.J. Carney, Y. Yang, Y. Cui, Nano Letters, 12 (2012) 904-909.

H. Wu, Y. Cui, Nano Today, 7 (2012) 414-429.

Han, S.; Wu, D.; Li, S.; Zhang, F.; Feng, X., Porous Graphene Materials for Advanced Electrochemical Energy Storage and Conversion Devices. *Advanced Materials* **2014,** *26* (6), 849-864.

Hang, T.; Mukoyama, D.; Nara, H.; Yokoshima, T.; Momma, T.; Li, M.; Osaka, T., Electrochemical impedance analysis of electrodeposited Si–O–C composite thick film on Cu microcones-arrayed current collector for lithium ion battery anode. *Journal of Power Sources* **2014,** *256* (0), 226-232.

Hang, T.; Nara, H.; Yokoshima, T.; Momma, T.; Osaka, T., Silicon composite thick film electrodeposited on a nickel micro-nanocones hierarchical structured current collector for lithium batteries. *Journal of Power Sources* **2013,** *222* (0), 503-509.

He, Y.; Downing, R. G.; Wang, H., 3D mapping of lithium in battery electrodes using neutron activation. *Journal of Power Sources* **2015,** *287* (0), 226-230.

Hertzberg, A. Alexeev, G. Yushin, Journal of the American Chemical Society, 132 (2010) 8548-8549.

http://www.foodsaver.com/vacuum-sealers/FSFSSL2244-P00.html#start=10.

http://www.scribner.com/.

Hu, L.; La Mantia, F.; Wu, H.; Xie, X.; McDonough, J.; Pasta, M.; Cui, Y., Lithium-Ion Textile Batteries with Large Areal Mass Loading. *Advanced Energy Materials* **2011,** *1* (6), 1012-1017.

Hu, Y.; Sun, X., Flexible rechargeable lithium ion batteries: advances and challenges in materials and process technologies. *Journal of Materials Chemistry A* **2014,** *2* (28), 10712-10738.

Huang, H. Yu, J. Chen, Z. Lu, R. Yazami and H. H. Hng, Advanced Materials, 2014, DOI: 10.1002/adma.201304467, n/a-n/a.

Huggins, W. Nix, Ionics, 6 (2000) 57-63.

Hui, W. Jianbo, Z. Chuanxin, M. Xiangyang, D. Ning, T. Jiangping and Y. Deren, Nanotechnology, 2008, 19, 035711.

J. B. Goodenough and K.-S. Park, Journal of the American Chemical Society, 2013, 135, 1167-1176.

J. Chen, Y. Liu, A. I. Minett, C. Lynam, J. Wang and G. G. Wallace, Chemistry of Materials, 2007, 19, 3595-3597.

J. Goodenough, J Solid State Electrochem, 16 (2012) 2019-2029.

J. Graetz, C. C. Ahn, R. Yazami and B. Fultz, Journal of The Electrochemical Society, 2004, 151, A698-A702.

J. Graetz, C.C. Ahn, R. Yazami, B. Fultz, J. Electrochem. Soc., 151 (2004) A698-A702.

J. Graetz, C.C. Ahn, R. Yazami, B. Fultz, Journal of The Electrochemical Society, 151 (2004) A698-A702.

J. K. Lee, K. B. Smith, C. M. Hayner and H. H. Kung, Chemical Communications, 2010, 46, 2025-2027.

J. Liang, Y. Zhao, L. Guo and L. Li, ACS Appl. Mater. Interfaces, 2012, 4, 5742-5748.

J. Liu and A. Manthiram, Chemistry of Materials, 2009, 21, 1695-1707.

J. Liu, A. Manthiram, Chemistry of Materials, 21 (2009) 1695-1707.

J. M. Zuo and J. C. Mabon, Microsc Microanal, 2004, 10.

J. Smith, J. C. Burns, S. Trussler and J. R. Dahn, Journal of The Electrochemical Society, 2010, 157, A196-A202.

J. Song, S. Chen, M. Zhou, T. Xu, D. Lv, M. L. Gordin, T. Long, M. Melnyk and D. Wang, Journal of Materials Chemistry A, 2014, 2, 1257-1262.

J. Sun, H. Liu, X. Chen, D. G. Evans and W. Yang, Nanoscale, 2013, 5, 7564-7571.

J. Wang, N. Du, H. Zhang, J. Yu, D. Yang, Journal of Materials Chemistry, 22 (2012) 1511-1515.

J.B. Goodenough, Y. Kim, Chemistry of Materials, 22 (2009) 587-603.

J.B. Goodenough, Y. Kim, Journal of Power Sources, 196 (2011) 6688-6694.

J.H. Seo, J. Park, G. Plett, A.M. Sastry, Electrochemical and Solid-State Letters, 13 (2010) A135-A137.

J.W. Choi, L. Hu, L. Cui, J.R. McDonough, Y. Cui, Journal of Power Sources, 195 (2010) 8311-8316.

Jet Pulverizer Works to Commercialize Emerging Lithium-Ion Battery Technology, http://www.jetpulverizer.com/news-and-events/article01.php, 2009.

Jo, I. Choi, H. Ahn, M.J. Park, Chemical Communications, 48 (2012) 3987-3989.

Johnson, B. A.; White, R. E., Characterization of commercially available lithium-ion batteries. *Journal of Power Sources* **1998,** *70* (1), 48-54.

Jorn, R. Kumar, D. P. Abraham and G. A. Voth, The Journal of Physical Chemistry C, 2013, 117, 3747-3761.

K. C. Klavetter, S. M. Wood, Y.-M. Lin, J. L. Snider, N. C. Davy, A. M. Chockla, D. K. Romanovicz, B. A. Korgel, J.-W. Lee, A. Heller and C. B. Mullins, Journal of Power Sources, 2013, 238, 123-136.

K. Evanoff, J. Benson, M. Schauer, I. Kovalenko, D. Lashmore, W. J. Ready and G. Yushin, ACS Nano, 2012, 6, 9837-9845.

K. Kercher, J. O. Kiggans and N. J. Dudney, Journal of The Electrochemical Society, 2010, 157, A1323-A1327.

K. M. Shaju, F. Jiao, A. Debart and P. G. Bruce, Physical Chemistry Chemical Physics, 2007, 9, 1837-1842.

K. Rhodes, M. Kirkham, R. Meisner, C. M. Parish, N. Dudney and C. Daniel, Review of Scientific Instruments, 2011, 82, 075107-075107-075107.

K. T. Nam, D.-W. Kim, P. J. Yoo, C.-Y. Chiang, N. Meethong, P. T. Hammond, Y.-M. Chiang and A. M. Belcher, Science, 2006, 312, 885-888.

K. Xu, Chemical Reviews, 2014, 114, 11503-11618.

K. Xu, Y. Lam, S. S. Zhang, T. R. Jow and T. B. Curtis, The Journal of Physical Chemistry C, 2007, 111, 7411-7421.

K.H. Seng, M.-H. Park, Z.P. Guo, H.K. Liu, J. Cho, Angewandte Chemie International Edition, 51 (2012) 5657-5661.

K.T. Lee, J. Cho, Nano Today, 6 (2011) 28-41.

Kasavajjula, C. Wang, A.J. Appleby, Journal of Power Sources, 163 (2007) 1003-1039.

Kennedy, E. Mullane, H. Geaney, M. Osiak, C. O'Dwyer and K. M. Ryan, Nano Letters, 2014, 14, 716-723.

Khurana, R.; Schaefer, J. L.; Archer, L. A.; Coates, G. W., Suppression of Lithium Dendrite Growth Using Cross-Linked Polyethylene/Poly(ethylene oxide) Electrolytes: A New Approach for Practical Lithium-Metal Polymer Batteries. *Journal of the American Chemical Society* **2014,** *136* (20), 7395-7402.

Kim, M. Noh, M. Choi, J. Cho and B. Park, Chemistry of Materials, 2005, 17, 3297-3301.

Klein, B. Jache, A. Bhide and P. Adelhelm, Physical Chemistry Chemical Physics, 2013, 15, 15876-15887.

L. Hu, F. La Mantia, H. Wu, X. Xie, J. McDonough, M. Pasta and Y. Cui, Advanced Energy Materials, 2011, 1, 1012-1017.

L. Hu, H. Wu, F. La Mantia, Y. Yang and Y. Cui, ACS Nano, 2010, 4, 5843-5848.

L. Hu, H. Wu, Y. Gao, A. Cao, H. Li, J. McDough, X. Xie, M. Zhou, Y. Cui, Advanced Energy Materials, 1 (2011) 523-527.

L. Hu, J. W. Choi, Y. Yang, S. Jeong, F. La Mantia, L.-F. Cui and Y. Cui, Proceedings of the National Academy of Sciences, 2009, 106, 21490-21494.

L. Hu, N. Yan, Q. Chen, P. Zhang, H. Zhong, X. Zheng, Y. Li and X. Hu, Chemistry – A European Journal, 2012, 18, 8971-8977.

L. Jabbour, C. Gerbaldi, D. Chaussy, E. Zeno, S. Bodoardo and D. Beneventi, J. Mater. Chem., 2010, 20, 7344-7347.

L. Jabbour, M. Destro, C. Gerbaldi, D. Chaussy, N. Penazzi and D. Beneventi, J. Mater. Chem., 2012, 22, 3227-3233.

L. Jabbour, M. Destro, D. Chaussy, C. Gerbaldi, N. Penazzi, S. Bodoardo and D. Beneventi, Cellulose (Dordrecht, Neth.), 2013, 20, 571-582.

L. Li, G. Zhou, X.-Y. Shan, S. Pei, F. Li and H.-M. Cheng, Journal of Power Sources, 2014, 255, 52-58.

L. Lu, M.L. Sui, K. Lu, Science, 287 (2000) 1463-1466.

L. Noerochim, J.-Z. Wang, D. Wexler, Z. Chao and H.-K. Liu, Journal of Power Sources, 2013, 228, 198-205.

L. Noerochim, J.-Z. Wang, S.-L. Chou, D. Wexler and H.-K. Liu, Carbon, 2012, 50, 1289-1297.

L. Ross and M. Bourgon, Canadian Journal of Chemistry, 1969, 47, 2555-2559.

L. Yue, H. Zhong and L. Zhang, Electrochimica Acta, 2012, 76, 326-332.

L. Zhan, Y. Wang, W. Qiao, L. Ling and S. Yang, Electrochimica Acta, 2012, 78, 440-445.

L.C. Yang, Q.S. Gao, L. Li, Y. Tang, Y.P. Wu, Electrochemistry Communications, 12 (2010) 418-421.

L.-F. Cui, L. Hu, J. W. Choi and Y. Cui, ACS Nano, 2010, 4, 3671-3678.

L.Y. Beaulieu, S.D. Beattie, T.D. Hatchard, J.R. Dahn, Journal of The Electrochemical Society, 150 (2003) A419-A424.

Lee, H. Kim, S.-G. Doo, J. Cho, J. Electrochem. Soc., 154 (2007) A343-A346.

Lee, M.G. Kim, C.H. Choi, Y.-K. Sun, C.S. Yoon, J. Cho, The Journal of Physical Chemistry B, 109 (2005) 20719-20723.

Li, C. R. Martin and B. Scrosati, Electrochemical and Solid-State Letters, 2000, 3, 316-318.

Li, Y.; El Gabaly, F.; Ferguson, T. R.; Smith, R. B.; Bartelt, N. C.; Sugar, J. D.; Fenton, K. R.; Cogswell, D. A.; Kilcoyne, A. L. D.; Tyliszczak, T.; Bazant, M. Z.; Chueh, W. C., Current-

induced transition from particle-by-particle to concurrent intercalation in phase-separating battery electrodes. *Nat Mater* **2014,** *13* (12), 1149-1156.

Liang, H. Yang, F. Fan, Y. Liu, X. H. Liu, J. Y. Huang, T. Zhu and S. Zhang, ACS Nano, 2013, 7, 3427-3433.

Lithium Batteries: Science and Technology, Springer, 2003.

Liu, J. Zhang, X. Wang, G. Chen, D. Chen, C. Zhou and G. Shen, Nano Letters, 2012, 12, 3005-3011.

Long, J. W.; Dunn, B.; Rolison, D. R.; White, H. S., Three-Dimensional Battery Architectures. *Chemical Reviews* **2004,** *104* (10), 4463-4492.

Lu, W.; Jansen, A.; Dees, D.; Nelson, P.; Veselka, N. R.; Henriksen, G., High-energy electrode investigation for plug-in hybrid electric vehicles. *Journal of Power Sources* **2011,** *196* (3), 1537-1540.

Lu, Y.; Tu, Z.; Archer, L. A., Stable lithium electrodeposition in liquid and nanoporous solid electrolytes. *Nat Mater* **2014,** *13* (10), 961-969.

M. Andersson and K. Edström, Journal of The Electrochemical Society, 2001, 148, A1100-A1109.

M. Chockla, J. T. Harris, V. A. Akhavan, T. D. Bogart, V. C. Holmberg, C. Steinhagen, C. B. Mullins, K. J. Stevenson and B. A. Korgel, Journal of the American Chemical Society, 2011, 133, 20914-20921.

M. Chockla, K. C. Klavetter, C. B. Mullins and B. A. Korgel, ACS Applied Materials & Interfaces, 2012, 4, 4658-4664.

M. H. Park, Y. S. Lee, H. Lee and Y.-K. Han, J. Power Sources, 2011, 196, 5109-5114.

M. Koo, K.-I. Park, S. H. Lee, M. Suh, D. Y. Jeon, J. W. Choi, K. Kang and K. J. Lee, Nano Letters, 2012, 12, 4810-4816.

M. M. Rahman, A. M. Glushenkov, T. Ramireddy and Y. Chen, Chemical Communications, 2014, 50, 5057-5060.

M. Mohamedi, S.-J. Lee, D. Takahashi, M. Nishizawa, T. Itoh and I. Uchida, Electrochimica Acta, 2001, 46, 1161-1168.

M. N. Obrovac and L. J. Krause, Journal of The Electrochemical Society, 2007, 154, A103-A108.

M. N. Obrovac, L. Christensen, D. B. Le and J. R. Dahn, Journal of The Electrochemical Society, 2007, 154, A849-A855.

M. Pedram and Q. Wu, presented in part at the Proceedings of the 36th annual ACM/IEEE Design Automation Conference, New Orleans, Louisiana, USA, 1999.

M. Roberts, P. Johns, J. Owen, D. Brandell, K. Edstrom, G. El Enany, C. Guery, D. Golodnitsky, M. Lacey, C. Lecoeur, H. Mazor, E. Peled, E. Perre, M. M. Shaijumon, P. Simon and P.-L. Taberna, Journal of Materials Chemistry, 2011, 21, 9876-9890.

M. T. McDowell, I. Ryu, S. W. Lee, C. Wang, W. D. Nix and Y. Cui, Advanced Materials, 2012, 24, 6034-6041.

M. T. McDowell, S. W. Lee, J. T. Harris, B. A. Korgel, C. Wang, W. D. Nix and Y. Cui, Nano Letters, 2013, 13, 758-764.

M. Wu, J. E. C. Sabisch, X. Song, A. M. Minor, V. S. Battaglia and G. Liu, Nano Letters, 2013, 13, 5397-5402.

M.-H. Park, K. Kim, J. Kim, J. Cho, Advanced Materials, 22 (2010) 415-418.

M.-H. Park, Y. Cho, K. Kim, J. Kim, M. Liu, J. Cho, Angewandte Chemie International Edition, 50 (2011) 9647-9650.

M.-H. Seo, M. Park, K.T. Lee, K. Kim, J. Kim, J. Cho, Energy & Environmental Science, 4 (2011) 425-428.

M.-J. Chun, H. Park, S. Park and N.-S. Choi, RSC Advances, 2013, 3, 21320-21325.

M.T. McDowell, S.W. Lee, I. Ryu, H. Wu, W.D. Nix, J.W. Choi, Y. Cui, Nano Letters, 11 (2011) 4018-4025.

Magasinski, B. Zdyrko, I. Kovalenko, B. Hertzberg, R. Burtovyy, C.F. Huebner, T.F. Fuller, I. Luzinov, G. Yushin, ACS Applied Materials & Interfaces, 2 (2010) 3004-3010.

Mei, J. Huang, L. Zhu, Z. Ye, Y. Mai and J. Tu, Journal of Materials Chemistry, 2012, 22, 9315-9321.

Miao, R.; Yang, J.; Feng, X.; Jia, H.; Wang, J.; Nuli, Y., Novel dual-salts electrolyte solution for dendrite-free lithium-metal based rechargeable batteries with high cycle reversibility. *Journal of Power Sources* **2014,** *271* (0), 291-297.

Mullane, T. Kennedy, H. Geaney and K. M. Ryan, ACS Applied Materials & Interfaces, 2014, 6, 18800-18807.

N. Li, Z. Chen, W. Ren, F. Li and H.-M. Cheng, Proceedings of the National Academy of Sciences, 2012, 109, 17360-17365.

N. Liu, Z. Lu, J. Zhao, M. T. McDowell, H.-W. Lee, W. Zhao and Y. Cui, Nat Nano, 2014, 9, 187-192.

N. Pahimanolis, A. Salminen, P. Penttilä, J. Korhonen, L.-S. Johansson, J. Ruokolainen, R. Serimaa and J. Seppälä, Cellulose, 2013, 20, 1459-1468.

N. Yan, L. Hu, Y. Li, Y. Wang, H. Zhong, X. Hu, X. Kong and Q. Chen, The Journal of Physical Chemistry C, 2012, 116, 7227-7235.

N.G. Rudawski, B.L. Darby, B.R. Yates, K.S. Jones, R.G. Elliman, A.A. Volinsky, Applied Physics Letters, 100 (2012) 083111-083114.

N.-S. Choi, K. H. Yew, K. Y. Lee, M. Sung, H. Kim and S.-S. Kim, Journal of Power Sources, 2006, 161, 1254-1259.

N.-S. Choi, K.H. Yew, K.Y. Lee, M. Sung, H. Kim, S.-S. Kim, Journal of Power Sources, 161 (2006) 1254-1259.

Nexeon, Nexeon Technology Overview, http://www.nexeon.co.uk/technology-2/.

Nishida, T.; Nishikawa, K.; Rosso, M.; Fukunaka, Y., Optical observation of Li dendrite growth in ionic liquid. *Electrochimica Acta* **2013,** *100* (0), 333-341.

Nishikawa, K.; Mori, T.; Nishida, T.; Fukunaka, Y.; Rosso, M., Li dendrite growth and Li+ ionic mass transfer phenomenon. *Journal of Electroanalytical Chemistry* **2011,** *661* (1), 84-89.

P. E. Company, Lithium Ion NCR18650, http://industrial.panasonic.com/lecs/www-data/pdf2/ACA4000/ACA4000CE240.pdf.

P. R. Abel, Y.-M. Lin, T. de Souza, C.-Y. Chou, A. Gupta, J. B. Goodenough, G. S. Hwang, A. Heller and C. B. Mullins, The Journal of Physical Chemistry C, 2013, 117, 18885-18890.

P. Zhang, J. Qiu, Z. Zheng, G. Liu, M. Ling, W. Martens, H. Wang, H. Zhao and S. Zhang, Electrochimica Acta, 2013, 104, 41-47.

Poetz, S.; Fuchsbichler, B.; Schmuck, M.; Koller, S., Development of a 3d current collector for the positive electrode in lithium-ion batteries. *J. Appl. Electrochem.* **2014,** *44* (Copyright (C) 2015 American Chemical Society (ACS). All Rights Reserved.), 989-994.

Popov, K.; Djokic, S.; Grugur, B., *Fundamental Aspects of Electrometallurgy*. Kluwer Academic Publishers: New York, 2002.

Qian, J.; Henderson, W. A.; Xu, W.; Bhattacharya, P.; Engelhard, M.; Borodin, O.; Zhang, J.-G., High rate and stable cycling of lithium metal anode. *Nat Commun* **2015,** *6*.

Qiu, H.; Zeng, L.; Lan, T.; Ding, X.; Wei, M., In situ synthesis of GeO2/reduced graphene oxide composite on Ni foam substrate as a binder-free anode for high-capacity lithium-ion batteries. *J. Mater. Chem. A* **2015,** *3* (Copyright (C) 2015 American Chemical Society (ACS). All Rights Reserved.), 1619-1623.

R. Abel, K. C. Klavetter, A. Heller and C. B. Mullins, The Journal of Physical Chemistry C, 2014, 118, 17407-17412.

R. Abel, Y.-M. Lin, H. Celio, A. Heller and C. B. Mullins, ACS Nano, 2012, 6, 2506-2516.

Rosso, M.; Gobron, T.; Brissot, C.; Chazalviel, J. N.; Lascaud, S., Onset of dendritic growth in lithium/polymer cells. *Journal of Power Sources* **2001,** *97–98* (0), 804-806.

Ruffo, S.S. Hong, C.K. Chan, R.A. Huggins, Y. Cui, The Journal of Physical Chemistry C, 113 (2009) 11390-11398.

S. Kikkawa, T. Miyai and M. Koizumi, Solid State Ionics, 1988, 28–30, Part 1, 743-746.

S. Komaba, T. Ishikawa, N. Yabuuchi, W. Murata, A. Ito and Y. Ohsawa, ACS Applied Materials & Interfaces, 2011, 3, 4165-4168.

S. Komaba, W. Murata, T. Ishikawa, N. Yabuuchi, T. Ozeki, T. Nakayama, A. Ogata, K. Gotoh and K. Fujiwara, Advanced Functional Materials, 2011, 21, 3859-3867.

S. Leijonmarck, A. Cornell, G. Lindbergh and L. Waagberg, Nano Energy, DOI: 10.1016/j.nanoen.2013.02.002, Ahead of Print.

S. Li, Y. Luo, W. Lv, W. Yu, S. Wu, P. Hou, Q. Yang, Q. Meng, C. Liu and H.-M. Cheng, Advanced Energy Materials, 2011, 1, 486-490.

S. Malmgren, K. Ciosek, M. Hahlin, T. Gustafsson, M. Gorgoi, H. Rensmo and K. Edström, Electrochimica Acta, 2013, 97, 23-32.

S. Y. Chew, S. H. Ng, J. Wang, P. Novák, F. Krumeich, S. L. Chou, J. Chen and H. K. Liu, Carbon, 2009, 47, 2976-2983.

S. Yoon, C.-M. Park, H.-J. Sohn, Electrochemical and Solid-State Letters, 11 (2008) A42-A45.

S.-C. Chao, Y.-C. Yen, Y.-F. Song, Y.-M. Chen, H.-C. Wu and N.-L. Wu, Electrochemistry Communications, 2010, 12, 234-237.

S.-C. Chao, Y.-F. Song, C.-C. Wang, H.-S. Sheu, H.-C. Wu and N.-L. Wu, The Journal of Physical Chemistry C, 2011, 115, 22040-22047.

S.-L. Chou, Y. Zhao, J.-Z. Wang, Z.-X. Chen, H.-K. Liu and S.-X. Dou, The Journal of Physical Chemistry C, 2010, 114, 15862-15867.

S.-O. Kim and A. Manthiram, Journal of Materials Chemistry A, 2014, DOI: 10.1039/c4ta06113f.

S.S. Zhang, Journal of Power Sources, 162 (2006) 1379-1394.

Sano, H.; Sakaebe, H.; Senoh, H.; Matsumoto, H., Effect of Current Density on Morphology of Lithium Electrodeposited in Ionic Liquid-Based Electrolytes. *Journal of The Electrochemical Society* **2014,** *161* (9), A1236-A1240.

Strobridge, F. C.; Orvananos, B.; Croft, M.; Yu, H.-C.; Robert, R.; Liu, H.; Zhong, Z.; Connolley, T.; Drakopoulos, M.; Thornton, K.; Grey, C. P., Mapping the Inhomogeneous Electrochemical Reaction Through Porous LiFePO4-Electrodes in a Standard Coin Cell Battery. *Chemistry of Materials* **2015,** *27* (7), 2374-2386.

Suo, L.; Hu, Y.-S.; Li, H.; Armand, M.; Chen, L., A new class of Solvent-in-Salt electrolyte for high-energy rechargeable metallic lithium batteries. *Nat Commun* **2013,** *4*, 1481.

T. Marks, S. Trussler, A. J. Smith, D. Xiong and J. R. Dahn, Journal of The Electrochemical Society, 2011, 158, A51-A57.

T. S. Arthur, D. J. Bates, N. Cirigliano, D. C. Johnson, P. Malati, J. M. Mosby, E. Perre, M. T. Rawls, A. L. Prieto and B. Dunn, MRS Bulletin, 2011, 36, 523-531.

U. Kasavajjula, C. Wang and A. J. Appleby, Journal of Power Sources, 2007, 163, 1003-1039.

Um, J. H.; Park, H.; Cho, Y.-H.; Glazer, M. P. B.; Dunand, D. C.; Choe, H.; Sung, Y.-E., 3D interconnected SnO2-coated Cu foam as a high-performance anode for lithium-ion battery applications. *RSC Advances* **2014,** *4* (101), 58059-58063.

Umeda, G. A.; Menke, E.; Richard, M.; Stamm, K. L.; Wudl, F.; Dunn, B., Protection of lithium metal surfaces using tetraethoxysilane. *Journal of Materials Chemistry* **2011,** *21* (5), 1593-1599.

V. L. Chevrier, L. Liu, D. B. Le, J. Lund, B. Molla, K. Reimer, L. J. Krause, L. D. Jensen, E. Figgemeier and K. W. Eberman, Journal of The Electrochemical Society, 2014, 161, A783-A791.

V. L. Pushparaj, M. M. Shaijumon, A. Kumar, S. Murugesan, L. Ci, R. Vajtai, R. J. Linhardt, O. Nalamasu and P. M. Ajayan, Proceedings of the National Academy of Sciences, 2007, 104, 13574-13577.

Verma, P.; Maire, P.; Novák, P., A review of the features and analyses of the solid electrolyte interphase in Li-ion batteries. *Electrochimica Acta* **2010,** *55* (22), 6332-6341.

W.-J. Zhang, Journal of Power Sources, 196 (2011) 13-24.

Wang, D. Li, C. O. Too and G. G. Wallace, Chemistry of Materials, 2009, 21, 2604-2606.

Wang, X. Li, B. Luo, Y. Jia and L. Zhi, Nanoscale, 2013, 5, 1470-1474.

Whittingham, M. S., Ultimate Limits to Intercalation Reactions for Lithium Batteries. *Chemical Reviews* **2014,** *114* (23), 11414-11443.

Wood Iii, D. L.; Li, J.; Daniel, C., Prospects for reducing the processing cost of lithium ion batteries. *Journal of Power Sources* **2015,** *275* (0), 234-242.

Wu, A. Heidelberg, J.J. Boland, Nat Mater, 4 (2005) 525-529.

X. Li, J. Yang, Y. Hu, J. Wang, Y. Li, M. Cai, R. Li and X. Sun, Journal of Materials Chemistry, 2012, 22, 18847-18853.

X. Rui, H. Tan, D. Sim, W. Liu, C. Xu, H. H. Hng, R. Yazami, T. M. Lim and Q. Yan, Journal of Power Sources, 2013, 222, 97-102.

X. Wang, L. Yu, X.-L. Wu, F. Yuan, Y.-G. Guo, Y. Ma and J. Yao, The Journal of Physical Chemistry C, 2009, 113, 15553-15558.

X. Wang, X. Cao, L. Bourgeois, H. Guan, S. Chen, Y. Zhong, D.-M. Tang, H. Li, T. Zhai, L. Li, Y. Bando and D. Golberg, Advanced Functional Materials, 2012, 22, 2682-2690.

X. Yang, K. Fan, Y. Zhu, J. Shen, X. Jiang, P. Zhao, S. Luan and C. Li, ACS Appl. Mater. Interfaces, 2013, 5, 997-1002.

X. Zhao, R. A. Dunlap and M. N. Obrovac, Journal of The Electrochemical Society, 2014, 161, A1976-A1980.

X.H. Liu, S. Huang, S.T. Picraux, J. Li, T. Zhu, J.Y. Huang, Nano Letters, 11 (2011) 3991-3997.

X.-J. Zhu, J. Hu, H.-L. Dai, L. Ding and L. Jiang, Electrochimica Acta, 2012, 64, 23-28.

X.-L. Wang, W.-Q. Han, H. Chen, J. Bai, T. A. Tyson, X.-Q. Yu, X.-J. Wang and X.-Q. Yang, Journal of the American Chemical Society, 2011, 133, 20692-20695.

Y. Hu and X. Sun, Journal of Materials Chemistry A, 2014, DOI: 10.1039/c4ta00716f.

Y. Li, B. Tan and Y. Wu, Nano Letters, 2007, 8, 265-270.

Y. Liu, K. Huang, Y. Fan, Q. Zhang, F. Sun, T. Gao, L. Yang and J. Zhong, Electrochimica Acta, 2013, 88, 766-771.

Y. Lu, Y. Wang, Y. Zou, Z. Jiao, B. Zhao, Y. He and M. Wu, Electrochemistry Communications, 2010, 12, 101-105.

Y. Qian, A. Vu, W. Smyrl and A. Stein, Journal of The Electrochemical Society, 2012, 159, A1135-A1140.

Y. Xiao, C. Hu and M. Cao, Journal of Power Sources, 2014, 247, 49-56.

Y.-M. Kang, M.-S. Song, J.-H. Kim, H.-S. Kim, M.-S. Park, J.-Y. Lee, H. K. Liu and S. X. Dou, Electrochimica Acta, 2005, 50, 3667-3673.

Y.-M. Lin, K. C. Klavetter, A. Heller and C. B. Mullins, The Journal of Physical Chemistry Letters, 2013, 4, 999-1004.

Y.-M. Lin, K. C. Klavetter, P. R. Abel, N. C. Davy, J. L. Snider, A. Heller and C. B. Mullins, Chemical Communications, 2012, 48, 7268-7270.

Y.-M. Lin, K.C. Klavetter, P.R. Abel, N.C. Davy, J.L. Snider, A. Heller, C.B. Mullins, Chemical Communications, (2012).

Z. X. Shu, R. S. McMillan, J. J. Murray and I. J. Davidson, Journal of The Electrochemical Society, 1996, 143, 2230-2235.

Z.-S. Wu, W. Ren, L. Wen, L. Gao, J. Zhao, Z. Chen, G. Zhou, F. Li and H.-M. Cheng, ACS Nano, 2010, 4, 3187-3194.

Zhang, Y. Zhang, Z. Miao, T. Wu, Z. Zhang and X. Yang, J. Power Sources, 2014, 248, 289-295.

Zheng, G.; Lee, S. W.; Liang, Z.; Lee, H.-W.; Yan, K.; Yao, H.; Wang, H.; Li, W.; Chu, S.; Cui, Y., Interconnected hollow carbon nanospheres for stable lithium metal anodes. *Nat Nano* **2014,** *advance online publication*.

Zheng, H.; Li, J.; Song, X.; Liu, G.; Battaglia, V. S., A comprehensive understanding of electrode thickness effects on the electrochemical performances of Li-ion battery cathodes. *Electrochimica Acta* **2012,** *71* (0), 258-265.

Zhou, F. Li and H.-M. Cheng, Energy & Environmental Science, 2014, 7, 1307-1338.

Vita

Kyle Klavetter graduated from Eldorado High School in 2006. Kyle attended the University of Tulsa from which he graduated in 2010 with a B.S. in chemical engineering. Kyle then enrolled in the chemical engineering Ph.D. program at the University of Texas at Austin where he worked with Professor C. Buddie Mullins. Notably, he was awarded the National Science Foundation Graduate Research Fellowship in 2010 and attended the 65th Lindau Meeting for Nobel Laureates in 2015.

Email address: kcklave@gmail.com

This dissertation was typed by the author.